Doctoral Thesis

Remote sensing error assessment for subsequent use in model confrontation

Author:

Mei Sun Yee

Bachelor of Engineering

(Environmental)

Supervisors:

Prof. Jeff Walker

Dr. Christoph Rüdiger

Dr. Edoardo Daly

A thesis submitted for the degree of Doctor of Philosophy at

Monash University in June 2016

SENSING TECHNOLOGIES

Department of Civil Engineering

Abstract

Remote sensing provides an unprecedented opportunity to evaluate land surface models (LSMs) run at distributed scales. Yet, with so many remote sensing products available, it is unclear which product is the best, and how they should be validated due to the scaling issues between *in situ* measurements and remote sensing product grids. Therefore, a three-fold approach has been demonstrated at the Yanco core validation site in Australia (Yanco), whereby i) the representativeness of *in situ* soil moisture and evapotranspiration (ET) measurements within remote sensing product grids were investigated; ii) these representative measurements were used to validate remote sensing soil moisture and ET products, and iii) the validated products were used to evaluate distributed simulations of soil moisture and ET from the Joint UK Land Environment Simulator (JULES).

In this research, the soil moisture stations within Yanco which provided representative measurements were identified based on geostatistical and temporal stability analysis of long-term soil moisture measurements and intensive measurements from three extensive field campaigns. Measurements from these stations were then used to validate soil moisture products from the Advanced Microwave Scanning Radiometer - 2 (AMSR-2) and Soil Moisture and Ocean Salinity (SMOS). Of these two sensors, soil moisture products from SMOS were found to perform best. In the case of ET, measurements from the same footprint derived using optical (LAS) and microwave (MWS) scintillometers, and an eddy covariance (EC) system were firstly inter-compared to understand their performances relative to each other. Subsequently, scintillometers were placed across different areas of a single 4 km Multi-functional Transport SATellites (MTSAT) ET grid established the representativeness of measurements from an EC system of the grid. EC measurements were consequently used to validate the performance of MTSAT 4 km ET products based on the Surface Energy Balance System (SEBS), Modified Priestley Taylor (PT-JPL) and Modified Penman Monteith (PM-Mu) models, whereby the PT-JPL model was found to perform the best.

The importance of having a good understanding of satellite data was demonstrated by using both the best and poor products in a model intercomparison study showing that wrong conclusions can easily be reached. These results confirmed the utility of the rigorous and systematic methodology developed in this research.

Declaration of Authorship

I, Mei Sun Yee, declare that this thesis titled, 'Remote sensing error assessment for subsequent use in model confrontation' and the work presented in it are my own. I confirm that:

- This work was done wholly or mainly while in candidature for a research degree at this University.
- Where any part of this thesis has previously been submitted for a degree or any other qualification at this University or any other institution, this has been clearly stated.
- Where I have consulted the published work of others, this is always clearly attributed.
- Where I have quoted from the work of others, the source is always given. With the exception of such quotations, this thesis is entirely my own work.
- I have acknowledged all main sources of help.
- Where the thesis is based on work done by myself jointly with others, I have made clear exactly what was done by others and what I have contributed myself.

Signed: ____

Date: ____

Dedicated to my dear Papa who lives forever in my heart ...

Acknowledgements

First and foremost, I'd like to thank Jeff for his guidance and encouragement for me to go the extra mile and achieve what I thought was impossible. I would also like to thank Chris and Edo for their advice and feedback which has helped improve my writing and widen my perspective.

I am ever grateful to my family for being supportive and patient throughout this journey. I would not have been able to do it without their continuous encouragement and support. Not to forget, the Muradoğlus who opened up their home and made sure that my stomach was always filled with good food.

I would especially like to thank those who have assisted me in my fieldwork. Those involved in collecting the soil moisture data sets from SMAPEx campaigns, Sandra and Ling for processing data from the soil moisture stations, and Frank and Tim for their invaluable efforts in the installation and maintenance of the monitoring stations, JAXA tower and scintillometers. Not to forget, Val, for the opportunity to work with his scintillometers, and the Japan Aerospace exploration Agency for the JAXA flux tower datasets which made this research possible.

Thank you to all room 156-ers (old and new), friends and colleagues for their friendship, support and listening ear. Negin, Stefania, Sandra and Ranmalee for their invaluable advice and encouragement in research, and in life. Not forgetting my fellow hikers and the beautiful regional Victoria and Yanco which provided me the inspiration and sanity to persist. Last but not least, I am indebted to my fiancé, Murat, for his continuous patience and support.

Contents

List of Figures

List of Tables

Abbreviations

AACES	Australian Airborne Cal/Val Experiment for SMOS
ABL	Atmospheric boundary layer
ACCESS	Australian Community Climate and Earth-System Simulator
AMSR	Advanced Microwave Scanning Radiometer
AMSR-E	Advanced Microwave Scanning Radiometer for the EOS
AMSR-2	Advanced Microwave Scanning Radiometer - 2
ASTER	Advanced Spaceborne Thermal Emission and Reflection Radiometer
AVHRR	Advanced Very High Resolution Radiometer
AWAP	Australian Water Availability Project
ASAR	Advanced Synthetic Aperture Radar
BREB	Bowen Ratio Energy Balance
CABLE	Community Atmosphere Biosphere Land Exchange
CATDS	Centre Aval de Traitement des Données SMOS
CHRIS	Compact High Resolution Imaging Spectrometer
CIA	Coleambally Irrigation Area
CLASS	Canadian Land Surface Scheme
CNES	Centre National d'Etudes Spatiales
cRMSD	Centered root mean square difference
EC	Eddy covariance
ENVISAT	Environmental Satellite
ESA	European Space Agency
ET	Evapotranspiration
ETM+	Enhanced Thematic Mapper Plus
FPAR	Fraction of photosynthetically active radiation
GCOM-W1	Global Change Observation Mission 1st - Water

GSWP	Global Soil Wetness Project
IRGA	Infrared gas analyzer
ISBA	Interaction Soil Biosphere Atmosphere
ISMN	International Soil Moisture Network
ITS	Index of time stability
JAMI	Japanese Advanced Meteorological Imager
JAXA	Japanese Aerospace exploration Agency
JULES	Joint UK Land Environment Simulator
LAS	Large aperture scintillometer
LAI	Leaf Area Index
L-MEB	L-band microwave emission of the biosphere
LPRM	Land Parameter Retrieval Model
LSM	Land surface model
LST	Land surface temperature
MAE	Mean absolute error
MetOp	Meteorological Operational series of satellites
MIRAS	Microwave Imaging Radiometer with Aperture Synthesis
MODIS	MODerate resolution Imaging Spectroradiometer
MOST	Monin-Obukhov Similarity Theory
MRD	Mean relative difference
MTSAT	Multi-functional Transport SATellites
MWS	Microwave scintillometer
NAFE	National Airborne Field Experiments
NASA	National Aeronautics and Space Administration
NDVI	Normalized Differenced Vegetation Index
NWP	Numerical Weather Prediction
NSE	Nash-Sutcliffe Efficiency
OzNet	OzNet Monitoring Network
PAR	Photosynthetically Active Radiation
PILPS	Project for Intercomparisons of Land-surface Parameterization Schemes
PLMR	Polarimetric L-band Multi-beam Radiometer
PM-Mu	Modified Penman Monteith (PM-Mu) model

PT-JPL	Modified Priestley Taylor (PT-JPL) model
r	Pearson correlation coefficient
R^2	Coefficient of determination
RD	Relative difference
RH	Relative humidity
RE	Relative error
RFI	Radio frequency interference
RMSD	Root mean square difference
RMSE	Root mean square error
SDRD	Standard deviation of the relative difference
SEBS	Surface Energy Balance System
SGP	Southern Great Plains
SiB	Simple Biosphere Model
SMAP	Soil Moisture Active Passive
SMAPEx	Soil Moisture Active Passive Experiments
SMEX	Soil Moisture Experiments
SMOS	Soil Moisture and Ocean Salinity
SMOSMANIA	Soil moisture observing system - meteorological automatic network integrated application
TIR	Thermal infrared
ubRMSD	Unbiased RMSD
VPD	Vapour pressure deficit
VWC	Vegetation water content

Symbols

α	Surface albedo	-
b	Clapp and Hornberger exponent	-
β	Bowen ratio	-
c_{p}	Specific heat capacity of dry air at constant pressure	J Kg^{-1} K^{-1}
C_{n}^2	Structure parameter of refractive index of air	-
C_{s}	Soil volumetric heat capacity	J m^{-3} K^{-1}
C_{Q}^2	Structure parameter of moisture	-
C_{T}^2	Structure parameter of temperature	-
C_{TQ}	Cross structural parameter of temperature and humidity	-
d_0	Displacement height	m
ϵ	Surface emissivity	-
e	Actual vapour pressure	Pa
e_{s}	Saturation vapour pressure	Pa
f	Frequency	Hz
f_{APAR}	Fraction of absorbed Photosynthetically Active Radiation	-
f_{c}	Fractional (green) vegetation cover	-
ϕ	Soil porosity	m
g	Acceleration of gravity	m s^{-2}
γ	Psychometric constant	Pa K^{-1}
G	Ground/soil heat flux	W m^{-2}
h_0	Average vegetation height	m
H	Sensible heat flux	W m^{-2}
κ_{s}	Soil thermal conductivity	W m^{-1} K^{-1}

$K\downarrow$	Inward/Incoming short-wave radiation	W m^{-2}
$K\uparrow$	Upward/Outgoing short-wave radiation	W m^{-2}
K^*	Net short-wave radiation	W m^{-2}
K_{Ex}	Annual average solar radiation	W m^{-2}
K_θ	Hydraulic conductivity	m^3 m^{-2} s^{-1}
λ	Wavelength	m
L	Distance	m
$L\downarrow$	Inward/Incoming long-wave radiation	W m^{-2}
$L\uparrow$	Upward/Outgoing long-wave radiation	W m^{-2}
L^*	Net long-wave radiation	W m^{-2}
L_{Ob}	Monin-Obukhov length	m
L_{v}	Latent heat of vaporization	J kg^{-1}
$L_{\mathrm{v}}E$	Latent heat flux	W m^{-2}
$L_{\mathrm{v}}E_{\mathrm{c}}$	Canopy transpiration	W m^{-2}
$L_{\mathrm{v}}E_{\mathrm{i}}$	Total evaporation comes from evaporation of water intercepted by the canopy	W m^{-2}
$L_{\mathrm{v}}E_{\mathrm{s}}$	Soil evaporation	W m^{-2}
ω	Angular frequency	rads^{-1}
P	Air pressure	Pa
Ψ	Soil water suction	m
Q	Absolute air humidity	kg kg^{-1}
r_{a}	Aerodynamic resistance	m^{-1}
r_{s}	Surface resistance	m^{-1}
ρ_{a}	Density of air	kg m^{-3}
R_{d}	Gas constant for dry	J K^{-1} kg^{-1}
R_{n}	Net radiation	W m^{-2}
r_{TQ}	Correlation coefficient between temperature and humidity fluctuations	-
R_{v}	Gas constant for water vapour	J K^{-1} kg^{-1}
σ	Stefan Boltzmann constant	W m^{-1} K^{-4}
θ	Soil moisture content	m^3 m^{-3}
T	Temperature	K
T_{a}	Absolute air temperature	K

T_{v}	Virtual temperature	K
$\overline{u}$	Mean value of the horizontal wind speed component	m s^{-1}
u	Average wind speed in the horizontal direction	m s^{-1}
u'	Instantaneous wind speed in the horizontal direction	m s^{-1}
u_*	Friction velocity	m s^{-1}
v	Average wind speed in the lateral direction	m s^{-1}
v'	Instantaneous wind speed in the lateral direction	m s^{-1}
w	Average wind speed in the vertical direction	m s^{-1}
w'	Instantaneous wind speed in the vertical direction	m s^{-1}
z_0	Roughness length	m
z_{s}	Effective beam height of scintillometer	m
$\triangle$	Slope of the saturation vapour pressure versus temperature	Pa K^{-1}
κ_{v}	von Kármán constant	-
T_{OPT}	Optimum plant growth temperature	K
W	Flux of water	m^3 m^{-2} s^{-1}
Z_{r}	Thickness of soil layer/depth of root zone which contributes to ET	m
z_{s}	Effective beam height	m
z_{u}	Wind speed height	m

Chapter 1

Introduction

1.1 Introduction

This research undertakes a comprehensive validation of remote sensing soil moisture and evapotranspiration (ET) products, which are subsequently used to assess a land surface model (LSM) run at distributed scales. Whilst the work in this research focused on a single site, the methodology is developed with a global application in mind, utilizing the products available from space-borne satellites.

1.1.1 Statement of Problem

In climate and weather forecasting, estimates of soil moisture and ET are needed at spatial scales beyond what is covered by monitoring networks. LSMs are the only way in which soil moisture and ET estimates can be provided continuously across all spatial and temporal scales. However, the accuracy of these LSM simulations are dependant on the accuracy of the input forcing variables used to drive the models, parameters prescribed within the models and physical equations within the models (Zhang et al., 2013). Consequently, simulations from LSMs need to be evaluated with observations to ensure their performance. Yet, dense observing networks for LSM evaluation are limited to experimental sites and test beds with the majority consisting of isolated stations. Furthermore, these isolated stations are unable to capture the large scale processes modelled by LSMs, and are not consistent with the scales of model grids. As such, it is important to understand the errors in LSMs based on evaluations against observations at the right scale.

The increasing availability, quality and resolution of remote sensing data provides an unprecedented opportunity for global evaluation of LSMs as it is able to quantify land surface heterogeneity at model grid scales (Refsgaard, 1997). However, the application of remote sensing products in LSM evaluation have often been carried out without prior understanding regarding the accuracy of these products. As remote sensing products are inferred based on retrieval models and/or derived relationships between the measured quantity and the state of interest, the direct evaluation of LSMs with remote sensing products can essentially be a comparison between the remote sensing retrieval models and the LSM. This complicates the separation of errors due to differences in remote sensing models and LSMs. Additionally, remote sensing products are typically verified through direct comparisons with single/limited point measurements which may not be representative of the satellite footprints. Thus, the ability to resolve the contrast between point scale measurements and satellite footprints is crucial for data products verification from current and upcoming satellite missions. The motivation for this study is to therefore develop a more systematic method for evaluating simulations from LSMs run at distributed scales through the utilization of validated remote sensing observations.

1.1.2 Objective and scope of work

The primary objective of this research is to demonstrate the evaluation of LSM simulations of soil moisture and ET when run at distributed scales using remote sensing data which have been rigorously validated.

The work presented in this research focused on validating: i) soil moisture products from Advanced Microwave Scanning Radiometer 2 (AMSR-2) and Soil Moisture and Ocean Salinity (SMOS), and ii) ET products based on observations of land surface temperature and cloud mask from the Multi-functional Transport SATellites (MTSAT) series at the study area. This study is confined within the Australian core validation area located at Yanco, Australia (Yanco). The Yanco study area (-34.65°N, -35.15°N, 145.85°E, 146.35°E) has been used due to its status as the Australian core validation site for the AMSR-2 and SMOS satellites. Consequently, there is a large amount of data available from long-term soil moisture measurements which are complemented by a number of

Table 1.1: Summary of datasets used and involvement of this thesis candidate in data collection and processing. Post-processing includes extraction, quality checks and conversion for utilization.

Datasets	**Chapter**	**Involvement**
Soil moisture products	4	Post-processing.
SMAPEx campaign data	3	Post-processing.
Soil moisture stations	3 and 4	Post-processing.
EC measurement from EC1, EC2 and ancillary meteorological data	6	Post-processing.
EC measurement from EC3 and ancillary meteorological data	5 and 6	Installation, quality check, processing and archiving.
Scintillometer measurements and ancillary meteorological data	5 and 6	Field campaigns, quality check, processing, archiving and surface flux derivation.
MTSAT products	6	Collection of input data and post-processing.
Land surface model simulations	7	Model set-up and simulations
Satellite derived soil parameters	7	Post-processing.
Radar derived precipitation data	7	Post-processing.

intensive field experiments. Further information on the soil moisture monitoring network (OzNet), can be found at www.oznet.org.au (Smith et al., 2012) and the field experiments at www.smapex.monash.edu.au.

In addition, field measurements of surface fluxes using eddy covariance (EC) systems, and optical and microwave scintillometers have been conducted in the study area as an explicit contribution of this project. During this field work, measurements of soil moisture and temperature, surface reflectance properties, and other meteorological information were also collected.

Finally, the Joint UK Land Environment Simulator (JULES) was used to demonstrate how the verified remote sensing products might be used to evaluate simulations from a LSM run at distributed scales (Best et al., 2011; Clark et al., 2011b). The atmospheric forcing data used to drive JULES were obtained from the Australian Community Climate and Earth-System Simulator (ACCESS; Bureau of Meteorology, 2010) and the Australian Water Availability Project (AWAP; Jones et al., 2007). In addition to that, derived soil moisture parameters based on the work of Bandara et al. (2015) and precipitation data from Shahrban et al. (2016) were also used. Table 1.1 summarizes the datasets used in this research and the involvement of this research in the derivation and processing of each dataset.

As the objective of this research is to demonstrate the potential of the proposed methodology within a selected site, no model improvements were carried out following the evaluation. Moreover, since the performance of remote sensing products may differ with locations, the methodology was developed with the intention that such an analysis can be repeated for other monitoring networks. Nevertheless, in the process of achieving the main objective, some additional outcomes were achieved. These outcomes include:

i the identification of the appropriate methodology to understand the representativeness of *in situ* soil moisture monitoring stations,

ii the identification of stations which provide measurements representative of the area average soil moisture of selected remote sensing product grids,

iii the determination of the performance of different remote sensing soil moisture products such that the appropriate product can be applied in the evaluation of distributed soil moisture simulations by an LSM,

iv understanding the differences in surface heat fluxes derived from an EC system, and optical and microwave scintillometers,

v verifying the representativeness of an EC system of a single 4 km MTSAT ET pixel using scintillometers,

vi assessing the performance of different remote sensing ET products that are best suited for evaluating ET simulations from a LSM run at distributed scales, and

vii demonstrating the effects of using different datasets to drive the LSM.

1.1.3 Outline of approach

The approach taken in this research was three-fold whereby firstly, extensive soil moisture and ET data collected from field campaigns were used to establish representative soil moisture stations and a representative EC tower within Yanco. This was done to minimize errors resulting from the spatial mismatch between point measurements from *in situ* methods, and the coarse footprint scale observed from satellites. Secondly, remote sensing products were validated using these representative measurements. This was to identify the most accurate remote sensing soil moisture and ET products within the study area. Finally, the verified remote sensing products were used to demonstrate the assessment of an LSM run at distributed scales. By contrasting the results obtained by evaluating LSM simulations at distributed scales using the best and poorest performing products, the importance of the systematic approach adopted by this research, specifically, the rigorous validation of remote sensing products prior to application in LSMs run at distributed scales was demonstrated. The rationale for this approach is that biases or inaccuracies of the remote sensing products (or retrieval algorithms) at grid scales, which still exist at spatial scales, may be more difficult to identify when applied at distributed scales. The prior validation of remote sensing products at selected grids provides an insight into the most appropriate product to use for evaluating simulations from the LSM at distributed scales.

1.1.4 Organization of research

The research embodied in this research is divided into four main sections, each comprising two chapters as follows:

1. Introduction and background (Chapters 1 and 2)
2. Soil moisture remote sensing validation (Chapters 3 and 4)
3. ET remote sensing validation (Chapters 5 and 6)
4. Demonstration of model evaluation and conclusions (Chapters 7 and 8)

Chapter 2 is a literature review which justifies the need to evaluate simulated soil moisture and ET from LSMs run at distributed scales with a global, consistent and accurate dataset. It includes an overview of remote sensing soil moisture and ET validation studies done so far including an assessment of their limitations, and a brief history of LSM and current status of LSM evaluation.

Chapter 3 uses datasets from the Yanco study area to investigate the representativeness of soil moisture stations within the study area based on a combination of geostatistical and temporal stability analysis. This work has published in the Journal of Hydrology as:

- Yee, M., Walker, J. P., Monerris, A., Rüdiger, C. and Jackson, T. J. (2016). On the identification of representative *in situ* soil moisture monitoring stations for the validation of SMAP soil moisture products in Australia. *Journal of Hydrology, 537,*, 367-381. doi:10.1016/j.jhydrol.2016.03.060

Subsequently, the most representative stations are used to validate remote sensing soil moisture products from AMSR-2 and SMOS for the Australian core validation site. This work is reported in **Chapter 4**. The results from this study have been submitted to Remote Sensing of Environment for review.

- Yee, M., Walker, J. P., Rüdiger, C., Robert M. Parinussa, Kerr, Y. and Koike, T. (2016). On the impact of using representative stations for passive microwave soil moisture validation. *Remote Sensing of Environment.* Manuscript in review.

Collection of field measurements of surface fluxes using EC systems, and using optical and microwave scintillometers were carried out in the study area to enable an inter-comparison of surface heat fluxes derived from an EC system and optical and microwave scintillometers. This work was reported in **Chapter 5**. The theory behind the derivation of surface heat fluxes based on different scintillometers, and the strength and limitations of each technique is discussed. Findings from this work have also been published as a journal article.

- Yee, M. S., Pauwels, V. R., Daly, E., Beringer, J., Rüdiger, C., McCabe, M. F., and Walker, J. P. (2015). A comparison of optical and microwave scintillometers with eddy covariance derived surface heat fluxes. *Agricultural and Forest Meteorology, 213,* 226-239. doi:10.1016/ j.agrformet.2015.07.004.

With an understanding of the individual performances of each scintillometer, **Chapter 6** reports a study that used these same methods to verify the representativeness of measurements from an EC system for a 4 km MTSAT ET pixel in the same Australian validation site. This representative EC measurements were eventually used for the validation of MTSAT derived ET products based on three different ET models. This involved another field campaign collecting measurements of surface heat fluxes within the 4 km MTSAT ET pixel. The findings from this study have been submitted to Remote Sensing of Environment for review.

- Yee, M., Ershadi, A., Pipunic, R., Daly, E., McCabe, M., Pauwels, V., Rüdiger, C., and Walker, J.P. (2016). Validation of remote sensing evapotranspiration products based on a representative flux station. *Remote Sensing of Environment.* Manuscript in review.

In **Chapter 7**, a study which draws from the precursor results to evaluate simulations from the Joint UK Land Environment Simulator (JULES) was presented as a demonstration of how such validated remote sensing products could be used. The following peer-reviewed conference paper corresponds with the work described in this chapter.

- Yee, M. S., Walker, J., Dumedah, G., Monerris, A., and Rüdiger, C. (2013). Towards land surface model validation from using satellite retrieved soil moisture. In J. Boland, & J. Piantadosi (Eds.), *20th International Congress on Modelling and Simulation* (pp. 2890-2896). Modelling and Simulation Society of Australia and New Zealand, Adelaide.

Finally, **Chapter 8** presents the conclusions from this research and discusses future opportunities for further research identified based on the work which has been carried out.

Chapter 2

Literature Review

2.1 Literature Review

Linkages and feedbacks between the Earth (consisting of land and ocean surface) and Atmosphere play a critical role in controlling our climate and weather systems. Of the interactions between the land surface and the atmosphere, the relationship between soil moisture and evapotranspiration (ET) is a key component. To better understand the importance of ET in linking the Earth and Atmosphere, this chapter begins with the theoretical background of energy and water exchange between the Earth and the Atmosphere. Following this, the role played by soil moisture and ET in linking the Earth's energy and water cycle is discussed. This underlines the importance of estimating soil moisture and ET at different spatial and temporal scales. As land surface models (LSMs) are the only way to simulate soil moisture and ET at different spatial and temporal scales, a brief history regarding the evolution of LSMs and limitations of current LSM evaluation is provided. Consequently, a method based on a rigorous end-to-end evaluation of LSMs is proposed. The rationale behind the approach taken in this research is explained. Finally, the objectives, methodology, and the structure of this dissertation are also presented.

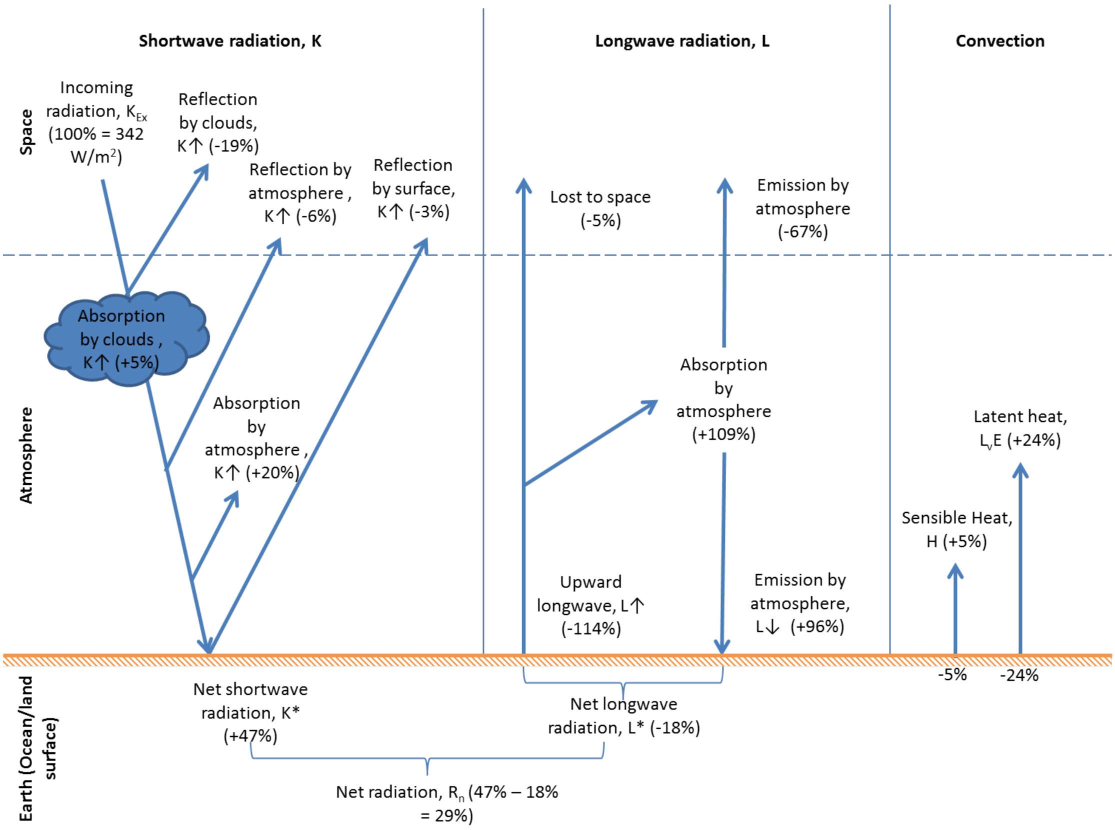

Figure 2.1: Schematic of the annual energy balance of the Earth-Atmosphere system. Energy terms are expressed as percentages of the annual average solar radiation, K_{Ex} (342 W m^{-2}). Modified from Oke (2002).

2.2 Energy Balance of the Total Earth and Atmosphere System

To understand why the land surface needs to be represented in climate models, this section provides a theoretical background concerning the exchange of energy between the Atmosphere and the Earth, and how the surface heat fluxes; sensible heat (H) and latent heat ($L_{\mathrm{v}}E$; an energy term of ET) play a crucial role in this exchange.

2.2.1 Earth-Atmosphere Energy Balance

Energy input into the Earth-Atmosphere system is emitted by the sun at approximately 1367 W m^{-2} (Wehrli, 1985). However, only about 342 W m^{-2} (K_{Ex}) reaches the top of the Atmosphere. Figure 2.1 shows a schematic of the annual energy balance of the Earth-Atmosphere system expressed as a percentage of K_{Ex}.

When solar radiation from the sun passes through the atmosphere, it is reflected and scattered by clouds and other atmospheric constituents such as water vapour, dust particles and various gases it encounters before reaching the Earth's surface. Approximately 28% (19% + 6% + 3% = 28%) of K_{Ex} is reflected back to space, 25% (20% + 5%) is absorbed by the atmosphere and 47% of K_{Ex} is absorbed by the Earth's surface (Oke, 2002).

The temperature of the bodies (i.e. atmosphere and earth's surface) which absorb radiative energy will increase and re-emit this energy at infrared wavelengths (long-wave). The amount of radiation that the Earth's surface emits depends on its surface temperature, T, and surface emissivity, ϵ. According to Stefan-Boltzmann's law, the amount of energy emitted by a body is equivalent to $\epsilon\sigma T^4$ where σ is the Stefan-Boltzmann constant (5.67×10^8 W m^{-1} K^{-4}). As the Earth's mean annual temperature is approximately 288 K, it emits an upward long wave radiation ($L\uparrow$) of 114% of K_{Ex}. This is possibly due to the existence of the Atmosphere which prevents the loss of $L\uparrow$. Of this, 5% is lost to space whereas 109% is absorbed by the Atmosphere. The Atmosphere on the other hand, emits 67% of long wave radiation to space and 96% to the Earth's surface (total loss of 163%).

The radiation budget of the Earth-Atmosphere system is in equilibrium as solar input is balanced by the sum of short-wave reflection and long-wave emission from Earth and atmosphere (100% - 19% - 6% - 3% - 5% - 67% = 0%). However, within the sub-systems, this is not in equilibrium. The Earth's surface receives a net short-wave radiation of 47% but loses 18% as long-wave radiation to the Atmosphere. The Atmosphere on the other hand, receives 25% as short-wave radiation, but looses 54% (109% - 163%). From this re-absorption and re-radiation process between the Earth's surface and the Atmosphere, the Earth's surface receives an annual radiant energy surplus (net radiation) of 29% (47% - 18%), R_{n}, whereas the Atmosphere loses 29% (25% - 54%). Considering the physical and thermal properties of the Earth's surface, this would suggest that the Atmosphere is cooling at 1°C a day and the Earth's surface would be warming at approximately 250°C a day. However, this is not observed as this surplus radiative energy from the Earth's surface is transported to the Atmosphere via convective transport of energy in the form of sensible heat (H) (5%) and latent heat ($L_{\mathrm{v}}E$) (24%).

2.2.2 Land surface Energy Balance

At the land surface, available energy at a given site, R_{n}, depends on the sum of all the individual incoming ($\downarrow$) and outgoing ($\uparrow$) short-wave (K) and long-wave (L) radiations such that

$$R_{\mathrm{n}} = K\downarrow - K\uparrow + L\downarrow - L\uparrow . \tag{2.1}$$

Radiative fluxes can be measured using pyranometers (short-wave) and pyrgeometers (long-wave). The pattern of incoming short-wave radiation ($K\downarrow$) at a site is governed by the azimuth and zenith angles of the Sun relative to the horizon. A proportion of $K\downarrow$ is reflected from the surface ($K\uparrow$) back to the atmosphere in amounts dependent on the surface albedo, α such that

$$K\uparrow = \alpha K\downarrow . \tag{2.2}$$

Thus, the net short-wave radiation is

$$K^{*} = (1-\alpha)K\downarrow . \tag{2.3}$$

As mentioned in the previous section, the Atmosphere emits long-wave radiation to the Earth's surface ($L\downarrow$) and this depends on the bulk atmospheric temperature and emissivity of the Atmosphere in accordance to the Stefan-Boltzmann law. Simultaneously, the Earth's surface also emits long-wave radiation which is dependent on its temperature and emissivity. The net long-wave radiation is therefore

$$L^{*} = L\downarrow - L\uparrow = \epsilon(\sigma T^{4} - L\downarrow). \tag{2.4}$$

Generally, L^{*} is negative and relatively small if the difference between the surface and air temperature is small. Over the course of a day, R_{n} is typically positive during the day when $K^{*} > L^{*}$, whereas during the night, as solar radiation (K) is absent and long-wave radiation continues to be radiated from the surface to the atmosphere, R_{n} is negative.

The surface energy is driven by two distinct physical processes: (i) convection, which is the transport of energy and mass from one location to another through the exchange of air masses and (ii) conduction, which is the transfer of heat within a substance due to the collision of rapidly moving molecules. The former describes the exchange of energy to or from the atmosphere (laminar boundary layer) as H and $L_\mathrm{v}E$, and the latter describes the exchange to and from the underlying soil as soil heat flux, G (sub-surface layer). Thus, the surface energy balance is given as,

$$R_\mathrm{n} = H + L_\mathrm{v}E + G. \tag{2.5}$$

Before going into detail regarding the surface energy balance, it is important to define the sign convention employed in this research. The sign convention is that non-radiative fluxes (H, $L_\mathrm{v}E$ and G) directing away from a surface or system (the Earth's surface in this case), i.e. the surface losing heat, is positive and negative when it is gaining heat. Conversely, for radiative fluxes, such as R_n, $K\downarrow$, $K\uparrow$, $L\downarrow$ and $L\uparrow$, positive represents a gain, and negative a loss from the surface.

The partitioning of the radiative surplus ($R_\mathrm{n} > 0$) or deficit ($R_\mathrm{n} < 0$) into H, $L_\mathrm{v}E$ or G is governed by the nature of the surface, and the relative ability of the soil and atmosphere to transport heat. The change in energy, which is reflected as a phase change of water with no change in temperature, is $L_\mathrm{v}E$. In each phase change, $L_\mathrm{v}E$ is either absorbed or released. When water from the surface is evaporated (liquid to gas), $L_\mathrm{v}E$ is absorbed and released to the atmosphere where water vapour condenses into cloud (gas to liquid), thereby transferring energy from the surface to the atmosphere. $L_\mathrm{v}E$ is usually larger than H when soil moisture is available for evaporation, or for plants to transpire and vice versa in water-limited conditions. At night, free convection is dampened by atmospheric temperature stratification; the atmosphere is then said to be stable. Therefore, R_n loss at night is most effectively replenished by upwards thermal conduction from the soil, G, and convection is least effective from $L_\mathrm{v}E$.

In the case of H and $L_\mathrm{v}E$, the rate in which convection occurs is controlled by surface resistance, r_s, aerodynamic resistance, r_a, specific heat of air, c_p (approximately 1005 J kg^{-1} K^{-1}) and the gradient of temperature or humidity, such that,

$$H = \frac{\rho c_\mathrm{p}(T_\mathrm{s} - T_\mathrm{a})}{r_\mathrm{a}}, \tag{2.6}$$

and

$$L_\mathrm{v}E = \frac{\rho L_\mathrm{v}(q_\mathrm{s}(T_\mathrm{s}) - q_\mathrm{a})}{(r_\mathrm{s} + r_\mathrm{a})}, \tag{2.7}$$

where ρ is air density (approximately 1.2 kg m^{-3}) and $L_\mathrm{v} = 2.45 \times 10^6$ J kg $^{-1}$ is the latent heat of vaporization. r_s and r_a depend on wind speed and the stability of the atmosphere. The movement of water vapour from leaves to the atmosphere is controlled by r_s through the opening and closing of plant stomata which depends on factors including light intensity, ambient temperature and humidity, carbon dioxide concentration and soil moisture availability, whereas, r_a controls the rate in which water vapour and heat is transferred between the surface and the atmosphere and is a function of wind speed and vegetation height.

In the case of G, which is governed mostly by conduction, its magnitude depends on the difference in temperature over the layer and soil thermal properties. During the day, heat flux travels downwards into a volume of soil and upwards by night. Soil heat flux can be expressed as

$$G = -\kappa_\mathrm{s}\frac{\mathrm{d}T_\mathrm{s}}{\mathrm{d}z} \simeq -\kappa_\mathrm{s}\frac{(T_2 - T_1)}{(z_2 - z_1)}, \tag{2.8}$$

where the subscripts refer to levels in the soil such that level 2 is deeper than 1. The sign indicates that the flux is in the direction of decreasing temperature. That is, during the day, when the temperature, T_2, of the soil in z_2 is lower than T_1, G is positive as heat is flowing into the soil, but away from the surface. The amount of heat flux transferred depends on the ability of the soil to conduct heat, i.e. its thermal conductivity, κ_s (W m^{-1} K^{-1}), which varies with depth and time, and depends on the conductivity of the soil particles, the soil moisture content, and soil porosity. Consequently, soil moisture content has a significant impact on the conductivity of soil as it not only increases the thermal contact between soil particles but also replaces pore air in the soil which has a much lower conductivity than pore water.

2.2.3 The Land Surface Water Balance

The previous sub-section has shown the roles played by ET and soil moisture in the land surface energy balance. This sub-section will provide a brief background regarding the roles they play within the land surface water balance.

At the surface, the exchange of water between the surface and the atmosphere depends on precipitation and ET. The water balance can be linked to the energy balance via the relationship

$$L_\mathrm{v}E = L_\mathrm{v} \cdot \mathrm{ET}, \tag{2.9}$$

where ET (mass flux density) is in kg m^{-2} s^{-1} and energy, $L_\mathrm{v}E$ (latent heat flux density), is expressed in W m^{-2}. ET is the combined evaporation from free surface water and soil pore water, and plant transpiration. Generally, the water balance can be written as

$$\frac{\mathrm{d}S}{\mathrm{d}t} = \mathrm{Precipitation} - \mathrm{ET} - \mathrm{runoff}, \tag{2.10}$$

where precipitation, ET and run-off are fluxes, and $\frac{\mathrm{d}S}{\mathrm{d}t}$ is change in storage (e.g. groundwater, soil moisture, ponding etc.) for the period t. ET over the ocean is larger than precipitation and the reverse is true over the land surface. Precipitation that passes through the plant canopy arrives at the soil surface as through-fall. Through-fall that reaches the soil surface is then distributed into run-off or infiltration. Surface run-off occurs when through-fall exceeds infiltration. This partitioning depends on initial soil moisture conditions and soil properties. At the same time, water mass can be lost from the surface to the atmosphere as ET.

Infiltrated water percolates into the soil thereby increasing soil moisture content which controls the opening of the stomata. In turn, the stoma controls the rate in which plant transpiration occurs. The movement of water within the soil layer can occur through saturated and unsaturated soil. The rate in which water moves within a soil column is determined by the soil's hydraulic conductivity, K_θ (volume per unit area per unit time), and the matric potential, Ψ. The flux of water, W, through the soil follows Buckingham-Darcy's law where

$$W = K_\theta \left(\frac{\partial \Psi}{\partial z} + 1 \right). \tag{2.11}$$

The physical constants, K_θ and Ψ, represent the rate in which soil transmits water under the influence of gravity alone, and the amount of adsorption which holds water to the soil particles (matric potential), respectively. For saturated soils, matric potential is low and hydraulic conductivity dominates. Conversely, for unsaturated soils, hydraulic conductivity is low and water flow is driven by the gradient in matric potential. The movement of water in unsaturated soils can be approximated using the Richard's Equation (Richards, 1931), a non-linear partial differential equation. Soil moisture can then be calculated using the soil characteristic functions which are mathematical simplifications of the relationship between soil moisture and Ψ. Three forms of these functions include those proposed by Brooks and Corey (1964), Van Genuchten (1980) and Clapp and Hornberger (1978). In this thesis, the Clapp and Hornberger (1978) function was selected for soil moisture simulations. This relationship can be described as

$$K_\theta = K_s \left(\frac{\theta}{\phi}\right)^{2b+3}, \tag{2.12}$$

where θ is the volumetric soil moisture content, ϕ is the soil porosity, and the exponent b is the Clapp and Hornberger exponent. The balance of these components leads to a change in the total amount of water stored in any layer of soil. This volume of water is usually described as volume per unit area (or depth) which is a product of soil moisture content, θ, and the thickness of the soil layer, Z_r, which is usually considered to be the depth of the root zone which contributes to ET. Assuming that S consists of only soil moisture (i.e. there is no influence from groundwater or ponding), $\frac{\mathrm{d}S}{\mathrm{d}t}$ in Eqn. 2.10 is equivalent to W_g (where g is gravitational acceleration) which causes a change in θ where

$$\frac{\mathrm{d}\theta}{\mathrm{d}t} Z_r = \frac{\mathrm{d}S}{\mathrm{d}t} = \text{Throughfall} - \text{runoff} - \text{ET}. \tag{2.13}$$

For a level terrain, run-off can be assumed to be negligible. When this water balance is combined with the surface energy balance (Eqn. 2.5), the role of soil moisture becomes more apparent. This is complicated by the differences in temporal scales in which these processes occur. The surface energy balance follows a daily diurnal pattern which depends on the rising and setting of the sun, precipitation occurs in short discrete bursts, whereas ET is a continuous process. This means that when precipitation (and therefore through-fall) is zero, the equation can be reduced to

$$\frac{\mathrm{d}\theta}{\mathrm{d}t} Z_r = -\text{ET}. \tag{2.14}$$

Therefore, the availability of soil moisture controls the rate in which ET occurs. When the soil moisture level closer to the surface (0-5 cm) is low, soil evaporation is low. At the same time, if soil moisture from within the root zone layer (1 - 2 m) is low, stomatal closure occurs and this reduces transpiration. Restricted soil moisture conditions leads to H being higher than $L_\mathrm{v}E$ and vice versa. As a result, the availability of soil moisture and its distribution at different depths play a key role in the partitioning of R_n into

H and $L_{\mathrm{v}}E$. This partitioning of heat fluxes into H and $L_{\mathrm{v}}E$ can be measured by the Bowen ratio, β, such that

$$\beta = \frac{H}{L_{\mathrm{v}}E} \tag{2.15}$$

Typical values of β are 0.2 for tropical rain forests, irrigated grass or orchards, 0.4 - 0.8 for temperate forests and grass lands, 2 - 6 for semi-arid regions, and 10 for deserts (Nobel, 1999).

2.2.4 Importance of quantifying soil moisture and ET

The importance of soil moisture in partitioning of available energy at the land's surface into ET, and the importance of ET in linking the energy and water balance between the Earth and the Atmosphere has been discussed in the previous section.

Despite comprising only a small portion of the global water budget, soil moisture plays an important role in controlling the partitioning of available energy into H and $L_{\mathrm{v}}E$ (Entekhabi et al., 2010b; Prigent et al., 2005), controlling the ratio of run-off to groundwater recharge (Delworth and Manabe, 1988; Wagner et al., 2003), and precipitation (Koster, 2004; Pal and Eltahir, 2003; Seneviratne, 2010). Furthermore, soil moisture availability controls the rate in which plants transpire and are photosynthetically active, which in turn will have effects not only on the water and energy cycle but also bio-geochemistry. Finally, soil moisture and ET are involved in a number of mutual and important interactions between the climate and weather systems at the local, regional and global scales (Dirmeyer et al., 1999; Dorigo et al., 2012; Entekhabi et al., 1996). The partitioning of R_{n} between H and $L_{\mathrm{v}}E$ is important in climate modelling as when ET decreases, less water vapour is allowed in the atmosphere which leads to a decrease in cloud formation and precipitation. In contrast, when H reduces, the planetary boundary layer cools and convection reduces (Betts et al., 1996). For semi-arid environments, these relationships are particularly important as total precipitation is returned to the atmosphere almost entirely as ET compared to an average of 60% across the globe (Brutsaert, 2005; Kurc and Small, 2007; Oki and Kanae, 2006).

Quantification of both the temporal and spatial variability of soil moisture and ET, particularly in semi-arid environments, is crucial for applications in climate modelling, meteorology, hydrology, ecology, irrigation scheduling and water resource management

(Allen et al., 2011; Betts et al., 1996; Biswas, 2004; Glenn et al., 2007). However, it is impossible to measure soil moisture and ET at the different temporal and spatial scales required for climate modelling, weather forecasting, water resource management or irrigation scheduling at multiple spatial scales (Prentice et al., 2015). The only way in which soil moisture and ET can be estimated at these different scales is through LSMs.

2.3 Land Surface Models (LSM)

LSMs are models which combine mechanistic and empirical sub-models concerning photosynthesis, ET and soil moisture redistribution to simulate the observed behaviour of the Earth's energy, water and carbon fluxes. These models provide the boundary conditions needed by climate and weather forecasting models, and have evolved over the past five decades from a simple bucket model to the more complex third generation LSMs of today (Dai et al., 2003).

2.3.1 The evolution of LSMs

First generation LSMs, as classified by Sellers et al. (1997a), were based on simple aerodynamic bulk transfer formulas. Surface parameters such as albedo, roughness length, and soil moisture holding capacity were prescribed as single values in these early generation models. Furthermore, vegetation was treated implicitly and did not vary in time. The soil layer was treated as a single layer and soil moisture was calculated using a simple bucket model (Manabe, 1969). In this bucket model, water level within the bucket decreased when evaporation exceeded precipitation and rose when precipitation exceeded evaporation. As vegetation effects were not accounted for, only evaporation from bare soil surfaces were considered (Stöckli and Vidale, 2005).

In the early 80s, the second generation LSMs wer developed to include crucial vegetation and soil parameters to better determine the interaction between the land-surface and the atmosphere. These interactions included radiation absorption, biophysical controls on ET, interception of precipitation and soil moisture availability based on root depth and density. Examples of second generation LSMs are the Simple Biosphere Model (SiB) (Sellers et al., 1986), Canadian Land Surface Scheme (CLASS) (Verseghy, 1991) and Interaction Soil Biosphere Atmosphere (ISBA) model (Noilhan and Planton, 1989). Second generation LSMs i) mimic the complex exchange of energy and water cycle within the land surface, ii) can be linked to hydrological models to capture hydrological processes at the catchment scale, and iii) suitably represent the land surface in climate studies (Pitman, 2003). The main limitation with these second generation models is that they do not differentiate soil evaporation and transpiration (big-leaf approximation). The need to account for heterogeneity within land surface processes led to the development of tile-, patch- or mosaic models as in Noilhan and Mahfouf (1996). These types of models allow the land surface to be divided into fractions to represent different land cover types such as bare soil, vegetation types, water bodies and so on, such that parameters corresponding to each of these land cover types can be defined.

Finally, the main development leading to third generation LSMs, which is the modern and current LSM, was the incorporation of photosynthesis and stomatal conductance to provide a better description of carbon exchange and vegetation growth (e.g. Calvet et al., 1998; Cox et al., 1998; Krinner et al., 2005).

2.3.2 JULES LSM

The Joint UK Land Environment Simulator, JULES, which will be used in this research, is a third generation LSM derived from the UK Met Office United Model (Best et al., 2011) (Fig. 2.3.2). JULES is a tiled model whereby nine different surface types can be prescribed in each grid box. These surface types are: broadleaf trees, needleleaf trees, C3 grass, C4 grass, shrubs, urban, inland water, bare soil and ice. The energy balance for each surface type is represented by tiles. The energy balance of each grid is then computed by weighting the values from each tile based on the area covered by each tile within the grid. Each grid box is prescribed with meteorological data (incoming short-wave and long-wave radiation, temperature, specific humidity, wind speed, surface pressure and rainfall), soil properties, and vegetation characteristics. The list of soil and vegetation data required, and other additional information about the model and its physics can be found in Clark et al. (2011a), Best et al. (2011), and Clark et al. (2011b). Version 3.0 has been used in this work.

Based on *in situ* measurements, JULES has been evaluated in previous studies for its ability to simulate surface heat and carbon fluxes using eddy covariance (EC) measurements from "FLUXNET" (Baldocchi et al., 2001, ,www.fluxnet.ornl.gov) (e.g. Blyth

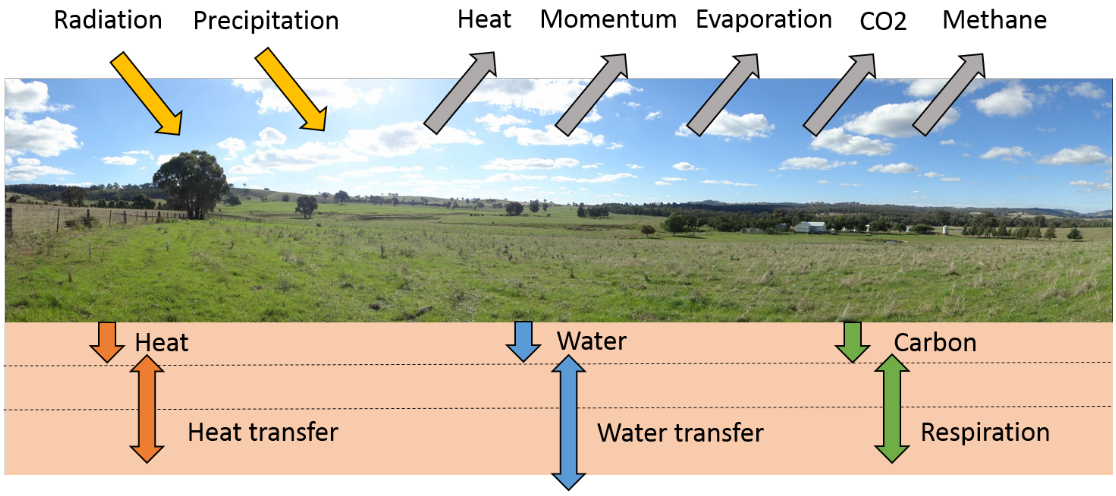

FIGURE 2.2: Schematic of JULES adapted from `https://jules.jchmr.org/model-description`

et al., 2011, 2010; Slevin et al., 2015) or other *in situ* measurements of through-fall, and surface and subsurface run-off (e.g. Zulkafli et al., 2013). These types of evaluation studies have helped to understand the model's performance and potential areas for improvement. For instance, Yang et al. (2014) assessed point-scale simulations of soil moisture from JULES in New Zealand based on measurements at 55 stations and found that reliable estimates of soil hydraulic and thermal properties is required to improve soil moisture simulations based on JULES. Similarly, in dry-lands, Blyth et al. (2010) found that modelled and observed evaporation had distinctly different diurnal variations. The authors suggested that uncertainties in the estimation of soil hydraulic parameters may have contributed to this. Based on these two studies, it is probable that inaccuracies in soil properties observed inYang et al. (2014) have led to inaccuracies in soil moisture simulations, which in turn led to differences in diurnal variations of ET observed in Blyth et al. (2010).

JULES is advantageous in that the depth of its soil layers can be altered, and the soil parameters and initial conditions for each layer specified. Previously, JULES has been shown to perform well within the Murrumbidgee Catchment based on *in situ* measurements of soil moisture with a root mean square error (RMSE) of approximately 0.03 m^3 m^{-3} (e.g. Bandara et al., 2011; Dumedah and Walker, 2014). Since soil moisture availability plays a crucial role in partitioning energy into H and L_vE, particularly in a semi-arid region such as the Murrumbidgee Catchment, it becomes imperative to ask whether correct soil moisture states translate to accurate ET simulations. As simultaneous evaluations of soil moisture and ET from JULES have never been carried out to date, this question remains unanswered. The objective of this research is therefore to demonstrate a joint evaluation of soil moisture and ET simulations from JULES to gain insights regarding differences in diurnal variations of ET that have been observed in previous studies.

2.3.3 Evaluation of LSMs

As described earlier, LSMs have evolved into more complex models over the last few decades. With an increasing wealth of information, LSMs are now commonly run in spatially distributed configurations. In a spatially distributed model, the land surface is divided into grids, and at each grid, the same model is applied. To represent spatial variability different parameters may be used at each grid (Refsgaard, 1997). However, when applied at regional or global scales ($\approx$1000 km), processes at the local scale ($\approx$1 m) may no longer be dominant, leading to a discrepancy between the derived and the actual land surface states and fluxes (Blöschl, 2001). For instance, soil heterogeneity which exists at small scales may average out at a catchment scale. On the other hand, processes not observed at the small scale ($\approx$1 m) such as preferential flow paths may become important at the catchment scale ($\approx$10 km) (Sivapalan et al., 2003). Additionally, uncertainties originating from errors in input forcings used to drive the models, parameters prescribed within the model physics, and structural errors within the models further contribute to errors in the simulations (Zhang et al., 2013). These errors can lead to further inaccuracies in climate studies and weather forecasting (Crossley et al., 2000; Pitman, 2003). The increase in complexity of these models may also lead to an increase in the risk of over-parameterization and for the model to give similar results from a number of different parameter combinations, also known as model parameter equifinality (Beven, 1993; Beven and Freer, 2001; Williams et al., 2009). Consequently, to build confidence in LSMs, there is a need to evaluate these models with observations of various hydrological states and fluxes for different ecosystem and climate conditions.

The main approaches generally used to evaluate these simulations include 1) model inter-comparison studies, 2) sensitivity analysis and/or 3) comparisons with *in situ* measurements. The Project for Inter-comparison of Land-surface Parameterization Schemes

(PILPS) and Global Soil Wetness Project (GSWP) (e.g. Chen et al., 1997; Dirmeyer, 2011; Henderson-Sellers et al., 1995, 1993; Schlosser et al., 2000) which inter-compared various LSM schemes found significant differences in simulated variables particularly in the partitioning of energy and water even when driven by the same atmospheric forcing inputs (Pitman and Henderson-Sellers, 1998). Furthermore, based on an an inter-comparison between H and $L_{\mathrm{v}}E$ derived from 12 LSMs and empirical relationships derived from meteorological drivers of H and $L_{\mathrm{v}}E$, Best et al. (2015) found that empirical models outperformed the LSMs, and therefore, concluded that current LSMs did not use the information available from atmospheric forcing data appropriately. Nevertheless, JULES has been previously inter-compared with Community Atmosphere Biosphere Land Exchange (CABLE) in Australia and was found to be superior (Bandara, 2013). Sensitivity analyses based on the single or multi-parameter approach enabled the identification of model parameters which had a larger impact on simulations of interest (e.g. Bandara et al., 2011; El Maayar et al., 2002; Gupta et al., 1999; Hou et al., 2012; Rosero et al., 2010). Ultimately, further information about these sensitivities can only be gleaned from observations. For instance, based on comparisons with *in situ* soil moisture measurements, Bandara et al. (2011) found that soil moisture simulations from JULES were most sensitive to the volumetric fraction of soil moisture at critical point and at saturation, as well as the Clapp and Hornberger exponent, b. The current view which is gaining attention in model evaluation is to assess the model for its reliability, robustness, and realism (Prentice et al., 2015). Since this research concentrates on the first, i.e. reliability, which relates to the ability of the model to reproduce observations, the third approach, which is to evaluate LSM simulations based on comparisons with *in situ* measurements may be more relevant here.

Efforts to combine datasets from different soil moisture monitoring stations such as the Global Soil Moisture Data Bank (Robock et al., 2000, `http://climate.envsci.rutgers.edu/soil_moisture`), and the International Soil Moisture Network (ISMN), which began with over 500 stations from 9 networks but have expanded to more than 2000 stations from 50 networks to date (Dorigo et al., 2011, `http://ismn.geo.tuwien.ac.at/networks/`), have been initiated. These datasets have been valuable in the evaluating soil moisture simulations from LSMs (e.g. Guo and Dirmeyer, 2006). Typically, when run at grid or distributed scales as opposed to a single point, observations at a single site, or the mean or interpolation of observations at several sites are used to evaluate the gridded soil moisture simulations. Of these methods, due to high spatial variability of soil moisture, the second method is preferred to minimize differences in scale (point vs grid). Thus, to obtain an area averaged soil moisture for the evaluating LSMs, a dense network of sensors need to be established. Yet, dense networks are limited to experimental plots and test-beds, e.g. OzNet, Oklahoma Mesonet, High Plains Regional Climate Center, Illinois Climate Network, SMOSMANIA; soil moisture observing system - meteorological automatic network integrated application, whereas most are sparsely located. In addition, installation and maintenance including periodic calibration of these monitoring networks involve high costs and can be intrusive, thereby causing biases in measurements (Heathman et al., 2012; Rüdiger et al., 2010). Furthermore, as these sites are managed by different groups, the lack of a standard measurement technique and a standard measurement protocol complicates interpretation of results. Although efforts to standardize these methods are increasing, (e.g. Baldocchi et al., 2001; Dorigo et al., 2011; Papale et al., 2006; Robock et al., 2000), these networks still do not cover the majority of the global land surface area, which has varying climate, vegetation, and soil conditions.

Studies which have evaluated ET simulations from LSMs are numerous with observations based on eddy-covariance (EC) the prime method for monitoring ET (e.g. Blyth et al., 2010; El Maayar et al., 2008; Fisher et al., 2008; Kaimal and Finnigan, 1994; North et al., 2015; Senay et al., 2016; Stöckli et al., 2008; Williams et al., 2009) with observations from the FLUXNET (Baldocchi et al., 2001, `http://www.fluxnet.ornl.gov/`). This is regarded to be the most physically correct method to directly measure H and $L_{\mathrm{v}}E$ with observations available over various land cover types and environments. Yet, while EC systems are able to measure over a footprint of a few hundred metres upwind, this footprint changes depending on wind direction and speed (Aubinet et al., 2000; Baldocchi et al., 2001; Schmid, 1994). Consequently, its representativeness of model grids, particularly in a heterogeneous landscape, is debatable (Ward et al., 2014). Furthermore, EC systems are known to be unable to close the surface energy balance due to measurement errors, neglected energy sinks, advection or secondary circulations (Foken, 2008; Wilson et al., 2002). Past evaluation studies based on EC systems have assumed that the energy imbalance will not affect the conclusions drawn in their studies (e.g. Best et al., 2015; Blyth et al., 2010). For instance, due to differences in the magnitude of energy non-closure of the sites, Blyth et al. (2010) had to assume an equal mis-measurement of H and $L_{\mathrm{v}}E$ (i.e. the Bowen-ratio correction). Despite this, the magnitude of this non-closure can differ from site to site (El Maayar et al., 2008). Moreover, for a semi-arid environment, this non-closure can be of equal or larger magnitude than $L_{\mathrm{v}}E$ (Yee et al., 2015). Nevertheless different methods to close this energy imbalance have been proposed and is currently under active research (e.g. Twine et al., 2000).

From the discussion above, it can be seen that due to the high spatial variability of soil moisture, and consequently ET, point-scale measurements used to evaluate LSM simulations may not be representative of the areal average values of model grids. Furthermore, dense-monitoring networks which can give a better areal estimate do not provide a gridded global coverage. To quote Klemeš (1986) (p.187S),

> "*It also seems obvious that (the) search for new measurement methods that would yield areal distributions, or at least reliable areal totals or averages, of hydrologic variables such as precipitation, ET, and soil moisture would be a much better investment for hydrology than the continuous pursuit of a perfect massage that would squeeze the nonexistent information out of the few poor anaemic point measurements...*"

Consequently, to gain confidence in LSM simulations, and to ensure that they are performing well for the right reason, there is a need to evaluate simulations from LSMs run at distributed scales with " measurement methods that would yield areal distributions, or at least reliable areal totals or averages".

2.4 Remote sensing

Much effort has been put into the evaluation of distributed simulations of surface flux, and to a lesser degree soil moisture, at specific sites against *in situ* measurements. Despite this, a truly comprehensive evaluation of these simulations at global scales, using observations of land surface variables at scales consistent with model grids is still lacking. The increasing availability, quality and resolution of remote sensing products, spanning from land surface temperature (LST), albedo, ET, soil moisture to vegetation indices, makes remote sensing a promising method in the evaluation of LSMs. This is because it is the only method to able to obtain land characteristics at scales larger than plots and experimental catchments without the complications related to field measurements (Refsgaard, 1997). This section provides a short review of previous studies using remote sensing in LSM evaluation and issues they faced followed by an overview of available remote sensing soil moisture and ET products. Issues regarding the validation of these products, and possible approaches to overcome them will also be presented.

2.4.1 A tool for LSM evaluation

Remote sensing is the science of obtaining information of a target by a sensor without physical contact with the target. This can be done based on detection and measurement of electromagnetic radiation, acoustic energy, which is emitted or reflected, or changes in gravitational fields. For the purpose of this research, remote sensing is the measurement of electromagnetic energy emitted or reflected from a location other than the point of measurement by instruments operated on air or space borne platforms. The reflected or emitted electromagnetic waves are received by sensors aboard the platform and the characteristics of these waves are dependent on the type or condition of the object (Campbell et al., 2002).

Previous studies have successfully used remote sensing data in evaluating LSMs. Using remote sensing data of snow and LST, Blyth et al. (2012) found that JULES was unable to correctly simulate the timing of transpiration and photosynthesis. The authors also noted that this inaccuracy was not detected in earlier works (Blyth et al., 2011) using ground based measurements including FLUXNET data for sites 'representative' of the major global biomes. Likewise, Ellis et al. (2009) used remote sensing products of vegetation and precipitation to evaluate soil moisture stress simulated from JULES and found that soil hydraulic properties were the main factors dictating seasonality of soil moisture within JULES, and that the partitioning of through-fall into evaporation and run-off determined the timing of soil moisture stress. They later concluded that a global soil moisture product would be useful for evaluating LSMs.

Although the utility of remote sensing in LSM evaluation have been shown in these studies, analysis of results were complicated by uncertainties which existed in both LSM simulations and observational data (Rhoads et al., 2001). This is because there was no prior understanding regarding the performance of the remote sensing datasets used to evaluate the simulations (Blyth et al., 2012). Moreover, most studies have concentrated on using remotely sensed LST. However, it is difficult to translate deviations between simulated and observed LST, or vegetation and precipitation, with deviations in actual soil moisture or ET due to the non-linear relationship between surface temperature and soil moisture or ET (Overgaard, Jesper and Rosbjerg, Dan and Butts, MB, 2006).

Space-borne sensors do not directly measure soil moisture and ET. Instead, observations made from space-borne sensors are converted based on retrieval models and other derived relationships between the observed quantity (electromagnetic radiation) and the state of interest (e.g. soil moisture, ET and vice versa). Therefore, the accuracy of products derived from remote sensing observations are affected by the model's formulation and its inputs, the parameterization scheme employed, and the assumptions made. All which can lead to errors in the derived states or fluxes. Furthermore, the observed signal is a combination of widely varying characteristics, which complicate interpretation when used to derive any products. Consequently, the direct evaluation of LSMs based on remote sensing products, as has been carried out in previous studies, is essentially a comparison between the remote sensing retrieval models and the LSM. To separate errors due to differences in remote sensing models and LSMs, the accuracy of satellite products will have to be understood prior to its application in evaluating simulations. Nonetheless, it is unclear which product is the most suitable for LSM evaluation. Therefore, it is desirable that, the assessments of soil moisture and ET simulated from LSMs to be based on remote sensing products i) of the same variables, i.e. soil moisture and ET themselves, and ii) of known accuracy or performance to ensure that these LSMs are able to perform well for the right reasons (Guzinski et al., 2015; Jiménez et al., 2009).

2.4.2 Remote sensing of soil moisture

The large contrast in dielectric properties between dry soil and water enables moisture content to be monitored based on the dielectric properties that are estimated from microwave techniques (Jackson et al., 1981). Microwave remote sensing uses the frequencies between 0.3 and 300 GHz of the electromagnetic radiation spectrum; corresponding to wavelengths between 1 m and 1 mm. Owing to their longer wavelengths, compared to visible and infrared radiation, microwaves are largely unaffected by cloud cover, haze, rainfall, and aerosols and so are not as susceptible to atmospheric scattering, which affects the shorter wavelengths (Engman, 1990; Schmugge et al., 2002). At microwave wavelengths, vegetation is semi-transparent thereby allowing observations of underlying surfaces, and measurements are not affected by solar illumination, thereby making observations possible both during the day and night (Jackson, 1993a).

Microwave remote sensing can be performed in passive and active modes. In passive mode, naturally emitted microwave electromagnetic radiation from the Earth's surface is measured, whereas in active mode, emissions are sent out by the instrument and the energy reflected from the surface is measured. Radiative transfer models relate the brightness temperatures of passive microwave and backscattering of active microwave to volumetric soil water content of soils in the top few centimetres through the dielectric constant. Soil moisture products are available from a range of passive sensors such as Microwave Imaging Radiometer with Aperture Synthesis, MIRAS, on-board SMOS ($\sim$35 km, 1 - 3 days), Windsat ($\sim$25 km, daily), and the Advanced Microwave Scanning Radiometer 2 (AMSR-2; $\sim$25 km, daily). An active remote sensing sensor is represented by the Advanced Scaterrometer (ASCAT; $\sim$25 km, 3 days) (Barrett and Petropoulos, 2013). Each of these methods have their strengths and weaknesses.

Although active microwave remote sensing can provide measurements with high spatial resolutions (tens of metres), signal interpretation is complicated due to the strong influence of surface roughness and vegetation, as well as distortion effects due to topography (Baghdadi et al., 2007). Moreover, the revisit period of active sensors is longer, ($\approx$35 days). Conversely, due to the weak signal of passive microwave emissions, a very large antenna and a highly sensitive radio receiver is needed. The consequence of having a large antenna leads to having a large beam width and therefore a poor spatial resolution, i.e. $\approx$40 km (Lillesand et al., 2004). Whilst Soil Moisture Active Passive (SMAP) integrates the advantages and disadvantages of active and passive sensors to produce a $\sim$9 km product, its radar instrument ceased making observations on the 7th of July 2015, only 5 months after launch. Therefore, it has a limited length of record within the time frame of this research.

Soil moisture is not directly measured by satellite borne sensors. Instead, brightness temperatures sensed by the radiometers are converted to soil moisture using algorithms based on radiative transfer and dielectric mixing models. Therefore, although remote sensing soil moisture products provide a promising alternative to *in situ* observations across the globe, these products need to be validated to ensure their quality prior to use.

In situ measurement of soil moisture is an established and invaluable tool for validating remotely sensed soil moisture data (e.g. Choi et al., 2008; Draper et al., 2009; Kim et al., 2015; McCabe et al., 2005; Rüdiger et al., 2009; Wagner et al., 2007). However, due to large discrepancies in scale between point measurements and footprint scales of space-borne radiometers, the soil moisture measured based on *in situ* methods are quite different quantities due to the different processes that occur across these two scales. Soil moisture at point scales is driven by soil properties, vegetation and topography which controls small scale processes such as infiltration and drainage (Vinnikov et al., 1999b). Conversely, soil moisture observed at the remote sensing scale is driven more by atmospheric forcing, particularly precipitation (Entin et al., 2000). Due to the high spatial variability of soil moisture, even the most dense network is inadequate for the validation of coarse resolution soil moisture products, and typically only covers a fraction of a single footprint (Crow et al., 2012).

Launched in November 2009, ESA SMOS satellite contains the MIRAS; a passive microwave 2-D interferometric radiometer which measures brightness temperature at L-band (1.4 GHz). SMOS operates in a sun-synchronous orbit with equator crossings at 6:00 am/pm (ascending/descending) local solar time with a repeat cycle of ≈3 days. Soil moisture products from SMOS have a spatial resolution of ≈40 km. Studies have shown that passive microwave remote sensing at L-Band (∼1 to 2 GHz) is the most promising for global monitoring of soil moisture as it responds to a deeper layer of soil (∼ top 5 cm), is applicable to all weather conditions, operates in a protected band, and has reduced effects from vegetation and surface roughness (Kerr et al., 2010).

Apart from SMOS, AMSR-2 is a multi-channel passive microwave sensor on-board the Global Change Observation Mission 1st - Water (GCOM-W1) satellite that was launched in May 2012 by the Japan Aerospace Exploration Agency (JAXA). AMSR-2 observes brightness temperatures in the following bands: C-band (6.9 GHz and 7.3 GHz) X-band (10.7 GHz), K-band (18.7 GHz), K_a-band (36.5 GHz) and E-band (89.0 GHz) (Imaoka et al., 2010). AMSR-2 is a follow on from Advanced Microwave Scanning Radiometer for the EOS (AMSR-E, ceased operations in 2011), and is planned to be carried on by GCOM-W2 and GCOM-W3 which will increase the existing record of data from AMSR-E, to more than 20 years. Whilst significant C-band Radio Frequency Interference (RFI) has been shown to contaminate data over North America, the Middle East and Japan, it has not been noted over Australia (Njoku et al., 2005). This makes soil moisture products from AMSR-2 suitable for use in Australia (Draper et al., 2009). Compared to SMOS, its temporal and spatial resolution is higher with products available every 2 days and due to oversampling provides products at 10 km and 25 km scales. AMSR-2 also operates in a sun-synchronous orbit with equator crossings at 1:30 am (descending/night-time) and 1:30 pm (ascending/day-time) local time.Two soil moisture products are available from AMSR-2; one derived by the JAXA algorithm (Fujii et al., 2009) and the other based on the Land Parameter Retrieval Model (LPRM) developed by the VU University Amsterdam, in collaboration with the NASA (Owe et al., 2008, 2001; Parinussa et al., 2015). The JAXA algorithm only provides soil moisture products based on observations at 10.7 GHz, whereas the LRPM algorithm also provides products based on observations at 6.9 and 7.3 GHz.

In Australia, soil moisture products from SMOS have been inter-compared with *in situ* observations of soil moisture and were found to have an RMSD of 0.10 m^3 m^{-3} (Su et al., 2013). However, the lookup method employed in this study to compute the mean area average soil moisture leads to inconsistencies in the quality of measurements used for validation. Similarly, using 7 cosmic-ray observations of soil moisture in Australia, it was found that the AMSR-2 soil moisture products based on the LPRM algorithm generally performed better whereas products based on the JAXA algorithm performed relatively better under dry conditions Kim et al. (2015). However, due to differences in area sensed by the cosmic-ray method and space-borne sensors, this study only validated the soil moisture products based on their correlations with ground observations. Whilst these studies have contributed to the development of remote sensing of soil moisture, absolute soil moisture values are crucial for applications in soil moisture forecast, data assimilation, water resource management and irrigation scheduling (Pauwels and Lannoy, 2015; Walker and Houser, 2004). Remotely sensed absolute soil moisture products based on different models and satellite observations have often been found to differ from each other (Koster et al., 2009). Consequently, *in situ* soil moisture stations used to validate remote sensing products also need to accurately capture the absolute soil moisture levels. Moreover, as RFI is not an issue in Australia a valuable opportunity to validate LPRM products based on 6.9 and 7.3 GHz presents itself. It is therefore necessary to reassess the quality of SMOS and AMSR-2 remote sensing soil moisture products in Australia.

To ensure that remote sensing soil moisture products are representative of absolute soil moisture levels, calibration and validation based on field campaigns where intensive ground measurements are taken, or sensors mounted on mobile platforms such as tractors or aircraft to obtain spatial averages, have been carried out. For example, the Southern Great Plains (SGP) 1999 Experiment (Jackson et al., 2002), Soil Moisture Experiments (SMEX02, SMEX03 and SMEX04) (Jackson et al., 2008), National Airborne Field Experiments (NAFE) 2005 and 2006 (Merlin et al., 2008; Panciera et al., 2008), Australian Airborne Cal/Val Experiment for SMOS (AACES) (Peischl et al., 2012) and Soil Moisture Active Passive Experiments (SMAPEx) (Panciera et al., 2014). Airborne soil moisture can be used as an intermediate scale measurement which can be aggregated to the footprint scale (Bindlish et al., 2006; Drusch et al., 2004). Whilst these mobile measurements are useful for applications at plot or field scale, they are expensive, require periodic calibration, and are limited to areas which are accessible to the mobile platform and intensive sampling periods.

Finally, another alternative is by using LSMs. LSMs are able to combine the effects of distributed rainfall, soil, vegetation and topographic characteristics to simulate soil moisture predictions over a large area. Crow et al. (2005) demonstrated that combining distributed modelling with ground-based observations is superior to simple averaging of ground based observations. However, the accuracy of up-scaled soil moisture products based on LSMs are limited by the lack of data to parameterize LSMs, and errors in the forcing used to drive these models. More importantly, as the end goal of research is to evaluate LSM simulations, up-scaling based on LSM is not applicable for this research.

Clearly, it can be seen that up-scaling of point measurements to the footprint size of space-borne radiometers is not a trivial task. Each of the different methods discussed above have their own strengths and weaknesses. *In situ* measurements are able to provide observations at high temporal scales but may not be representative of the satellite footprint. Field-campaigns allow areal average soil moisture levels to be captured but provide only a snapshot in time. Since an unparalleled suite of spatially distributed data of soil moisture from past field campaigns (SMAPEx, Panciera et al., 2014) and long-term soil moisture and EC measurements (OzNet Monitoring Network; OzNet, Smith et al., 2012) are available, this research combines the strengths of these different datasets. As there are only a limited number of sites and very few aircraft campaigns globally, it is important to ensure that these datasets are fully exploited. Furthermore, the merit of up-scaling these point measurements, based on representative stations rather than geostatistical methods or a combination with LSMs, is the potential reduction in cost and resources needed to upkeep extensive monitoring networks if such a station can be identified. Vinnikov et al. (1999a) found that having a dense instrument network does not necessarily mean result in a higher accuracy than a lower density instrument network. Additionally, as networks age and/or support for these monitoring networks wane, it is anticipated that resources to maintain these networks will decrease. In spite of this, long-term records are still needed for long-term validation purposes. Consequently, the ability to identify some subset of stations which can provide the same information for validating satellites is valuable for reducing the resources needed to maintain extended networks (Bittelli, 2011; Crow et al., 2012; Gruber et al., 2013).

2.4.3 Remote sensing ET

A growing number of global ET products have become available in recent times (Ershadi et al., 2014; Fisher et al., 2008; Mu et al., 2007; Vinukollu et al., 2011). ET estimation derived from models can be in the form of reference, potential or actual ET (Kalma et al., 2008; Wang and Dickinson, 2012). Whilst reference and potential ET can be easily estimated based on meteorological conditions, the scaling of potential and reference ET to actual ET is difficult due to the need for information regarding aerodynamic and surface resistances which are difficult to estimate. This is particularly true in regions where water availability is limited, such as the semi-arid environments of Australia (McCabe et al., 2013).

The basic idea behind the derivation of remote sensing ET products is based on using remotely sensed surface temperature derived from thermal infrared (TIR) data to infer the state of the surface and the partitioning of available energy into H and $L_{\mathrm{v}}E$. As the process of ET cools the land's surface, a reduction in transpiration causes an increase in canopy temperatures; these temperature variations can be detected by space-borne sensors in the TIR bands. Parameterization of the soil-plant-atmosphere system and other bio-physiological constraints can then be obtained from biophysical variables from remote sensing data such as surface albedo, α, vegetation cover and characteristics (e.g. Leaf Area Index (LAI), water content, height) and soil properties (e.g. soil water content, soil roughness). The reader is directed to Allen et al. (2011); Kalma et al.

(2008); Wang and Dickinson (2012) and Li et al. (2009) for a comprehensive review on current methodologies used to produce ET products from remotely sensed data.

Information of LST and vegetation conditions needed by these models can be obtained from remote sensing observations at TIR and visible band. Space borne sensors operating in the optical range (infrared and visible) can be of high resolution (e.g. Advanced Spaceborne Thermal Emission and Reflection Radiometer, ASTER; Compact High Resolution Imaging Spectrometer, CHRIS; Enhanced Thematic Mapper Plus, ETM+) or moderate resolution (e.g. Advanced Very High Resolution Radiometer, AVHRR; Moderate Resolution Imaging Spectroradiometer, MODIS; Japanese Advanced Meteorological Imager, JAMI). Generally, high resolution optical imagers have a spatial resolution of 10s of metres but with repeat periods of up to 16 days at best (e.g. ASTER has a repeat cycle of 16 days and a resolution of 15 m for visible bands/90 m for TIR bands) whereas moderate resolution optical imagers have a spatial resolution in the order of kilometres and its temporal resolution varies from two images a day to one every 16 days (e.g. MODIS has a repeat cycle of 1 to 2 days and a spatial resolution of 1 km for surface temperature). Accordingly, satellites with a higher temporal resolution often have a lower spatial resolution and those with a higher spatial resolution often have a lower temporal resolution (McCabe and Wood, 2006).

Most remote sensing ET models uses observations from polar-orbiting satellites such as the Moderate Resolution Imaging Spectroradiometer (MODIS) and the Advanced Very High Resolution Radiometer (AVHRR) which have a 250 m to 1 km spatial resolution but a temporal resolution of one day. However, ET information is required over a range of temporal (hourly to monthly) and spatial resolutions (field to regional) for applications in drought monitoring, agriculture, and catchment management (Anderson et al., 2011). Consequently, the instantaneous measurements have to be extrapolated to estimate the daily total ET (Cammalleri et al., 2014; Ferguson et al., 2010). Thus, the up-scaling of instantaneous ET to daily ET can lead to biases which differ depending on the up-scaling method used, cloud conditions, and season (Cammalleri et al., 2014). Such biases can be large as it is often assumed in these up-scaling processes that the sky is clear throughout the day, which is not always the case (Van Niel et al., 2012). Geostationary satellites are satellites which are able to provide observations with a higher temporal resolution as they are always directly over the same place on the Earth's surface. The use of observations from geostationary satellites can therefore enable ET to be mapped at hourly scales (e.g Anderson et al., 2007; Cammalleri et al., 2014; Fensholt et al., 2007; Schüttemeyer et al., 2007).

Launched in February 2005 and operational since 2008, the MTSAT series of geostationary satellites cover East Asia and the Western Pacific. Images in the thermal-infrared band from the MTSAT series of satellites are available hourly at 4 km resolution, which can be combined with other remote sensing data and an ET model to derive a 4 km hourly ET remote sensing product. Himawari-8 (7 July 2015 -2022) and Himawari-9 (scheduled for launch in 2016), both parts of the MTSAT series, provide observations every 10 minutes. This provides an opportunity to increase the temporal resolution of ET from daily observations to hourly. On-board the MTSAT satellites is JAMI, a moderate resolution optical imager that operates at 4 infrared channels (3.5 - 4 μm, 6.5 - 7 μm, 10.3 - 11.3 μm and 11.5 - 12.5 μm) and one visible channel (0.55 - 0.90 μm). Images in the thermal-infrared band from the MTSAT series of satellites were available hourly at 4 km resolution every 30 minutes allowing the diurnal variation of ET to be detected. Using the hourly observations of land surface temperature (thermal-infrared) and cloud mask from MTSAT a 4 km hourly ET products could be derived (Ershadi, A., 2015, personal communication). The MTSAT ET product used in this research was based on three different models, i.e. the Surface Energy Balance System (SEBS) (Su, 2002), the modified Penman Monteith (PM-Mu) (Mu et al., 2011) model and the modified Priestley Taylor (PT-JPL) (Fisher et al., 2008) model (Table 2.1). These products were based on previous work done by Ershadi et al. (2014). Still, as ET is not directly measured by space-borne sensors, but is derived based on models, the product's accuracy may be affected by assumptions in the models and parameters used (e.g. Rana and Katerji, 2000; Sellers et al., 1997b). Therefore, these remote sensing ET products have to be validated with ET field measurements prior to its application in evaluating simulations from an LSM.

Based on surface flux observations from eddy covariance towers, PT-JPL was found to be the best performing model, whereas SEBS was found to overestimate, and PM-Mu was found to underestimate by 78 W m^{-2} (McCabe et al., 2015). However, as described in the earlier section (Section 2.3), the footprint measured by EC systems varies with wind direction and speed (Aubinet et al., 2000; Baldocchi et al., 2001; Schmid, 1994). Despite this, previous validation of ET derived from remote sensing observations were carried out using FLUXNET stations without a prior understanding regarding

Table 2.1: Models used to derive ET products

Model	**Reference**
SEBS	Su, Z. (2002). "The Surface Energy Balance System (SEBS) for estimation of turbulent heat fluxes." Hydrology and Earth System Sciences Discussions, 6(1): 85-100.
PM-Mu	Mu, Q., et al. (2011). "Improvements to a MODIS global terrestrial evapotranspiration algorithm." Remote Sensing of Environment 115(8): 1781-1800.
PT-JPL	Fisher, J. B., et al. (2008). "Global estimates of the land-atmosphere water flux based on monthly AVHRR and ISLSCP-II data, validated at 16 FLUXNET sites." Remote Sensing of Environment 112(3): 901-919.

the representativeness of measurements of an entire model grid. Nevertheless, it is undeniable that measurements of surface heat fluxes from EC stations has and will continue to play a crucial role in improving our understanding regarding the exchange of water and energy fluxes between the land surface and the atmosphere at plot scales.

To overcome issues related to representativeness of measurements from EC systems of a remote sensing product grid, researchers have turned to scintillometers as a bridge for verification of coarser scale ET products. Due to its ability to measure path integrated sensible heat fluxes ranging from a few hundred metres to 10 km (Baghdadi et al., 2007; Beyrich et al., 2002; Meijninger and De Bruin, 2000; Samain et al., 2012b), scintillometers are suitable for long-term evaluation of model simulations and remotely sensed surface heat flux products (Hemakumara et al., 2003; Hendrickx, Jan MH and Kleissl, Jan and Vélez, Jesús D Gómez and Hong, Sung-ho and Duque, José R Fábrega and Vega, David and Ramírez, Hernán A Moreno and Ogden, Fred L, 2007; Kleissl et al., 2009a). Specifically, for the verification of remotely sensed derived ET products from energy balance models, optical scintillometers have been used to derive H. Together with measurements of R_{n} and G, $L_{\mathrm{v}}E$ (or ET) can then be derived as a residual of the surface energy balance (Andrews et al., 2001; Finnigan et al., 2003; Hill et al., 1980). Samain et al. (2012b) and Hoedjes et al. (2002) went a step further to up-scale measurements from scintillometers with EC tower measurements, LSMs and other satellite measurements to validate remote sensing ET products. Despite their success, in comparison to EC systems, scintillometry is still restricted to research catchments and due to the complexity in operating and interpreting its measurements, long-term measurements from scintillometers are still limited. Other efforts to up-scale measurements based on

EC measurements to validate global estimations of ET have also received considerable attention (Fang et al., 2015; Jung et al., 2009; Xiao et al., 2012, 2011). These up-scaling methods include machine learning approaches, light efficiency models and empirical or processed based models (Xiao et al., 2012). However, the accuracy of these ET estimates are constrained by the reliability of the land surface cover maps used for up-scaling the observations.

From the discussion above, it can be seen that despite the different methods to verify remote sensing ET products, these techniques are limited due to discrepancies in measurement scale, or they depend on land surface modelling, or satellite observations which have low temporal resolutions. Furthermore, they pose formidable resource demands in the way of highly sophisticated instruments. Based on numerical simulations, Bai et al. (2015) found that flux footprints from both EC systems or scintillometers cannot fully cover a coarse satellite pixel. Spatially representative data is needed for the validation of remote sensing surface flux products. Whilst the different ET models (SEBS, PT-JPL and PM-Mu) described earlier have been shown to work well (McCabe et al., 2015), the performance of each model will differ according to the region and climatic conditions in which it is applied to, and the data used to force the model. Therefore, since the location, forcing data and observations used to derive the ET products here differ with those of existing studies, a re-evaluation based on an improved understanding of the representativeness of EC measurements used for validation is deemed necessary.

This research seeks to overcome the issue of obtaining spatially representative data of ET by combining the high temporal resolution of EC and scintillometer systems to measure area averaged surface fluxes to identify spatially representative stations. Whilst this is only carried out at one site in this research, it is envisioned that such an analysis can be repeated for other EC stations to understand the spatial representativeness of a coarse satellite or model pixel. Subsequently, the EC system can be used to provide satellite-pixel-area-averaged surface flux measurements with high temporal resolution for long-term validation of remote sensing ET products. This method differs from existing efforts to understand the representativeness of flux tower networks which utilizes a cluster based tool (Sulkava, Mika and Luyssaert, Sebastiaan and Zaehle, Sönke and Papale, Dario, 2011). The value in the proposed method is the ability to continue using existing EC towers whilst minimizing the resources required for extensive networks.

2.5 Towards Land Surface Model evaluation

The ability to measure, estimate or predict soil moisture and ET globally is important for applications in climate and weather forecasting (Section 2.2.4). LSMs are the only way in which information regarding soil moisture and ET can be provided continuously across all spatial and temporal scales. However, there are large uncertainties in the outputs from LSM models due to errors in the input forcing data and parameters prescribed within the models, and model structural errors due to the model's physical equations. Dense observation networks are limited to experimental sites and test beds with the majority consisting of isolated stations. These isolated stations are unable to commensurate large scale variations of soil moisture and ET consistent with model grids (Section 2.3). Consequently, there is a demonstrated need for an approach to ensure the global performance of these models, based on global observations at scales consistent with model grids.

The increasing availability of remote sensing observations provides a global, near-real-time and consistent data record which can be used to assess LSMs without the spatial constraints inherent to *in situ* networks or temporal constraints of field campaigns. Therefore, this research proposes to evaluate simulations of soil moisture and ET from JULES based on remote sensing derived products of soil moisture and ET (Section 2.4). Importantly, prior to the application of remote sensing products in the evaluation of JULES simulations for a semi-arid demonstration site in southern NSW, Australia, the accuracy of the remote sensing products themselves needed to be verified. The only way remote sensing products can be verified is based on permanent monitoring stations underpinned by intensive field experiments. This is because one of the issues posed by remote sensing products validation is the scale mismatch between the satellite's footprint and the ground measurements (point scale). The ability to resolve the contrast between these spatial scales is crucial for meaningful verification of data products from satellite missions. Therefore, a better understanding of the representativeness of the ground measurements to the satellite footprint is required so as to minimize the impact of spatial sampling errors on the verification of satellite products based on point measurements.

To overcome the knowledge gaps identified in the earlier sections, the main objective of this research is to assess the ability of a LSM to accurately describe land surface processes which controls the redistribution of soil moisture, and partitioning of water

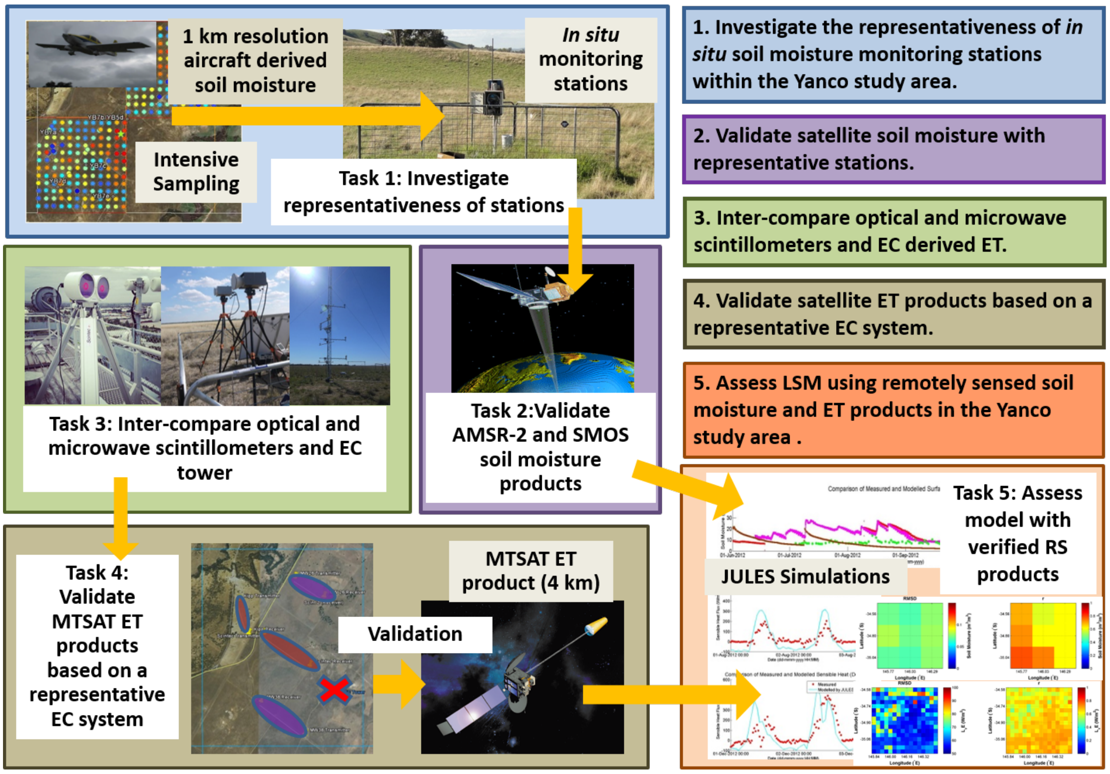

Figure 2.3: Methodology Flow Chart.

into ET (or energy into L_vE) using remote sensing products. To achieve this objective, this research can be divided into three main parts which can further be broken into five tasks (Fig. 2.3).

1. Soil moisture remote sensing validation.
    - Investigate the representativeness of *in situ* soil moisture monitoring stations within the Yanco study area (Chapter 3).
    - Validate satellite soil moisture with representative stations (Chapter 4).
2. ET remote sensing validation.
    - Inter-compare optical and microwave scintillometers and EC derived ET (Chapter 5).
    - Validate satellite ET products based on a representative EC system (Chapter 6).
3. Assessment of LSM soil moisture and ET simulations: A demonstration.

Scale	Examples	Advantages	Limitations	Research question	Approach / Task	Chapter	Additional outcomes
In situ (Point)	EC flux towers, soil moisture stations.	Direct observations, accurate, high temporal resolution.	Unrepresentative, limited global coverage.	How representative are point measurements of the regional area of satellite pixel?	Use field campaign measurements to understand the representativeness of measurements from soil moisture stations and EC tower.	3 and 5	• Identifying the appropriate methodology to understand the representativeness of *in situ* soil moisture monitoring stations. • Inter-comparing surface heat fluxes derived from an EC system, and optical and microwave scintillometers.
Regional scale observations restricted to experimental test beds	Field experiments, aircraft observations, scintillometers.	Areal average of plot and regional scale.	Expensive, short periods, limited coverage.				
Regional scale global observations	Remote sensing.	Areal average, global, consistent.	Inaccuracies in radiative transfer models.	How accurate are these products?	Use representative measurements to validate remote sensing products.	4 and 6	• Determining the performance of different remote sensing soil moisture products. • Assessing the performance of different remote sensing ET products .
Distributed land surface model simulations	CABLE, JULES, TOPLAST, SiB.	High spatial and temporal resolution.	Models developed at point scale might not capture larger scale processes.	How to evaluate distributed simulations from LSMs with a global, spatially consistent and accurate dataset?	Use validated remote sensing products to evaluate grid scale soil moisture simulations from an LSM.	7	• Demonstrating the effects of using different datasets to drive the LSM.

: Flow of research logic

TABLE 2.2: Summary of approach, research questions, flow of logic and additional outcomes.

- Assess LSM using validated remotely sensed soil moisture and ET products in the Yanco study area (Chapter 7).

The approaches developed from this research are generic and can be applied for the verification of soil moisture and ET products from different satellites and study areas. To demonstrate the methodology, this research will focus on validating soil moisture products from the AMSR-2 and SMOS, and ET products from MTSAT satellites at the Australian core validation site (Yanco). Yanco is situated on the central plains of the Murrumbidgee catchment area. Table 2.2 summarizes the end-to-end approach taken by this research to investigate the different research questions, the rationale of the approach taken and how these different tasks and parts relate to each other (Table 2.2). Chapters where the additional outcomes are described in **Chapter 1** have been also included.

2.6 Chapter summary

The importance of understanding the interactions between soil moisture and ET has been discussed. However, the quantification of soil moisture and ET remains a challenging task. Land surface modelling can provide estimates of soil moisture and ET with high temporal and spatial resolutions, but its accuracy is constrained by the accuracy of its forcing data, prescribed parameters, and the ability of the model itself to mimic the processes within the soil and between the land surface and the atmosphere. Due to the inadequacy of current monitoring networks to capture the spatial variability of soil moisture and ET at global scales, remote sensing products were proposed as an alternative method. However, as remote sensing products are also derived from models, the accuracy of these products need to be understood prior to the application in evaluating LSMs. One of the knowledge gaps in validating remote sensing products is the disparity in scales between point measurements and satellite footprints. Therefore, this research proposes a methodology for long-term evaluation of distributed LSM simulations using remote sensing soil moisture and ET products which have been validated with representative *in situ* measurements.

Chapter 3

Representativeness of *in situ* soil moisture monitoring stations in the Yanco study area

The high spatio-temporal variability of soil moisture complicates the validation of remotely sensed soil moisture products using *in situ* monitoring stations. Therefore, a standard methodology for selecting the most representative stations for the purpose of validating satellites is essential. This chapter utilizes i) long-term soil moisture measurements from the Yanco region of the OzNet Monitoring Network (OzNet), ii) high resolution soil moisture measurements taken during three extensive field campaigns, and iii) airborne soil moisture products derived for the area. This data are used to investigate the representativeness of stations within OzNet of Soil Moisture Active Passive (SMAP) soil moisture product grids. The methods employed to carry out this investigation include temporal stability analysis, point to pixel comparisons, and centered variogram analysis. Different performance indicators applied in previous temporal stability analyses were also compared. Based on the results of this study, recommendations were made regarding i) the representativeness of soil moisture stations within the Yanco study area, ii) application of the temporal stability method, and iii) the prospects of the centred-variogram analysis and airborne soil moisture products for identifying representative stations. The work in this chapter has been accepted subject to minor changes by the Journal of Hydrology.

3.1 Introduction

Soil moisture plays a critical role in land surface-atmosphere interaction through the partitioning of available energy into sensible and latent heat fluxes (Entekhabi et al., 2010b; Prigent et al., 2005), controlling the ratio of run-off to groundwater recharge (Delworth and Manabe, 1988), and influences climate variability through its feedback between precipitation (Koster, 2004; Pal and Eltahir, 2003; Taylor et al., 2013). Advances in remote sensing and the launch of dedicated soil moisture satellites such as the European Space Agency's (ESA) Soil Moisture and Ocean Salinity (SMOS) (Kerr et al., 2010) and the National Aeronautics and Space Administration's (NASA) Soil Moisture Active Passive (SMAP) (Entekhabi et al., 2010b) provide a mechanism for estimating soil moisture at global scales, which is impossible using only field measurements (Refsgaard, 1997). These soil moisture products can be assimilated into models to improve flood, weather and climate forecasting, as well as irrigation management and cropping practices (Brocca et al., 2012b; de Wit and van Diepen, 2007; Engman, 1991; Koster, 2004; Koster et al., 2009; Walker and Houser, 2001).

However, as remote sensing soil moisture products are derived from algorithms that rely on indirect physical quantities, namely brightness temperature, validation of long term and large-scale remote sensing measurements is imperative. This research proposes to identify a subset of stations which can provide such observations at the Yanco core validation site based on the identification of representative stations; i.e. stations which can provide measurements representative of average soil moisture within a satellite footprint. One of the ways in which representative stations can be identified is based on temporal, rank or order stability (You-Jun, 2006). Vachaud et al. (1985) observed that at certain points within a field, due to its soil properties, soil moisture values at those points do not vary much across long time scales with respect to the average soil moisture, whereas other points are consistently wetter (wet-biased) or drier (dry-biased) than the areal average. This concept has been applied in the past to identify representative locations for long-term validation of remotely sensed soil moisture products or model simulations (e.g. Cosh, 2004; De Lannoy et al., 2006; Gómez-Plaza et al., 2000; Jacobs et al., 2004; Li and Shao, 2015; Martínez-Fernández and Ceballos, 2005; Schneider et al., 2008; Zhou et al., 2015) as it can reduce the number of soil moisture monitoring stations needed to provide the same information for validation activities (Cosh et al., 2006). However, these studies assume that the average of measurements from all stations provide an accurate estimation of the areal average soil moisture.

In principle, a location which is able to capture the mean of the field with a small bias (low mean relative difference: MRD) and low variability (i.e. low standard deviation of the relative difference: SDRD) would be a representative station (refer to eq. 3.1 to eq. 3.4 in section 3.4.1). However, this can be difficult to define and it is dependent on the scale in question (Cosh, 2004). Previous studies have identified representative stations based on an MRD <0.1 m^3/m^3 and a low SDRD (e.g. Schneider et al., 2008), or purely based on MRD or SDRD (e.g. Grayson and Western, 1998; Martínez-Fernández and Ceballos, 2003), or a combination of both (e.g. Jacobs et al., 2004). The index which combines both MRD and SDRD to overcome the limitations intrinsic to the use of MRD or SDRD on its own was first introduced by Jacobs et al. (2004) as root mean square error (RMSE) and later coined as index of time stability (ITS) by Zhao et al. (2010) to prevent confusion with the general definition of RMSE. Based on a simulation study, Martínez et al. (2014) showed that the performance indicators used for selecting representative locations was most consistent based on MRD whereas those based on SDRD changed depending on weather patterns and sampling patterns. Conversely, several authors including Hu et al. (2012) and Gao et al. (2013) have compared the use of different time stability indicators using *in situ* measurements and recommended using ITS (or RMSE). Following this, Penna et al. (2013) successfully identified representative locations for two hillslopes based on RMSE. However, as these studies were conducted at scales ranging from 0.005 km^2 to 0.31 km^2 it would be valuable to compare them at larger scales, because even operational soil moisture products retrieved from the Sentinel-1 satellites acquiring SAR data in C-band, will be at 1 km^2 (Wagner et al., 2009).

Since the identification of a time-stable location requires long-term *a posteriori* information, the ability to identify a time-stable location using *a priori* information is of more value as it eliminates the need for establishing extensive soil moisture networks (Gómez-Plaza et al., 2000; Grayson and Western, 1998; Zhao et al., 2010). Several studies have tried to relate soil, vegetation, topographic and land use features of time-stable locations to features which can be used as *a priori* information for identifying a time-stable location (e.g De Lannoy et al., 2006; Jacobs et al., 2004; Mohanty and Skaggs, 2001; Zhao et al., 2010). Another method with potential is a slight modification of the regular variogram to characterize the spatial variability of soil moisture with respect to the stations (herein referred to as the centered-variogram). The centered-variogram represents the spatial variability of the variable under consideration radiating outwards from a point. It has previously been applied to determine the spatial representativeness of air-temperature records (Janis and Robeson, 2004) and tower albedo measurements (Román et al., 2009) but its potential to determine the spatial representativeness of soil moisture monitoring stations has not been explored. The possibility of using a centered-variogram to identify a representative station is attractive since it can possibly be used to identify representative points prior to setting up a soil moisture network based on observations from an airborne sensor.

The availability of a unique suite of data which includes intensive ground soil moisture measurements (250 m spacing), aircraft measurements (1 km) and long-term soil moisture stations (~5 years) measurements across scales ranging from local (3 km) up to regional (36 km), distinguishes it from other small areas (e.g. Brocca et al., 2012b; De Lannoy et al., 2006; Hu et al., 2012) or short term studies (e.g. Cosh, 2004; Cosh et al., 2006; Famiglietti et al., 2008; Martínez-Fernández and Ceballos, 2005). Consequently, using the Yanco core calibration/validation site for SMAP as a case study, this study compares a temporal stability analysis based on long-term soil moisture observations from OzNet, with high resolution soil moisture measurements taken during three extensive field campaigns (SMAPEx 1-3, Panciera et al., 2014) and airborne soil moisture products derived for the area (Gao et al., 2016, in preparation). This is to assess the representativeness of stations within OzNet and make recommendations on the design of future networks. As SMAP integrates measurements from an L-band radar and an L-band radiometer to provide i) ~3 km high resolution (radar only), ii) ~36 km low resolution (radiometer only) and iii) ~9 km intermediate resolution (combined radar-radiometer) soil moisture products, the analysis was carried out at these different scales.

3.2 Study area

The *in situ* soil moisture data for this study was obtained from the Yanco site (34.561°S to 35.170°S, 145.826°E to 146.439°E), a 60 km × 60 km intensive study area within the Murrumbidgee River catchment in New South Wales, Australia (Fig. 3.1) and a subset of the wider OzNet soil moisture network (Smith et al., 2012). The Yanco area is generally

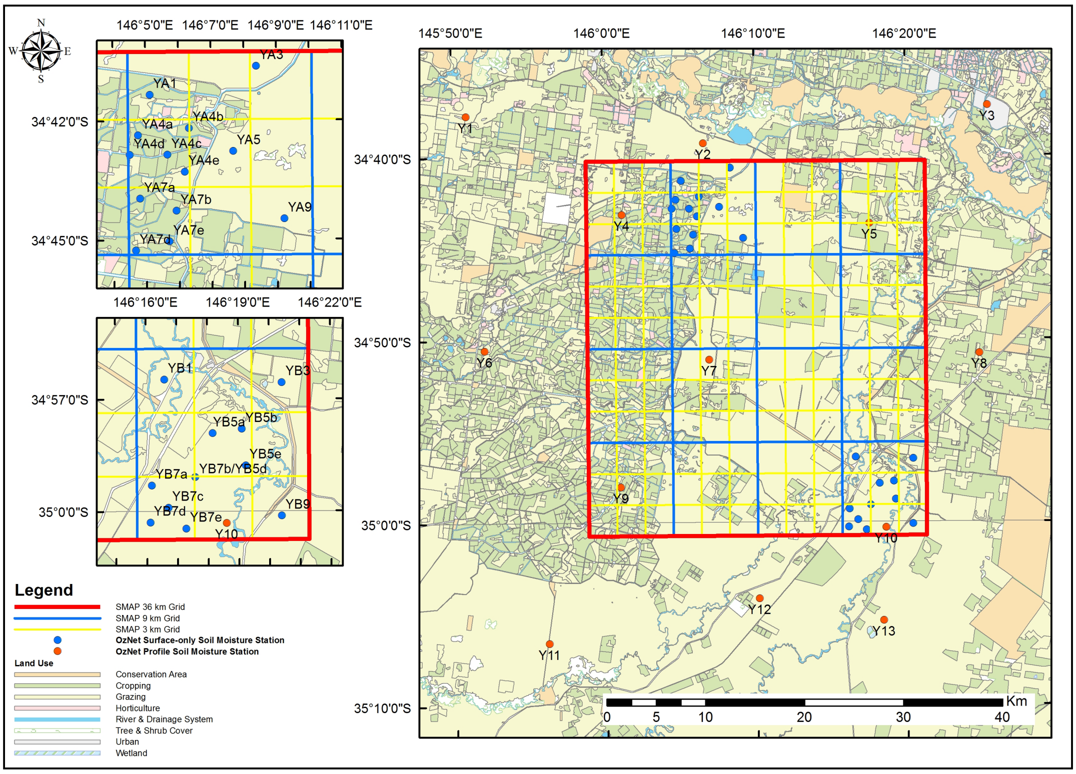

FIGURE 3.1: Land use of study area overlaid with SMAP 3 km (yellow lines), 9 km (blue lines) and 36 km (red lines) pixels and locations of permanent Y- stations. Left insets show the distribution of the cluster YA- and within the 9 km pixels (top: YA, bottom: YB).

flat with elevations ranging from 117 m to 150 m, and its soil types are predominantly clays, red brown earth, transitional red brown earth, sands over clay, and deep sands. According to data from 1981 to 2010 (Bureau of Meteorology station ID. 074037), the region has a mean daytime temperature that varies from 32.1°C in January to 13.5°C in July. Annual rainfall has a mean of 418.5 mm, mostly falling during winter and late autumn.

This area has been extensively monitored for remote sensing research, with soil moisture monitoring stations for soil moisture at various depths. Moreover, a series of field experiments has been performed, contributing to the pre- and post-launch algorithm development of missions such as SMOS and SMAP; National Airborne Field Experiment 2006 (Merlin et al., 2008), Australian Airborne Cal/Val Experiments for SMOS (Peischl et al., 2012) and Soil Moisture Active Passive Experiments (SMAPEx) (Panciera et al., 2014).

3.3 Data sets

To identify the representative stations, long-term soil moisture measurements from the OzNet soil moisture network, intensive measurements from a series of three airborne field experiments, SMAPEx-1 to -3, and 9 days of high-resolution soil moisture maps derived from airborne observations were used in this study (Table 3.1).

Table 3.1: Datasets used in study. Notation i, x and y indicates the number or alpha character used to differentiate stations within different SMAP grids. HDAS: Hydraprobe Data Acquisition System. PLMR: Polarimetric L-band Multibeam Radiometer. SMAP: Soil Moisture Active Passive.

Stations		**SMAP reference grid (km)**	**Type**	**Resolution**	**Period**
Permanent:	Yi; i =1:13	Yanco	Point	-	Dec 2009- Feb 2015
Clusters:	YAx; x = 1,3,5,9	9	Point	-	Dec 2009- Feb 2015
	YBx; x = 1,3,9	9			
	YA4y; y = a,b,c,d,e	3			
	YA7y; y = a,b,d,e	3			
	YB5y; y = a,b,d,e	3			
	YB7y; y = a,b,c,d,e	3			
PLMR		36	Average	1 km	9 days (SMAPEx-3)
HDAS (Intensive)		3	3 samples per point	250 m	SMAPex-1 to -3

3.3.1 OzNet Soil Moisture Monitoring Network

The *in situ* soil moisture data of Yanco is part of the soil moisture monitoring network known as OzNet, which has been recording soil moisture data since 2001 (www.oznet.org.au, Smith et al., 2012). Within the study area, there are 13 sparsely distributed permanent stations (Y1-Y13), and two densely located clusters of stations (YA and YB) installed specifically for the SMAPEx field experiments (Fig. 3.1). This nomenclature is based on Smith et al. (2012) and Panciera et al. (2014).

Of the 13 permanent stations, 5 stations fall within one of the 36 km SMAP product pixels. These permanent stations were installed in 2003 and are equipped with a vertically installed Stevens Water Hydraprobe impedance sensors and Campbell Scientific CS616 frequency domain reflectometers to measure the soil moisture content at the sites, a Hydrological Services TB4 rain-gauge and a thermistor at 2.5 cm and 15 cm for soil temperature observations. The cluster stations only measure surface soil moisture using a Hydraprobe inserted vertically from the surface and soil temperature using Unidata 6507A temperature sensors at 1 cm, 2.5 cm and 5 cm. These cluster stations are concentrated within the YA and YB areas, which correspond to two nominal 9 km SMAP validation grid pixels (Fig. 3.1). The YA area is largely located within the Coleambally Irrigation Area (CIA) which consists of farms with a mix of flood irrigation and dryland cropping, whereas the YB area mainly consists of pastures for grazing. These cluster stations were installed in 2009 - 2010 with site locations selected in such a way that 4 - 5 stations would fall within each of two 3 km $\times$ 3 km focus areas for each of the 9 km areas (YA4 and YA7 within the YA area, and YB5 and YB7 within the YB area), thus corresponding to four nominal 3 km SMAP high resolution product pixels.

To differentiate the stations, permanent stations with profile measurements are denoted with the prefix 'Y-' whereas cluster stations with are denoted 'YA-' and 'YB-', and stations further concentrated within the 3 km pixels are denoted with 'YA4-', 'YA7-', 'YB5-' and 'YB7-' (Table 3.1). Half hourly surface soil moisture measurements (top 5 cm) from the period 1st December 2009 to 28th February 2015 were used in this study.

3.3.2 SMAPEx field campaigns

The Soil Moisture Active Passive Experiments (SMAPEx-1 to -3), aimed at the development and validation of SMAP high resolution soil moisture products, were carried out at the site from 2010 to 2011. SMAPEx-1 (Austral winter, 5 - 10 July 2010) and SMAPEx-2 (Austral summer, 4 - 8 December 2010) were conducted over a single week, whereas SMAPEx-3 (Austral spring, 5 - 23 September 2011) was performed across three weeks. More details regarding these campaigns including the experimental plan and site conditions can be found in Panciera et al. (2014).

During these campaigns, intensive ground sampling of soil moisture was carried out within the 3 km YA- and YB- pixels at a 250 m spacing (Table 6.1). Measurements from 0 - 5 cm were acquired using the Hydraprobe Data Acquisition System (HDAS), a spatial data acquisition tool which integrates a Hydraprobe and a hand-held PC with GPS (Merlin et al., 2008). Three measurements were taken within a radius of 1 m at each sampling location and these values averaged during post-processing. The calibration approach applied to the station and HDAS measurements were as described in Merlin et al. (2007) and were verified using gravimetric samples. Due to heavy rainfall prior to SMAPEx-2, some areas were flooded meaning soil moisture observations were not available in the YB7 area.

3.3.3 Airborne soil moisture product

This study uses passive microwave data derived from regional flights during SMAPEx-3, prior to the launch of SMAP. The regional flights covered an area which coincided with the single SMAP 36 km radiometer pixel in Fig. 3.1. On-board the aircraft was the Polarimetric L-band Multibeam Radiometer (PLMR; 1413 MHz and bandwidth of 24 MHz, V-H polarization) installed in a push-broom configuration; meaning that the six beams are arranged across the flight path to enable a larger coverage of the area, and with a footprint resolution of approximately 1 km at 3 km flying altitude. The L-band brightness temperature data translates into 0 - 5cm observation depth. The brightness temperature was then used with parameters such as vegetation water content (VWC), soil surface roughness and soil temperature to derive an airborne soil moisture product at 1 km resolution using a τ-ω radiative transfer model (Gao et al., 2016, in preparation). Rainfall events occurred from the 5th to the 7th ($\sim$ 5 mm) and 10th to 12th of September 2011 ($\sim$ 3 mm).

3.4 Methodology

A representative station is defined in this study as a station which measures soil moisture content close to the areal average of the SMAP pixel of interest, or one that can be used to obtain the average over an extended period (Vanderlinden et al., 2012). To do so, the representativeness of the stations in Fig. 3.1 were evaluated based on temporal stability analysis, comparisons between station measurements and high density roving measurements (point to pixel comparison), and geostatistical analysis (variogram and centered-variogram analysis) based on both high intensity ground measurements and 1 km airborne soil moisture product.

3.4.1 Temporal stability analysis

As temporal stability is well-documented in previous studies (e.g. De Lannoy et al., 2006; Gómez-Plaza et al., 2000; Martínez-Fernández and Ceballos, 2003), its theory will not be repeated here. The data record used in these studies have ranged from less than 1 year to 3 years; compared to the 5 years and 3 months of data here. Temporal stability analyses were performed here for 1) four 3 km pixels (YA4, YA7, YB5 and YB7); 2) two 9 km pixels (YA and YB); and 3) a single nominal SMAP 36 km pixel. Only the representative stations from the 3 km pixels were used in the subsequent analysis at 9 km, and likewise, only the most representative stations of the 9 km pixels were used for the 36 km pixel. The rationale for this was to avoid biasing the spatial mean from having more soil moisture stations in a certain area. Similarly, stations were only considered when at least 75% of the monitoring station's data were available. In addition, measurements which fell outside a station's 90% confidence interval over the entire study period were discarded to remove extreme outliers (Rüdiger et al., 2009). This resulted in the removal of more than 50% of the available dataset. From the analysis, MRD and SDRD were derived for each station. The areal mean soil moisture at time j for N stations is

$$\overline{\theta_j} = \frac{1}{N} \sum_{s=1}^{N} \theta_{s,j}, \tag{3.1}$$

where $\theta_{s,j}$ represents soil moisture observed by the s^{th} station and j^{th} time step, respectively. Therefore, the relative difference, RD, for station s at time j can be expressed as

$$\mathrm{RD}_{s,j} = \frac{\theta_{s,j} - \overline{\theta_j}}{\overline{\theta_j}}, \tag{3.2}$$

which gives MRD as

$$\mathrm{MRD}_s = \frac{1}{m} \sum_{j=1}^{m} \mathrm{RD}_{s,j}, \tag{3.3}$$

and SDRD as

$$\mathrm{SDRD}_s = \sqrt{\frac{1}{m-1} \sum_{j=1}^{m} (\mathrm{RD}_{s,j} - \mathrm{MRD}_s)^2}. \tag{3.4}$$

A station which measures soil moisture close to the spatial mean would have an MRD close to 0. At the same time, a low SDRD (time or rank stable) indicates that the station has a similar temporal pattern as the spatial mean soil moisture (De Lannoy et al., 2006). Ideally, a representative station would have a MRD and SDRD which is close to 0. It is noteworthy that temporally stable sites having a non-zero MRD can be used to represent the areal average soil moisture if the offset between the site and the areal average soil moisture is known (Grayson and Western, 1998). However, the assumption based on this method is that the offset is constant regardless of time and this has been questioned by previous studies (Gao et al., 2016; Heathman et al., 2012).

Following Jacobs et al. (2004), to combine both MRD and SDRD, the root mean square error (RMSE) of the biases (MRD) and its precision (SDRD) was computed as

$$\mathrm{RMSE}_s = \sqrt{\mathrm{MRD}_s^2 + \mathrm{SDRD}_s^2}, \tag{3.5}$$

where s is the soil moisture station to account for both MRD and SDRD. For the remainder of this chapter, the subscripts will be removed for MRD and SDRD as it should be understood that MRD and SDRD are station specific. However, to avoid confusion with RMSE used in statistics as a measure of the differences between values, RMSE_s will be retained to describe the RMSE of the RD. Note that MRD is a ratio and therefore is unitless.

In this study, a representative station is considered to be one with the lowest RMSE_s. However, as discussed previously, different studies have used different performance indicators to define representative stations. Therefore, to examine how different performance indicators can affect the results, the analysis was also carried out based on MRD (stations with MRD closest to zero) and SDRD (stations with SDRD closest to zero, i.e. time or rank stable) alone. Unless specified, the representative stations described in this study are based on using RMSE_s as an indicator. Moving from a smaller (9 km) to a larger scale (36 km), it is assumed that the single stations within 9 km pixels without intensive sampling are also representative of the field scale. Subsequently, temporal stability analysis and point-to-pixel comparisons were conducted to identify the most representative stations within the 36 km pixel. This analysis was also extended beyond the 36 km SMAP pixel perimeter to include the nearby permanent (Y) stations.

3.4.2 Point to pixel comparison

Representative stations are identified above based on a set of stations. However, due to the low density of stations within each pixel, it is unclear whether those individual stations are actually representative of the soil moisture conditions at the local scale. Therefore, to investigate a station's representativeness locally, comparisons were made between daily averages for each station and intensive sampling performed on the same day. Similarly, using the airborne soil moisture product, the average soil moisture for the 36 km pixel was compared with the daily mean soil moisture for each station on the day the flight was made. Stations with the lowest mean bias compared to the average of all intensive measurements were considered as the most representative of the areal average. Bias here was computed as

$$\text{Bias} = |(\overline{\theta_A} - \overline{\theta_B})|, \tag{3.6}$$

where $\overline{\theta_A}$ is the spatial mean from sample A and $\overline{\theta_B}$ is the spatial mean from sample B.

3.4.3 Centered-variogram

To characterize the spatial distribution of soil moisture within the SMAP product, omnidirectional variograms (herein referred to as standard variograms) for each pixel were derived in the same manner as previous studies (e.g. De Lannoy et al., 2006; Joshi and Mohanty, 2010; Western et al., 1998). The experimental variogram of soil moisture pairs at separation distance h, is then given by

$$\gamma(h) = \frac{1}{2n(h)} \sum_{i,j} (\theta_i - \theta_j)^2, \tag{3.7}$$

where $n(h)$ is the number of pairs of observations at separation distance h, θ_i and θ_j are soil moisture values at i and j. These experimental variograms were then fitted with the Whittle's elementary correlation function (Whittle, 1954) (herein referred to as the Whittle function). Although previous studies have applied the exponential model (e.g. De Lannoy et al., 2006; Western et al., 1998), by comparing several variogram models, the Whittle function was found to perform the best in this case based on goodness of fit statistics. The Whittle function is given by

$$\gamma(h) = c_0 + c\left[1 - \frac{h}{r} K_1\left(\frac{h}{r}\right)\right], \tag{3.8}$$

where c is the sill, c_0 is the nugget, r is the distance parameter and K_1 is the modified Bessel function of the second kind. The effective range of the Whittle function is defined as the distance when the variance reaches 95% of the sill, which is approximately equivalent to $4r$. A least squares minimization of the error between the Whittle function and the experimental variogram was performed to derive c, c_0 and r. The standard variogram was derived using intensive ground measurements for each 3 km pixel during each campaign (one per week) and using the 9 days of airborne soil moisture over a 36 km pixel to characterize the spatial variability of soil moisture within these pixels.

The point-centered-variogram was fashioned similarly to the standard variogram in Eq. (3.7) with a modification such that

$$\gamma(h) = \frac{1}{2n(h)} \sum_{i,s} (\theta_i - \theta_s)^2, \tag{3.9}$$

where θ_s is the daily average soil moisture of the stations and θ_i is the intensive soil moisture (ground or airborne) measured at distance h from the station. Each experimental centered-variogram was fitted with the Whittle function to derive c, c_0 and r as with the standard variograms. However, unlike the standard variograms, centered-variograms are limited in the number of inter-station pairs. As the field campaigns were designed for the validation of airborne soil moisture products rather than representativeness of stations, biases caused by lack of data was expected for stations close to the edge of the sampling grid. Therefore, the results from the centered-variogram analysis conducted here are more applicable to recommending how future airborne campaigns for soil moisture monitoring networks could be designed in order to identify representative stations.

As the nugget, sill and range derived from each variogram change with mean soil moisture conditions, and are therefore spatially varying, the spatial representativeness was evaluated based on the ability of each station to resolve the coherent spatial variability across each pixel size. The hypothesis is that if the model derived based on fitting the Whittle function to a station's centered-variogram fits well with that of the standard variogram derived for the pixel under consideration, the station is representative of that pixel. The goodness of fit between the centred-variogram and standard variogram was based on the coefficient of determination, R^2, and RMSE between the two fitted variogram models. This provides a reliable and conclusive means of determining representative stations. The analysis was carried out using the intensive ground measurements at 250 m spacing for the 3 km pixels, and with 1 km resolution airborne soil moisture for evaluation at the 36 km pixel.

Table 3.2: Representative stations based on different methods for each pixel and recommendations for long-term validation

Pixel	Focus area	Method of Identification					Rep.[1] station
		Temporal Stability[2]			Point to Pixel[3]	Centered Variogram[3]	
		MRD	SD	RMSE	MRD	Best fit	
3 km	YA4 YA7 YB5 YB7	YA4b YA7d YB5a YB7a	YA4e YA7e YB5a YB7b	YA4e YA7d YB5a YB7a	YA4b YA7b YB5e YB7e	YA4e YA7e YB5d YB7a	YA4b/Weight[4] YA7b/Weight[4] YB5e YB7e
9 km	YA YB	YA1 (YA1) Y10 (YB7d)	YA7e (YA7e) YB7b (YB7a)	YA5 (YA5) YB7a (YB7c)	– –	– –	YA5 YB7a
36 km	Y	Y7 (YA4c)	YB5d/YB7b (YB5d/YB7b)	YA5 (YB7c)	YB7e, YA5	YB3	YA5
Yanco	Y	Y3 (YA4c)	YB5d/YB7b (YB5d/YB7b)	YA5 (YB7c)	YB7e, YA5	YB3	YA5

3.5 Results and Discussion

3.5.1 Temporal stability analysis

Stations derived from temporal stability analysis using long-term soil moisture measurements were ranked from the smallest to the largest MRD, with error bars indicating the SDRD (Fig. 3.2). The RMSE_s for each station is indicated by the shaded bars. The position of the station within the graph indicates whether the station systematically underestimates (negative MRD) or overestimates (positive MRD) the areal average soil moisture. SDRD indicates the rank stability, whereby a low SDRD indicates a time or rank stable locations. As RMSE_s takes into account both the MRD and SDRD, a station with a low RMSE_s would have a near zero MRD and a small SDRD. Results based on different indicators (solely based on MRD, SDRD or RMSE_s) are summarized in Table 3.2.

Average MRD within the YA4 (0.20) 3 km pixel was the highest followed by YA7 (0.16), and YB5 and YB7 (both 0.12). The larger RD between stations and the areal average soil moisture within YA4 and YA7 may be attributed to the presence of mixed irrigation and cropping activities, as opposed to the YB areas which are mainly semi-arid grassland. Consequently, the average SDRD was the also the highest for YA4, followed by YA7, YB5 and YB7 (YA4: 0.47, YA7: 0.35; YB5: 0.27, YB7: 0.24). Except for the YB5 area, representative stations identified from the different indicators, MRD, SDRD or

[1]Representative

[2]Based entirely on stations. Stations in brackets are representative stations when analysis was carried out without eliminating stations from one pixel scale to another.

[3]Based on intensive ground samples for 3 km pixel and airborne soil moisture for 36 km and Yanco pixel.

[4]Weighted average of different stations based on landuse area occupied by the station.

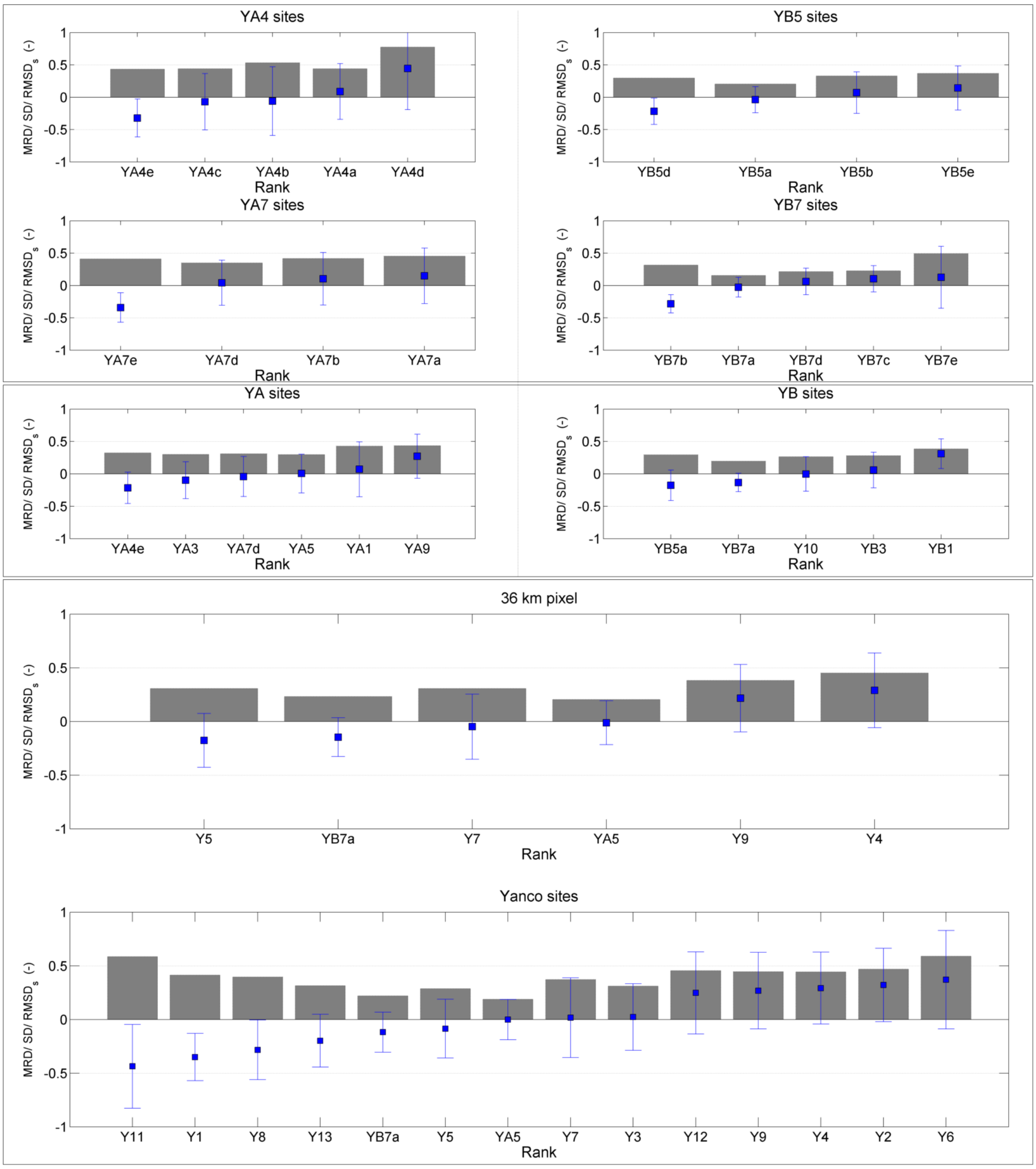

FIGURE 3.2: Rank-ordered MRD for stations within YA4, YA7, YB5 and YB7 3 km pixels; YA and YB 9 km pixels, the 36 km SMAP pixel and the Yanco study area. Squares: Mean relative difference, MRD; Error bars: Standard deviation of MRD, ±SDRD; Shaded bars: Root mean square error of MRD and SDRD, RMSE$_s$.

$RMSE_s$, differed (Table 3.2). This suggests that the indicator used to select the most representative station may affect the results.

For the 9 km pixels, the non-representative stations at the 3 km scale were discarded and the analysis repeated with the additional stations. Fig. 3.2 shows results from temporal stability analysis after retaining representative stations based on $RMSE_s$. This time, YA5 and YB7a were found to be the most representative based on $RMSE_s$. Brocca et al. (2012b), Vanderlinden et al. (2012) and Zhao et al. (2010) found that the range of MRD and/or SDRD increased with area due to the greater variability in soil type, vegetation cover and land use. A mixed result is observed here for the YA area (MRD: 0.12, SDRD: 0.32) and the YB area (MRD: 0.14, SDRD: 0.24). This may be an effect of selecting only the representative stations when moving from the 3 km to 9 km pixel. Fig. 3.3 shows the results of the temporal stability analysis if stations were not eliminated when moving from a smaller to larger pixel scale.

Comparing the average SDRD when all stations were included, the average MRD and the average SDRD was 0.21 and 0.43 for YA, and 0.13 and 0.29 for the YB 9 km pixel. The elimination of stations from one scale to another increased MRD and decreased SDRD for the YB area. On the other hand, both MRD and SDRD decreased for the YA 9 km pixel and is even lower than the average MRD and SDRD for the individual 3 km pixels. This is likely due to the higher concentration of cropping activities within YA4 and YA7 as seen in Fig. 3.1.

Nevertheless, stations which were found to be representative of the YA 9 km pixel were the same with or without eliminating stations (Table 3.2). However, for the YB 9 km pixel, the results differed. Based on MRD, YA1 and Y10 were found to be representative of the 9 km pixels (Table 3.2). In an earlier study, based on a shorter record of data, Disseldorp et al. (2013) also found that YA1 and Y10 were the most representative of the 9 km pixels based on MRD. In fact, despite the different datasets used, both studies found YA4b and YA7d to be most representative of YA4 and YA7 3 km pixels based on MRD. Results for the YB5 and YB7 area were slightly different, but this is due to the small MRD between sites within the YB5 and YB7 area. This shows that the stations are well-distributed within the 9 km pixels and gives a good estimate of the 9 km areal soil moisture.

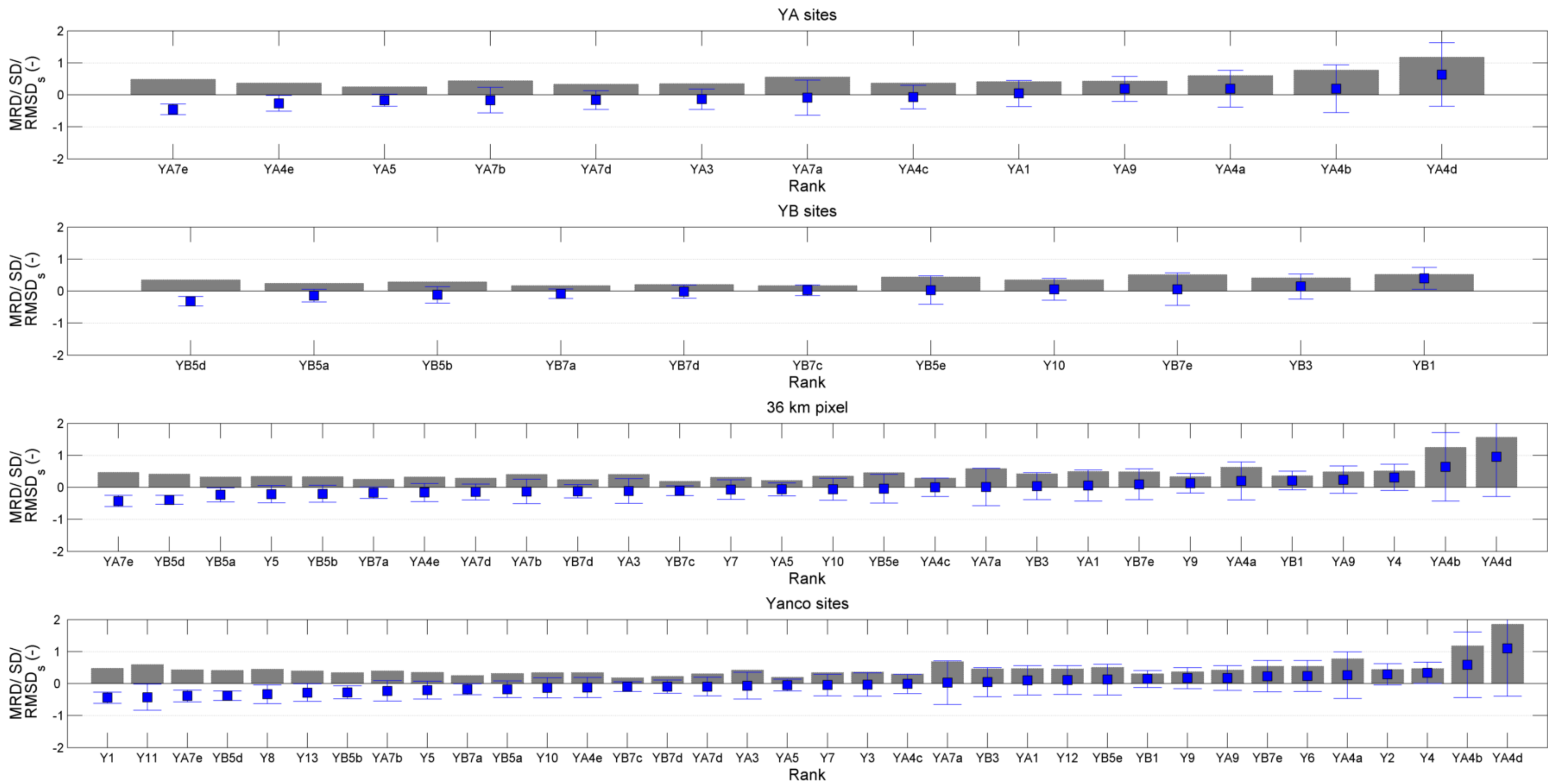

FIGURE 3.3: Rank-ordered MRD for stations within the 36 km SMAP pixel and the Yanco study area without elimination of stations from one scale to another. Squares: Mean relative difference, MRD; Error bars: Standard deviation of MRD, ±SDRD; Shaded bars: Root mean square error of MRD and SDRD, RMSE$_s$. YB5d and YB7b are the same station but is indicated as YB5d here due to space limitation

For the 36 km pixel (Fig. 3.2), YA5 was found to be the most representative station based on $RMSE_s$ and Y7 based on MRD, whereas YA5d/YB7b was found to be representative based on SDRD. By including all other stations beyond the 36 km pixel (Yanco), although the range of MRD and SDRD increased (Fig. 3.2), results remained the same based on $RMSE_s$ and SDRD. Similarly, comparing with results based on not eliminating stations, a closer inspection of Fig. 3.3 reveal that YA5 and YB7a had the lowest $RMSE_s$ after YB7c for the 9 km, 36 km and wider Yanco area. As for the 9 km pixels, stations within each pixel scale are likely to be sufficiently well-distributed to be able to give a representative measurement of soil moisture for their respective grid. As a result, whether stations are eliminated or not when moving from one scale to another does not affect the results of the analysis. In the same way, a smaller subset of stations can be used to provide the same information for this study area.

Fig. 3.4 shows the time-series of average near-surface soil moisture during SMAPEx-3 (top) and between January 2013 to December 2014 (bottom) based on measurements from all stations without elimination (green), stations within the 36 km pixel (cyan), and stations within the entire Yanco area (yellow) after eliminating non-representative stations within the 3 km and 9 km pixels based on $RMSE_s$. Generally, the temporal dynamics of the three combinations agree with one another. As seen previously, this also indicates that the distribution of sites within OzNet is able to capture the spatial variability of rainfall events despite having more stations in the YA or YB area. In contrast to the 3 km and 9 km pixel, at 36 km pixels, rainfall is likely to be more influential in controlling the spatial variability of soil moisture than soil type, vegetation cover and land use at the event scale. Therefore, at 36 km scale, a few stations are adequate for estimating the areal average soil moisture providing they are representative (Brocca et al., 2012b).

Although YB7c (light blue) follows a similar pattern with that of the average of all stations, its peaks after a precipitation event are lower in magnitude compared to the average of all stations, thereby making it more temporally stable (small SDRD) in comparison to other stations. Drier sites have previously been found to be more time-stable (Hu et al., 2012; Martínez et al., 2014). In the same way, YB7c which is drier after precipitation events will also have a smaller SDRD and therefore smaller $RMSE_s$. As a result, choosing a representative station based on time or rank stability would favour drier stations when SDRD or $RMSE_s$ is used as an indicator. If YB7c were to be used

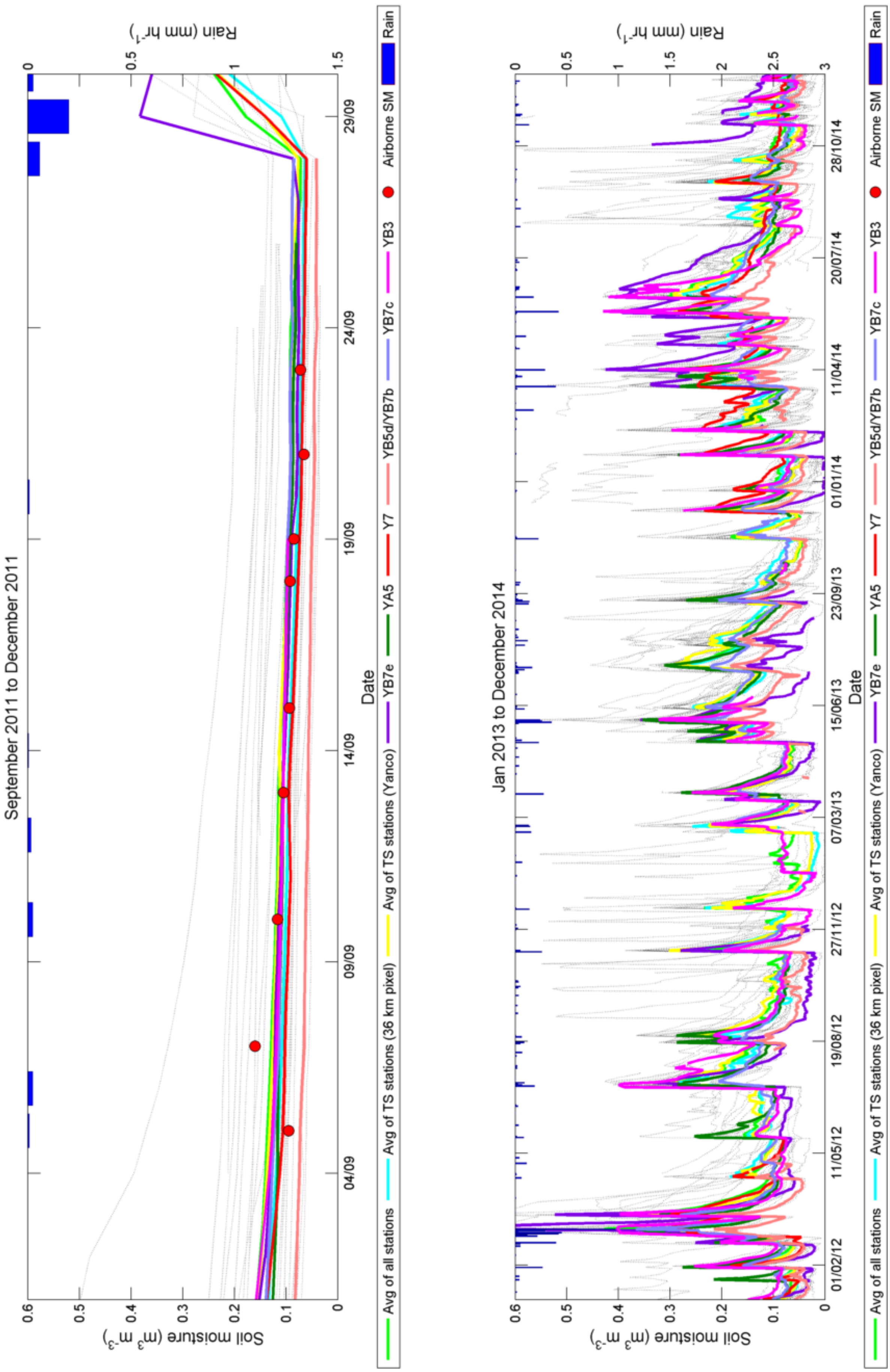

FIGURE 3.4: Timeseries of near-surface (0-5 cm) soil moisture measurements comparing different representative soil moisture stations at 36 km scales identified based on different methods. The gray lines are measurements from stations which were not selected.

for the validation of remote sensing soil moisture products, the products will appear to overestimate after a precipitation event.

In addition, the YB area is likely to have low SDRD values due to its location in a land used mainly for grazing activities. Conversely, where mixed land use is present, such as within the YA areas, both the spatial variation of soil moisture is also expected to differ from season to season depending on decisions made by farmers, which are difficult to forecast or predict. This leads to high MRD and SDRD of stations within the YA area. For the purpose of measuring the temporal dynamics of an area it has been suggested by Schneider et al. (2008) that temporal stability may be adequate; however, if the objective is to validate satellite products, the ability of a station to represent the spatial mean of the satellite product pixel is more important. A station which is located within an area where mixed land use is present will unlikely be temporally stable. But, this does not mean that it is unrepresentative or that it cannot provide any information regarding the spatial variability of soil moisture. This is further investigated in the next section.

3.5.2 Point to pixel

In this analysis, intensive ground sampling taken across the four 3 km SMAP pixels was divided into 1 km pixels to enable comparisons between stations at 1 km and 3 km scales. Intensive soil moisture measurements were found to be wetter compared to stations for the YA7 (0.12 m^3 m^{-3}), YB5 (0.06 m^3 m^{-3}) and YB7 (0.05 m^3 m^{-3}) areas (Fig 3.5). This may be caused by the establishment of the station itself and/or selection of the location of the station (which in YB was largely along the fence line). Moreover, the daily variation of soil moisture for each station was largest during SMAPEx-2 (Fig. 3.5 for all stations due to a dry-down event after extreme rainfall which fell before the campaign and on the last day of the campaign (53 mm between November 1 and December 1).

Some stations located in cropping areas also registered an increase of soil moisture due to flooding irrigation. For example, YA7a was also found to be almost 0.30 m^3 m^{-3} higher than the closest intensive sample during SMAPEx-2, but during SMAPEx-1, it was 0.10 m^3 m^{-3} lower (Fig 3.5). The data for these periods were not removed from the analysis, as by doing so the spatial average soil moisture would appear lower. In the case of temporal stability, when a station shows a behaviour which is different from that

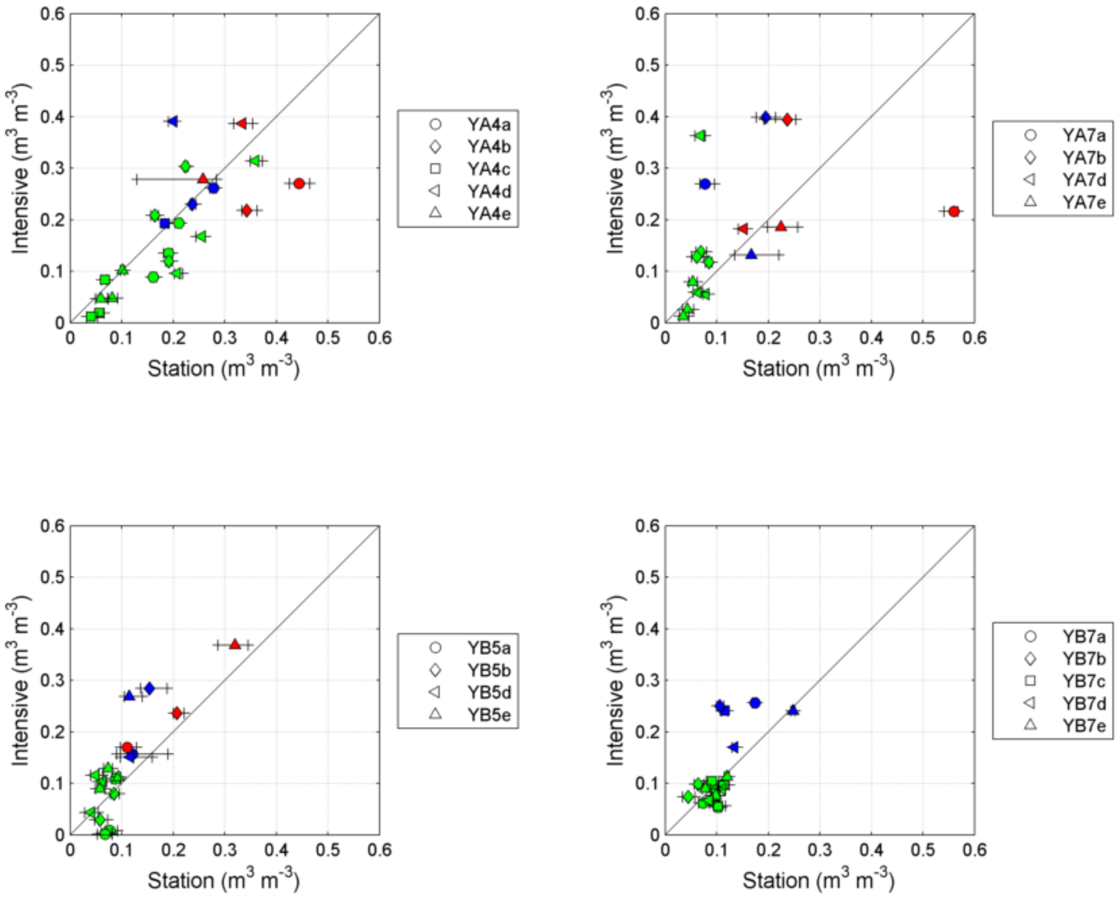

FIGURE 3.5: Stations vs closest intensive sampling soil moisture for each focus area. Horizontal whiskers: daily variation of the station. The intensive sampling points used to compare with the daily average from the stations are nodes closest to the station. Blue: SMAPEx-1, Red: SMAPEx-2, Green: SMAPEx-3.

of other stations, it would be penalized and therefore, deemed to be unrepresentative (as seen from the previous section). However, in terms of spatial average, it is actually representing the irrigated or flooded areas of the pixel.

For 1 km pixels, the spatial variation within each pixel was larger than the daily variation measured at the stations, at times up to 0.20 m^3 m^{-3} (Fig. 3.6). Generally, the spatial variation within a pixel was the highest for YA4 followed by YA7, YB5 and the lowest for YB7, as expected due to the presence of agricultural and cropping activities in the YA areas. During SMAPEx-1 and SMAPEx-2, soil moisture from intensive sampling were generally found to be wetter than the stations (YA4: 0.06 m^3 m^{-3}; YA7: 0.07 m^3 m^{-3}; YB5: 0.05 m^3 m^{-3}; YB7: 0.06 m^3 m^{-3}). Compared to Fig. 3.5, by taking an average of station measurements within the 1 km pixel, the majority of points from intensive measurements at YA7 moved closer to the 1:1 line, as the uncertainty in

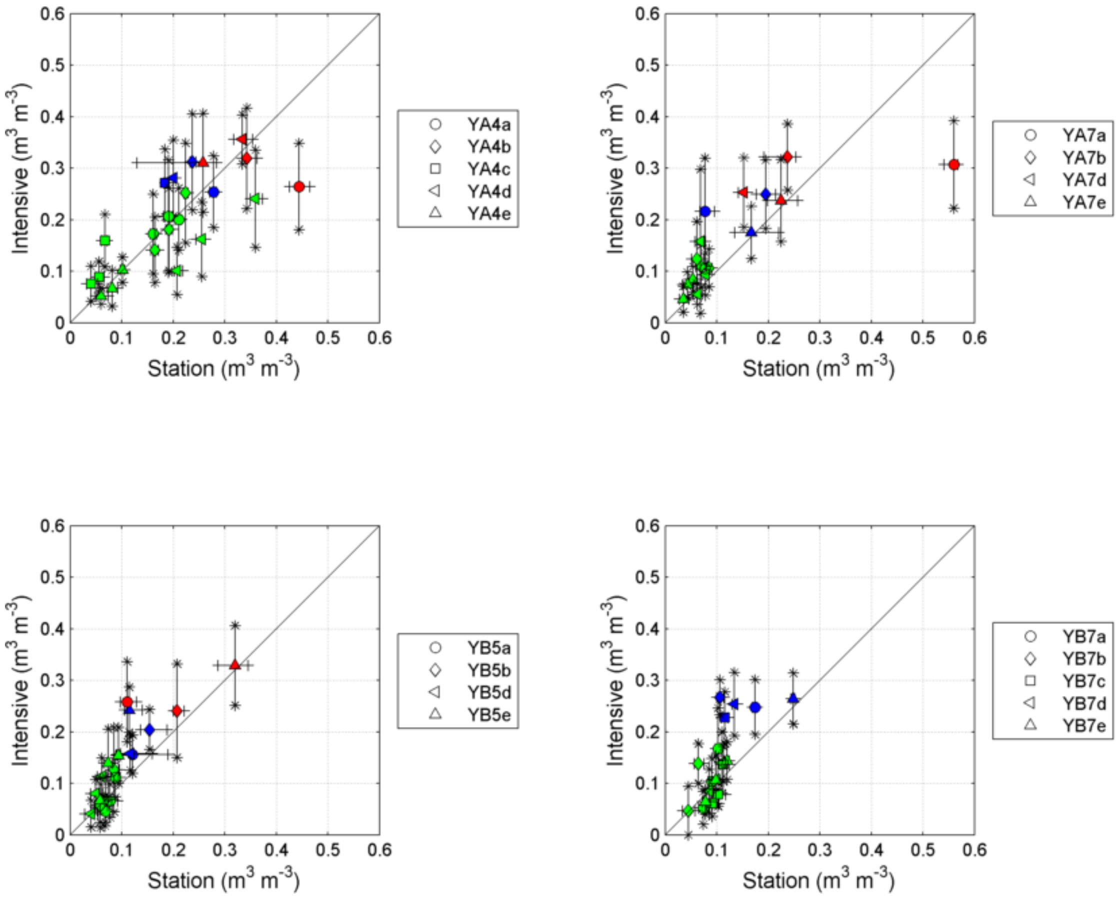

FIGURE 3.6: Station vs intensive sampling soil moisture within 1 km for each focus area. Horizontal whiskers: daily variation of the station. Vertical whiskers: standard deviation of the intensive samples within the pixel. Blue: SMAPEx-1, Red: SMAPEx-2, Green: SMAPEx-3

each measurement decreased with more measurements. For the YB5 and YB7 pixels, little change is observed between Fig. 3.5 and 3.6. This is likely due to the relative homogeneity of both soil properties and land use within the YB area.

In the case of 3 km pixels, whilst some individual stations seem to perform better (whereas others performed worse, stations that performed well generally did so for all campaigns (e.g. YA7b). Nevertheless, YA4b, YA7b and YB5e were identified as the representative stations of their respective 3 km pixels based on point to pixel comparisons, with dry biases of 0.04 m^3 m^{-3}, whereas YB7e was representative of the YB7 3 km pixel, with an overall bias of 0.01 m^3 m^{-3}. On average, all stations were drier than the average intensive measurements with biases ranging up to a maximum of 0.09 m^3 m^{-3} for YA4, 0.12 m^3 m^{-3} for YA7, 0.06 m^3 m^{-3} for YB5 and 0.08 m^3 m^{-3} for YB7. As all stations within these homogeneous pixels were relatively close to the spatial mean,

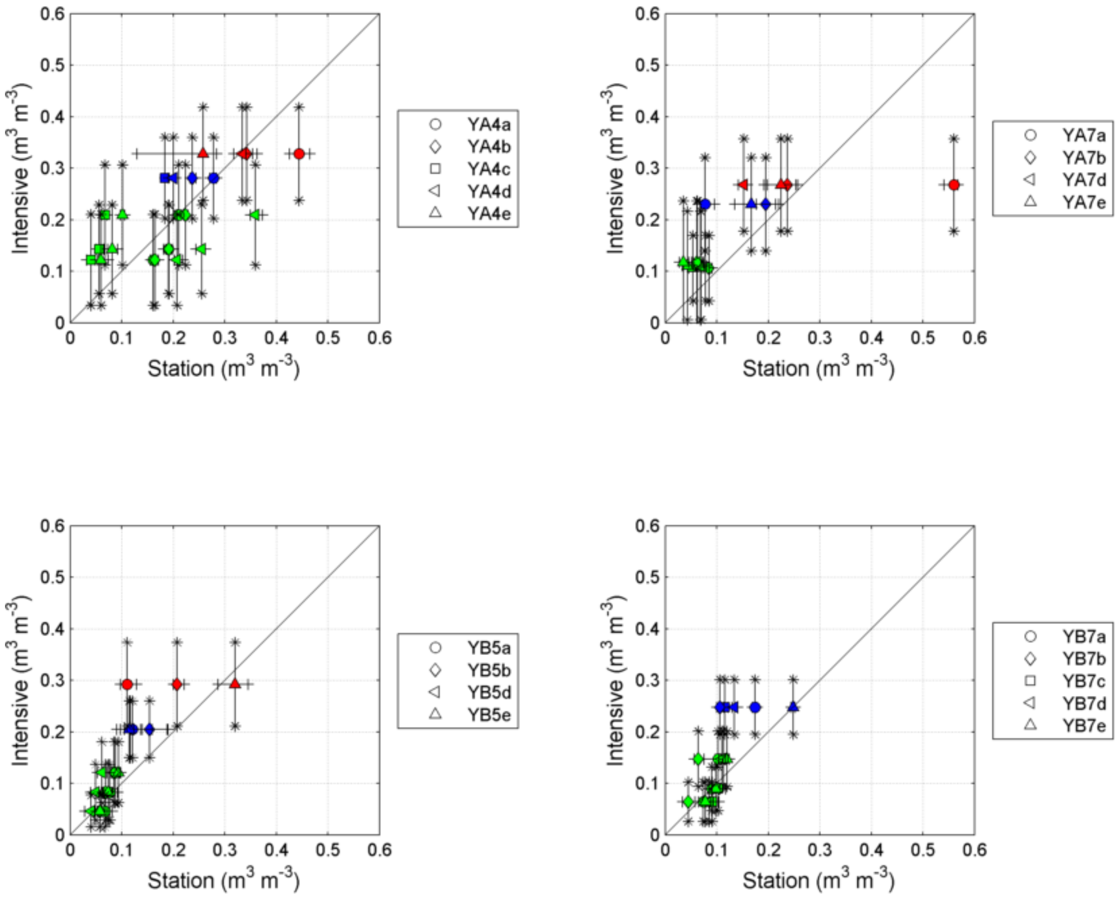

FIGURE 3.7: Individual station vs intensive sampling soil moisture within 3 km for each focus area. Horizontal whiskers: daily variation of the station. Vertical whiskers: standard deviation of the intensive samples within the pixel. Blue: SMAPEx-1, Red: SMAPEx-2, Green: SMAPEx-3

a single station was found to be adequate for estimating areal average soil moisture of homogeneous areas; a result also found by Chen et al. (2014).

Intensive sampling is compared with the average of all stations within their respective 3 km pixels in Fig. 3.8. Daily variation of soil moisture from the stations show a large range, particularly during SMAPEx-2 due to high variability between stations, caused by the high spatial rather than temporal variability of soil moisture. Generally, the average of all stations compared well with the areal average from intensive sampling (e.g. YA4 3 km pixel). The average biases were 0.07 $m^3\ m^{-3}$ within YA4 and YA7 3 km pixels, 0.05 $m^3\ m^{-3}$ within YB5, and 0.03 $m^3\ m^{-3}$ for stations within the YB7 3 km pixel. However, it can be seen by that using a representative station (e.g. YA4a, YA7b, YB5e and YB7e based on Fig. 3.7) instead of the average of all the stations (Fig. 3.8), better agreement can be found between the representative stations and the average of

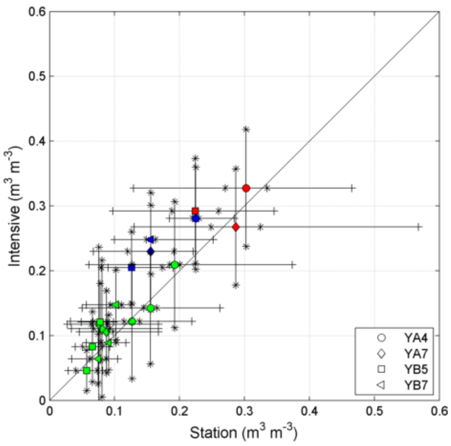

FIGURE 3.8: Average of all stations vs intensive sampling soil moisture within 3 km. Horizontal whiskers: daily variation based on all stations within the focus area. Vertical whiskers: standard deviation of the intensive samples within the 3 km pixel. Blue: SMAPEx-1, Red: SMAPEx-2, Green: SMAPEx-3.

all intensive samples.

The bias between YA7b and the average of the intensive samples was 0.04 m^3 m^{-3} whereas the bias between the average of all stations compared to intensive sampling was 0.12 m^3 m^{-3}. Recall that YA7a was previously found to highly overestimate soil moisture (Fig. 3.6). However, by including it when averaging all stations for YA7, comparisons with intensive measurements moved closer to the 1:1 line. If YA7a was eliminated, the bias between intensive samples and station averages would be greater. This reiterates the importance of understanding the spatial representativeness of each station for satellite validation.

Another observation is that representative stations identified based on the average of the intensive measurements were different from those identified in the previous section based on temporal stability analysis (Table 3.2). In fact, YB7e, which had almost no bias compared to intensive measurements was found to be the least representative based on the temporal stability analysis (Fig. 3.2). Likewise, YB5e and YA7b were not representative based on the temporal stability analysis regardless of the indicator used to determine representativeness. However, as shown from doing the temporal stability analysis with and without eliminating stations from one scale to another, replacing these stations into the temporal stability analysis is unlikely to have a large effect at 9 km and 36 km scales. In addition, intensive measurements (Fig. 3.7) showed that stations within the YB7 3 km pixel were generally drier than intensive measurements with the exception of YB7e. This was also observed in Fig. 3.5, 3.6 and 3.8 whereby station measurements were mostly lower than the intensive measurements.

Heathman et al. (2012) also found that permanent sensors tend to be biased, and that they varied more than areal average soil moisture conditions. Whilst it is difficult to identify the cause, site installation and/or maintenance activities might increase disturbance around the immediate surroundings of the station. Cattle are also drawn towards these stations, thereby further increasing disturbance to the surroundings. This makes it difficult for vegetation to establish itself around the station and leads to bare ground surfaces, which leads to an increase in soil evaporation. If this was the case, it may explain the reason why YA7b, YB5e and YB7e were found to be the least representative stations based on the temporal stability analysis when the opposite may be true.

Finally, for the 36 km pixel, the station measurements were compared with the average of data retrieved from airborne observation. Based on this comparison, it was found that YB7e was the most representative followed by YA5, with overall biases of 0.009 m^3 m^{-3} and 0.010 m^3 m^{-3} respectively. However, since there were only 9 days of airborne soil moisture observations during the Austral spring, any conclusions on the representative stations need to be tempered by this fact. While YB7e agrees well with the areal average during the campaign, it does not appear to be representative for periods outside the campaign (Fig. 3.4; bottom panel). Nevertheless, despite being only based on 9 days of airborne soil moisture product, this analysis identifies YA5 as a station that agrees best with the aircraft soil moisture with and overall bias of 0.010 m^3 m^{-3}, followed by Y7 and Y5 (overall biases of 0.014 m^3 m^{-3} and 0.015 m^3 m^{-3} respectively) which were also identified based on a temporal stability analysis. Similarly, based on 11 days of airborne soil moisture derived from the National Airborne Field Experiment (NAFE), Azcurra and Walker (2009) identified Y5, Y7, Y10 and Y12 to be representative of Yanco's areal average soil moisture within an accuracy of 0.04 m^3 m^{-3}.

3.5.3 Geostatistical analysis

3.5.3.1 Variograms

Standard variograms were derived for each 3 km pixel based on intensive samples. The range and sill derived from fitting the Whittle model to the experimental standard variograms are plotted as the black line in Fig. 3.9. Fitting variograms to observations within YA4 and YA7 was less accurate due to the presence of mixed land use. Nuggets derived from the model fitting were mostly 0 or close to, which indicates that measurement errors and variation within distances smaller than the sampling interval (250 m) were small. Referring to comparisons between stations and closest intensive samples, the underestimation by stations compared to intensive samples were larger than these nuggets, and the observed constant offset may therefore be related to disturbance around the immediate surroundings of the station as discussed previously, rather than measurement errors or small scale variability.

A positive relationship between range and sill with mean soil moisture can be observed for pixels within the YB area as in De Lannoy et al. (2006). Conversely, although the sill for both YB5 and YB7 were well defined, this was not the case for YA4 and YA7. In fact, YA4 showed multi-scale nested variograms which changed across campaigns (not shown here). However, of these nested variograms, one with the shortest range (< 0.5 km) was consistently the same for all seasons and was similar to that of the other 3 km pixels. This consistent correlation length is likely caused by land surface features which remain constant, or which vary slowly, such as vegetation and soil texture (Ryu and Famiglietti, 2006). Longer correlation lengths or ranges are likely to coincide with the sizes of fields. Compared to YA4, the presence of multi-scale variograms was less pronounced as variability within YA7 was lower. For instance, during SMAPEx-3, wheat and bare soil planted with corn could be found in YA7, whereas wheat, barley, linseed, bare soil and pasture could be found within the YA4 pixel. Based on these variograms, agricultural activities within the YA4 pixels clearly had a large influence on the spatial variability of soil moisture within the 3 km pixels.

As with the intensive samples, standard variograms were also derived for the 36 km pixel based on airborne soil moisture. Time-series of the range, nugget and sill derived for the standard variograms, (black line in Fig. 3.10, left panels) correlated well with the wetting and drying cycles during the campaign. From the 5th to the 7th of September 2011, 5 mm of rain was recorded at the site, and from the 10th to the 12th another 3 mm of rain fell. After rainfall events, the derived variogram parameters changed and would decrease during the dry-down period. While the change in nugget and sill were correlated to each other, this relationship was less clear in the case of range. The change of correlation length has been observed in many previous studies, but the dependency of correlation length with soil moisture status is still inconclusive (Vereecken et al., 2014). The experimental standard variograms for each day of flight are also plotted in Fig. 3.10 (right panels). Note that the variogram is the same for all three right panels in Fig. 3.10 as it is derived from the same 36 km pixel. Based on the standard variograms for each day, the geostatistical structure of the 36 km pixel is seen to evolve with soil moisture conditions as also observed by Western et al. (1998) for the Tarrawarra catchment. Compared to 3 km pixels, at 36 km, the effect of anthropogenic activities (∼1 km) on soil moisture variation diminishes as the influence of soil and vegetation properties and precipitation takes over (∼10 - 30 km) (Ryu and Famiglietti, 2006).

3.5.3.2 Centered-variogram

In the case of the centered-variograms, due to the high variability of soil moisture within close distances (250 m spacing), the goodness of fit between the experimental centered-variograms and its fitted models were low for intensive measurements (R^2 ranged from 0.08 to 0.49). Fig. 3.9 shows how the parameters for the centered-variograms evolved during separate campaigns (different colours for each 3 km pixel) in comparison to that of the standard variogram (black). Differences between stations were smaller for YB7 compared to the other 3 km pixels. Some stations displayed the same dynamics as that of the standard variograms whereas others showed the opposite. Due to the poor fit of the models and edge-effects due to location of stations close to edges of the sampling grid, not much could be deduced from these parameters. Nevertheless, based on the correlation of parameters derived from the standard and centered-variograms, YA4e, YA7e, YB5d and YB7a would have been identified as representative stations of their respective 3 km pixels. The results were not consistent with any of the other identification methods. As the derived range based on standard variograms was 0.5 km and approximately 3 km based on centered-variograms, it is recommended for future studies seeking to apply the

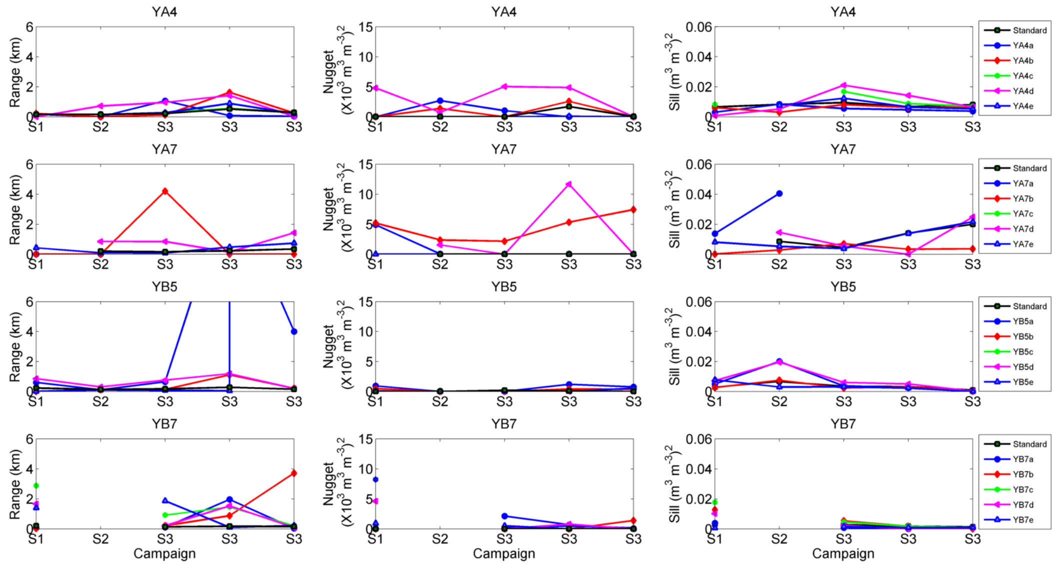

FIGURE 3.9: Timeseries of parameters derived from fitting the Whittle model to the standard and centered-variogram of all stations based on intensive measurements for each 3 km pixel. S1: SMAPEx-1; S2: SMAPEx-2; S3: SMAPEx-3.

centered-variogram to extend intensive sampling at least 3 km away from the station with sampling intervals of less than 500 m to prevent edge-effects.

In the case of airborne soil moisture, the standard variogram models were on average able to explain more than 70% of the variability of the experimental centered-variogram derived from the airborne soil moisture product, a huge improvement compared to R^2 of intensive measurements due to the increase in sampling scale. Parameters derived from fitting the experimental centered-variograms are compared to the standard variogram in Fig. 3.10. Changes in the derived parameters correspond to rainfall events. By comparing the correlation between the derived parameters from standard and centered-variograms based on airborne soil moisture, multiple stations were found to exhibit similar spatial structures at 36 km. Correlation between models derived from standard and centered-variogram of stations ranged from 0.19 to 1.00 with an average of 0.70 whereas RMSE was between 0.002 $(m^3/m^3)^2$ and 0.054 $(m^3/m^3)^2$ with an average of 0.008 $(m^3/m^3)^2$. This shows that the majority of the stations within the network were able to capture the rainfall events during SMAPEx-3. YB3, Y2 and Y12 were found to perform the best and the experimental centered-variograms from these stations are shown in Fig. 3.10 (right panels).

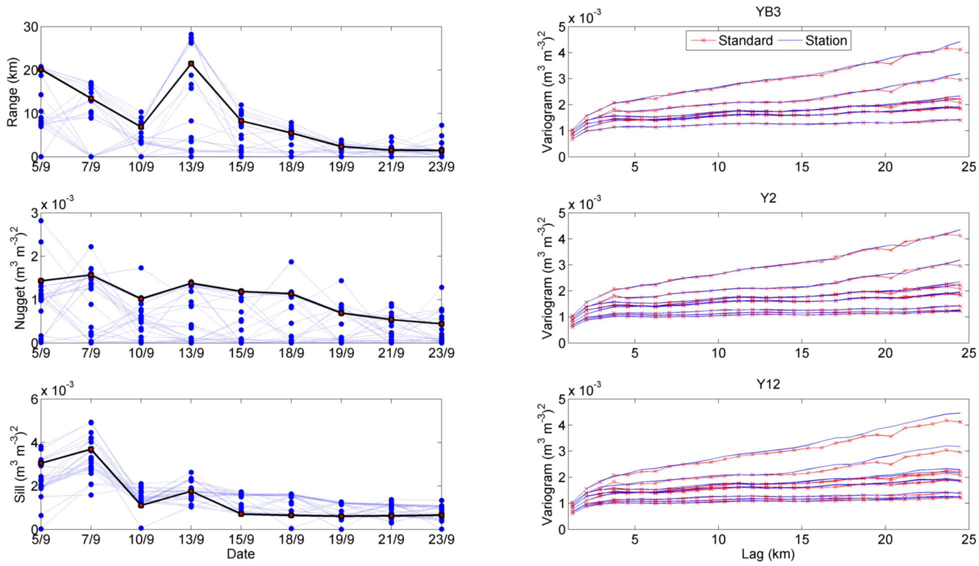

FIGURE 3.10: Left panels: Timeseries of parameters derived from fitting the Whittle model to the standard (black) and centered-variogram (blue) of all stations based on airborne derived soil moisture. Right panels: Comparison of experimental variograms derived from standard variograms and centered-variogram of representative stations (YB3, Y2 and Y12) for different days.

3.5.4 Recommendations

Table 3.2 summarizes the representative stations identified based on different indicators from the temporal stability analysis, point to pixel comparisons using intensive ground measurements or airborne soil moisture products, and the centered-variogram analysis. Representative stations identified using different methods, or by using the average of all stations, were generally able to capture the rainfall events from January 2013 to December 2014 (Fig. 3.4, bottom panel). Moreover, based on the results and observations in this study, land use, and soil and vegetation properties play an important role at local (3 km and 9 km) scales whereas rainfall patterns are expected to be more crucial at regional (36 km) scales. While the study site contained a mix of land use/cover, it is to be noted that the effects of topography on soil moisture variability were not considered as the region has little relief, typical of most Australian landscapes. As this study serves as a concept study, further application of this methodology to other field sites is required to further fine-tune the approach. Considering this, the following recommendations are made.

1. Where intensive measurements are available, stations which are most representative of the areal mean should be used (Cosh, 2004). Stations YB5e and YB7e, with

an estimated error of 0.03 m^3/m^3 and 0.01 m^3/m^3, respectively, are recommended for validating 3 km SMAP products within the YB area.

2. In the presence of agricultural activities, stations which are most representative of the areal average rather than the most ranked stable station should be used. Stations YA4b and YA7b, with estimated errors of 0.04 m^3/m^3, should be used for validating SMAP 3 km products within the YA area.

3. As decisions made by farmers are difficult to predict and have effects on the rank-stability of the stations, temporal stability analysis is not recommended in the presence of cropping activities. Instead, a good distribution of stations to account for variability within the pixel is important. A weighting method based on sizes of agricultural fields can then be applied.

4. Where intensive measurements are not available and the difference in MRD between stations are small, temporal stability analysis is adequate providing that stations are well distributed within the area of interest and the appropriate performance indicator selected, i.e. RMSE_s.

5. As the stations are well distributed in the Yanco study area, YA5 and YB7a, identified based on temporal stability methods, are likely to provide a good measure of the areal average of 9 km SMAP products.

6. Spatial average soil moisture based on airborne measurements, can be used for identifying representative stations at the 36 km scale, such as YA5. Other datasets such as the 1 km soil moisture product based on the ENVISAT ASAR Global Mode (Doubkova et al., 2009) and Sentinel-1 (Wagner et al., 2009) can possibly be used in the same way as the airborne data if of sufficient quality.

7. The results based on the centered-variogram analysis are biased due to edge-effects and are therefore non-conclusive. Consequently, it is recommended that this analysis to be repeated with observations extending at least 5 km from all stations for low resolution products and 500 m for higher resolution products (e.g. 3 km and 9 km) before the utility of centered-variograms can be verified.

8. Should resources become limited, priority should be given to maintain representative stations shown in Table 3.2.

3.6 Key findings

Validation of satellite soil moisture products is faced with difficulties due to differences in scales between point measurements and satellite products. The ability to represent a mean temporal pattern and the areal average soil moisture is important in the validation of satellite soil moisture products. Therefore, the study described in this chapter sought to investigate the representativeness of soil moisture stations within the study area based on both temporal and spatial statistical methods.

Comparisons carried out with long-term soil moisture records and a limited set of intensive measurements revealed that stations identified as representative based on temporal stability analysis are not necessarily representative of the areal average soil moisture. Moreover, rank or time stable locations have a tendency to favour dry-biased stations. In addition, site installation and management activities may lead to biases in the station measurements. Therefore, where intensive measurements are available, they should be used to identify the most representative station. Yet, as intensive measurements are not always available, temporal stability was shown to be useful provided that the stations used to identify the most representative locations are well-distributed across the area of interest.

As stations within the Yanco study area were well distributed within different land use types, OzNet was shown to be useful in providing areal average soil moisture measurements for long-term validation and calibration of satellite soil moisture products and hydrological models. Based on available resources, representative stations or methods to estimate the areal average soil moisture for each SMAP pixel were also recommended in Table 3.2. Finally, airborne soil moisture products have been shown to be useful as *a priori* information for identifying representative locations based on point-to-pixel comparisons whereas further investigation is needed for the centered-variogram analysis.

3.7 Chapter summary

Combining long-term soil moisture records and limited intensive measurements from three field campaigns, this study identified YA5 and YB7a as the most representative stations of the YA and YB 9 km grids respectively, and YA5 of the entire 36 km Yanco region. Where available, intensive measurements were recommended for use in identifying the most representative stations. However, as this is not always available, temporal stability analysis can be applied provided that the stations are well-distributed within the area, and $RMSE_s$ is used as the performance indicator. Therefore, the representative stations identified here will be used to validate remote sensing soil moisture products within the Yanco study area in the next chapter.

Chapter 4

On the impact of using representative stations for passive microwave soil moisture validation

This chapter utilizes the most representative stations identified from Chapter 3 to validate two versions of Advanced Microwave Scanning Radiometer (AMSR-2) Level 3 (L3) soil moisture products based on the Japanese Aerospace exploration Agency (JAXA) and Land Parameter Retrieval Model (LPRM) algorithm, and compares them with the Soil Moisture and Ocean Salinity (SMOS) L3 product. The results are also contrasted against the use of 'random' stations to validate these products. Moreover, performance of these products across different seasons and overpass periods were compared. Following this, the effect of bias correcting soil moisture retrievals based on cumulative distribution function (CDF) matching was investigated. The work in this chapter will be submitted to a journal for publication.

4.1 Introduction

Recent advances in remote sensing technologies have increased the availability of soil moisture observations. The large contrast between the dielectric constant of soil and water at microwave bands enables active and/or passive remote sensing observations to provide information on soil moisture content (Owe et al., 2008). Current space-borne soil moisture sensors operating at X- (e.g. 10.7 GHz) and/or C-band (e.g. 6.9 GHz) include the Advanced Microwave Scanning Radiometer (AMSR-2) on-board Global Change Observation Mission - Water (GCOM-W1) and Advanced Scatterometer (ASCAT) on-board the Meteorological Operational (MetOp) series of satellites (Wagner et al., 2013). Operating at L-band (e.g. 1.4 GHz) are Soil Moisture and Ocean Salinity (SMOS) (Kerr et al., 2012) and Soil Moisture Active Passive (SMAP) (Entekhabi et al., 2010a).

The depth of soil sensed by these space-borne sensors is dependant on the wavelength of the emitted or reflected microwaves. Consequently, L-band observations corresponds to a deeper soil ($\approx$ 3 - 5 cm) compared to shorter wavelengths such and X- and C-band ($\approx$ 1 - 2 cm), and are less affected by the overlying layer of vegetation (Naeimi et al., 2009). This makes L-band the theoretically more optimal frequency for soil moisture estimation (Escorihuela et al., 2010; Kerr et al., 2012). In addition to frequency choice, microwave sensors can also operate as an active or passive system. Nevertheless, this study concentrates on the latter.

Microwave emissions from the land surface, commonly referred to as brightness temperature, is proportional to the product of effective temperature from the emitting layer and surface emissivity (Schmugge et al., 2002). Measurements of brightness temperature from space borne sensors are converted into soil moisture products through radiative transfer models (e.g. Jackson, 1993b; Njoku and Li, 1999; Owe et al., 2001; Wen and Su, 2003). Consequently, the accuracy of these products are not only subject to errors from the sensors themselves, including the frequency of observation, but also the parameters and assumptions applied in the transfer models. Moreover, satellite missions such as AMSR-2 and SMOS have defined a specific set of performance requirements to achieve. In the case of AMSR-2 soil moisture products, the 'desired standard accuracy' of Level 2 50 km soil moisture products is ± 0.10 m^3 m^{-3} and the 'desired goal accuracy' is ± 0.05 m^3 m^{-3}. Accuracy is defined as the mean absolute error (MAE) of the instantaneous observations. However, the research product (Level 3; 25 km), has a 'goal accuracy' of ± 0.08 m^3 m^{-3} (JAXA, nd; Maeda et al., 2011). For SMOS, the goal is a maximum root mean square error, RMSE < 0.04 m^{3}m^{-3} in the top 5 cm without accounting for long-term bias correction (Kerr et al., 2010). However, the validation of these soil moisture products are complicated by errors in both data sets and differences between the horizontal (spatial) and vertical (depth) scales sensed by remotely sensed and ground-based soil moisture measurements (e.g. Crow et al., 2012). Validation of remote sensing soil moisture products has often been based on arbitrarily selected stations or the average of stations which fall within the satellite pixel (e.g Albergel et al., 2012; Brocca et al., 2012a; Cho et al., 2015; Choi, 2012; Dente et al., 2012b; Draper et al., 2009; Jackson et al., 2012; Kim et al., 2015; Su et al., 2013; Wu et al., 2015), and by assuming these measurements are representative of the satellite's sensor resolution.

In some studies, *in situ* measurements have been up-scaled based on geostatistical methods such as block-kriging or triangulation interpolation methods, or land surface model simulations (e.g. Brocca et al., 2011; Dall'Amico et al., 2012; Rötzer et al., 2014). The downside of depending on a number of stations is that measurements are not always available from all sites. To overcome this, Su et al. (2013) and van der Schalie et al. (2015) employed a lookup method whereby the stations were ranked according to their representativeness of the mean area average. This unfortunately can lead to an inconsistency in the quality of measurements used for validation. Finally, the uncertainties in land surface model simulations may emanate from inaccuracies in the input forcings used to drive the models, parameters prescribed within the model physics, and the structure of the model to relate inputs and outputs between different sub-models (Crow et al., 2005; Seneviratne, 2010; Wang et al., 2011; Zhang et al., 2013).

In this study, to address the issue of non-representativeness, and demonstrate the impact of poorly selected stations, validation of remote sensing soil moisture products here are based on the careful selection of stations in Chapter 3. This also allow resources to be concentrated on representative stations when resources become limited. Here, the most representative stations have been used to validate soil moisture products from AMSR-2 and SMOS. Furthermore, the AMSR-2 products validated were derived from two different algorithms including different versions of the algorithm. These include the algorithm developed by the Japan Aerospace exploration Agency (JAXA) and the Land Parameter Retrieval Model (LPRM). Whilst, previous studies have validated the AMSR-2 soil moisture products from these two algorithms (e.g. Kim et al., 2015; Wu et al., 2015), a calibration misalignment between AMSR-E and AMSR-2 led to reprocessed products from the JAXA (JAXA, 2015) and LPRM algorithms (Parinussa et al., 2015). This necessitates a comparison between the different versions from each algorithm. Moreover, products have been derived based on the LPRM algorithm for observations at the C-band (6.9 GHz and 7.3 GHz, hereon denoted as C1 and C2 respectively) and to the X-band (10.7 GHz, hereon denoted as X). The occurrence of radio frequency interference (RFI) at C-band has often prevented the use of C-band observations in North America, Middle East and Japan (Njoku et al., 2005). Similarly, RFI at X-band has been detected in Italy and Great Britain (e.g. Lacava et al., 2012), and at L-band in Europe, China and Canada. However, as Australia has been found to be largely unaffected by RFI (e.g. Draper et al., 2009), an opportunity to compare products from these different frequencies presents itself. The inclusion of products from SMOS extends the comparison of wavelengths to the L-band (1.4 GHz) and highlights the impact of using poorly chosen stations. Consequently, this comprehensive comparison of different soil moisture products affords 1) an understanding of how well each product meets their respective performance requirements under very controlled analysis, and 2) identification of the best performing product under the conditions of this site.

4.2 Data and methods

4.2.1 Study area and in-situ soil moisture data

This validation study was carried out for the Yanco site which is within the Murrumbidgee River catchment in New South Wales, Australia (Fig. 4.1). The site, including the soil moisture station measurements available from OzNet has been described in Chapter 3. The western side of the study area includes the Coleambally Irrigation Area (CIA), which consists of farms with a mix of flood irrigation and dryland cropping. Main crops grown during summer include rice, corn, and soybeans whereas wheat, oat, barley and canola are grown during winter. Flood irrigating of rice crops occur in November (Panciera et al., 2014). Conversely, land use to the eastern side consists of pastures for grazing. As in Chapter 3, YA is used to describe the cropping area, and YB for the grazing area.

To compare as closely as possible with the depth sensed by the microwave sensors, only measurements from hydraprobes vertically installed from the surface (0-5 cm) were used here (Adams et al., 2015). Average soil moisture based on station measurements was obtained by taking the average of available measurements from stations which fall within

Table 4.1: Overview of passive microwave soil moisture satellites used in this study.

Spacecraft	**SMOS**		**GCOM-W1**	
Sensor	Microwave Imaging Radiometer using Aperture Synthesis (MIRAS)		The Advanced Microwave Scanning Radiometer 2 (AMSR-2)	
Swath width	1000 km		1445 km	
Sensor accuracies	1.8 K (at 180 K) 2.2 K (at 220 K)		0.66 K (at 100 K) 0.68 K (at 250 K)	
Frequency	1.41 GHz (L-band)		6.9, 7.3 and 10.7 GHz (C-band)	
Footprint dimensions (km^2)	43 km on average over the circle field of view		24 - 35 km $\times$ 42 - 62 km ellipse	
Sampling interval (km)	$\approx$ 15		$\approx$ 10	
Product posting (km)	$\approx$ 25		$\approx$ 10/$\approx$ 25	
Temporal Resolution	2 - 3 days		1 - 2 days	
Launch Date	2nd Nov. 2009		18th May 2012	
Target accuracy	RMSE < 0.04 m^3 m^{-3}		MAE < 0.08 m^3 m^{-3}	
Node	Ascending	Descending	Descending	Ascending
Equator crossing	6:00 AM	6:00 PM	1:30 AM	1:30 PM
M/E	Morning	Evening	Morning	Evening

the satellite pixel at each time-step. Unlike Chapter 3, no pre-processing was carried out to eliminate time-steps where less than 75% of the monitoring station's data were available, or measurements which fell outside a station's 90% confidence interval.

4.2.2 Satellite soil moisture data

4.2.2.1 AMSR-2

AMSR-2 on-board the GCOM-W1 satellite was launched in May 2012 as a follow-on of the Advanced Microwave Scanning Radiometer (AMSR, December 2002 to 2003) and AMSR for the EOS (AMSR-E, May 2002 to Oct 2011). Compared to AMSR/AMSR-E, AMSR-2 has a larger antenna (2.0 m diameter) than AMSR-E (1.6 m diameter), an additional C-band (7.3 GHz) channel to mitigate RFI (e.g. de Nijs et al., 2015), and an improvement in calibration accuracy through a change in thermal design (Imaoka et al., 2010; Maeda et al., 2011). Observations from AMSR-2 are available twice (ascending/evening and descending/morning) every one to two days (Table 4.1).

The two AMSR-2 products compared here are based on the JAXA (Fujii et al., 2009; Maeda and Taniguchi, 2013) and LPRM (Owe et al., 2001; Parinussa et al., 2015) algorithms. Due to an improvement in calibration of AMSR-2, both JAXA and LPRM products have been reprocessed. The JAXA AMSR-2 Level 3 soil moisture content products, version 1.11 (herein referred to as JX1) and version 2.21 (herein referred to

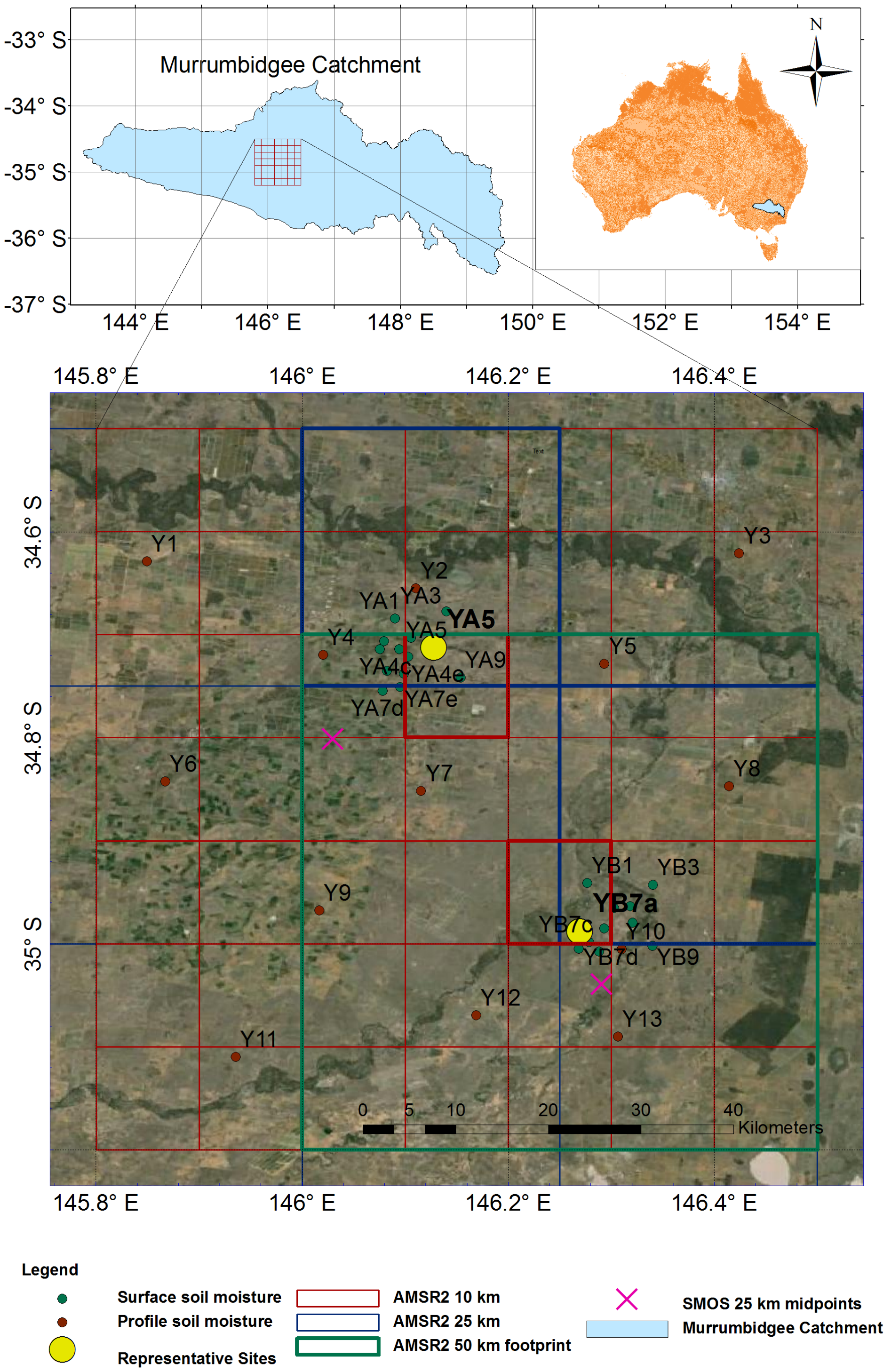

FIGURE 4.1: Map of study area showing locations of most representative stations and satellite pixels selected for validation. Top left inset: Relative location of the study area within the Murrumbidgee catchment. Top right inset: Relative location of Murrumbidgee catchment within the Australian continent.

as JX2), were obtained from the GCOM-W1 Data Providing Service (https://gcom-w1.jaxa.jp/). As JX1 was only available up till the end of 2014; and to obtain an equal number of seasons, soil moisture products from July 2012 to July 2014 were considered here. This study differs from the validation study carried out by Wu et al. (2015) over the United States in that they did not differentiate the two product versions, and Zeng et al. (2015) which only used JX1. As for the LPRM products, the former version (herein referred to as LP1) were obtained from Goddard Earth Sciences Data and Information Services Center (GES DISC) (http://disc.sci.gsfc.nasa.gov/hydrology/) whereas the updated version (herein referred to as LP2) were reprocessed following (Parinussa et al., 2015) and (Kim et al., 2015).

The AMSR-2 products are available at 10 km and 25 km grid resolutions although the area observed by the sensor, i.e. its footprint is approximately 50 km $\times$ 50 km. These coarse scale observations are usually posted onto a 25 km grid whereas the 10 km product is based on an smoothing filter-based intensity modulation downscaling technique (Parinussa et al., 2014). Hence, whilst this study focuses on the 25 km grid product, the 10 km and an assumed 50 km footprint product were included in the analysis for both ascending (1:30 pm) and descending (1:30 am) overpasses. A more comprehensive description of the JAXA and LPRM algorithms and inter-comparison at a global scale can be found in Kim et al. (2015).

4.2.2.2 SMOS

Launched in 2009, the radiometer on-board SMOS measures L-band at 1.4 GHz every 3-days. Whilst the resolution of SMOS is approximately 43 km (Kerr et al., 2001), the soil moisture L3 products are binned to a 25 km grid (Table 4.1). These products are derived based on the L-band microwave emission of the biosphere (L-MEB) model which involves an iterative algorithm to minimize a cost function computed from the differences between measured and modelled brightness temperature from all available incidence angles (Wigneron et al., 2007). The data used here was obtained from the Centre Aval de Traitement des Données SMOS (CATDS), operated for the Centre National d'Etudes Spatiales (CNES, France) by IFREMER (Brest, France) (Jacquette et al., 2010). The daily 25 km SMOS Level 3 products, both ascending/morning (6:00 am) and descending/evening (6:00 pm), CATDS version 2.72 which is aligned with version

6.11 Level 2 products were used. Although night-time retrievals have generally been shown to be more accurate than day-time retrievals (e.g Al-Yaari et al., 2014; Njoku et al., 2003), recent studies have suggested that day-time retrievals are just as good (e.g. Rowlandson et al., 2012). Following Al-Yaari et al. (2014), instances when the soil moisture data quality index (DQX) was larger than 0.06 were removed. As the reanalysis soil moisture products (EASE grid) were only available for 2012 to 2013, the operational product was used for 2014 (EASE2 grid). For consistency, it is assumed here that the operational products are also on the EASE grid.

To differentiate the products, where applicable, AMSR-2 and SMOS products, have subscripts denoting the observed frequency used (X, C1 or C2), the overpass (M: morning/AM, E: evening/PM), and product resolution (10 or 25), whereas superscripts denote the area being validated (YA or YB). For instance, $\mathrm{JX1}^{\mathrm{YA}}_{\mathrm{X(M)},25}$ is the 25 km soil moisture product based on the JAXA algorithm (version 1), derived from observations at X-band during morning/AM overpasses at the YA area. To enable comparisons of overpasses between AMSR-2 and SMOS, AMSR-2 ascending/day (1:30 PM) overpasses will be considered as evening/PM overpasses, whereas AMSR-2 descending/night (1:30 AM) overpasses will be considered as morning/AM (Table 4.1).

4.2.3 Analysis

Based on results in Chapter 3, incorrect conclusions and biases may be introduced into the results unless there is a good understanding of the sites. Therefore, coarse scale passive microwave remote sensing soil moisture products are validated here based on stations which have been identified as most representative within the YA and YB area using field data. Since stations within the Yanco area are well distributed, based on temporal stability methods, YA5 and YB7a were found to provide a good measure of the areal average of the YA and YB area ($\approx$ 9 km $\times$ 9 km), and YA5 for the Yanco region ($\approx$ 36 km $\times$ 36 km). Therefore, although results from the previous analysis focused on SMAP grids, it is assumed that they are transferable to the AMSR-2 25 km grids. Pixels with center points closest to these areas were selected for validation, and are summarized in Table 4.2. As the native footprint of the satellites overlaps the adjacent pixels, the stations which fall around the pixels were also used to compute an average for the entire pixel (also shown in Table 4.2).

TABLE 4.2: Pixel centre of soil moisture products, and corresponding stations selected for validation study.

	Resolution	**Pixel centre**		**Focus Area**		
Product	**(km)**	**Lat**	**Lon**	**YA/YB**	**Stations**	**Rep. station**
AMSR-2	25	-34.625	146.125	YA	Y2, Y4, Y7, YA1, YA3, YA4a,	YA5
AMSR-2	10	-34.75	146.15	YA	YA4b, YA4c, YA4d, YA4e, YA5,	
SMOS	25	-34.7	146.15	YA	YA7a, YA7b, YA7d, YA7e, YA9	
AMSR-2	25	-34.75	146.375	YB	Y10, Y12, Y13, YB1, YB3, YB5a,	YB7a
AMSR-2	10	-34.95	146.25	YB	YB5b, YB5e, YB7a, YB7b/YB5d,	
SMOS	25	-34.99	146.41	YB	YB7c, YB7d, YB7e, YB9	

Consistent with mission objectives, the statistical metrics which are used to evaluate the products include bias, root mean square difference (RMSD) (similar to RMSE), Pearson correlation coefficient (r), MAE and unbiased RMSD (ubRMSD). Bias was computed as the difference in averages of soil moisture based on the remote sensing products from averages based on ground measurements. MAE is the average of the absolute errors, and differs from RMSD in that the squaring of the errors in RMSD gives a greater weight to larger errors.

Taylor diagrams are used to combine measures of r, standardized centered RMSD (cRMSD) and standardized standard deviation with ground soil moisture measurements (Taylor, 2001). Taylor diagrams provides a comprehensive visualization of how well two datasets relate to each other in terms of r, RMSD and their standard deviations. They have also recently been applied for soil moisture validation by Champagne et al. (2015). The geometric relationship between these statistics allows the Taylor diagram to be plotted. For N discrete points of two variables, f_n and g_n, r is given as

$$r = \frac{1}{\sigma_f \sigma_g} \sum_{n=1}^{N} (f_n - \overline{f})(g_n - \overline{g}) \tag{4.1}$$

where $\overline{f}$ and $\overline{g}$ are their means, and σ_f and σ_g are the standard deviations, of f and g respectively. The cRMSD, which is the unbiased RMSD (ubRMSD), is then given by

$$\text{cRMSD} = \sqrt{\frac{1}{N} \sum_{n=1}^{N} [(f_n - \overline{f})(g_n - \overline{g})]^2}. \tag{4.2}$$

The maximum soil moisture established in the JAXA algorithm is 0.60 m^3 m^{-3} whereas the LPRM algorithm is 1.00 m^3 m^{-3} (Kim et al., 2015). Therefore, assuming f_g is the reference dataset, these statistics were then further standardized by σ_g such that standardized cRMSD, $\widehat{\text{RMSD}} = \text{cRMSD}/\sigma_g$, and standardized σ_f, $\hat{\sigma}_f = \sigma_f/\sigma_g$ (Albergel et al., 2012). Note that although this procedure was referred to as normalization in Taylor (2001), the term standardization is used here. Consequently, $\hat{\sigma}_g = 1$. Therefore, the radial distance of f_n from the origin, represents $\hat{\sigma}_f$, the radial distance from the reference represents $\widehat{\text{RMSD}}$, and finally, the azimuthal position represents r between f_g and f_n. A more comprehensive description regarding the derivation and use of the Taylor diagram can be found in Taylor (2001).

As the general consensus within the remote sensing community is that morning/AM observations are more ideal than during the day (referred to as evening/PM here), due to the difference in temperature between vegetation canopy and soil surface being at a minimum, the analysis here will firstly concentrate on morning/AM observations and 25 km products. Comparisons with evening/PM observations and 10 km and an assumed 50 km footprint product will be introduced in latter sections of this chapter.

4.3 Results and discussion

4.3.1 Representativeness

Table 4.3 summarizes the statistics from the comparison of individual stations with SMOS soil moisture products for each season within the YA and YB area respectively as Taylor diagrams. The red squares indicate the representative stations, green diamonds, the average based on all stations, and blue circles, all other individual stations. Generally, the closer a point is to the baseline (black point), the better its performance. Similar comparisons with soil moisture products can be found in Appendix A.

The scatter of blue dots within the Taylor diagrams for the YA area (Table 4.3), particularly during summer and winter, indicates that the statistics differ depending on the stations used for validation. Some individual stations were found to have an r of < 0.1 (stations with $r < 0$ are not shown) or a cRMSD > 1.5 m^3 m^{-3}. Further investigation (not shown here) revealed that during summer and autumn, YA4b and YA4d recorded high soil moisture values (> 0.40 m^3 m^{-3}); likely due to irrigation. Individually, when compared to SMOS 25 km soil moisture products (morning/AM overpasses), YA4b and YA4d had an overall r of 0.07 and -0.16, RMSD of 0.14 m^3 m^{-3} and 0.28 m^3 m^{-3}, and

Product	Summer	Autumn	Winter	Spring
$\mathrm{SMOS}^{\mathrm{YA}}_{\mathrm{L(M)},25}$	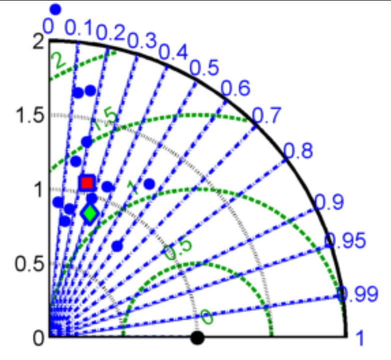	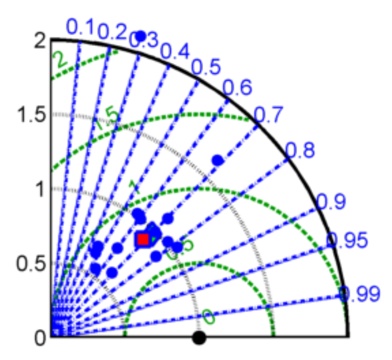	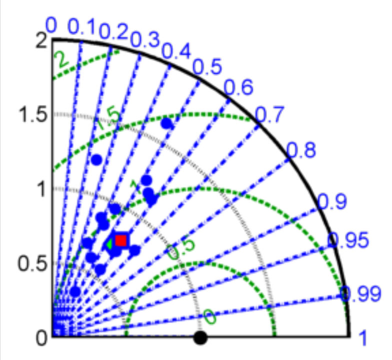	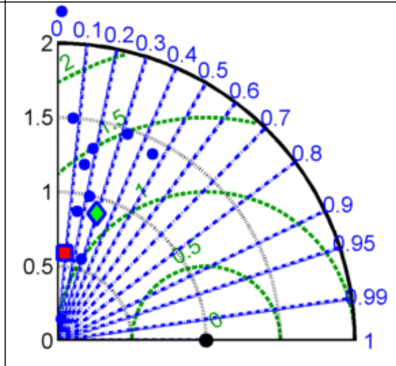
$\mathrm{SMOS}^{\mathrm{YB}}_{\mathrm{L(M)},25}$	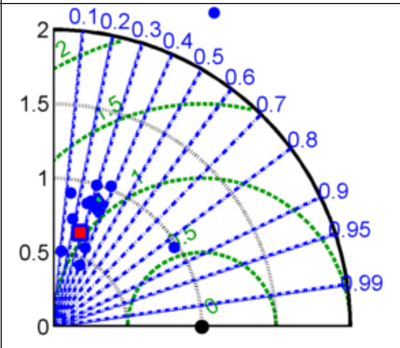	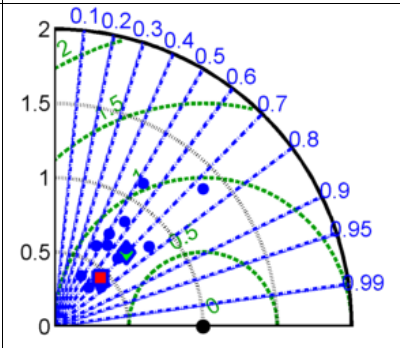	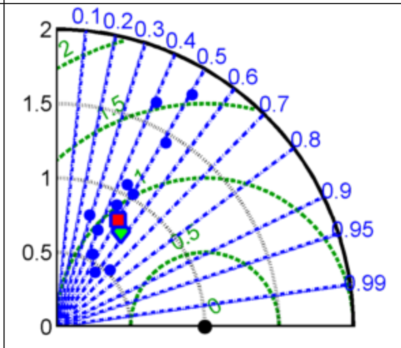	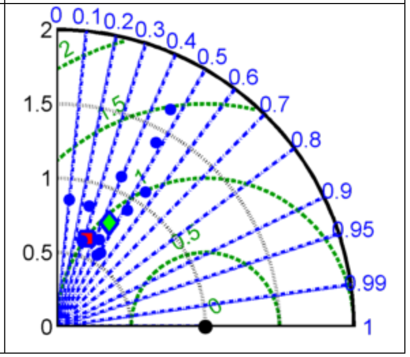

TABLE 4.3: Taylor diagrams for SMOS 25 km morning products in the YA and YB area. Satellite products are treated as the baseline soil moisture (black dot). □: Representative station. ◇: Average. ○: Individual stations.

bias of 0.09 m^3 m^{-3} and 0.22 m^3 m^{-3} respectively. Other stations had an r ranging between 0.24 to 0.68, RMSD between 0.07 m^3 m^{-3} to 0.14 m^3 m^{-3}, and bias between 0 m^3 m^{-3} to 0.09 m^3 m^{-3}. Although each of these irrigated plots consist of approximately 0.10% of the entire 25 km pixel, they can have a large impact on the average soil moisture if an appropriate weighting to each station based on area as recommended in Chapter 3 is not applied.

In the case of the YB area, the scatter in r values (Table 4.3) is seen to be less apparent due to homogeneity of the area. In comparison to SMOS 25 km soil moisture products (morning/AM overpasses), r ranged between 0.53 to 0.73, RMSD 0.07 m^3 m^{-3} to 0.10 m^3 m^{-3}, and bias between 0.01 m^3 m^{-3} to 0.09 m^3 m^{-3}. As expected, r and RMSD between the average of all stations and the representative stations has similar results (as identification of the representative station was largely based on its ability to represent the mean), whereas a big variation can be found if a single station was used without prior knowledge of its representativeness. This also demonstrates that, whilst the absolute accuracy of a representative station is difficult to determine, by directing limited resources to the most representative stations, similar results can be obtained as having a large number of stations. Results here have shown the importance of understanding the representativeness of soil moisture stations prior to using them for validation. Ideally, if intensive data collected according to the AMSR-2 grids were available, the representativeness of stations within the AMSR-2 grid could be determined with greater confidence. However, as such data had not been collected, the satellite soil moisture products will be validated based on the representative stations YA5 and YB7a for the YA and YB area (see Chapter 3) respectively which was determined based on SMAP grids (Chapter 3).

4.3.2 Overall performance

Based on comparisons with the representative stations, there is a noticeable seasonal impact on the performance of absolute soil moisture based on JX1 and JX2 whereby cRMSD decreased sequentially from summer, autumn, spring and winter (Table A.1 and A.4). This was more consistent for LP1, LP2 and SMOS, where cRMSD was approximately one throughout the year. The JAXA algorithm assumes that surface and canopy temperature are both equal and constant throughout the year at 295 K. Whilst canopy temperatures were not compared here, it is expected that this assumption would be valid only during winter. Consequently, cRMSD is lowest during winter and highest during summer.

Fig. 4.2 and 4.3 compares measurements from 25 km (morning/AM) soil moisture products from JX1, JX2, LP1, LP2 and SMOS within the YA area with YA5, and within the YB area with YB7a. Generally, JX1 and JX2 underestimated soil moisture by > 0.05 $m^3\ m^{-3}$ and had an r of approximately 0.5, while LP1 and LP2 overestimated (ranging from 0.04 $m^3\ m^{-3}$ to 0.20 $m^3\ m^{-3}$), particularly when soil moisture conditions were > 0.10 $m^3\ m^{-3}$. Based on the scatterplots, it can be seen that the performance of the JAXA algorithm decreased with increasing soil moisture values whereas the opposite is true for LPRM. Kim et al. (2015) found similar results when comparing AMSR-2 soil moisture products based on the JAXA and LPRM algorithm globally. Only a slight improvement was observed in the latter version of the JAXA products (JX2) with a reduction of MAE from 0.06 $m^3\ m^{-3}$ to 0.05 $m^3\ m^{-3}$. Moreover, JX1 and JX2 did not show strong seasonal effects. Whilst LP1 had a larger RMSD (0.13 - 0.23 $m^3\ m^{-3}$) and MAE (0.10 - 0.20 $m^3\ m^{-3}$) than JX1 and JX2, they decreased to 0.06 - 0.11 $m^3\ m^{-3}$ and 0.07 - 0.13 $m^3\ m^{-3}$ respectively in LP2. The correlation of C-band observations also increased to > 0.55 but did not change appreciably for X-band observations (Fig. 4.2 and 4.3). SMOS was observed to slightly underestimate, agreeing with the findings of previous studies (Al Bitar et al., 2012; Collow et al., 2012; Su et al., 2013) but its slope was closer to 1 than that of LP2.

Generally, from the scatter plots, the C-band observations based on LP1 did not meet the AMSR-2 mission objectives of achieving an MAE of less than ±0.08 $m^3\ m^{-3}$, whereas those based on LP2, only C-band observations met the objectives at the YA and YB area. Likewise, RMSD of SMOS observations exceeded the mission requirements of 0.04 $m^3\ m^{-3}$ accuracy. However, in terms of MAE, SMOS satisfies the mission objective of AMSR-2. Although JX1 and JX2 managed to meet their own mission objective, overall, their correlation with station measurements were lower. As the latter products based on the JAXA and LPRM algorithm were found to be superior over the former versions, in the following analyses, only JX2, LP2 ('X-' and C-band) and SMOS are discussed in detail.

4.3.3 Overpass periods

Fig. 4.4 and 4.5 show the time-series of morning/AM (top) and evening/PM (bottom) retrievals from JX2, LP2 and SMOS compared to station measurements for the YA and YB area respectively. The large variation in soil moisture measurements based on individual stations (gray lines) re-emphasizes the need for validation with most representative stations. These unrepresentative measurements would have affected the average soil moisture (magenta). Generally, it can be seen that soil moisture retrieved based on JX2 was the driest followed by SMOS, $LP2_X$, $LP2_{C2}$ and $LP2_{C1}$ for both morning/AM/AM and evening/PM overpasses. The variation in soil moisture was also lower during evening/PM overpasses. Soil moisture retrieved based on JX2 fell close to measurements form the stations but showed little seasonal effects and failed to capture the peak soil moisture after rainfall events. During July 2014 (Austral winter), there was a clear underestimation by JX2 with a more noticeable difference in morning/AM retrievals rather than evening/PM. Moreover, as LP2 and SMOS did not display this pattern, the underestimation is most likely due to the algorithm. Overall, SMOS soil moisture products appears to perform the best.

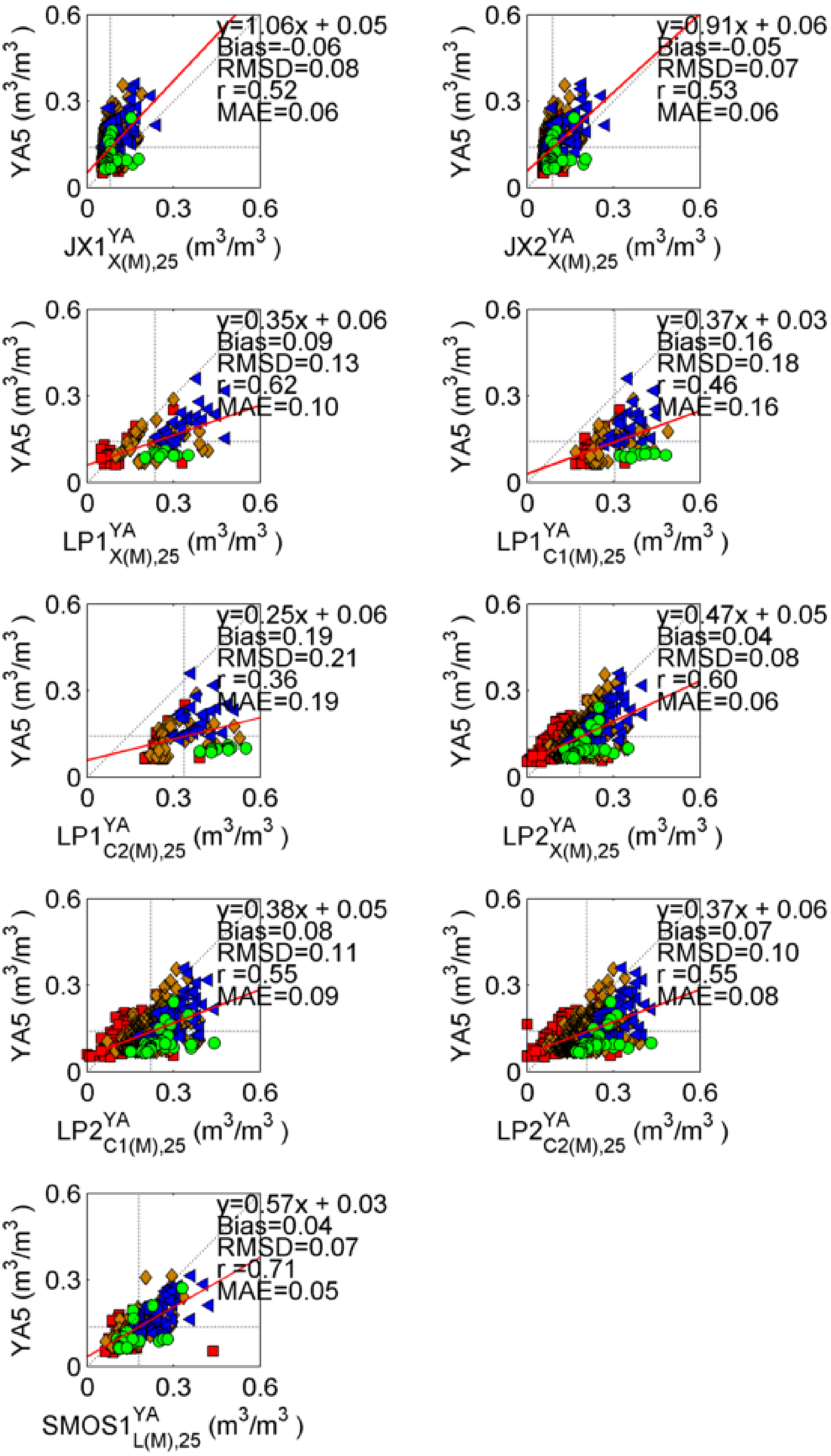

FIGURE 4.2: Scatterplots comparing different soil moisture products (morning/AM overpass) based on JX1, JX2, LP1, LP2, and SMOS soil moisture products in the a) YA area with YA5 (baseline). Summer: □, Autumn: ◇, Winter: ◁, Spring: ◯.

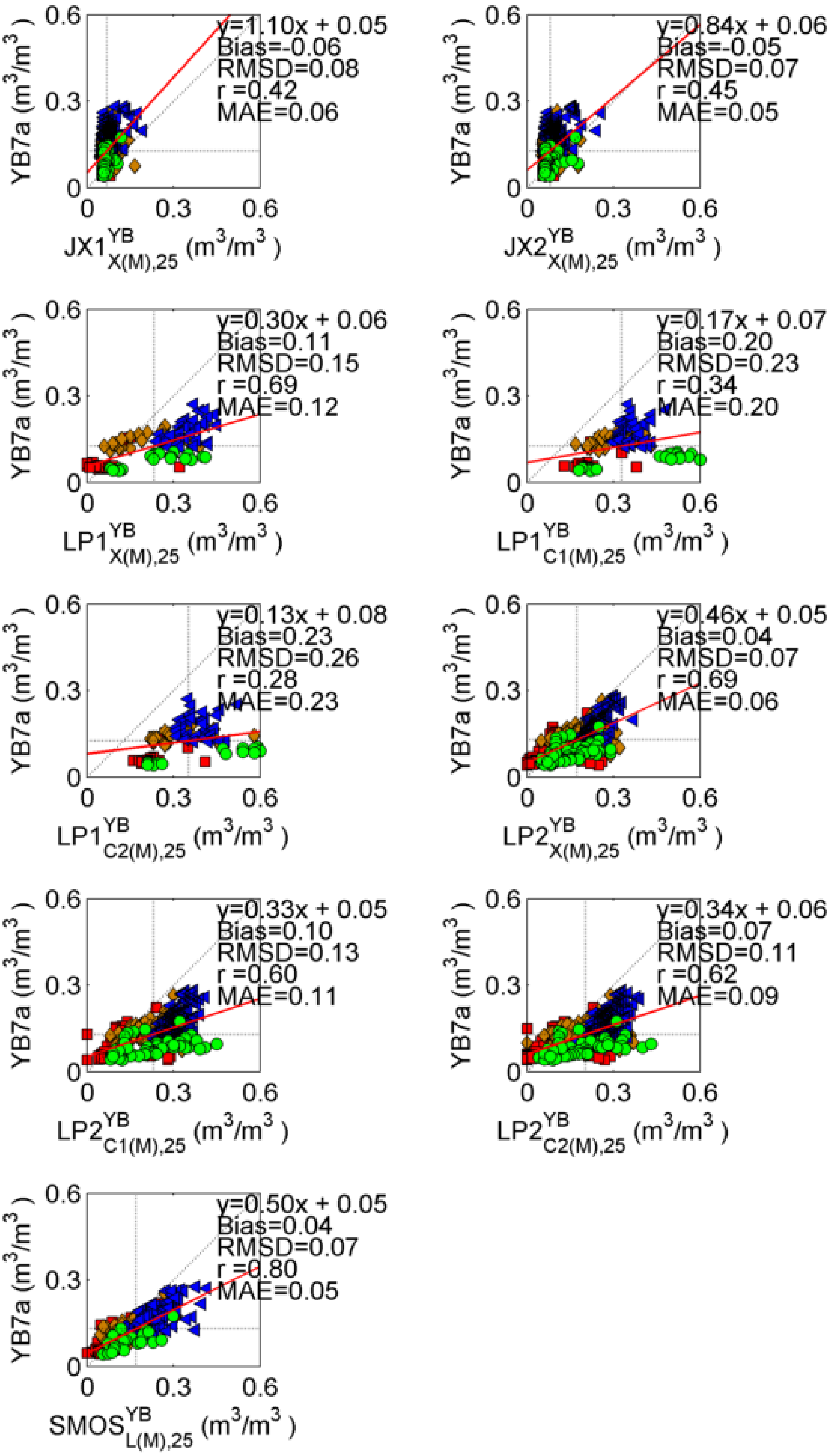

FIGURE 4.3: Scatterplots comparing different soil moisture products (morning/AM/AM overpass) based on JX1, JX2, LP1, LP2, and SMOS soil moisture products in the YB area with YB7a (baseline). Summer: □, Autumn: ◇, Winter: ◁, Spring: ◯.

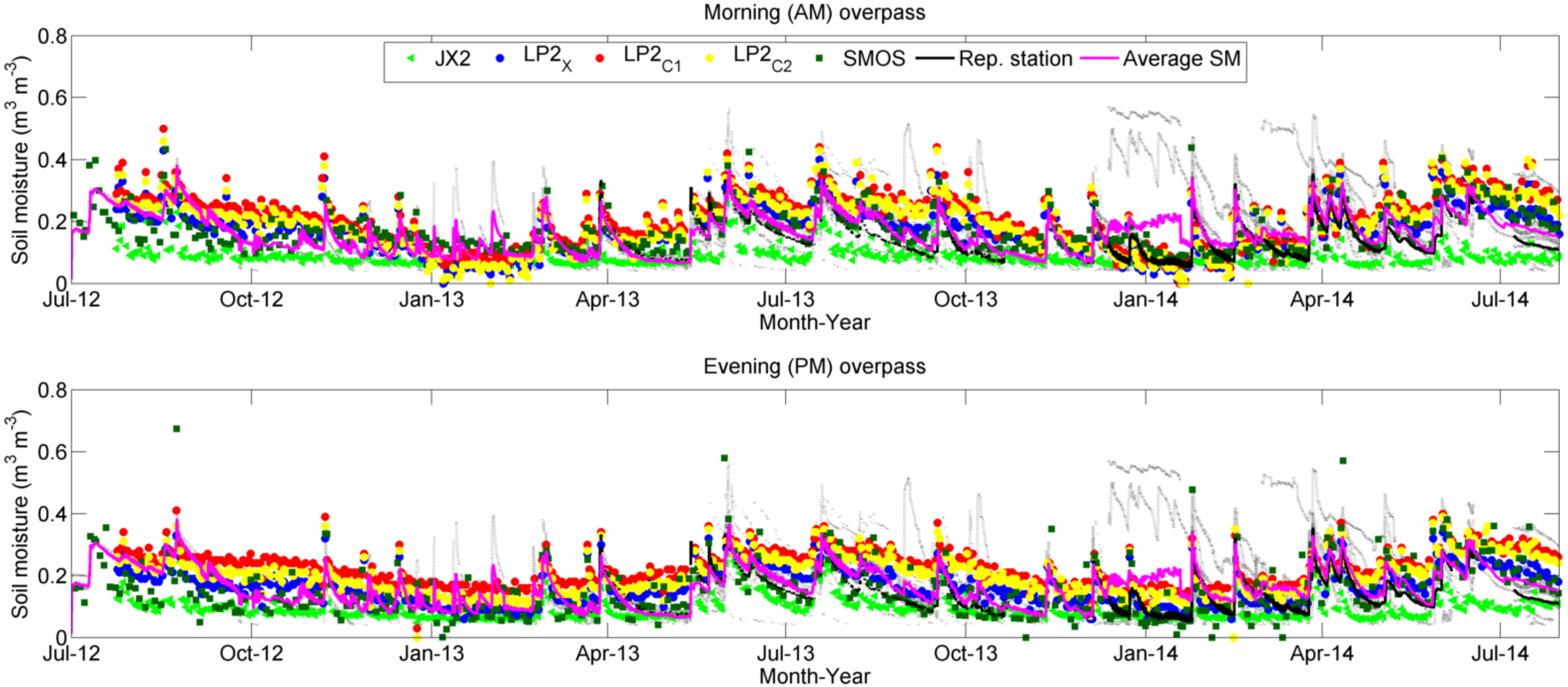

Figure 4.4: Timeseries of morning/AM (top) and evening/PM (bottom) observations based on different 25 km satellite products from July 2012 to July 2014 for the YA area.

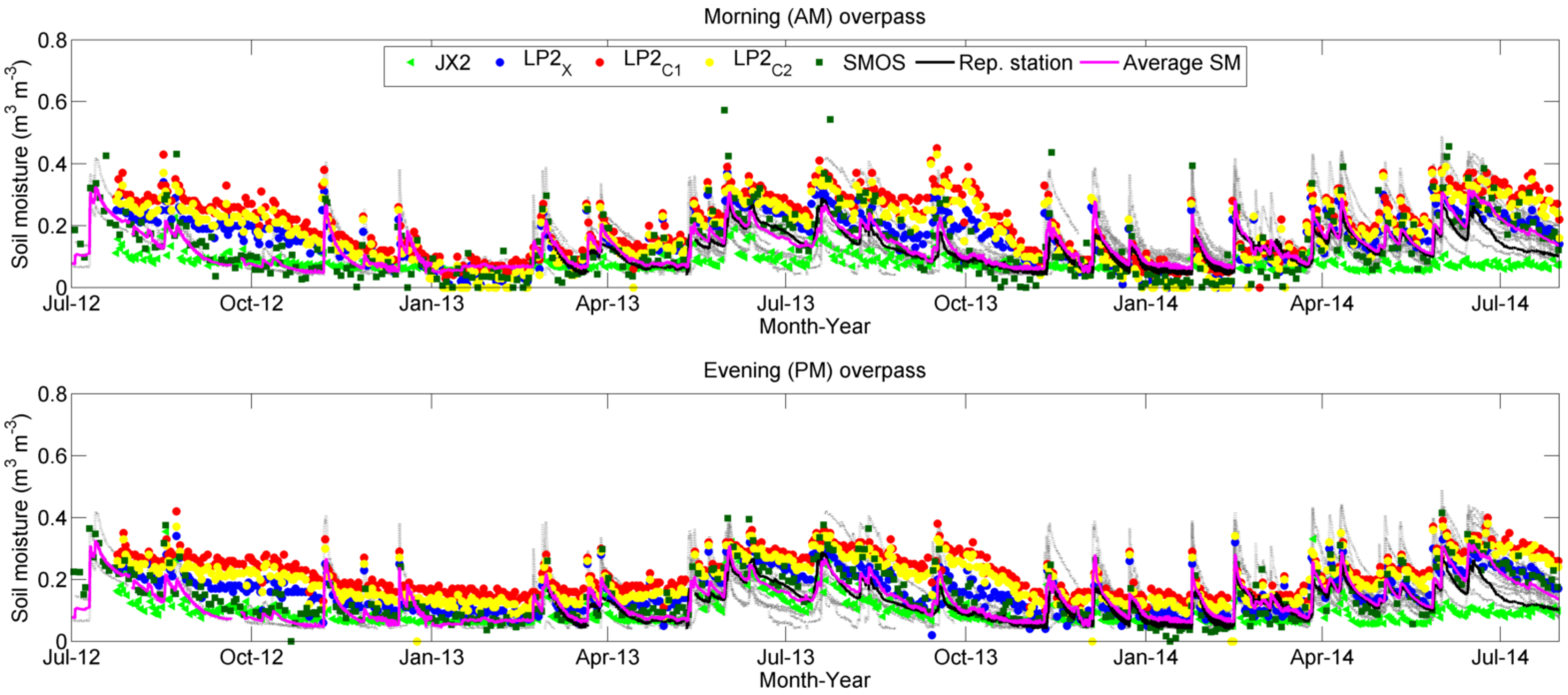

FIGURE 4.5: Timeseries of morning/AM (top) and evening/PM (bottom) observations based on different 25 km satellite products from July 2012 to July 2014 for the YB area.

Fig. 4.6 summarizes the performance of each product based on comparisons with the most representative stations. Both JX1 and JX2 showed the lowest variations whereby $\sigma_{\hat{JX1}}$ and $\sigma_{\hat{JX2}}$ ranged between 0.5 and 1. Correspondingly, this led to the underestimation observed earlier and its cRMSD was the lowest in all cases.

$\mathrm{LP1_X}$ showed the largest variation in all cases with $\sigma_{\hat{LP1}_\mathrm{X}} > 1.5$ in most cases. In cases where $\mathrm{LP1_{C1}}$ and $\mathrm{LP1_{C2}}$ had a positive correlation, r was still the lowest among other products with C2 (7.3 GHz) performing worse than C1 (6.9 GHz). In the case of LP2, $\mathrm{LP2_{C2}}$ performed only slightly better than $\mathrm{LP2_{C1}}$ and $\mathrm{LP2_X}$ performed the best. Theoretically, one would expect retrievals based on observations at 6.9 GHz (C1) to correlate better with the 5 cm soil moisture measurements since the depth sensed at lower frequencies should correspond more closely with the 5 cm depth of soil moisture probes and be less affected by the vegetation. However, results showed 10.7 GHz performed better than 6.9 GHz which overestimated and had a larger variance compared to the station measurements. This is in-line with the findings of Owe et al. (2008) and Draper et al. (2009) who found little differences between X- and C-band retrievals in Australia. Moreover, based on the probability of RFI provided by the SMOS product, the percentage of RFI detected in the Yanco study area was negligible (at most 1.5%) and Njoku et al. (2005) previously found very little RFI in X-band over Australia. Consequently, we postulate that most AMSR-based studies have concentrated on the development of the higher frequencies, and thus the algorithms have been calibrated to match X-band due to widespread occurrence of RFI at the C-band in North America, Europe and East Asia.

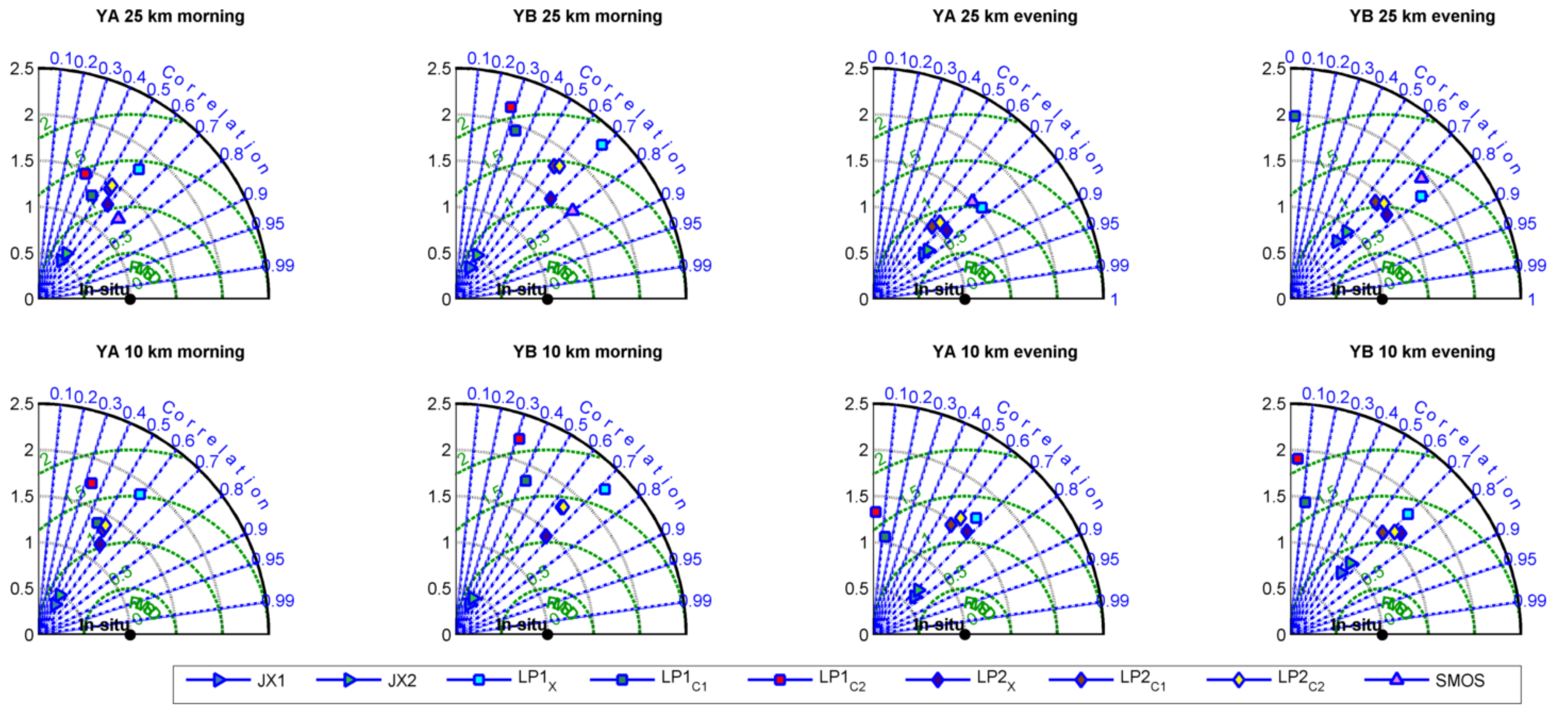

FIGURE 4.6: Taylor diagrams comparing 25 km (top) and 10 km (bottom) morning/AM and evening/PM products for the YA and YB area. Note: SMOS products at 10 km resolution is not available.

In addition, evening overpass (1:30 pm) products were found to perform better for both the LPRM and JAXA algorithm than the morning passes (1:30 am). Moreover, the variation of soil moisture based on the evening/PM overpasses matches better with that of the stations ($\hat{\sigma}_f$ closer to 1) than morning/AM overpasses. Due to the negative r for 25 km evening/PM retrievals based on $LP1_{C1}$ and $LP1_{C2}$, they were not visible in the diagrams. SMOS showed a more consistent performance for both evening/PM and morning/AM retrievals (cRMSD $\approx$1, 0.6 $<$ r $<$ 0.7, $\hat{\sigma}_f < 1.5$).

Fig. 4.7 shows soil temperature measurements at 1 cm and 5 cm depth. In all cases, the temperature difference was the lowest during winter, followed by autumn, spring and summer. Temperature difference was almost at its maximum at 1:30 pm (1.2°C – 4.6°C) and still exists at 1:30 am and 6 am (0.77°C – -2.23°C). Although the common assumption is that soil temperature difference is smallest in the morning, during SMOS's 6 pm overpass, the difference was smallest (-0.3°C and 1.3°C). This is similar to findings of Hornbuckle and England (2005) who showed that the temperature gradient at 1:30 pm was the largest followed by 1:30 am, and lower at 6 pm than 6 am. Correspondingly, SMOS, evening/PM retrievals were found to perform slightly better than morning/AM. In the case of AMSR-2, although the temperature gradient was highest at 1:30 pm, evening/PM retrievals were found to perform better than morning/AM retrievals.

Previous validation studies regarding morning/AM and evening/PM observations have yielded mixed results for both AMSR-E/AMSR-2 and SMOS (e.g. Brocca et al., 2011; Dente et al., 2012a; Djamai et al., 2015; Draper et al., 2009; Griesfeller et al., 2015; Peng et al., 2015; Rowlandson et al., 2012; Su et al., 2013). Recently, Lei et al. (2015) found that the performance of morning/AM and evening/PM retrievals from passive microwave remote sensing varies according to land cover. Peng et al. (2015), van Emmerik et al. (2015) and Brocca et al. (2011) attributed the better performance of observations during the day to a higher transparency of vegetation canopy during the day due to higher temperatures which therefore minimizes attenuation of soil emissions. However, this is unlikely to have a large impact due to the low vegetation canopy at the site. Du et al. (2012) and Raju et al. (1995) stipulated issues in inverse modelling of soil moisture at night or early morning for frequencies higher than 5.05 GHz when dry soil is slightly wetted as a consequence of dew or early stages of rainfall. This effect would be less on L-band observations which senses a deeper layer. Other factors such as Faraday rotation and difference in temperatures between near surface soil and vegetation can also affect

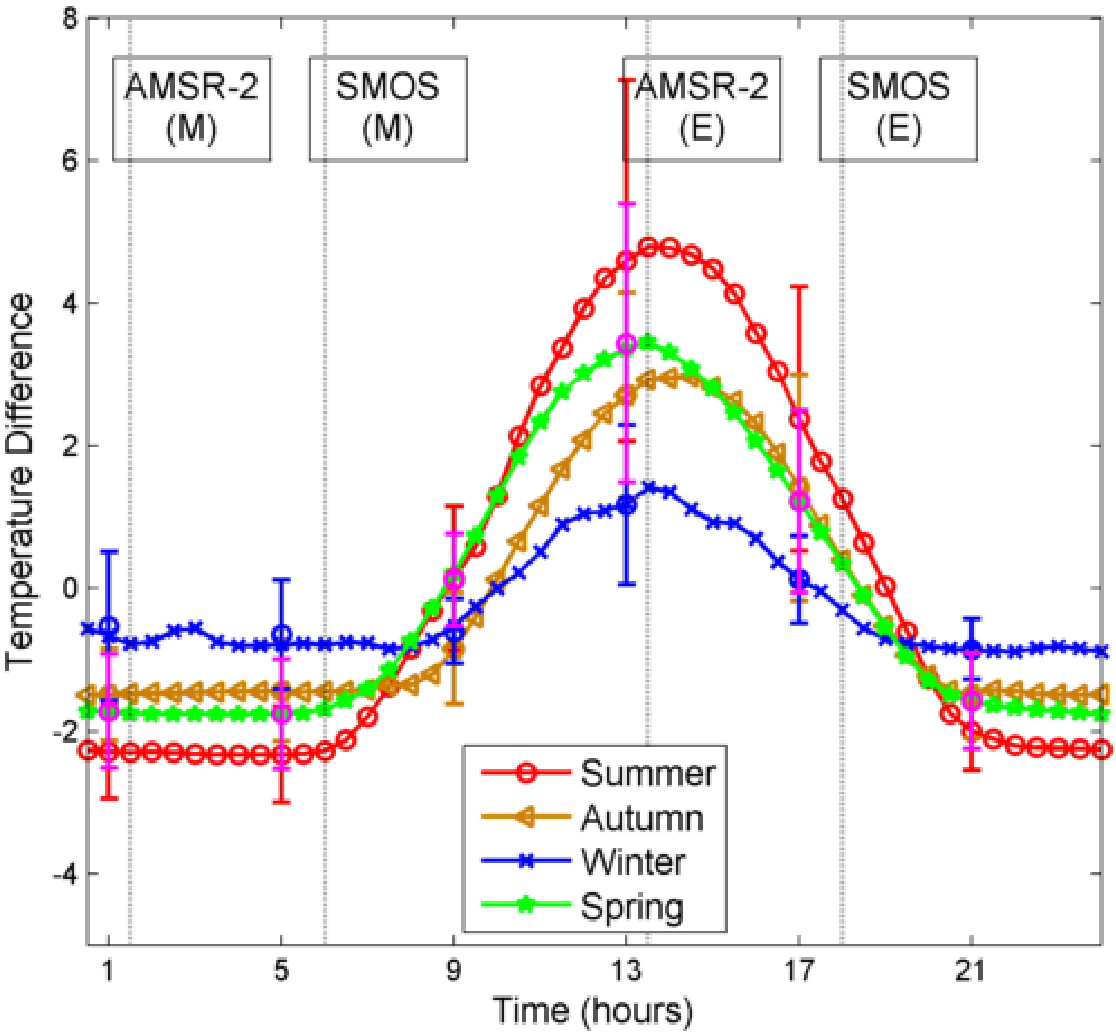

FIGURE 4.7: Mean diurnal variation of vertical difference in temperature between soil layers at a depth of 1 cm and 5 cm (temperature at 1 cm - temperature at 5 cm) for each season. The dotted black lines indicate the overpass times, whereas the error bars indicate the maximum and minimum difference.

the accuracy of the retrievals (Entekhabi et al., 2010a; Kerr et al., 2010). A combination of these different factors may have led to the mixed results for AMSR-2 retrievals and a more in-depth study will be needed to verify the cause.

4.3.4 CDF-matching

To eliminate systematic differences between datasets, several studies have used the cumulative distribution function (CDF) matching approach to bias correct microwave soil moisture retrievals (e.g. Choi and Jacobs, 2008; Drusch et al., 2005; Liu et al., 2011; Reichle and Koster, 2004). Here, CDF-matching was applied to match the distribution from the satellite soil moisture products to that of the most representative stations. Fig 4.8 shows the time-series of CDF-matched satellite soil moisture for both morning/AM and evening/PM retrievals. Statistics comparing representative stations with satellite retrievals before and after CDF-matching are also tabulated in Table 4.4 and 4.5.

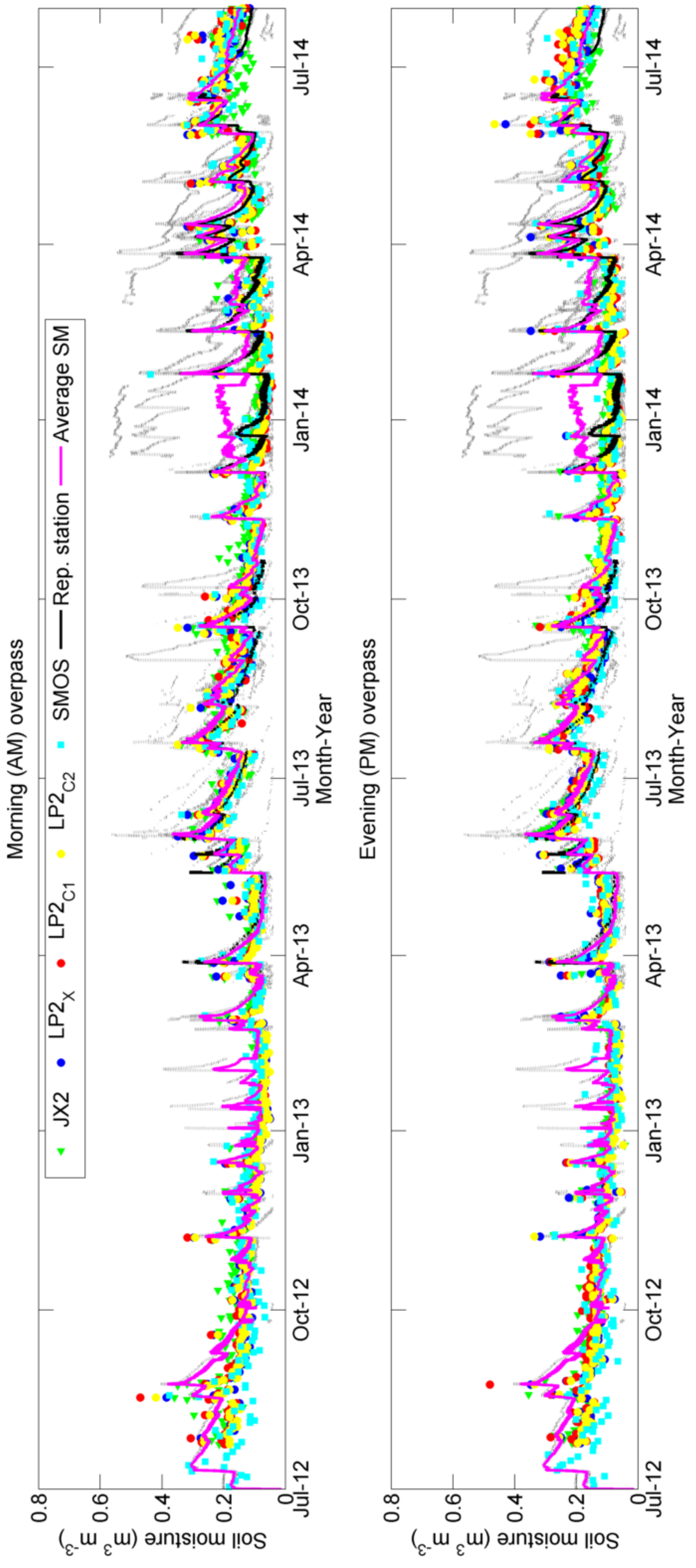

Figure 4.8: Same as Fig. 5 but with CDF-matched morning/AM (top) and evening/PM (bottom) observations based on selected 25 km satellite products from July 2012 to July 2014 for the YA area.

Table 4.4: Statistics comparing the original and CDF matched, morning and evening 25 km satellite products with the most representative stations for YA area. Satellite data is baseline data.

		Original					CDF matched				
Product	Area	Bias	RMSD	r	MAE	ubRMSD	Bias	RMSD	r	MAE	ubRMSD
		$m^3\ m^{-3}$	$m^3\ m^{-3}$		$m^3\ m^{-3}$	$m^3\ m^{-3}$	$m^3\ m^{-3}$	$m^3\ m^{-3}$		$m^3\ m^{-3}$	$m^3\ m^{-3}$
$JX1_{X(M)}$	YA	-0.06	0.08	0.52	0.06	0.05	0.02	0.06	0.54	0.05	0.06
$JX2_{X(M)}$		-0.05	0.07	0.53	0.06	0.05	0.01	0.06	0.55	0.05	0.06
$LP1_{X(M)}$		0.09	0.13	0.62	0.10	0.09	0.01	0.07	0.58	0.05	0.06
$LP1_{C1(M)}$		0.16	0.18	0.46	0.16	0.07	0.01	0.07	0.43	0.05	0.07
$LP1_{C2(M)}$		0.19	0.21	0.36	0.19	0.09	0.01	0.09	0.25	0.06	0.09
$LP2_{X(M)}$		0.04	0.08	0.59	0.06	0.07	0.01	0.06	0.59	0.04	0.06
$LP2_{C1(M)}$		0.08	0.11	0.54	0.09	0.08	0.01	0.06	0.54	0.05	0.06
$LP2_{C2(M)}$		0.07	0.10	0.55	0.08	0.08	0.01	0.06	0.55	0.05	0.06
SMOS		0.04	0.07	0.71	0.05	0.05	0.01	0.05	0.69	0.03	0.05
Average		0.07	0.12	0.54	0.10	0.07	0.01	0.06	0.53	0.05	0.06
$JX1_{X(E)}$	YA	-0.05	0.06	0.75	0.05	0.04	0.00	0.04	0.74	0.03	0.04
$JX2_{X(E)}$		-0.05	0.06	0.75	0.05	0.04	0.01	0.04	0.75	0.03	0.04
$LP1_{X(E)}$		0.04	0.07	0.77	0.06	0.06	0.00	0.04	0.77	0.03	0.04
$LP1_{C1(E)}$		0.23	0.25	-0.03	0.23	0.09	0.00	0.10	-0.07	0.07	0.10
$LP1_{C2(E)}$		0.27	0.29	-0.13	0.27	0.11	0.00	0.11	-0.08	0.07	0.11
$LP2_{X(E)}$		0.03	0.05	0.74	0.04	0.04	0.00	0.05	0.75	0.03	0.05
$LP2_{C1(E)}$		0.09	0.10	0.64	0.09	0.05	0.00	0.05	0.66	0.04	0.05
$LP2_{C2(E)}$		0.07	0.08	0.66	0.07	0.05	0.00	0.05	0.67	0.04	0.05
SMOS		0.02	0.07	0.72	0.05	0.06	0.00	0.05	0.72	0.03	0.05
Average		0.07	0.12	0.54	0.10	0.06	0.00	0.06	0.54	0.04	0.06

TABLE 4.5: Statistics comparing the original and CDF matched, morning and evening 25 km satellite products with the most representative stations for YB area. Satellite data is baseline data.

		Original					CDF matched				
Product	Area	Bias	RMSD	r	MAE	ubRMSD	Bias	RMSD	r	MAE	ubRMSD
		$m^3\ m^{-3}$	$m^3\ m^{-3}$		$m^3\ m^{-3}$	$m^3\ m^{-3}$	$m^3\ m^{-3}$	$m^3\ m^{-3}$		$m^3\ m^{-3}$	$m^3\ m^{-3}$
$JX1_{X(M)}$	YB	-0.06	0.08	0.42	0.06	0.05	0.01	0.06	0.41	0.05	0.05
$JX2_{X(M)}$		-0.05	0.07	0.46	0.05	0.05	0.01	0.05	0.48	0.04	0.05
$LP1_{X(M)}$		0.11	0.15	0.66	0.12	0.10	0.01	0.05	0.64	0.04	0.05
$LP1_{C1(M)}$		0.20	0.23	0.32	0.20	0.11	0.01	0.08	0.26	0.05	0.08
$LP1_{C2(M)}$		0.23	0.26	0.27	0.23	0.12	0.01	0.08	0.32	0.05	0.07
$LP2_{X(M)}$		0.05	0.08	0.66	0.06	0.06	0.01	0.05	0.68	0.03	0.05
$LP2_{C1(M)}$		0.10	0.13	0.59	0.11	0.08	0.01	0.06	0.56	0.04	0.06
$LP2_{C2(M)}$		0.08	0.11	0.58	0.09	0.08	0.01	0.05	0.58	0.04	0.05
SMOS		0.04	0.07	0.80	0.05	0.05	0.01	0.04	0.80	0.03	0.04
Average		0.08	0.13	0.53	0.11	0.08	0.01	0.06	0.53	0.04	0.06
$JX1_{X(E)}$	YB	-0.04	0.06	0.63	0.04	0.04	0.00	0.04	0.65	0.03	0.04
$JX2_{X(E)}$		-0.03	0.05	0.65	0.04	0.04	0.01	0.04	0.67	0.03	0.04
$LP1_{X(E)}$		0.05	0.08	0.78	0.06	0.06	0.00	0.04	0.79	0.03	0.04
$LP1_{C1(E)}$		0.25	0.28	0.03	0.25	0.11	-0.01	0.09	0.10	0.06	0.09
$LP1_{C2(E)}$		0.29	0.32	-0.03	0.29	0.13	-0.02	0.06	0.26	0.05	0.06
$LP2_{X(E)}$		0.04	0.06	0.75	0.05	0.05	0.00	0.04	0.76	0.03	0.04
$LP2_{C1(E)}$		0.10	0.11	0.66	0.10	0.05	0.00	0.05	0.67	0.04	0.05
$LP2_{C2(E)}$		0.08	0.09	0.70	0.08	0.05	0.00	0.04	0.71	0.03	0.04
SMOS		0.02	0.08	0.74	0.06	0.07	0.00	0.05	0.68	0.03	0.05
Average		0.08	0.12	0.54	0.11	0.07	0.00	0.05	0.59	0.04	0.05

Prior to correction, based raw statistics (as opposed to standardized statistics of Taylor diagrams or CDF-matching), SMOS performed the best based on morning/AM retrievals only for both YA and YB area (bias: 0.05 m^3 m^{-3}; RMSD: 0.07 m^3 m^{-3}; r: 0.62; MAE: 0.05 m^3 m^{-3}) whereas $LP2_X$ performed the best based on evening/PM retrievals (bias: 0.03 m^3 m^{-3}; RMSD: 0.06 m^3 m^{-3}; r: 0.74; MAE: 0.04 m^3 m^{-3}). However, as the differences were small, and the observation points used for comparisons were not the same (a total of 558 observations for SMOS and 599 for $LP2_X$), it can be said that both products performed equally well. It is to be noted that the JX2 evening/PM products are just as good (bias: -0.04 m^3 m^{-3}; RMSD: 0.06 m^3 m^{-3}; r: 0.70; MAE: 0.05 m^3 m^{-3}). Considering both areas (YA and YB) and overpasses (morning/AM and evening/PM), JX2, $LP2_X$ and SMOS met the 'goal accuracy' of $\pm$0.08 m^3 m^{-3} with an MAE of 0.05 m^3 m^{-3} but none of the products achieved SMOS's goal of achieving an RMSD $<$ 0.04 m^3 m^{-3}.

After CDF-matching, overall bias, RMSD, MAE and ubRMSD decreased by an average of 0.07 m^3 m^{-3}, 0.06 m^3 m^{-3}, 0.06 m^3 m^{-3} and 0.01 m^3 m^{-3} respectively. Yet, r improved in some cases, but worsened for others. Overall, it reduced by 0.01. In terms of bias correction, LP1 products benefited the most from the CDF-matching whereas SMOS benefited the least, followed closely by $LP2_X$. Moreover, JX2 appears to capture the increase in soil moisture at the end of July 2014 (Fig. 4.8), which as seen in Fig. 4.4, it did not. Whilst CDF-matching improves the absolute performance of the retrievals, certain considerations need to be taken into account prior to its application. First, unless a representative station is available, there is no reference dataset to carry out this correction. Even if model simulations were used, the accuracy of models are subjected to the forcing and input parameters prescribed to it. Second, if the user is only interested in the temporal variability, it has been shown here that CDF-matching has little effect on r and may even degrade r in some instances. Finally, if the user requires prior knowledge regarding the absolute value of soil moisture, CDF-matching can lead to biases of up to 0.06 m^3 m^{-3}. Pauwels and Lannoy (2015) have demonstrated that assimilation of rescaled observations (such as through CDF-matching) will not improve the absolute values of model simulations, and therefore, assimilation of prior knowledge regarding the absolute value is more desirable. Consequently, since bias correction requires a reference dataset (truth), and mission objectives are usually based on errors in absolute soil moisture prior to correction, SMOS (evening/PM and morning/AM) is the most

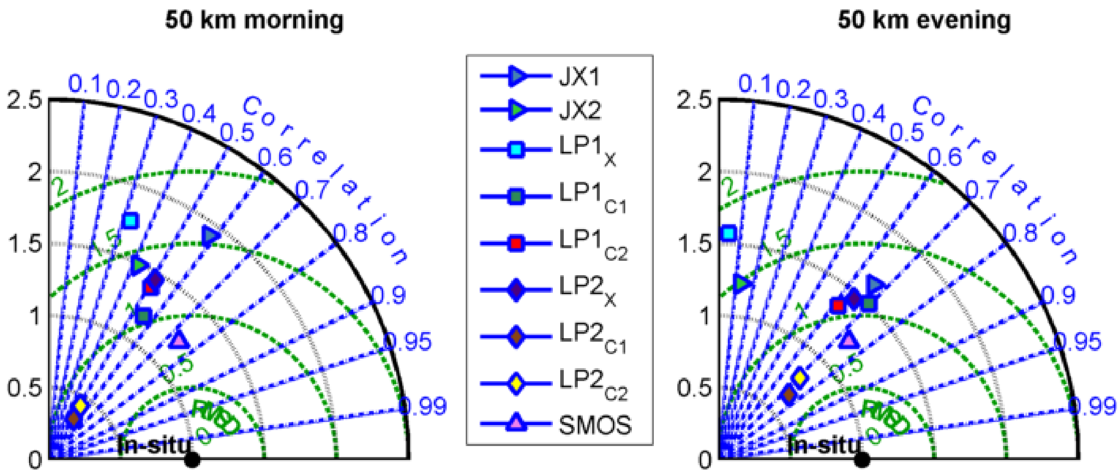

FIGURE 4.9: Taylor diagrams comparing 50 km morning/AM and evening/PM products for the Yanco area.

favourable due to its consistent performance in detecting temporal and absolute soil moisture conditions. If $LP2_X$ were to be used, morning/AM and evening/PM retrievals should be used separately due to differences in performance.

4.3.5 Resolutions

Moving down from 25 km to 10 km resolution, there was a very slight change in cRMSD (radial distance from baseline) due to homogeneity of the area (Fig. 4.6). Similarly, Champagne et al. (2015) emphasized that non-representativeness of stations at the coarser scale may be more important than the impact of land cover on soil moisture retrievals. Fig. 4.9 compares the morning/AM and evening/PM retrievals based on an assumed 50 km footprint product. The 10 km AMSR-2 product located within the centre of the Yanco study area was used here. As SMOS does not have a 10 km product, the 25 km product which was closest to the centre of the study area was selected. These retrievals were then validated based on measurement from YA5, as this station was found to be most representative of the regional Yanco study area in Chapter 3. According to the Taylor diagrams, SMOS and LP2 performed the best overall during morning/AM and evening/PM overpasses respectively. This backs the assumption that measurements from YA5 and YB7a are representative of the wider spatial footprint observed by the space-borne sensors.

4.4 Key findings

This study validated AMSR-2 soil moisture products from two different versions of two different algorithms (JAXA and LPRM), and the SMOS soil moisture product, using the most representative stations identified by an earlier study. It was shown that the use of unrepresentative stations can have a large impact on validation results (r of -0.16 as opposed to 0.61) particularly for non-homogeneous areas. Therefore, it is paramount that representativeness of stations be well understood prior to use for any validation purposes. While the absolute accuracy of a representative station is difficult to determine, having a representative station enables the reduction of resources needed to maintain a network of stations whilst providing consistent reliable data.

Generally, the later versions of the JAXA (JX2) and LPRM (LP2) products were confirmed to be superior over the former ones. Furthermore, JAXA products were found to underestimate the soil moisture by ≈ 0.05 m^3 m^{-3} whereas LPRM products overestimated by between 0.04 - 0.20 m^3 m^{-3}. LP1 C-band observations performed badly with negative correlations and therefore should not be used. This was earlier found in Parinussa et al. (2015) and is likely an effect of model miscalibration which was rectified in LP2.

Performance of soil moisture products during different seasons revealed varying performance of JAXA products, possibly due to assumptions that the difference in temperature between the soil surface and canopy is constant throughout the year. In the case of LP2, X-band retrievals performed better than C-band. Similarly, evening/PM retrievals at X-band from AMSR-2 performed better than morning/AM retrievals, whereas performance for both morning/AM and evening/PM retrievals was consistent for SMOS. Overall, JX2, LP2$_X$ and SMOS met the 'goal accuracy' of ± 0.08 m^3 m^{-3} with an MAE of 0.05 m^3 m^{-3}, but none of the products achieved SMOS's goal of achieving an RMSD $<$ 0.04 m^3 m^{-3}. Whilst SMOS performed the best based on morning/AM retrievals (RMSD: 0.07 m^3 m^{-3}; r: 0.62), and LP2$_X$ performed best based on evening/PM retrievals (RMSD: 0.06 m^3 m^{-3}; r: 0.74). Whilst based on Taylor diagrams and statistics JX2 evening/PM products performed comparably well (RMSD: 0.06 m^3 m^{-3}; r: 0.70), based on visual inspections, JX2 did not show any seasonal effects and failed to capture the peaks after rainfall events.

Consequently, depending on the interest of the user of the products, different soil moisture products should be applied. If soil moisture is used as an indicator of wetness condition, i.e. the ability to capture temporal variability is prioritized, $LP2_X$ evening/PM overpasses are recommended for use. However, where accuracy in absolute soil moisture is needed, SMOS retrievals are recommended due to its ability to capture both the temporal and absolute variability of soil moisture for both morning/AM and evening/PM observations with the same confidence. Finally, these results need to be considered in the light that this study focuses on two carefully selected pixels and may not reflect the product accuracy at other sites. Therefore, it is important that such careful analysis can be conducted at other sites.

4.5 Chapter summary

This chapter investigated the performance of soil moisture retrievals from AMSR-2 and SMOS. The AMSR-2 soil moisture products analysed included two versions of products based on the JAXA and LPRM algorithm. It was found that the two versions of JAXA products and $LP2_X$ met the mean average error (MAE) 'goal accuracy' of the AMSR-2 mission (MAE < 0.08 m^3 m^{-3}) with an MAE of 0.05 m^3 m^{-3}. However, none of the products achieved SMOS's goal of achieving an RMSD < 0.04 m^3 m^{-3}. An intercomparison between different acquisition times (morning/AM and evening/PM) of the JX2 and LP2 algorithm resulted in a better performance from evening/PM overpasses as opposed to morning/AM overpasses. This was similar for SMOS but the difference was marginal. Moreover, when different frequencies of LP2 products were compared, X-band outperformed C-band retrievals. Overall, considering both temporal and absolute accuracy, SMOS performed the best followed closely by $LP2_X$ Consequently, considering the results in this study, both morning/AM and evening/PM retrievals from SMOS can be combined with confidence that they will be consistent to capture both temporal and absolute variability. As such, with a better understanding regarding the performance of these products, SMOS L3 products will be used to demonstrate the application of validated soil moisture products for LSM evaluation in Chapter 7.

Chapter 5

Comparison of eddy covariance, optical and microwave scintillometer derived evapotranspiration

The purpose of the study in this chapter was to inter-compare the eddy covariance (EC) method with the stand-alone optical scintillometers (LAS) of two different manufacturers, the stand-alone microwave scintillometers (MWS) of two frequencies and two polarizations, and different combinations of the LAS and MWS in the two-wavelength method. This is to test the application of scintillometers to measure sensible heat (H) and latent heat ($L_{\mathrm{v}}E$) fluxes in a semi-arid environment. A 3-month field campaign was conducted to collect data required for this assessment. This is the first time that such a comprehensive comparison has ever been carried out using MWS in a semi-arid environment. This study also compares the different methods to close the energy balance. The work presented in this chapter has been published in Agricultural Forest and Meteorology (Yee et al., 2015).

5.1 Introduction

The ability to quantify the energy and mass exchange between the land surface and atmosphere is important for improving models used in water resource management. Field measurements of H and $L_{\mathrm{v}}E$ are also crucial for the validation of remote sensing surface heat flux products (Brunsell et al., 2011; Fritschen et al., 1992; Jung et al., 2009; Kite and Droogers, 2000).

The most popular approach adopted to measure surface heat fluxes is based on the EC method (Kaimal and Finnigan, 1994), with EC systems deployed globally through the FLUXNET network (Baldocchi et al., 2001; El Maayar et al., 2008). However, as the footprint of EC systems changes with meteorological conditions, its representativeness of model grids and satellite pixels, particularly in heterogeneous landscapes is debatable (Ward et al., 2014). Scintillometry presents an alternative method, as meteorological changes have little impact on its footprint and is able to measure path integrated sensible heat fluxes ranging from a few hundred meters to 10 km (Baghdadi et al., 2007; Beyrich et al., 2002; Meijninger and De Bruin, 2000; Samain et al., 2012b), thereby making it more suitable for long-term validation of model simulations and remote sensing surface heat flux products (Hemakumara et al., 2003; Hendrickx, Jan MH and Kleissl, Jan and Vélez, Jesús D Gómez and Hong, Sung-ho and Duque, José R Fábrega and Vega, David and Ramírez, Hernán A Moreno and Ogden, Fred L, 2007).

A scintillometer consists of a transmitter that emits electromagnetic signals to a receiver, which records the intensity of this signal from a distance. As the signal propagates through the atmosphere towards the receiver, it is scattered by turbulent eddies in the atmosphere. This scattering is detected as fluctuations in the intensities of the signal recorded by the scintillometer's receiver (i.e. scintillations). These eddies are driven by surface forcing, such as wind shear from frictional drag of winds flowing over the ground, heat fluxes from the ground caused by solar incident radiation, and turbulent wakes from obstacles like trees (Stull, 1988). Consequently, by combining theoretical principles of atmospheric turbulence with the physics of electromagnetic wave propagation, surface heat fluxes can be derived (e.g. Van Kesteren, 2012).

The turbulence causing scintillations in the atmosphere can be quantified by the structural parameter of the refractive index, C_{n}^2, and are mainly affected by the structural parameters of temperature, C_T^2, humidity, C_Q^2, and the cross structural parameter of temperature and humidity, C_{TQ} (Kohsiek, 1982). C_T^2 is directly related to H whereas C_Q^2 is directly related to L_vE. Temperature fluctuations given by C_T^2 are the dominant cause of scintillation in the optical wavelengths, and therefore optical scintillometers can be applied to measure H without making measurements of or assumptions on humidity fluctuations. Refer to Appendix B for more details regarding the theory behind the derivation of surface heat fluxes based on scintillometry. Commercially available optical scintillometers have been widely used and have shown to perform similarly to Bowen ratio energy balance (BREB) techniques, hydrological models, and satellite and EC measurements over different types of landscapes (e.g. Brunsell et al., 2011; Chehbouni et al., 2000; Ezzahar et al., 2009; Lagouarde et al., 2002; Liu et al., 2013; McJannet et al., 2011; Meijninger et al., 2002a,b; Pauwels et al., 2008; Samain et al., 2012a, 2011, 2012b; Savage, 2009; Zeweldi et al., 2010), including open water and urban areas (Lagouarde et al., 2006; McJannet et al., 2013; Samain et al., 2011; Ward et al., 2013).

Conversely, no wavelengths have been identified in which C_Q^2 is most dominant. Therefore, to derive C_Q^2, the microwave (or millimeter wave) scintillometer (MWS), which is sensitive to both humidity and temperature fluctuations, can be used in combination with an LAS by making assumptions on the value of r_{TQ} (e.g. Evans, 2009; Meijninger et al., 2002a) or measuring r_{TQ} based on the bichromatic correlation method (Beyrich et al., 2005; Lüdi et al., 2005; Ward et al., 2015a,b). The combined use of MWS and LAS is commonly referred to as the two-wavelength method. As for MWS systems, they were not used independently until Kohsiek and Herben (1983) derived surface heat fluxes using a stand-alone MWS (frequency, f = 30 GHz) by making assumptions regarding r_{TQ} and the Bowen ratio (β). Leijnse et al. (2007) showed that by introducing the energy budget constraint to derive the surface heat fluxes, the standalone MWS (f = 27 GHz) can be used to measure H and L_vE in relatively moist environments. Given the success of LAS in measuring area-averaged H, the possibility of using a stand-alone MWS in the same way to measure area-averaged L_vE is undeniably attractive. However, to this date, no studies using the two-wavelength method or a stand-alone MWS have been carried out in a semi-arid environment. Due to differences in the frequencies used in different studies, it is also of value to understand the effect this might have on the measurements.

Consequently, the aim of this study is to test the application of scintillometers to measure

H and L_vE in a semi-arid environment. Here, the results from comparing an EC system with two different LAS manufacturers, Kipp and Zonen (LAS) and Scintec (BLS 900) (herein referred to as Kipp and Scintec, respectively), two MWS with frequencies of 26 GHz and 38 GHz (herein referred to as MW26 and MW38, respectively) and two polarizations (horizontal, h- and vertical, v-), and different combinations of LAS and MWS in the two-wavelength method, are presented.

5.2 Methods

5.2.1 Site description

The site of this inter-comparison is located within the Yanco study area (contained between 34.56°S and 35.17°S, and 145.83°E and 146.4°E) (Fig. 5.1) described in the Chapter 3. The dominant wind directions are from the south-west and north-east. The site consists of a homogeneous flat grassland that is used for cattle grazing. The grassland is dominated by perennial tussock grasses, such as kangaroo and wallaby grasses (Natural Resources Advisory Council, 2010). The soil type is sand over clay (loamy sand) and typical porosity of this soil type is about 0.30 m^3 m^{-3} (Hornbuckle et al., 1999; Smith et al., 2012).

5.2.2 Measurement description

The EC system was mounted on a 20 m tower (located at 34.99°S and 146.30°E) at 6 m above the ground, and has been in operation since May 2012 (Figure 5.2). The EC system consists of a CSAT3 3-D sonic anemometer (Campbell Scientific, Inc.) and a LI-7500 open path infrared gas analyzer (IRGA) (LI-COR Inc., U.S.) with a sampling frequency of 10 Hz following the general approach of Beringer et al. (2007) and Hutley et al. (2005).

In November 2012, the two LAS systems, Kipp and Scintec (Figure 5.3), were deployed along a 1 km path (L) (Figure 5.1). The receivers were situated about 1 km west of the EC tower and the transmitters were installed approximately 10 m from the foot of the EC tower (Figure 5.1 and 5.4). Due to the complexity of setting up multiple towers within a flat and remote open area, both LAS systems were set up with an effective beam height,

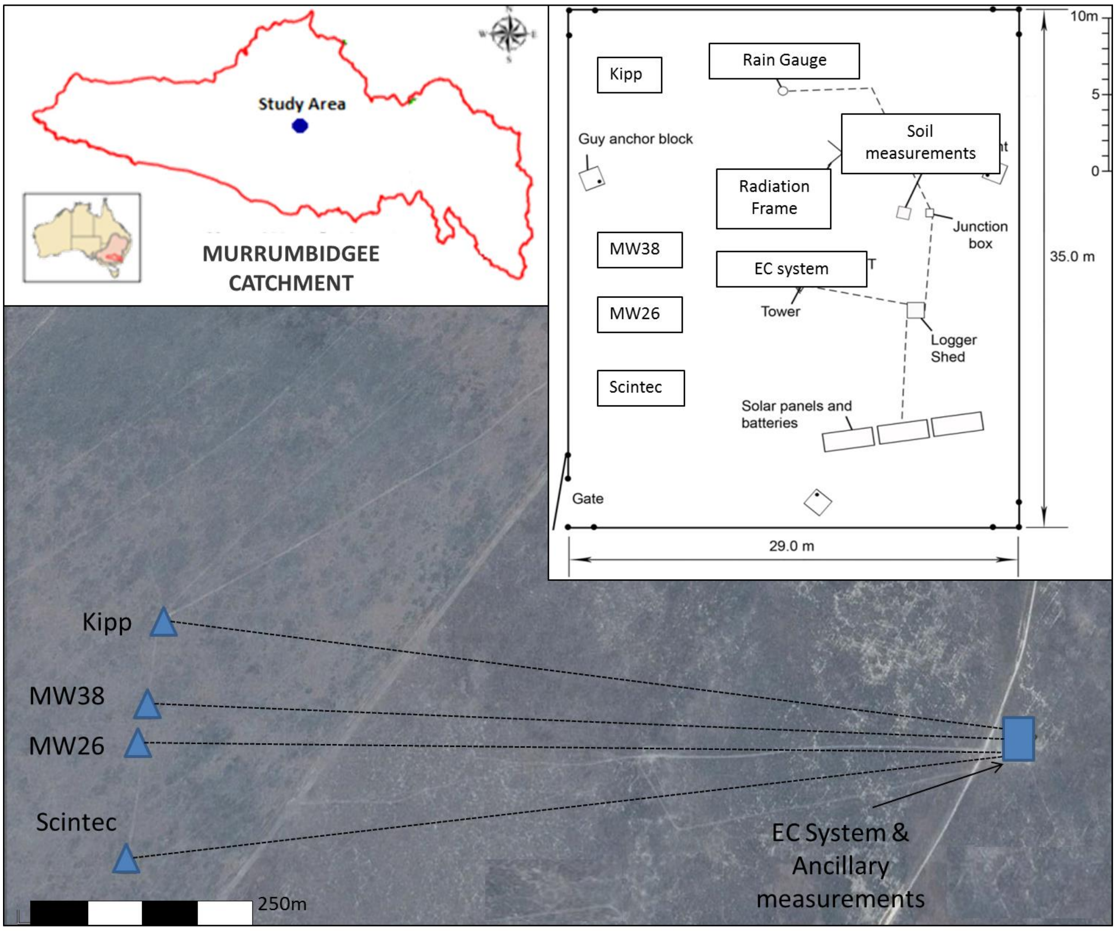

FIGURE 5.1: Layout of the experimental site. Dotted lines indicate the propagation paths of the transmitters' signal to the receivers which are located close to the EC tower. Left inset: Location of the study area within the Murrumbidgee River catchment. Right inset: Plan view of the EC system site with locations of the CSAT and IRGA on the tower, scintillometer receivers, frame mounted radiometers, soil measurement plot, and other ancillary measurements.

z_s, of 2.50 m. Despite the seemingly low height, due to the success of other studies in using scintillometers below the blending height (e.g. Ezzahar et al., 2007; Meijninger et al., 2002a), and the homogeneity and low vegetation height (< 0.30 m) at the site, this was deemed to be acceptable. To avoid interference, the two LAS transmitters were installed approximately 250 m apart. The 1-min values of C_n^2, computed internally by the LAS systems provided by the manufacturers, were used to derive H and L_vE.

The two MWS systems, MW26 and MW38 (Figure 5.5 and 5.4), were deployed in November 2013 between the two LAS systems. Both MWS systems also have an effective beam height of 2.50 m. The MWS transmitters transmit signals rotated from the horizontal plane by 45° to allow splitting by an ortho-mode transducer on the receiver antenna

FIGURE 5.2: EC tower.

into identical h- and v- polarization receiver channels. The raw voltages measured at 10 Hz frequency by the MWS receivers were converted to intensities, I as provided by the manufacturer of the MWS system. To avoid absorption effects, the lower cut-off frequency for the MWS was 0.03 Hz respectively (Green et al., 2001). Values of C_{n}^2 every minute were calculated from the intensities as

$$C_{\mathrm{n}}^2 = \frac{2^{14/3}\Gamma\left(\frac{7}{3}\right)\cos\left(\frac{\pi}{12}\right)}{\pi\sqrt{3\pi}\Gamma\left(\frac{8}{3}\right)} k^{-7/6} L^{-11/6} \sigma_{\ln(I)}^2, \tag{5.1}$$

where $\Gamma(\cdot)$ is the gamma function and k=$2\pi/\lambda$ is the wave number of the electromagnetic wave and λ its wavelength (Leijnse et al., 2007).

Net radiation (R_{n}) was derived from incoming and outgoing short- and long-wave radiation measured using two CMP-21 Pyranometers and two CRG-4 Pyrgeometers (Kipp and Zonen), which were installed in a stand-alone configuration approximately 13 m

FIGURE 5.3: Optical scintillometers used. Right: Kipp. Left: Scintec.

north-east of the EC system and 2 m above the soil surface (Figure 5.1). Ground heat flux (G) was determined by combining measurements from soil heat flux plates (Hukseflux HFP01) buried at a depth of 7 cm, and soil temperature (PT-100 Soil Temperature Sensor) and moisture probes (TRIME-PICO 32) at 3 cm and 10 cm depth. Soil volumetric heat capacity, C_s, was calculated using a site specific linear regression (M. Lukowski, personal communication) derived from in-situ measurements which reads,

$$C_\mathrm{s} = 0.06\ \theta + 1.21, \tag{5.2}$$

where θ is the soil volumetric content. Equation 5.2 was derived using measurements of C_s, soil temperature and soil moisture from 95 samples across the Murrumbidgee catchment. Additionally, a weather station, which measured wind speed (u) and direction (2 m above ground, z_u), air temperature (T), pressure (P), humidity (Q) and precipitation, was installed next to the Scintec. Averages of these measurements were recorded every 10-min as well as the rainfall totals. All available data was averaged and synchronized over regular 30 minute intervals. Similarly, rainfall totals were aggregated over the 30

FIGURE 5.4: Relative location of scintillometer receivers to the EC tower.

minute intervals. This regular and synchronized dataset was then used to calculate H and $L_{\mathrm{v}}E$. The campaign period for this study was from the 23rd of November 2013 to the 18th of February 2014 (end of spring to summer in the southern hemisphere). The roughness length z_0 and the displacement height, d_0, were calculated as shown in Eq. C.9 using a vegetation height value, h_0, of 0.3 m.

5.2.3 Data analysis

Only daytime data (i.e. unstable conditions) were used in the analysis. Stable and unstable conditions were determined based on Monin-Obukhov length (L_{Ob} [m]) derived from the EC system. During a rainfall event, measurements taken between 30-min before and after the event were not considered. The time-window was selected to account for the distance between the scintillometers and the rain gauge, which can generate lags between times of precipitation at the locations of the rain gauge and scintillometers.

The surface heat fluxes derived from all sensors were averaged to 30-min. To compare H and $L_{\mathrm{v}}E$ derived from different sensors, an orthogonal regression was performed for each pair of sensors (x and y) to derive the slope and intercept of the line. Additionally,

FIGURE 5.5: Microwave scintillometers.

Root Mean Square Difference (RMSD), coefficient of determination (R^2) and bias ($\overline{x}-\overline{y}$) were also computed. The sensor specific processing steps that have been carried out are summarized in the following sections.

5.2.3.1 Eddy covariance

This data was processed using the software EddyPro (version 5.2.1) to obtain average fluxes at 30-min intervals. The corrections implemented in the analysis included spike detection and removal, lag correction relative to the vertical wind component based on covariance maximization method, linear de-trending, sonic virtual temperature correction, coordinate rotation using the planar fit method, spectral corrections for low and high pass filtering effects (Moncrieff et al., 2005) and the Webb-Pearman-Leuning correction (Webb et al., 1980).

5.2.3.2 Scintillometers

The method used to convert the scintillometer measurements to surface heat fluxes follows that of Leijnse et al. (2007) and is summarized in Appendix C. MWS systems are sensitive to both temperature and humidity fluctuations; the same measurement of C_{n}^2 can lead to two different values of β, and thus H and $L_{\mathrm{v}}E$ (Leijnse et al., 2007; Ward et al., 2015b). For common atmospheric conditions in temperate climates, one solution, β_1, is typically below 2.5 whereas the other, β_2, is larger than 2.5. The smaller β solution will be referred to as β_1, and the larger as β_2. Only the surface heat fluxes derived from β_1 are shown in the results as, for the majority of the time, β_2 was unrealistically large. However, it is important to be aware of the existence of β_2 as this will be referred to in the discussion section.

As Evans (2009) and Ward et al. (2015a) observed under and over-closure of energy balance based on measurements from the two-wavelength method, to ensure closure of the energy balance, β derived from the scintillation measurements were used to scale scintillometer derived fluxes proportionally up or down to meet the total available energy, $R_{\mathrm{n}} - G$. Analysis carried out by varying r_{TQ} between 0.8 and 1 showed that the performance of the scintillometers did not change substantially. For this reason, r_{TQ} was assumed to be 1 here. Details of the procedure used to derive H and $L_{\mathrm{v}}E$ from the two-wavelength method can also be found in Appendix C.

In addition to the 2 LAS and 4 MWS outputs, in the two-wavelength method, 8 possible combinations of LAS and MWS outputs have been used to derive surface heat fluxes, thereby yielding a total of 14 derived H and $L_{\mathrm{v}}E$ estimates from scintillometers at 30-min time-steps. To differentiate the results, subscripts are used to denote the scintillometer used to derive H or $L_{\mathrm{v}}E$ from stand-alone scintillometers according to 'K' (Kipp) or 'S' (Scintec) or frequency such as '26' (26 GHz) or '38' (38 MHz) followed by polarization 'h' (horizontal) and 'v' (vertical) for the MWS. For example, H derived from Kipp is annotated as H_{K}, and $L_{\mathrm{v}}E$ derived from the h-polarization of MW26 is referred to as $L_{\mathrm{v}}E_{26\mathrm{h}}$. For the two-wavelength method, the optical scintillometer used is denoted as the subscript and the MWS used as the superscript (e.g. $L_{\mathrm{v}}E_{\mathrm{K}}^{38\mathrm{v}}$).

5.3 Results and discussion

In general, H_{EC} was the dominant surface heat flux, whereas $L_{\mathrm{v}}E_{\mathrm{EC}}$ remained lower than 200 W m^{-2} for most of the study period. Low soil water availability during the study period was likely the cause of this (< 0.10 m^3 m^{-3} for most of the period). Moreover, vegetation at the site was visibly suffering water stress and soils were beginning to crack. Bowen ratio averaged approximately 4 throughout the study period based on measurements from the EC system, 2 based on LAS systems, varying from 0.4 to 1.5 based on β_1 and 5.5 to 20 for β_2 of MWS systems. In semi-arid environments, β is around 4 and can increase to around 15 (Beringer et al., 2007).

5.3.1 Energy balance closure of EC system

Consistent with the energy balance closure observed in many studies, the orthogonal regression for the energy balance of the EC system, calculated using 30-min averages, was found to have a slope of 0.79 and an intercept of 11.15 W m^{-2}, with an RMSD of 93.60 W m^{-2} (Figure 5.6). Possible causes for this may be attributed to errors in measurements of R_{n} and G, and in turbulent fluxes from the sonic anemometer, energy losses unaccounted for during stable conditions, advection and inadequate accounting of other storage terms (Foken, 2008; Leuning et al., 2012; Wilson et al., 2002). Additionally, as the soil moisture and soil parameters used to derive soil heat storage were from a single point, the estimated soil heat storage may not be representative of the study area. Errors in the computation of available energy will also affect the magnitude of surface heat fluxes derived from scintillometry.

5.3.2 Comparison between EC and scintillometers

5.3.2.1 Sensible heat

H values derived from the scintillometers were compared to H_{EC}. The results are presented in Figure 5.7 and Table 5.1. While H from the LAS systems were similar to H_{EC}, especially for lower values of H, a wider scatter was observed when H was larger than approximately 350 W m^{-2}. Regarding the MWS systems, this wider scatter as H increases is also apparent. Moreover, results from MW38 were closer to the EC system

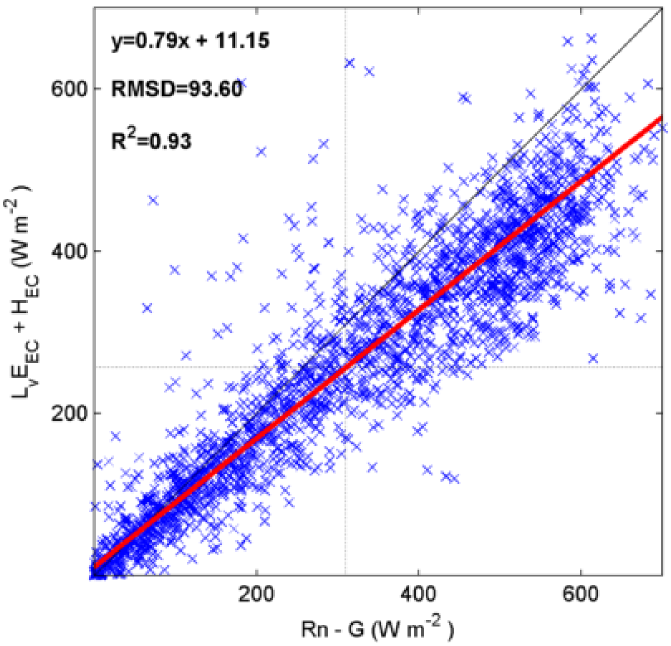

FIGURE 5.6: Energy balance closure of EC station. Solid black line: 1:1 line. Solid red line: fitted line from orthogonal regression. Dotted black lines: mean of $(R_\mathrm{n} - G)$ and $(L_\mathrm{v}E_\mathrm{EC} + H_\mathrm{EC})$.

than MW26. For instance, the slope for $H_{38\mathrm{h}}$ was 0.82 whereas the slope for $H_{26\mathrm{h}}$ was 0.79. As the MWS systems were installed at a lower height due to site restrictions, a portion of turbulent fluctuations may have been missed, thereby underestimating C_n^2. The performance of MWS improved when using the two-wavelength method.

Similarity theory adopted by scintillometry to enable the derivation of surface heat fluxes assumes that the turbulent transport of heat and water vapour is similar. However, the diffusivity of heat has been shown to be typically higher than water vapour in a semi-arid grassland (Alfieri et al., 2009). Furthermore, it is assumed here that the structure parameter of temperature and humidity are perfectly correlated ($r_{TQ} = 1$, in Eq. C.13), but lower values have been used in some studies (Lüdi et al., 2005). Ward et al. (2015b) have also shown that the choice of similarity function can alter daily ET by more than 15% - 20%, possibly leading to an underestimation of H from the LAS systems compared to that from the EC system. Moreover, studies have shown that uncertainty in h_0 can lead to inaccuracy in the derived fluxes (Evans and De Bruin, 2011; Hartogensis et al., 2003). In this study, h_0 was assumed to be constant. While the study area was flat, an inaccurate assignment of h_0 could impact the estimation of the heat fluxes, since $(z_\mathrm{s} - d_0)$ determines the scaling, and therefore the magnitude, of H and $L_\mathrm{v}E$ (Eq. C.10 and C.12). The above uncertainties likely explain systematic differences in Figure 5.7.

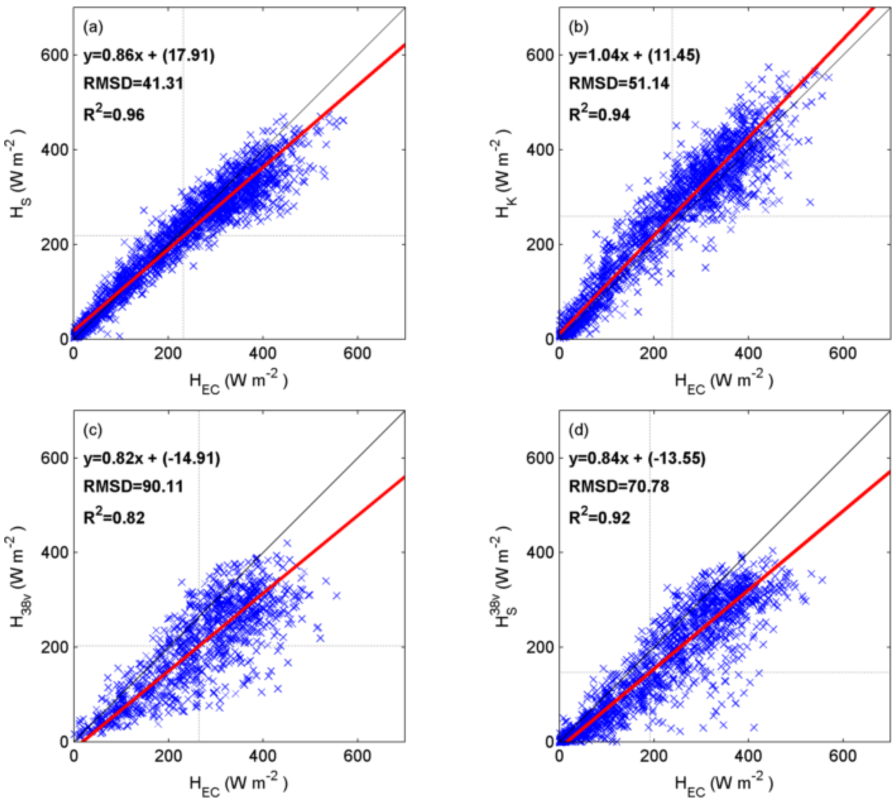

FIGURE 5.7: Comparison of H derived from a) Scintec, b) Kipp, c) $\mathrm{MW}_{38\mathrm{v}}$, and d) $\mathrm{MW}_{\mathrm{S}}^{38\mathrm{v}}$ with H measured by the EC system. Solid black line: 1:1 line. Solid red line: fitted line from orthogonal regression. Dotted black lines: mean H of each corresponding system.

5.3.2.2 Latent heat

Comparison between $L_\mathrm{v}E_\mathrm{EC}$ and $L_\mathrm{v}E$ from the scintillometers showed very low correlations (R^2 between 0.37 and 0.53) (Figure 5.8, left side). The derived slopes ranged from 3.19 to 4.44, thereby indicating that $L_\mathrm{v}E$ from the scintillometers were significantly higher than $L_\mathrm{v}E_\mathrm{EC}$. Since H between the EC system and scintillometers agreed well, the discrepancy between $L_\mathrm{v}E_\mathrm{EC}$ and $L_\mathrm{v}E$ from the scintillometers can be partly attributed to underestimation of $L_\mathrm{v}E_\mathrm{EC}$ as also observed by Ward et al. (2015a).

Since the non-turbulent portion of the energy balance can be measured with higher accuracy, the quality of the turbulent fluxes measured by the EC system and scintillometers can be improved if the energy budget is forced to close. This can be done in two ways: the ‘residual-LE closure’ method or ‘β closure’ method (Twine et al., 2000).

In the first method, it is assumed that H is accurately measured, and that the non-closure of the energy balance of the EC system comes from an underestimation of $L_\mathrm{v}E_\mathrm{EC}$.

Therefore, the energy budget was forced to close based on the estimate of $L_\mathrm{v}E_\mathrm{EC}$ derived as a residual from the energy balance (i.e., $L_\mathrm{v}E_\mathrm{EC}^\mathrm{Res} = R_\mathrm{n} - G - H_\mathrm{EC}$) (Figure 5.8). In the second method, assuming that β derived from the EC system is accurately measured, H and $L_\mathrm{v}E$ are adjusted to close the energy balance of the EC system using Eq. C.1 and C.2 (herein referred to as $H_{\beta\mathrm{EC}}$ and $L_\mathrm{v}E_{\beta\mathrm{EC}}$) (Figure 5.9).

In-comparison to $H_{\beta\mathrm{EC}}$ and $L_\mathrm{v}E_{\beta\mathrm{EC}}$, $L_\mathrm{v}E_\mathrm{EC}^\mathrm{Res}$ show better agreement with the scintillometers. Therefore, the non-closure of the energy balance of the EC system is more likely to come from underestimation of $L_\mathrm{v}E$. When $L_\mathrm{v}E_\mathrm{EC}^\mathrm{Res}$ was compared with the scintillometers, RMSD reduced to a third and R^2 quadrupled in some cases (Figure 5.8, right side). However, when $L_\mathrm{v}E$ was approximately less than 200 W m^{-2}, the MWS systems resulted in $L_\mathrm{v}E$ consistently larger than $L_\mathrm{v}E_\mathrm{EC}^\mathrm{Res}$. As mentioned earlier, the sensitivity of scintillometers reduce when β is above 2.5. Also, there are two possible solutions for β when solving for the stand-alone MWS systems. It was assumed in this study that β_1 was the correct solution. However, as β approaches 2.5 it becomes increasingly uncertain as to which β is more reliable. Moreover, the value of the two solutions get closer to each other as β_1 increases, thereby leading to the large scatter observed at low magnitudes of $L_\mathrm{v}E$ (higher β). In addition, r_{TQ} determines the relationship between C_n^2 and β (Eq. C.13). Therefore, the accuracy of the β solutions also depend on the accuracy of r_{TQ}. An inaccurate assumption of r_{TQ} would further contribute to the mismatch between heat fluxes derived from the EC system and standalone MWS systems. These field observations agree with the deductions made by Leijnse et al. (2007) regarding the effect that assumptions of r_{TQ} will have towards derived surface heat fluxes. To enable the use of a stand-alone MWS in semi-arid environments, further studies will need to be conducted.

When additional information is provided to the system of equations, β is no longer a non-unique solution. In this case, scintillometer derived $L_\mathrm{v}E$ resulted more similar to $L_\mathrm{v}E_\mathrm{EC}^\mathrm{Res}$ with correlations increasing to between 0.77 and 0.82 and slopes of 0.92 to 1.04 (Table 5.2). A comparison of β derived from the scintillometers and the EC system also showed a diminishing correlation as β approached 2.5 for the MWS systems, whereas correlations with the LAS systems were significantly higher (not shown here). Finally, it cannot be dismissed that the accuracy of the derived surface heat fluxes from the scintillometers are highly dependent on the accuracy of measurements of R_n and G, as the remaining available energy is partitioned into H and $L_{\mathrm{v}}E$ based on β derived from scintillometer measurements.

In this study, while the two-wavelength method performed comparably well, it can be said that the standalone LAS still performs the best when compared with EC for both $L_{\mathrm{v}}E$ and H without the MWS.

5.3.3 Scintillometer inter-comparison

Here we compare i) H from stand-alone LAS from different manufacturers, ii) $L_{\mathrm{v}}E$ from stand-alone MWS of the same frequencies but different polarization, iii) MWS of two different frequencies, and iv) both H and $L_{\mathrm{v}}E$ from the stand-alone methods with the two-wavelength method.

It can be seen in Figure 5.10 that the correlation between H derived from the two LAS systems was high, 0.98, with an RMSD of 49.06 W m^{-2}. However, H_{S} was approximately 20% lower than H_{K} (bias of -37.80 W m^{-2}), which is consistent with results from previous studies (e.g. Kleissl et al., 2009b; Solignac et al., 2012; Van Kesteren et al., 2015). They attributed these differences to absorption, and electronic and optical problems of the scintillometers. To reduce the effect of absorption, as in Solignac et al. (2012), the BLS900 from Scintec is recommended due to its ability to correct for absorption based on its dual beam configuration (two different pulse coding frequencies are used). On the other hand, Van Kesteren et al. (2015) found that the equations applied by Scintec to determine 1) the variance of the logarithmically transformed I, $\sigma^2_{\ln(I)}$, and 2) covariance of I from a time series, results in an underestimation when saturation occurs. A comparison of C_{n}^2 derived from both Kipp and Scintec on a linear scale showed an increasing deviation between the two scintillometers as C_{n}^2 increases (similar to Fig. 1 of Van Kesteren et al., 2015). Corresponding to this, the bias between H_{S} and H_{K} or H_{EC} is also seen to increase with increasing H (Figure 5.7 and 5.10).

In comparing the two different polarization of MW26 and MW38, H derived from v-polarization of both MW26 or MW38 were found to be higher than those of their corresponding h-polarization. The higher H derived from v-polarization may indicate that the majority of the scintillations detected by the MWS occur in the vertical direction.

TABLE 5.1: Statistics derived from orthogonal regression of H.

Sensor 1 (x)	Sensor 2 (y)	Slope	Intercept	RMSD	R^2	Bias
H_S	H_K	1.20	-6.55	49.06	0.98	-37.80
	H_{38v}	0.99	-43.83	76.76	0.79	45.10
	H_{38h}	0.99	-39.01	73.77	0.81	42.61
	H_{26v}	1.08	-48.70	67.52	0.82	29.42
	H_{26h}	1.03	-68.68	91.03	0.70	61.18
	H^{38v}	0.96	-26.09	57.75	0.91	33.87
	H_S^{38h}	0.96	-23.62	55.68	0.92	31.63
	H_S^{26v}	1.02	-28.47	55.06	0.91	23.94
	H_S^{26h}	0.96	-38.16	71.26	0.89	47.95
	H_K^{38v}	0.99	-25.43	54.24	0.92	27.27
	H_K^{38h}	0.99	-22.98	52.36	0.92	25.11
	H_K^{26v}	1.04	-27.41	52.96	0.91	18.42
	H_K^{26h}	0.98	-37.51	66.76	0.90	41.19
H_{38v}	H_{38h}	0.99	5.51	12.11	0.99	-3.43
	H_{26v}	1.08	7.41	36.29	0.96	-23.74
	H_{26h}	1.06	-28.96	38.36	0.91	14.31
	H_K	1.28	22.20	105.36	0.82	-82.56
	H_S^{38v}	0.96	24.01	23.40	0.98	-15.42
	H_S^{38h}	0.96	25.90	26.83	0.98	-17.32
	H_S^{26v}	1.06	19.19	42.26	0.96	-30.53
	H_S^{26h}	1.02	-0.52	31.32	0.95	-3.49
	H_K^{38v}	0.98	26.22	29.69	0.98	-22.87
	H_K^{38h}	0.98	28.04	32.53	0.98	-24.67
	H_K^{26v}	1.08	21.48	47.49	0.96	-36.85
	H_K^{26h}	1.05	2.29	33.39	0.95	-11.42
H_S^{38v}	H_S^{38h}	1.00	1.60	6.88	1.00	-1.97
	H_S^{26v}	1.07	0.28	22.25	0.99	-11.14
	H_S^{26h}	0.99	-8.16	24.29	0.98	9.03
	H_K^{38v}	1.03	1.01	7.72	1.00	-5.38
	H_K^{38h}	1.03	2.58	10.96	1.00	-7.28
	H_K^{26v}	1.10	1.47	25.92	0.99	-15.77
	H_K^{26h}	1.03	-7.05	22.60	0.98	3.40
H_{EC}	H_S	0.86	17.91	41.31	0.96	13.67
	H_K	1.04	11.45	51.14	0.94	-20.38
	H_{38v}	0.82	-14.91	90.11	0.82	61.92
	H_{38h}	0.82	-13.44	86.61	0.84	58.61
	H_{26v}	0.90	-23.64	81.97	0.83	50.02
	H_{26h}	0.79	-23.61	109.84	0.74	83.52
	H_S^{38v}	0.84	-13.55	70.78	0.92	44.84
	H_S^{38h}	0.84	-12.05	69.05	0.93	42.90
	H_S^{26v}	0.88	-14.70	67.21	0.92	38.72
	H_S^{26h}	0.80	-19.91	84.43	0.91	58.70
	H_K^{38v}	0.86	-13.35	67.02	0.92	39.46
	H_K^{38h}	0.87	-11.85	65.39	0.93	37.59
	H_K^{26v}	0.90	-14.22	64.34	0.92	34.19
	H_K^{26h}	0.83	-19.66	79.91	0.91	53.18

As the horizontal and vertical components are subjected to different boundary conditions due to the low measurement height of the MWS systems, the differences observed in measurements from h- and v- polarizations may be caused by the outer scale effect. Turbulent eddies which are longer than the outer scale (often approximated as the measurement height) are no longer isotropic. Further studies will be required to explore the cause for these differences.

Comparisons of surface heat fluxes derived from the MWS of different frequencies showed that $L_{\mathrm{v}}E$ was the lowest for MW26v, followed by MW38h, MW38v and MW26h in increasing order (Figure 5.11). Additionally, agreement between derived fluxes from MW26v and MW38v was better than that between MW26v and MW26h. The results are non-conclusive and may be related to several reasons including MW26 being more prone to absorption (Nieveen and Green, 1999). The wavelength selection is important because of its effect on the estimation of fluxes. The Fresnel zone, which is a function of wavelength, affects the requirements on the minimum measurement height. Moreover, while scintillometers with longer wavelengths (MW26) may cost less, they are less sensitive to scintillation (Eq. 5.1) and more prone to water vapour absorption; this would have a greater effect on the data quality of MW26 than MW38 depending on the environment.

Comparisons of the resultant surface heat fluxes derived from the stand-alone method and the two-wavelength method provided an insight in the robustness of the iteration and minimization procedure applied in this study to solve for β of the standalone MWS. In comparison, the stand-alone MWS and two-wavelength method were more comparable, thereby demonstrating that a stand-alone MWS combined with the energy balance equation is able to solve for the same β as the two-wavelength method. However, referring to section 5.3.2.1 and 5.3.2.2, the stand-alone LAS performed better in comparison to the standalone MWS and two-wavelength method.

Evans et al. (2010) have shown that r_{TQ} is important for an accurate derivation of $L_{\mathrm{v}}E$ for the two-wavelength method, while Wesely (1976) and Leijnse et al. (2007) have shown that uncertainties in r_{TQ} can cause large errors in the derived fluxes for dry conditions. Similarly, it can be observed that differences in H from a stand-alone LAS and the two-wavelength method increases with increasing magnitude of H. Therefore, despite the agreement between the stand-alone MWS and the two-wavelength method, a combination of dry conditions and the adopted value of r_{TQ} here may have contributed to the inaccuracy in the H and $L_{\mathrm{v}}E$ derived from these systems. Although using the bichormatic correlation method may help to improve the results here, the reduced sensitivity of scintillometers at high β may be a bigger issue (Ward et al., 2015a).

TABLE 5.2: Statistics derived from orthogonal regression of L_vE.

Sensor 1 (x)	Sensor 2 (y)	Slope	Intercept	RMSD	R^2	Bias
L_vE_S	L_vE_K	0.88	-20.60	49.06	0.93	37.80
	L_vE_{38v}	0.89	69.83	88.83	0.65	-53.77
	L_vE_{38h}	0.90	65.61	85.46	0.67	-50.86
	L_vE_{26v}	0.75	69.97	76.60	0.64	-35.78
	L_vE_{26h}	0.86	96.79	109.38	0.50	-74.97
	$L_vE_S^{38v}$	0.88	50.24	57.75	0.85	-33.87
	$L_vE_S^{38h}$	0.87	48.47	55.68	0.86	-31.63
	$L_vE_S^{26v}$	0.80	49.68	55.06	0.83	-23.94
	$L_vE_S^{26h}$	0.93	57.28	71.26	0.81	-47.95
	$L_vE_K^{38v}$	0.84	48.29	54.24	0.85	-27.27
	$L_vE_K^{38h}$	0.84	46.71	52.36	0.86	-25.11
	$L_vE_K^{26v}$	0.77	47.91	52.96	0.83	-18.42
	$L_vE_K^{26h}$	0.89	55.34	66.76	0.81	-41.19
L_vE_{38v}	L_vE_{38h}	0.99	-3.76	18.54	0.98	4.99
	L_vE_{26v}	0.81	11.26	47.00	0.87	26.11
	L_vE_{26h}	0.95	28.99	51.78	0.78	-17.86
	L_vE_K	0.84	-55.93	113.38	0.56	87.12
	$L_vE_S^{38v}$	0.91	-5.77	38.82	0.92	22.83
	$L_vE_S^{38h}$	0.91	-7.57	41.43	0.91	24.97
	$L_vE_S^{26v}$	0.77	6.56	55.91	0.87	38.10
	$L_vE_S^{26h}$	0.90	7.91	43.38	0.86	12.09
	$L_vE_K^{38v}$	0.87	-5.18	43.71	0.92	29.98
	$L_vE_K^{38h}$	0.87	-6.55	46.57	0.91	32.04
	$L_vE_K^{26v}$	0.74	7.11	60.86	0.87	44.22
	$L_vE_K^{26h}$	0.86	8.25	46.40	0.86	19.64
$L_vE_S^{38v}$	$L_vE_S^{38h}$	0.99	-0.92	6.88	1.00	1.97
	$L_vE_S^{26v}$	0.91	1.48	22.25	0.98	11.14
	$L_vE_S^{26h}$	1.04	3.52	24.29	0.97	-9.03
	$L_vE_K^{38v}$	0.96	-0.32	7.72	1.00	5.38
	$L_vE_K^{38h}$	0.96	-1.09	10.96	1.00	7.28
	$L_vE_K^{26v}$	0.88	1.00	25.92	0.98	15.77
	$L_vE_K^{26h}$	1.00	3.09	22.60	0.97	-3.40
$L_vE_{EC}^{Res}$	L_vE_S	1.16	-5.88	40.76	0.90	-12.94
	L_vE_K	1.00	-21.82	50.58	0.83	22.09
	L_vE_{38v}	1.07	57.41	96.32	0.62	-66.92
	L_vE_{38h}	1.08	53.59	93.68	0.64	-63.89
	L_vE_{26v}	0.89	65.88	86.55	0.57	-52.75
	L_vE_{26h}	1.10	80.02	122.27	0.44	-92.92
	$L_vE_S^{38v}$	1.05	38.36	66.47	0.81	-43.42
	$L_vE_S^{38h}$	1.04	37.05	64.40	0.82	-41.25
	$L_vE_S^{26v}$	0.96	41.54	63.49	0.78	-36.59
	$L_vE_S^{26h}$	1.13	45.59	82.94	0.77	-59.61
	$L_vE_K^{38v}$	1.00	37.25	61.81	0.82	-37.11
	$L_vE_K^{38h}$	0.99	35.99	60.03	0.82	-35.02
	$L_vE_K^{26v}$	0.92	40.26	60.12	0.78	-31.26
	$L_vE_K^{26h}$	1.08	44.31	77.69	0.76	-53.12

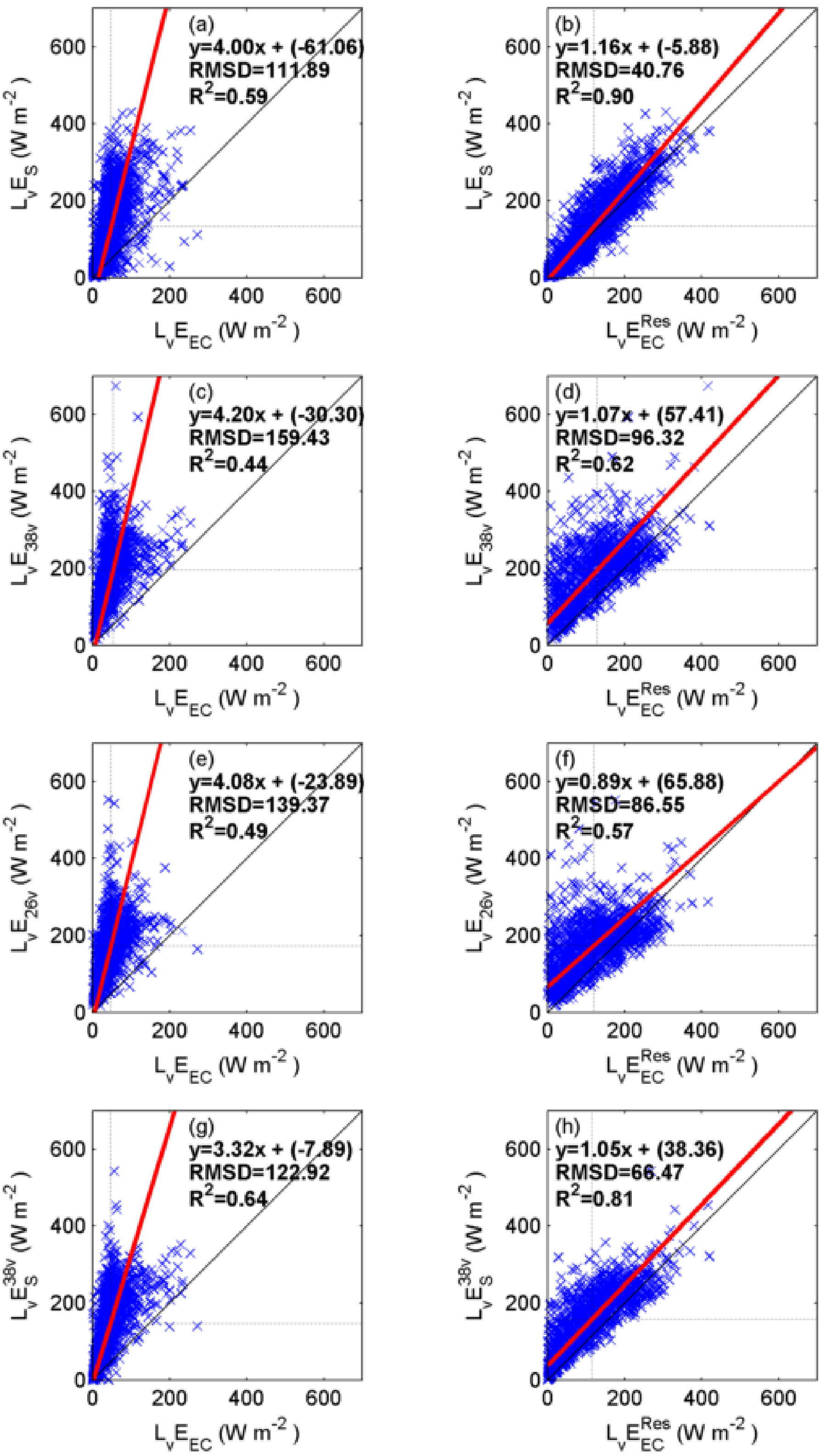

FIGURE 5.8: Comparison of L_vE from (a) , (b): Scintec; (c), (d): MW38v; (e), (f) MW26v and (g), (h): $\mathrm{MW}_\mathrm{S}^{38v}$ with L_vE_{EC} (left column) and $L_vE_{\mathrm{EC}}^{\mathrm{Res}}$ (right column). Solid black line: 1:1 line. Solid red line: fitted line from orthogonal regression. Dotted black lines: mean L_vE of each corresponding system.

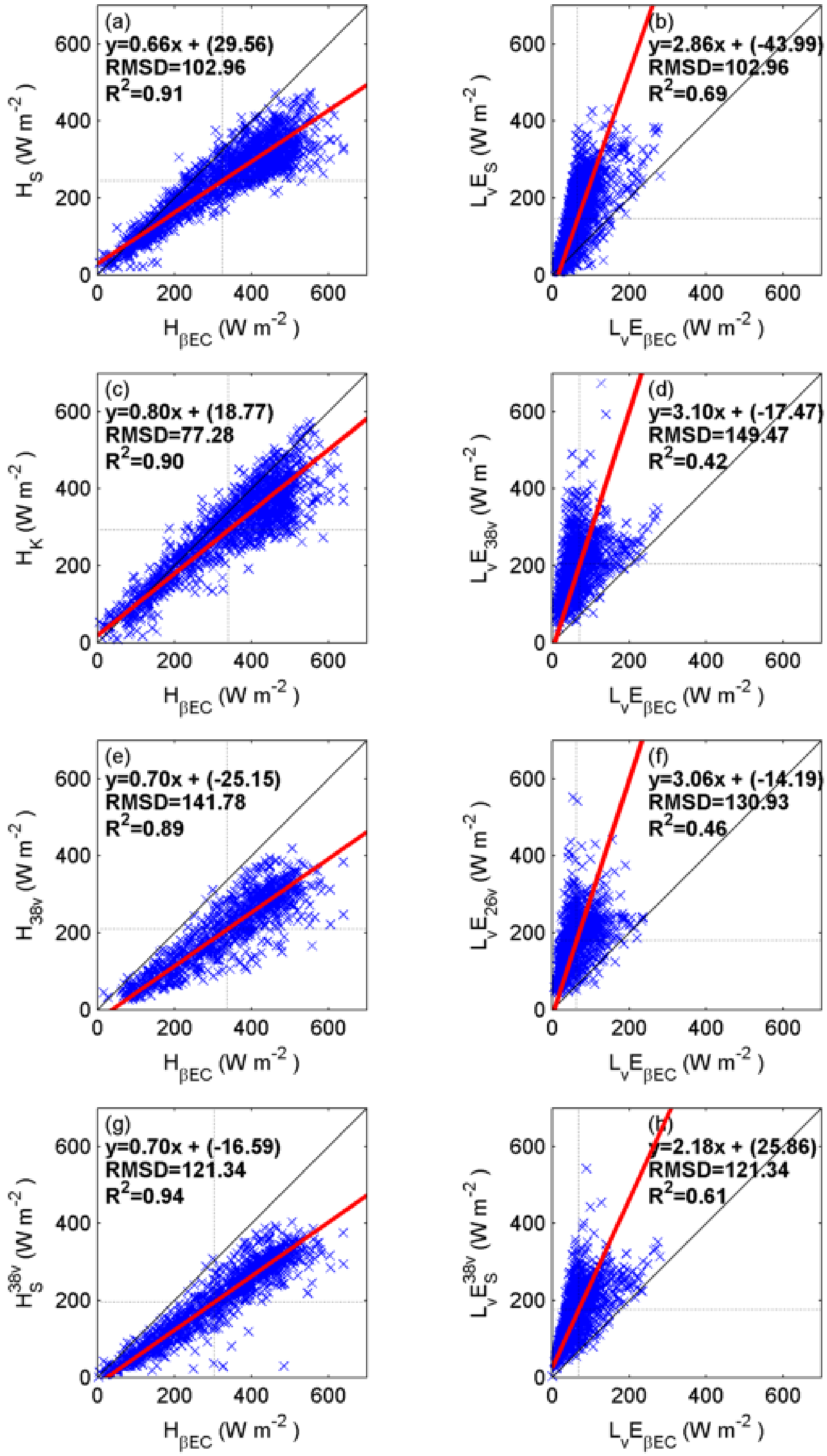

FIGURE 5.9: Comparison of $H_{\beta\mathrm{EC}}$ (left column) and $L_\mathrm{v}E_{\beta\mathrm{EC}}$ (right column) where (a) $H_{\beta\mathrm{EC}}$ vs H_S; (b): $L_\mathrm{v}E_{\beta\mathrm{EC}}$ vs $L_\mathrm{v}E_\mathrm{S}$; (c) $H_{\beta\mathrm{EC}}$ vs H_K (d): $L_\mathrm{v}E_{\beta\mathrm{EC}}$ vs $H_{38\mathrm{v}}$; (e) $H_{\beta\mathrm{EC}}$ vs $H_{38\mathrm{v}}$; (f) $L_\mathrm{v}E_{\beta\mathrm{EC}}$ vs $L_\mathrm{v}E_{26\mathrm{v}}$ (g) $H_{\beta\mathrm{EC}}$ vs $H_\mathrm{S}^{38\mathrm{v}}$; and (h): $L_\mathrm{v}E_{\beta\mathrm{EC}}$ vs $L_\mathrm{v}E_\mathrm{S}^{38\mathrm{v}}$. Solid black line: 1:1 line. Solid red line: fitted line from orthogonal regression. Dotted black lines: mean $L_\mathrm{v}E$ of each corresponding system.

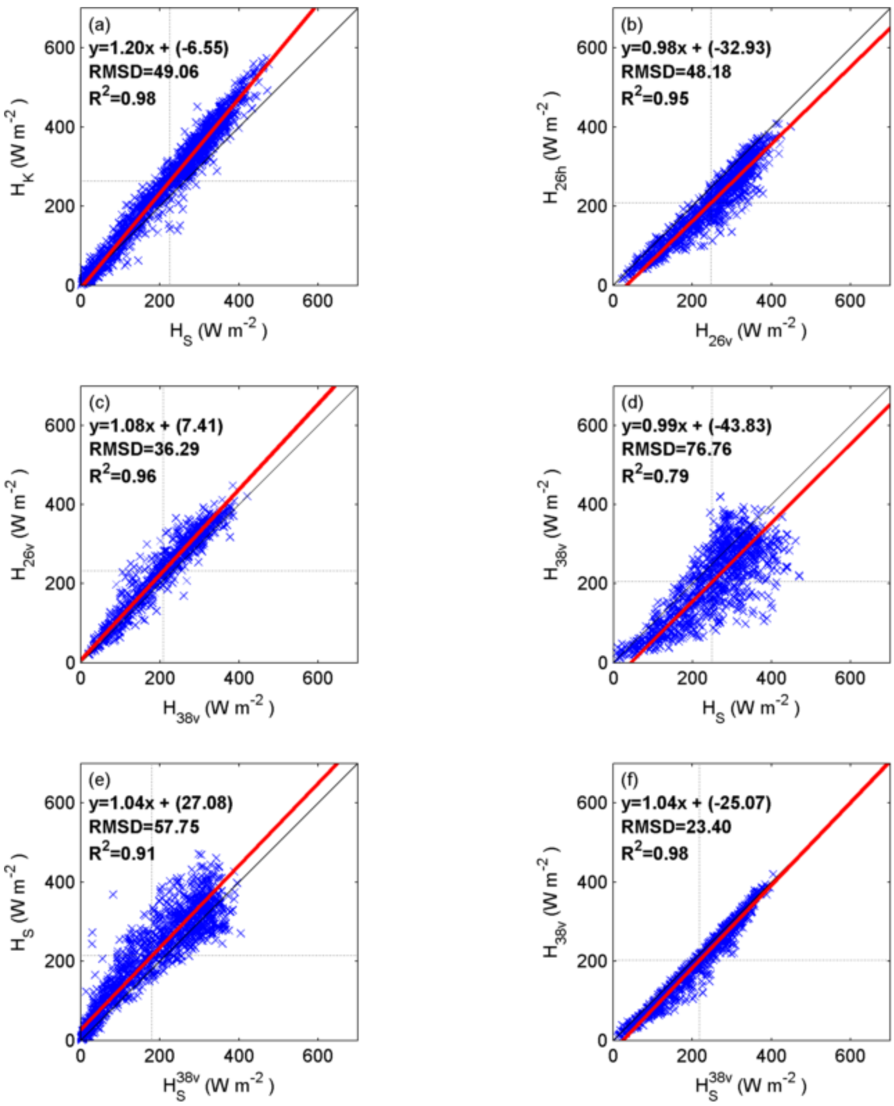

FIGURE 5.10: Comparison of H derived from a) Scintec and Kipp; b) MW26v and MW26h; c) MW38v and MW26v; d) Scintec and MW38v; e) Scintec - MW38v and Scintec; and f) Scintec - MW38v and MW38v. Solid black line: 1:1 line. Solid red line: fitted line from orthogonal regression. Dotted black lines: mean H of each corresponding system.

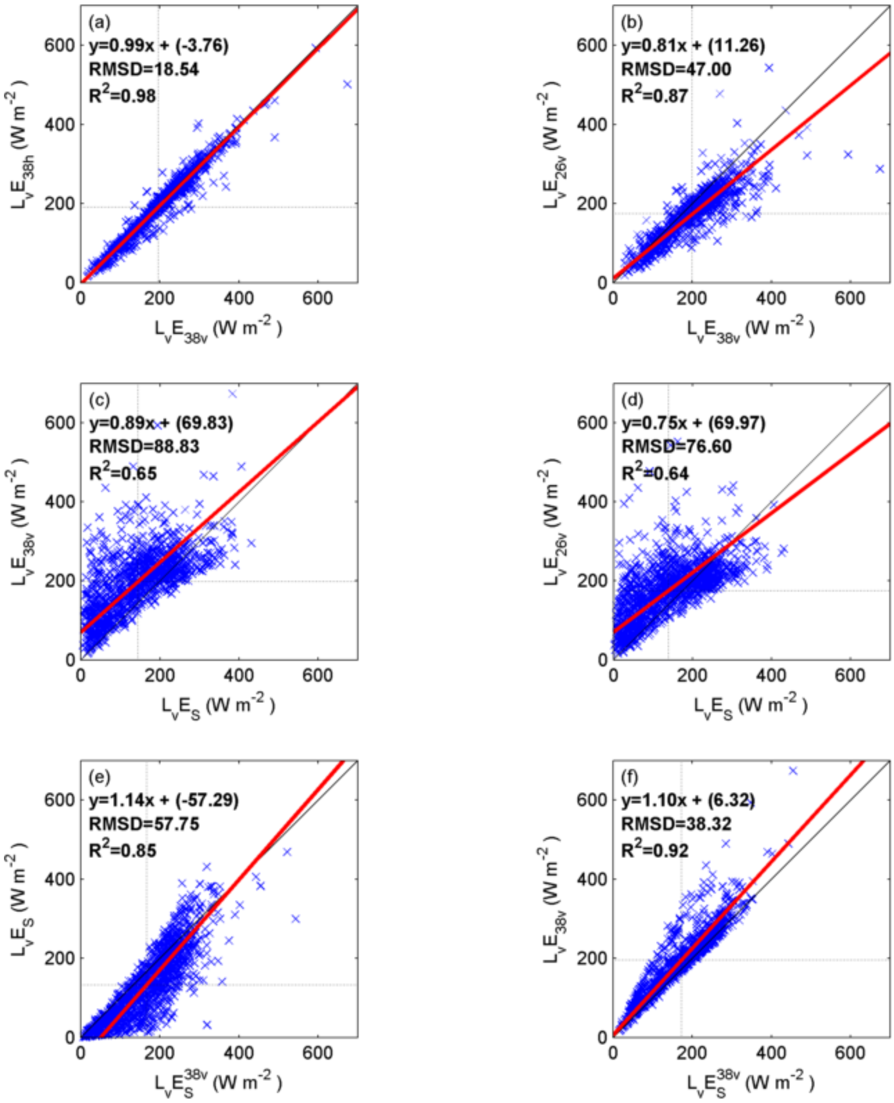

FIGURE 5.11: Comparison of L_vE derived from a) MW38v and MW38h; b)MW38v and MW26v; c) Scintec and MW38v; d) Scintec and MW26v; e) Scintec - MW38v and Scintec; and f) Scintec - MW38v and MW38v. Solid black line: 1:1 line. Solid red line: fitted line from orthogonal regression. Dotted black lines: mean L_vE of each corresponding system.

5.4 Key findings

This study compared measurements of surface heat fluxes using an EC system, two LAS systems from two different manufacturers, and two MWS systems at different frequencies and polarizations including the use of the two-wavelength method. A large discrepancy between $L_{\mathrm{v}}E_{\mathrm{EC}}$ and $L_{\mathrm{v}}E$ from the scintillometers was suspected to be attributed to an underestimation of $L_{\mathrm{v}}E$ by the EC system. Therefore, $L_{\mathrm{v}}E_{\mathrm{EC}}$ was corrected by forcing the energy budget to close based on the ‘ residual-LE closure method$'$. Based on the results of this study, it is hypothesized that differences in H and $L_{\mathrm{v}}E$ are caused by differences in the theoretical principles of the methods, and uncertainty in parameters such as r_{TQ}, z_{s}, and h_0. Nevertheless, a stand-alone LAS combined with an energy budget constraint has been shown to be sufficient to derive both H and $L_{\mathrm{v}}E$ with an acceptable accuracy in a semi-arid environment.

In the case of the MWS systems and the two-wavelength method, assumptions made regarding r_{TQ} were possibly the main cause for differences with the EC system. For a stand-alone MWS, this uncertainty increased with increasing β due to the non-unique solution in β.

This study also compared the different types of scintillometers against each other. Whilst the Scintec BLS900 is recommended for use over the Kipp and Zonen LAS due to its in-built ability to correct for absorption, the difference between the two LAS were small (R^2: 0.93, RMSD: 49.06 W m^{-2}). Likewise,the two MWS of different frequencies agreed with an R^2 of 0.87, and RMSD of 47.00 W m^{-2}. Slight differences may be attributed to outer scale effect as a result of low measurement heights.

Consequently, although the stand-alone LAS agrees the most with the EC system as opposed to the two-wavelength method and stand-alone MWS method due to differences in their sensitivities at different site conditions (Ward et al., 2015b), when similar methods are compared, derived fluxes still agree well.

5.5 Chapter summary

Measurements derived from EC systems are the most common method used for validating remote sensing surface flux products. However, the footprint of EC systems changes with meteorological conditions thereby deeming its representativeness of satellite pixels questionable. Scintillometers are able to measure path integrated fluxes ranging from a few hundred meters to 10 km. Yet, performances of MWS systems and the two-wavelength method have not previously been verified in semi-arid environments. Therefore, the work presented in this chapter inter-compared surface heat fluxes measurement derived from an EC system, two LAS systems from two different manufacturers, and two MWS systems at different frequencies and polarizations and the two-wavelength method. Differences in theoretical principles and uncertainty in parameters such as r_{TQ}, z_{s}, and h_0 were found to cause discrepancies in derived measurements. Despite this, the two stand-alone LAS were shown to compare well with the EC system and the two MWS agreed well with each other. Consequently, the scintillometers can be used to evaluate the representativeness of measurements from the EC system of a MTSAT 4 km ET product grid over the long-term in the following chapter (Chapter 6).

Chapter 6

Validation of MTSAT-1R evapotranspiration product with eddy covariance systems

This chapter evaluates the representativeness of evapotranspiration (ET) measurements derived from the eddy covariance (EC) system using surface heat fluxes derived from the LAS and MWS scintillometers evaluated in Chapter 5. In a stand-alone configuration, the four scintillometers were placed within different locations of a single 4 km $\times$ 4 km Multi-functional Transport SATellites (MTSAT) pixel during a field campaign which lasted approximately 9 months. The derived surface heat fluxes were then compared with those from the EC system to establish its representativeness. Subsequently, MTSAT ET products based on the Surface Energy Balance System (SEBS), the three-source Penman-Monteith model (PM-Mu), and a modified Priestley-Taylor model (PT-JPL) were validated using measurements from the EC system. To prolong the length of record used to validate the model, EC measurements from two separate field campaigns were included.

6.1 Introduction

As ET (or latent heat flux, $L_{\mathrm{v}}E$) is a significant component of the water and energy balance linking the land surface and the atmosphere, the ability to quantify both its spatial and temporal variability is important for applications in agriculture, climate modelling, weather forecasting and water resource management (Brunsell et al., 2011). *In situ* methods for measuring surface heat fluxes such as Bowen ratio systems, lysimeters, sapflow measurements or eddy covariance (EC) systems have been widely used (Gash and Shuttleworth, 2007). However, these methods only measure surface fluxes at a point scale, or up to several hundred square meters with large scale measurements being limited to field experimental sites. Nevertheless, significant progress in satellite observations of physical variables such as surface temperature, soil moisture and vegetation have enabled the retrieval of consistent and spatially distributed measurements of surface heat flux at regional to global scales without the issues inherent to field measurements.

Approaches used to derive actual ET consist of surface energy balance models, combination models, complementary models and radiation-based models (Brutsaert, 2005; Ershadi et al., 2014; Vinukollu et al., 2011). The formulation of these models are centered around the transfer of water vapour and sensible heat (H) from a land surface to the atmosphere as described by the Monin-Obukhov similarity theory (MOST) (Monin and Obukhov, 1954). In this chapter, the focus is on the validation of three such models; a surface energy balance approach (Surface Energy Balance System; SEBS, Su, 2002), a combination-type method (the three-source Penman-Monteith model; PM-Mu developed by Mu et al., 2011), and a radiation-based technique (the modified Priestley-Taylor model; PT-JPL, Fisher et al., 2008). In a recent validation of these models using surface flux observations from forty-five globally distributed eddy covariance towers, PT-JPL was found to have the best performance, with a coefficient of determination, R^2, of 0.72 and RMSD of 0.65, whereas SEBS was found to overestimate by 101 W m^{-2}, and PM-Mu was found to underestimate by 78 W m^{-2} (McCabe et al., 2015). Whilst these different ET models have been shown to work well in different areas, the performance of each model differs according to the region and climatic conditions in which it is applied, and the data used to drive the model. Therefore, there is a need to extensively validate these ET models using long-term *in situ* measurements that are known to be representative of the areal average ET so that users are aware of the accuracy of each ET product.

This chapter validates the MTSAT ET products of Ershadi et al. (2014) and McCabe et al. (2015) based on the SEBS, PM-Mu and PT-JPL models. As this product utilizes observations from the MTSAT geostationary satellite, it is gridded according to the

MTSAT 4 km pixels and is available at hourly time-scales. The most popular approach adopted to validate remote sensing surface heat fluxes is based on the eddy covariance (EC) method (Kaimal and Finnigan, 1994), with EC systems deployed globally through the FLUXNET network (Baldocchi et al., 2001; El Maayar et al., 2008). However, two of the inherent problems of satellite validation with EC systems are i) the differences in spatial scale of the EC system's footprint and the scale which is sensed by the space borne sensor, and ii) the inability of EC systems to close the energy balance. As the footprint of EC systems changes with meteorological conditions, its representativeness of coarse scale satellite products, particularly in a heterogeneous landscape, is debatable (Ward et al., 2014). To understand the representativeness of the surface flux measured using *in situ* techniques or aircraft measurements for the purpose of validating pixels of remote sensing products, studies have combined footprint analyses with remotely sensed vegetation indices or thermal properties of the land surface (e.g. Barcza et al., 2009; Chen et al., 2009, 2012; Hoedjes et al., 2007; Kim et al., 2006; Ogunjemiyo et al., 2003; Prueger et al., 2005; Su et al., 2005). However, the relationship between these remotely sensed surface variables and surface fluxes are not linear, and variability of these surface properties vary with scale (Brunsell and Gillies, 2003a,b; Li et al., 2008). Therefore, there is still a need for advancement in obtaining measurements which are accurate and representative of the satellite pixel (Bai et al., 2015).

Scintillometry presents an alternative method to measure path integrated fluxes ranging from a few hundred meters to 10 km, i.e. equivalent to a satellite pixel (Baghdadi et al., 2007; Beyrich et al., 2002; Meijninger and De Bruin, 2000; Samain et al., 2012b). They have been shown to perform well in the estimation of surface heat fluxes over different types of landscapes (e.g. Brunsell et al., 2011; Chehbouni et al., 2000; Ezzahar et al., 2009; Lagouarde et al., 2002; Liu et al., 2013; McJannet et al., 2011; Pauwels et al., 2008; Samain et al., 2012a, 2011; Savage, 2009; Yee et al., 2015; Zeweldi et al., 2010), including open water and urban areas (Lagouarde et al., 2006; McJannet et al., 2013; Samain et al., 2011; Ward et al., 2013). However, one of the factors which affects the distance at which scintillometers can measure integrated fluxes is the height in which the scintillometers are installed. To extend the distance measured by scintillometers, these scintillometers can be placed on towers or across valleys in urban and mountainous areas. In spite of this, in areas which are flat and where population density is low such as Australia, the distance which can be measured by scintillometers are constrained by resources available to place these scintillometers on a higher ground or towers. Consequently, although scintillometry presents an alternative to measuring area averaged surface heat fluxes equivalent to a satellite pixel, its operation and interpretation of its measurements is complex. Therefore, considering the availability of EC measurements globally, it is desirable for EC systems to continue to be used for the long-term validation of satellite retrieved surface heat flux products.

This study attempts to validate remote sensing ET products by combining the strength of EC systems (i.e. more established and available method) and scintillometry (i.e. area averaged and consistent with satellite pixel). The focus of this study is firstly to understand how well the measurements derived from EC systems truly represent fluxes observed by the space-borne sensors (regional) in the study area. The hypothesis is that the study area is ideal due to its homogeneity, such that measurements from the EC tower are similar to fluxes within a satellite pixel and thus, its measurements can be used for long-term validation of remotely sensed surface flux products. To verify the homogeneity of the site, a field campaign was carried out whereby four scintillometers were placed across different locations within a single satellite pixel where an EC system has been established. If the location of the EC system is representative of the satellite pixel, regardless of the wind-direction, and therefore footprint of the scintillometers or EC tower, differences between the scintillometers and EC tower should be within the order of magnitude of errors associated with differences in measurement techniques (i.e. according to the results in Chapter 5). Following this, hourly 4 km resolution actual ET products based on SEBS, PM-Mu and PT-JPL were validated using measurements from the EC system.

6.2 Site description and field measurements

The satellite pixel of interest is located within the Yanco Study Area which has been described in the previous chapters (Fig. 6.1, top left pixel). It is situated within the center of the Murrumbidgee River catchment, in New South Wales, Australia (Smith et al., 2012). The dominant wind directions are from the south-west and north-east (Fig. 6.2). Soil at the site is sand over clay (loamy sand) which has a typical porosity of about 0.30 m^3 m^{-3} (Hornbuckle et al., 1999; Smith et al., 2012).

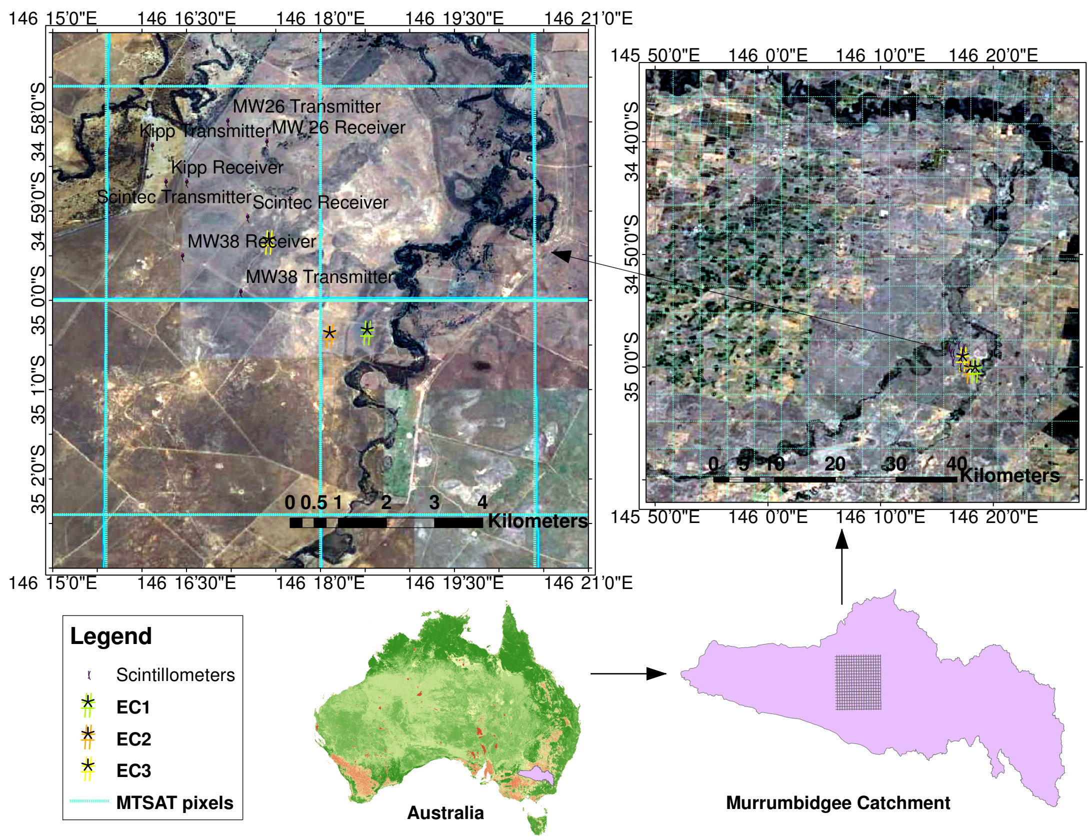

FIGURE 6.1: Top left: Location of EC stations (EC1, EC2 and EC3) and scintillometers within the satellite pixel of interest and adjacent pixels. Top right: Yanco study area overlaid with 4 km MTSAT pixels.

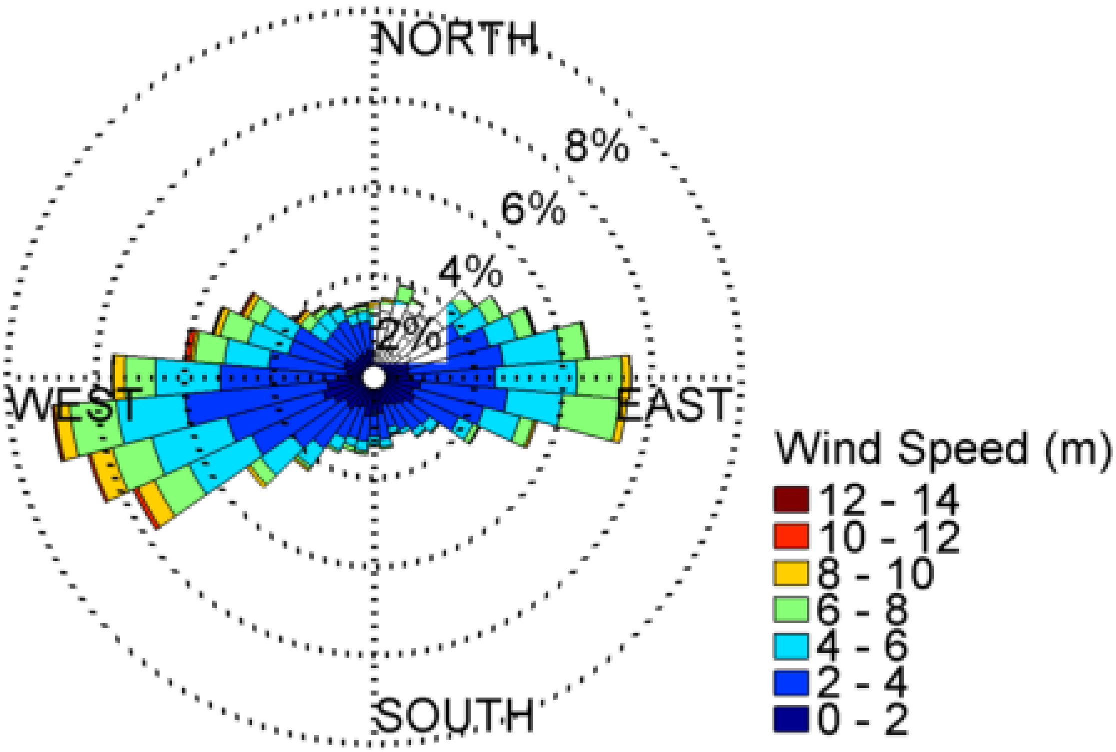

FIGURE 6.2: Windrose showing wind direction and speeds during experimental period.

6.3 Methodology and Data

6.3.1 Methodology

Scintillometers were placed in different locations within the 4 km × 4 km MTSAT pixel as shown in Fig. 6.1. Measurements from the scintillometers were then compared with those from the EC systems to understand how representative the tower is of the entire pixel. On the basis that this location is representative, and therefore ideal for satellite product validation due to its homogeneity, remotely sensed ET products at that pixel were validated against EC measurements. However, as the EC system was only commissioned in May 2012 (from this point onwards referred to as EC3), and the remote sensing ET products available to this study only extended up to May 2013, the length of EC record used to validate the ET product was extended by using measurements from EC stations set up close to EC3; from the 21st of November 2009 to the 20th of October 2010, and from the 2nd of May 2011 to the 11th of April 2012 (from this point onwards referred to as EC1 and EC2 respectively). EC1 and EC2 were located ∼100 m and ∼730 m south-west of EC3 respectively (Fig. 6.1).

6.3.2 Scintillometer measurements

Optical scintillometers of two different manufacturers, Kipp and Zonen and Scintec (herein referred to as Kipp and Scintec, respectively), two microwave scintillometers (MWS) with a frequency, f, of 26 GHz and 38 GHz (herein referred to as MW26 and MW38, respectively) and two polarizations (horizontal, h and vertical, v) were used to measure latent heat flux in this study. These are the same pairs of scintillometers used in the Chapter 5. Due to instrument maintenance, Kipp and MW26 were installed on the 21st of September 2014 whereas MW38 was installed on the 21st of December 2014, and Scintec on the 6th of February 2015. Therefore, the data which has been used for this study was from the 21st of September 2014 (start of spring) up to the 15th June 2015 (start of winter). The locations in which each scintillometer pair were located are shown in Fig. 6.1. Location, height, measurement periods and distances of the scintillometer receivers from their transmitters are also summarized in Table 6.1. The steps which were taken to derive the surface heat fluxes are similar to that in Chapter 5.

TABLE 6.1: ET datasets used where start and end indicates the period used in this study. T: Transmitter. R: Receiver.

Name	**T/R?**	**Lat (°)**	**Lon (°)**	**Distance (m)**	**Height (m)**	**Start**	**End**
Kipp	T	34.971	146.269	800	2.95	19-Sep-14	15-Jun-16
	R	34.978	146.271				
MW26	T	34.967	146.283	792	2.73	19-Sep-14	15-Jun-16
	R	34.970	146.290				
Scintec	T	34.978	146.275	1267	2.68	6-Feb-15	15-Jun-16
	R	35.006	146.286				
MW38	T	34.998	146.285	1240	2.71	21-Dec-15	15-Jun-16
	R	34.992	146.274				
EC1	-	35.006	146.309	-	3.00	21-Nov-09	20-Oct-10
EC2	-	34.711	146.099	-	3.00	2-May-11	11-Apr-12
EC3	-	34.989	146.291	-	6.00	1-Jun-12	current
ET products	-			4 km × 4 km	-	1-Jan-10	1-May-13

Only daytime (i.e. unstable conditions) data were used for comparisons between scintillometers and EC3. The same weather station which was used in Chapter 5 to measure wind speed and direction, air temperature, pressure, humidity and precipitation, was installed next to Kipp in this experiment. These variables were used to derive surface heat fluxes from the scintillometers as described in Chapter 5 with an assumed vegetation height of 0.3 m. Measurements taken between 30-min before and after a rainfall event were not considered.

6.3.3 EC measurements

For validation of the remote sensing ET products, all three EC systems used for comparisons consisted of a CSAT3 3-D sonic anemometer (Campbell Scientific, Inc.) and an open path infrared gas analyzer (IRGA) (LI-COR Inc., U.S.) with a sampling frequency of 10 Hz following the general approach of Beringer et al. (2007) and Hutley et al. (2005). Fluxes were then computed and averaged at 30-min intervals. EC1 (-35.00^o, 146.31^o, 21st of November 2009 to the 10th of October 2010) and EC2 (-35.00^o, 146.30^o, 25th of May 2011 to the 11th of April 2012) were elevated ∼3 m above the ground, giving a fetch of about 300 m. As mentioned before, EC3 was at 6 m height and is the same EC system used previously in Chapter 5. As 10 Hz data were available for EC2 and EC3, they were processed using the software EddyPro (version 5.2.1) to calculate average fluxes at 30-min intervals. Corrections and processing implemented included spike detection and removal, lag correction relative to the vertical wind component based on covariance maximization method, linear de-trending, sonic virtual temperature correction, coordinate rotation using the double rotation method, spectral corrections for low and high pass filtering effects (Moncrieff et al., 2005) and the Webb-Pearman-Leuning correction (Webb et al., 1980). However, as 10 Hz data were not available for EC1, the 30-min fluxes computed within the logger program were corrected based on Webb-Pearman-Leuning correction (Webb et al., 1980) and used for comparisons with ET derived from the remote sensing models.

Following Ershadi et al. (2014), only daytime measurements from EC systems were used for comparisons with the models. This was defined based on downward short-wave radiation measured at the site whereby measurements were only used when net radiation (R_n) was greater than 20 W m^{-2}. Measurements were also removed during rain events and when H or $L_\mathrm{v}E$ was less than 0 W m^{-2}. All EC systems were equipped with weather stations which included sensors for measuring incoming and outgoing radiation for the derivation of R_n, and soil heat and moisture properties for the derivation of ground heat flux (G) and precipitation. Measurements and processing of R_n and G were as in Chapter 5.

6.3.4 MTSAT ET product

6.3.4.1 Forcing data

The MTSAT ET products based on SEBS, PM-Mu and the PT-JPL models have been derived and validated from January 2010 to the end of May 2013. The models were forced with short- and long-wave downward radiation, wind speed, air temperature, humidity and atmospheric pressure from the Australian Community Climate Earth System Simulator - Australia (ACCESS-A). ACCESS-A is the Australian operational numerical weather prediction (NWP) system which provides hourly meteorological data at a resolution of 12 km (Table 6.2).

Additionally, Normalized Difference Vegetation Index (NDVI) from MODIS (temporal resolution of 16 days at 250 m scales) (MOD13Q1 product) was interpolated and used as an input in the models to derive Leaf Area Index (LAI), emissivity, Fraction of Photosynthetically Active Radiation (FPAR) and albedo. The reader is referred to Ershadi et al. (2014) for more details on the how this interpolation and conversion

Table 6.2: Input data required for each model and their sources.

Variables	**Source**	**SEBS**	**PM-Mu**	**PT-JPL**
Incoming short - and long-wave radiation	ACCESS	x	x	x
Wind-speed	ACCESS	x		
Air Temperature	ACCESS	x	x	x
Humidity	ACCESS	x	x	x
Atmospheric Pressure	ACCESS	x	x	x
NDVI	MODIS	x	x	x
LAI	derived from NDVI	x	x	
Emissivity	derived from NDVI	x	x	x
FPAR	derived from NDVI	x	x	x
Albedo	derived from NDVI	x	x	x
Land surface temperature	MTSAT	x		
Cloud mask	MTSAT	x		

was carried out. These vegetation parameters are important for the parameterization of roughness parameters (SEBS), aerodynamic and surface resistance parameters (PM-Mu) and constraint functions (PT-JPL). Finally, land surface temperature (LST) and cloud mask (4 km) from MTSAT were also used (Table 6.2). These products were derived based on the previous work of Ershadi et al. (2014) and McCabe et al. (2015).

6.3.4.2 The Surface Energy Balance System (SEBS)

SEBS is a physically based model which calculates surface heat fluxes based on information regarding the land surface, atmospheric conditions and vegetation information (Table 6.2). SEBS provides formulations to estimate roughness parameters using NDVI. Based on temperature gradient, wind speed and roughness parameters, SEBS estimates H for dry and wet conditions using either MOST or the Bulk Atmospheric Similarity Theory equations. $L_{\mathrm{v}}E$ is finally derived as a residual term of the energy balance equation. The accuracy of SEBS is very much dependent on the accuracy of R_{n}, LST, air temperature, humidity, wind speed and vegetation phenology used in the model (Ershadi et al., 2014; McCabe et al., 2015; Su, 2002). Generally, SEBS has been found to overestimate evaporation except where short canopies exist, such as grasslands and cropland. Refer to Su (2002) for a comprehensive description of the model formulation.

6.3.4.3 Three-source Penman Monteith (PM-Mu)

PM-Mu is a physical model based on the Penman-Monteith equation (Monteith, 1965). The version used to retrieve the ET products here is a three source model whereby total evaporation comes from evaporation of water intercepted by the canopy ($L_\mathrm{v}E_\mathrm{i}$), canopy transpiration ($L_\mathrm{v}E_\mathrm{c}$) and soil evaporation ($L_\mathrm{v}E_\mathrm{s}$). Evaporation from each component was derived based on the Penman Monteith equation but weighted based on fractional vegetation cover (determined based on FPAR), relative surface wetness (based on relative humidity, Fisher et al., 2008), and available energy. In the PM-Mu model, aerodynamic and surface resistance parameters which are often difficult to obtain or measure are based on biome specific parameters from a Biome Properties Lookup Table. Leaf scale parameters are extended to the canopy scale using meteorological information such as R_n, air temperature, humidity, pressure and vegetation phenology (FPAR, NDVI and LAI) as in Ershadi et al. (2015). Resistance parameters in this lookup table were derived based on data from a set of EC towers. Equations and details on PM-Mu can be found in Mu et al. (2011, 2013).

6.3.4.4 PT-JPL

PT-JPL is also a three source model with total ET contributed from $L_\mathrm{v}E_\mathrm{i}$, $L_\mathrm{v}E_\mathrm{c}$ and $L_\mathrm{v}E_\mathrm{s}$. Using minimal meteorological and radiation information, PT-JPL computes the potential evaporation from each of these sources using the Priestley Taylor model. Based on bio-physiological properties of the land surface, potential evaporation is scaled using reduction functions which represent the impacts of the fraction of green canopy, relative wetness of the canopy, air temperature, and plant and soil water stress. Information for this scaling is provided by NDVI, relative humidity, air temperature, and pressure. The accuracy of $L_\mathrm{v}E$ derived from this model depends on the accuracy of optimum plant growth temperature (T_{OPT}), which is defined as the air temperature at the time of peak canopy activity when FPAR that is absorbed, and radiation is the highest, and minimum vapour pressure deficit (VPD) occurs. This optimum temperature is used to determine temperature constraints in the reduction function for scaling potential evaporation of canopy to actual evaporation. This is based on the assumption that the optimal canopy stomatal conductance happens when green leaf area, light and temperature are high, and VPD is low. For a dry site like Yanco, it is expected that the constraints posed by plant and soil water stress in scaling canopy and soil evaporation would play a bigger role in the accuracy of the derived ET. For further details on the PT-JPL, refer to Fisher et al. (2008).

6.3.5 Statistical evaluation

Comparisons between the scintillometers, the EC systems and MTSAT ET products were based on the root mean square difference (RMSD), Pearson's correlation coefficient (r), bias (negative when the observed value is lower), relative error (RE) and the Nash–Sutcliffe Efficiency (NSE) coefficient where,

$$\mathrm{RE} = \frac{\mathrm{RMSD}}{\overline{L_\mathrm{v}E_{obs}}}, \tag{6.1}$$

and

$$\mathrm{NSE} = 1 - \frac{\sum_{i=1}^{n}(L_\mathrm{v}E_{i,\mathrm{obs}} - L_\mathrm{v}E_{i,\mathrm{sim}})^2}{\sum_{i=1}^{n}(L_\mathrm{v}E_{i,\mathrm{obs}} - \overline{L_\mathrm{v}E_{\mathrm{obs}}})^2}. \tag{6.2}$$

Observed $L_\mathrm{v}E$ data are from the EC system with their mean denoted as $\overline{L_\mathrm{v}E_{\mathrm{obs}}}$; $L_\mathrm{v}E_{i,\mathrm{obs}}$ is the i^{th} observed $L_\mathrm{v}E$ from the EC system. Similarly, $L_\mathrm{v}E_{i,\mathrm{sim}}$ is the i^{th} simulated $L_\mathrm{v}E$ by the model (i.e. SEBS, PM-Mu or PT-JPL) for n total number of observations. It should be noted that NSE is sensitive to extreme values and can yield sub-optimal results when the dataset contains large outliers. Additionally, whilst it is assumed in this study that the EC measurements represent the "truth", one should be aware of uncertainties in the EC measurements.

6.4 Results and discussion

6.4.1 Comparison between scintillometers

Fig. 6.3 shows scatterplots comparing H derived from the scintillometers distributed across the 4 km $\times$ 4 km satellite grid. The different coloured points represent the wind direction of the derived surface heat flux. The red line shows the linear regression derived from comparing each pair of sensors in the current experiment whereas the blue line represents the linear regression derived by comparing the same pair of sensors in Chapter 5, when the sensors were placed within the footprint of the EC system. As in the previous chapter, bias here is equivalent to $\overline{\mathrm{x}} - \overline{\mathrm{y}}$ where $\overline{\mathrm{x}}$ is the mean of measurements on the x-axis and $\overline{\mathrm{y}}$ is the mean of measurements on the y-axis.

Due to differences in how surface heat fluxes are derived from optical and microwave scintillometers, measurements from Scintec are compared with measurements from Kipp

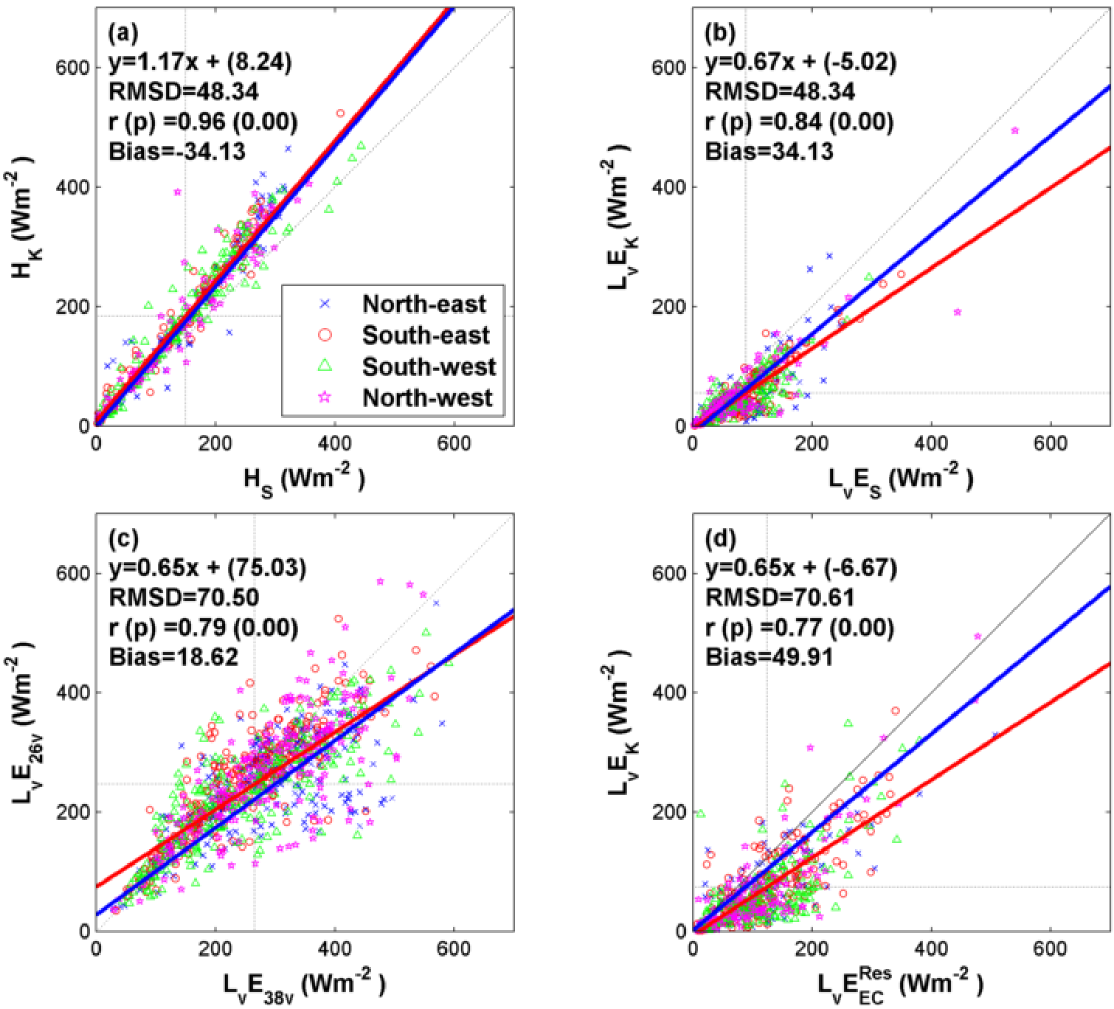

FIGURE 6.3: Scatterplots comparing a) H and b) $L_{\mathrm{v}}E$ derived from LAS (subscript K: Kipp, S: Scintec); c) $L_{\mathrm{v}}E$ from microwave scintillometers (subscript 38v: MW38v, 26v: MW26v); and d) $L_{\mathrm{v}}E$ from Kipp and $L_{\mathrm{v}}E_{\mathrm{EC}}^{\mathrm{Res}}$ EC3. Red line: Regression line derived from current experiment. Blue line: Regression line derived from experiment in Chapter 5. 'p' is the probability from testing the hypothesis of no correlation against the alternative that there is a non-zero correlation.

(optical with optical) and measurements from MW38 with that from MW26 (microwave with microwave). As seen from Fig. 6.3(a), despite being in different locations, H derived from Kipp and Scintec agreed well with a correlation of 0.97 and a bias of 34.13 Wm^{-2} regardless of wind direction.

Table 6.3 summarizes the statistics derived from comparing different scintillometers in the previous experiment with those from the current experiment. Generally, H derived from optical scintillometers compared well with each other and the EC system. Correspondingly, it can be seen that $L_{\mathrm{v}}E$ derived from the optical scintillometers agreed well with an r of 0.84 and an RMSD of 48.34 Wm^{-2}. Fig. 6.3 (c) shows that $L_{\mathrm{v}}E$ derived

Table 6.3: Summary statistics comparing derived H from current experiment and previous experiment.

		Previous experiment					**Current experiment**				
x	**y**	**r**	**RMSD**	**Bias**	**NSE**	**RE**	**r**	**RMSD**	**Bias**	**NSE**	**RE**
H_S	H_K	0.98	49.06	-37.80	0.81	0.22	0.96	48.34	-34.13	0.74	0.32
	H_{38v}	0.79	76.76	45.10	0.36	0.31	0.20	158.54	128.24	-2.26	0.79
	H_{38h}	0.81	73.77	42.61	0.44	0.30	0.14	166.69	137.87	-2.77	0.80
	H_{26v}	0.82	67.52	29.42	0.53	0.27	0.25	181.20	156.81	-2.99	0.81
	H_{26h}	0.70	91.03	61.18	-0.13	0.34	0.23	206.43	190.22	-6.45	0.85
H_K	H_{38v}	0.82	105.36	82.56	0.17	0.35	0.35	195.09	156.56	-1.64	0.80
	H_{38h}	0.84	102.73	79.44	0.25	0.35	0.33	202.35	166.66	-2.03	0.79
	H_{26v}	0.83	91.16	63.91	0.38	0.31	0.59	178.83	151.36	-1.39	0.64
	H_{26h}	0.67	127.45	103.09	-0.67	0.39	0.39	230.63	206.89	-3.98	0.75
H_{38v}	H_{38h}	0.99	12.11	-3.43	0.98	0.06	0.98	11.21	2.27	0.97	0.14
	H_{26v}	0.96	36.29	-23.74	0.84	0.17	0.49	71.93	-19.44	-0.26	0.85
	H_{26h}	0.91	38.36	14.31	0.78	0.17	0.26	89.14	7.65	-0.36	0.95
H_{26v}	H_{26h}	0.95	48.18	38.94	0.71	0.19	0.75	79.95	54.20	0.16	0.55
H_{EC}	H_S	0.96	41.31	13.67	0.90	0.18	0.88	60.05	-20.95	0.75	0.34
	H_K	0.94	51.14	-20.38	0.85	0.21	0.93	70.66	-48.09	0.71	0.38
	H_{38v}	0.82	90.11	61.92	0.36	0.34	0.26	198.31	159.15	-1.94	0.82
	H_{38h}	0.84	86.61	58.61	0.44	0.34	0.25	202.95	167.12	-2.31	0.81
	H_{26v}	0.83	81.97	50.02	0.50	0.31	0.39	198.05	168.92	-2.31	0.75
	H_{26h}	0.74	109.84	83.52	-0.11	0.38	0.32	225.56	201.32	-3.88	0.81

from the two microwave scintillometers also agreed despite being in different locations with an r of 0.79 and an RE of 0.27 which is very similar to that of the previous experiment, i.e. 0.24. Although H derived from the microwave scintillometers did not perform well, this is in-line with findings from Chapter 5, where microwave scintillometers were found to be less accurate for semi-arid environments such as the study area.

Finally, measurements from the scintillometers were compared with measurements from the EC system (Table 6.3 and 6.4). H derived from the optical scintillometers compared well with H measured by the EC system with an r of 0.88 and 0.93 for Scintec and Kipp respectively. In Chapter 5, it was shown that the LASs compared well with the EC data by assuming perfect closure of the energy balance. Therefore, L_vE derived from the EC systems were corrected based on the 'residual-LE closure' method (Twine et al., 2000). The energy budget was forced to close based on the estimate of L_vE_{EC} derived as a residual from the energy balance (i.e., $L_vE_{EC}^{Res} = R_n - G - H_{EC}$). Fig. 6.3(d) compares $L_vE_{EC}^{Res}$ with L_vE derived from Kipp. Comparing the slopes from the current experiment (red) and the previous experiment (blue), the underestimation of L_vE from the optical scintillometers is larger in magnitude (lower slope) compared to the previous experiment. This is likely an effect of the better energy balance closure for

TABLE 6.4: Summary statistics comparing derived L_vE from current experiment and previous experiment.

		Previous experiment					**Current experiment**				
x	**y**	**r**	**RMSD**	**Bias**	**NSE**	**RE**	**r**	**RMSD**	**Bias**	**NSE**	**RE**
L_vE_S	L_vE_K	0.93	49.06	37.80	0.67	0.33	0.84	48.34	34.13	0.41	0.54
	L_vE_{38v}	0.65	88.83	-53.77	-0.04	0.62	0.42	158.54	-128.24	-6.35	1.92
	L_vE_{38h}	0.67	85.46	-50.86	0.05	0.60	0.39	166.69	-137.87	-6.96	1.98
	L_vE_{26v}	0.64	76.60	-35.78	0.21	0.55	0.33	181.20	-156.81	-9.12	2.24
	L_vE_{26h}	0.50	109.38	-74.97	-0.76	0.73	0.41	206.43	-190.22	-7.75	1.90
L_vE_K	L_vE_{38v}	0.56	113.42	-87.12	-1.38	1.00	0.44	195.09	-156.56	-8.23	2.50
	L_vE_{38h}	0.58	109.66	-83.50	-1.21	0.97	0.40	202.35	-166.66	-8.97	2.51
	L_vE_{26v}	0.55	95.20	-66.37	-0.69	0.85	0.38	178.83	-151.36	-6.98	2.16
	L_vE_{26h}	0.37	137.19	-110.22	-2.66	1.15	0.40	230.63	-206.89	-10.42	2.41
L_vE_{38v}	L_vE_{38h}	0.98	18.54	4.99	0.95	0.09	1.00	11.21	-2.27	0.99	0.04
	L_vE_{26v}	0.87	47.00	26.11	0.66	0.24	0.79	70.50	18.62	0.60	0.27
	L_vE_{26h}	0.78	51.78	-17.86	0.52	0.25	0.69	86.54	-7.52	0.41	0.31
L_vE_{26v}	L_vE_{26h}	0.87	59.16	-44.89	0.18	0.33	0.83	79.95	-53.77	0.22	0.33
L_vE_{EC}	L_vE_S	0.59	118.43	-92.96	-9.52	2.32	0.40	71.53	-39.94	-2.27	1.72
	L_vE_K	0.51	92.02	62.96	-5.06	1.71	0.28	71.77	-20.34	-1.46	1.31
	L_vE_{38v}	0.44	164.26	-148.64	-17.92	2.96	0.14	242.29	242.29	-37.53	4.80
	L_vE_{38h}	0.47	160.26	-144.74	-17.10	2.91	0.12	249.42	-221.85	-40.07	4.88
	L_vE_{26v}	0.49	143.95	-130.57	-18.91	2.90	0.23	249.90	-230.88	-55.12	5.76
	L_vE_{26h}	0.37	189.34	-175.99	-35.15	3.62	0.40	284.34	-267.01	-65.64	6.19
$L_vE_{EC}^{Res}$	L_vE_S	0.90	40.70	-12.94	0.72	0.34	0.69	58.32	23.48	0.33	0.56
	L_vE_K	0.82	50.58	22.09	0.56	0.38	0.77	70.61	49.91	0.17	0.57
	L_vE_{38v}	0.62	96.28	-66.92	-0.55	0.75	0.33	190.69	-152.72	-6.61	1.78
	L_vE_{38h}	0.63	93.68	-63.89	-0.45	0.74	0.33	195.08	-160.45	-6.88	1.77
	L_vE_{26v}	0.57	86.55	-52.75	-0.28	0.71	0.33	191.80	-163.53	-6.83	1.74
	L_vE_{26h}	0.44	122.27	-92.92	-1.77	0.93	0.44	221.04	-197.15	-8.02	1.90

the current experiment (slope: 0.85) compared to the previous experiment (slope: 0.79). As a result, it is postulated that the reduced performance of H and L_vE derived from the microwave scintillometers may also be related to R_n - G measured for this experimental period. As seen in Chapter 5, the accuracy of surface heat fluxes derived from microwave scintillometers are very prone to errors in the assumption made regarding parameters such as vegetation height, and R_n - G, particularly for a semi-arid environment and when scintillometer heights are low. As the experimental period here encompassed three seasons as opposed to one in the previous experiment, a larger variation in vegetation height and meteorological conditions were expected, thereby increasing the uncertainty of the derived fluxes. Nevertheless, comparisons between optical scintillometers and microwave scintillometers showed good agreement, which supports the hypothesis that the fluxes from different areas within the 4 km pixels are similar due to homogeneity of the site.

The difference between measurements from the EC system and the scintillometers were then delineated based on wind direction. Based on Fig. 6.4, it can be seen that regardless

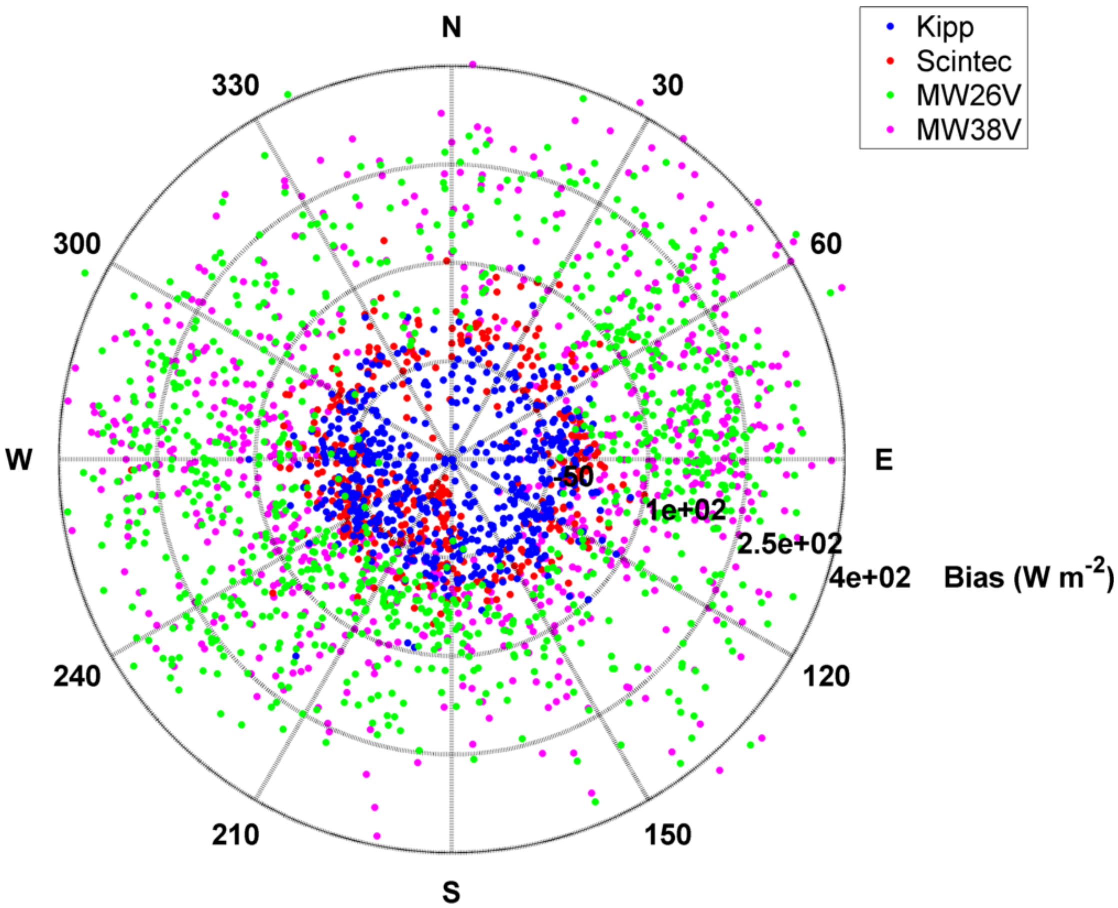

FIGURE 6.4: Scatterplots showing difference in $L_\mathrm{v}E_\mathrm{EC}^\mathrm{Res}$ (in Wm^{-2}) derived from the EC system and scintillometers according to wind-direction. Colours indicates scintillometer.

of wind direction, the difference between measurements from EC3 and the scintillometers are of the same order. Likewise, if these differences were delineated based on wind speed (Fig. 6.5), there was little correlation between wind speed and the flux differences.

Based on these comparisons which have been carried out in this section, it can be concluded that i) the spatial distribution of surface heat fluxes within the MTSAT 4 km pixel is homogeneous and therefore, ii) measurements from EC3 is representative of the areal surface heat flux of the MTSAT 4 km pixel. Moreover, this hypothesis can be extended to EC1 and EC2.

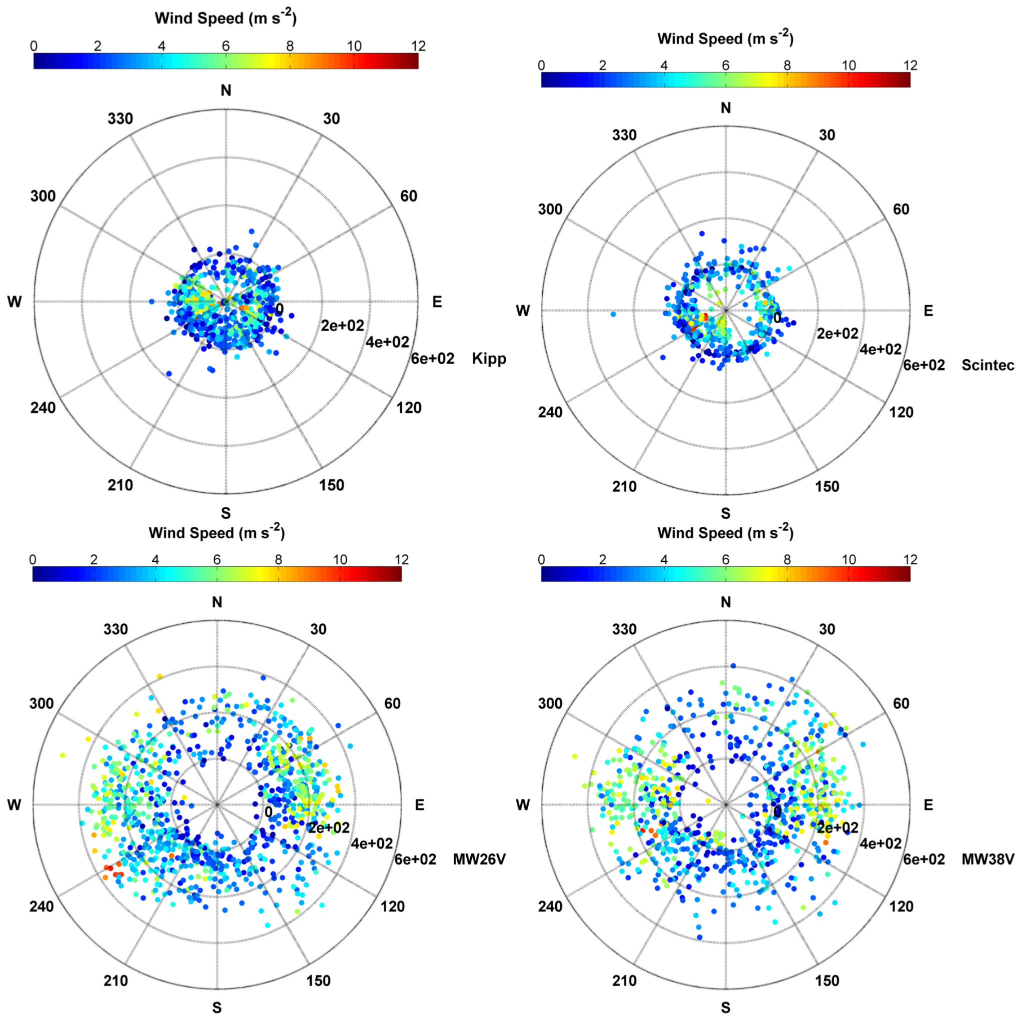

FIGURE 6.5: Scatterplots showing difference in $L_v E_{EC}^{Res}$ (in Wm^{-2}) derived from the EC system and scintillometers (as indicated by name) according to wind-direction. Colours indicate magnitude of wind speed.

6.4.2 Validation of remote sensing ET product

6.4.2.1 Overall Performance

As it has been shown that EC3 is representative of the MTSAT satellite pixel, as well as EC1 and EC2 by default, measurements from EC1, EC2 and EC3 are used to validate the MTSAT ET products. Due to the homogeneity of the grassland where the EC systems were located, it is assumed that the measurements from all EC stations are representative of the MTSAT pixel in which EC3 is located. The energy balance closure of the different stations were investigated and shown to have a slope of 1.04, 0.75 and 0.87 respectively (Fig. 6.6).

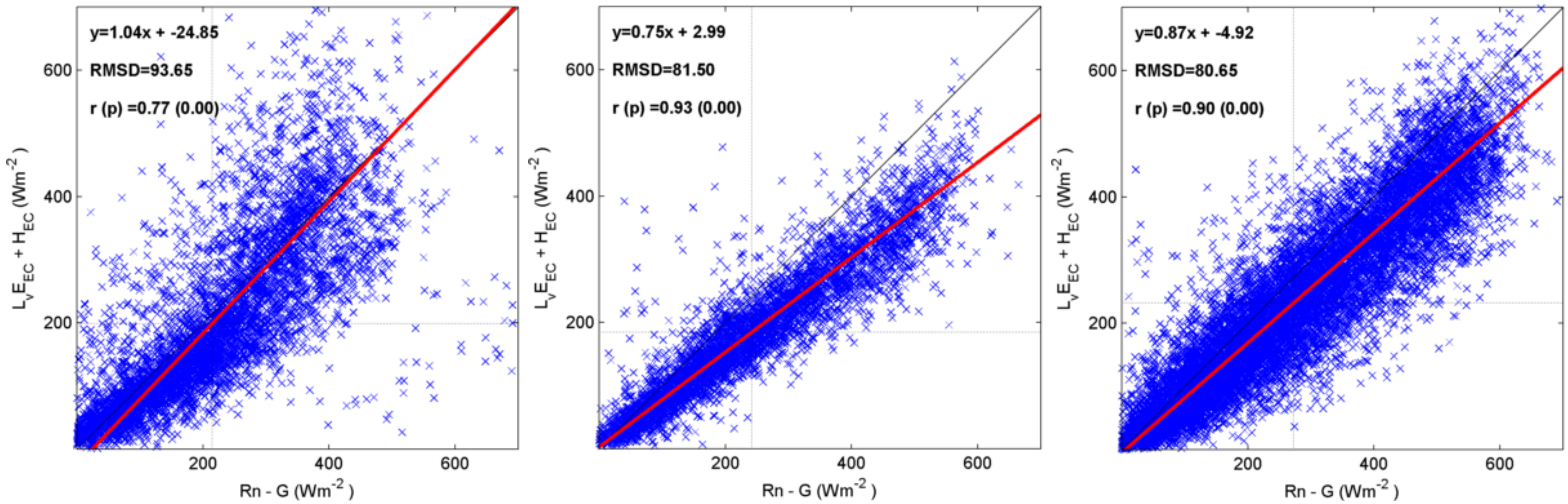

FIGURE 6.6: Energy balance closure of EC1, EC2 and EC3 (left to right). Solid black line: 1:1 line. Solid red line: fitted line from orthogonal regression.

Measurements from EC1, EC2 and EC3 have been collated into a single dataset which is referred to collectively as measurements from the EC system. These $L_{\mathrm{v}}E$ measurements from the EC system ($L_{\mathrm{v}}E_{\mathrm{EC}}$) (first row) were also corrected based on the 'residual-LE closure' ($L_{\mathrm{v}}E_{\mathrm{EC}}^{\mathrm{Res}}$) (2nd row) and β correction technique ($L_{\mathrm{v}}E_{\mathrm{EC}}^{\beta}$) (third row) before comparison with $L_{\mathrm{v}}E$ derived from the SEBS, PM-Mu and PT-JPL remote sensing ET models in Fig. 6.7. The EC measurements have been re-sampled at the hourly time-steps when remote sensing ET products were available. Hourly data from the EC system and the model were then filtered in such a way that only times where measurements were available from the EC system and all three models were available.

Generally, it can be seen that regardless of the $L_{\mathrm{v}}E$ used for comparison, PT-JPL out-performed the other two models with an r which ranged from 0.68 to 0.71 and an RMSD ranging from 51.05 W m^{-2} to 63.27 W m^{-2}. This is in-line with the results of previous studies (e.g. Ershadi et al., 2014; McCabe et al., 2015). When $L_{\mathrm{v}}E$ and $L_{\mathrm{v}}E_{\mathrm{EC}}^{\mathrm{Res}}$ were used, SEBS performed better than PM-Mu whereas PM-Mu performed better when compared with $L_{\mathrm{v}}E_{EC}^{\beta}$. Comparison of H from SEBS and the EC system, resulted in an underestimation by SEBS with an RMSD of 92.90 W m^{-2} and r of 0.75. Another observation is that NSE derived from the comparisons of SEBS and PM-Mu showed that the models did not perform well with NSE < 0 for the majority of the pairs. This indicates that the observed mean is a better predictor than the model. As pointed out by Ershadi et al. (2014), depending on $L_{\mathrm{v}}E$ used for comparisons, the performance will differ. This is because $L_{\mathrm{v}}E$ from SEBS is calculated as a residual from observations of H whereas the PM-Mu method assumes similarity between H and $L_{\mathrm{v}}E$ which would be in-line with assumptions of the β correction method. As Foken et al. (2011) have shown, $\mathrm{L_vE_{EC}^{\beta}}$ may be less accurate due to the lower reliability of the IRGA compared to the sonic anemometer, and lack of similarity between the transportation of H and $L_{\mathrm{v}}E$. Accordingly, unless specified, $L_{\mathrm{v}}E_{\mathrm{EC}}^{\mathrm{Res}}$ is used for computing RMSD, r, bias, RE and NSE in the remaining sections of this chapter.

To better understand the distribution of $L_{\mathrm{v}}E_{\mathrm{EC}}^{\mathrm{Res}}$ derived from the EC system and models, Fig. 6.8 summarizes their median, quartile, minima and maxima. It can be seen from the boxplots that the distribution of the observations have a positive skewness. All models and the EC system have the same minima as measurements lower than 0 W m^{-2} were filtered prior to comparisons. Table 6.5 also summarizes the mean and standard

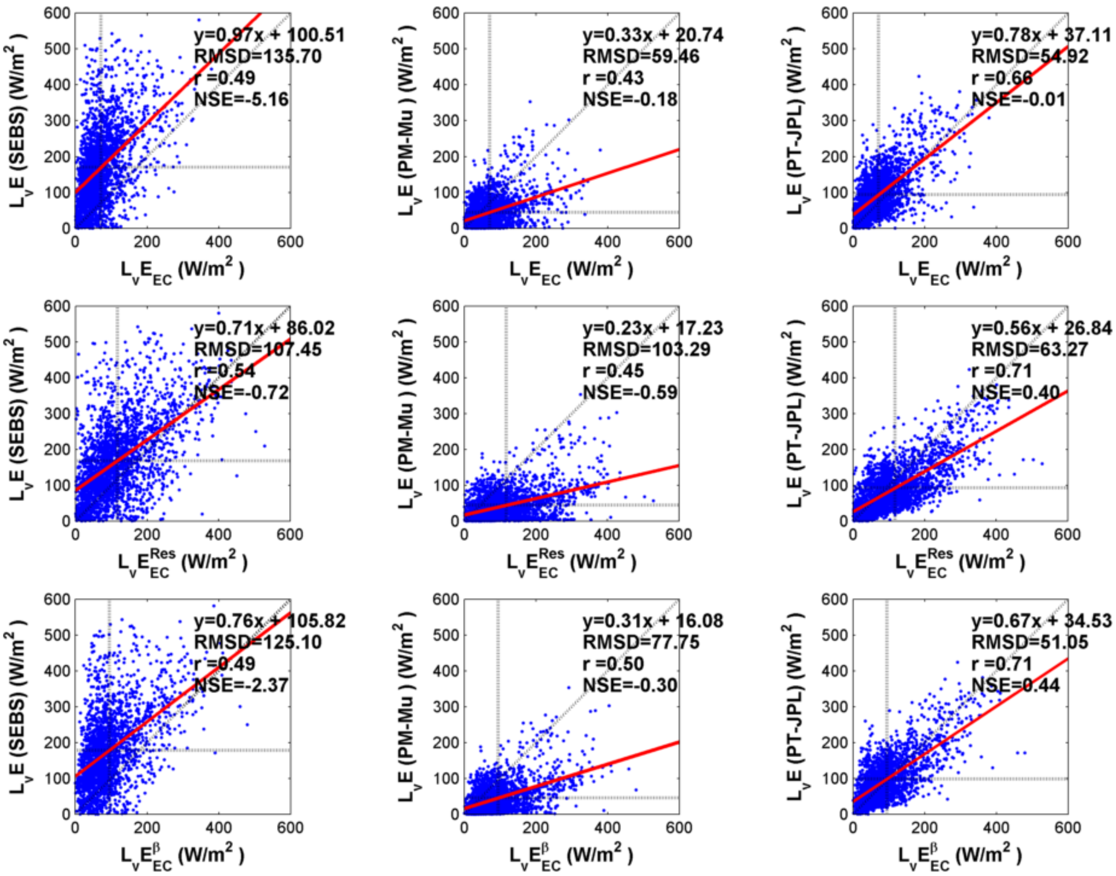

FIGURE 6.7: Scatterplots comparing $L_{\mathrm{v}}E$ measured (top row), derived as a residual (middle row) and β-corrected (bottom row) from EC systems against $L_{\mathrm{v}}E$ based on SEBS, PM-Mu and PT-JPL (left to right). Red solid line: Linear regression. Black dotted line: Mean of corresponding measurements and the 1:1 line.

deviations of $L_{\mathrm{v}}E_{\mathrm{EC}}^{\mathrm{Res}}$ and $L_{\mathrm{v}}E$ based on MTSAT products. The Kruskal-Wallis non-parametric test was repeated for each pair, showing that the distribution of all datasets did not have the same median ($p < 0.01$). Additionally, as the Pearson's correlation assumes a linear relationship, the correlation between the $L_{\mathrm{v}}E_{\mathrm{EC}}^{\mathrm{Res}}$ and the models were computed using Kendall's Tau correlation coefficient, τ. Whilst the τ (and Spearman's rank) were lower than Pearson's correlation for all cases, PT-JPL still performed the best (Table 6.5).

From Table 6.5, it can be seen that due to the large differences in means, NSE alone is not enough to gauge the performance of the MTSAT ET products. Moreover, the NSE coefficient assumes that the distributions are normal. To further complicate the diagnosis, as mentioned in Ershadi et al. (2014), it is possible that measurement uncertainty might be equal to modelling uncertainty when $L_{\mathrm{v}}E$ is low. In fact, for an arid or semi-arid environment, such as the study area, mean $L_{\mathrm{v}}E_{\mathrm{EC}}^{\mathrm{Res}}$ is of the same magnitude

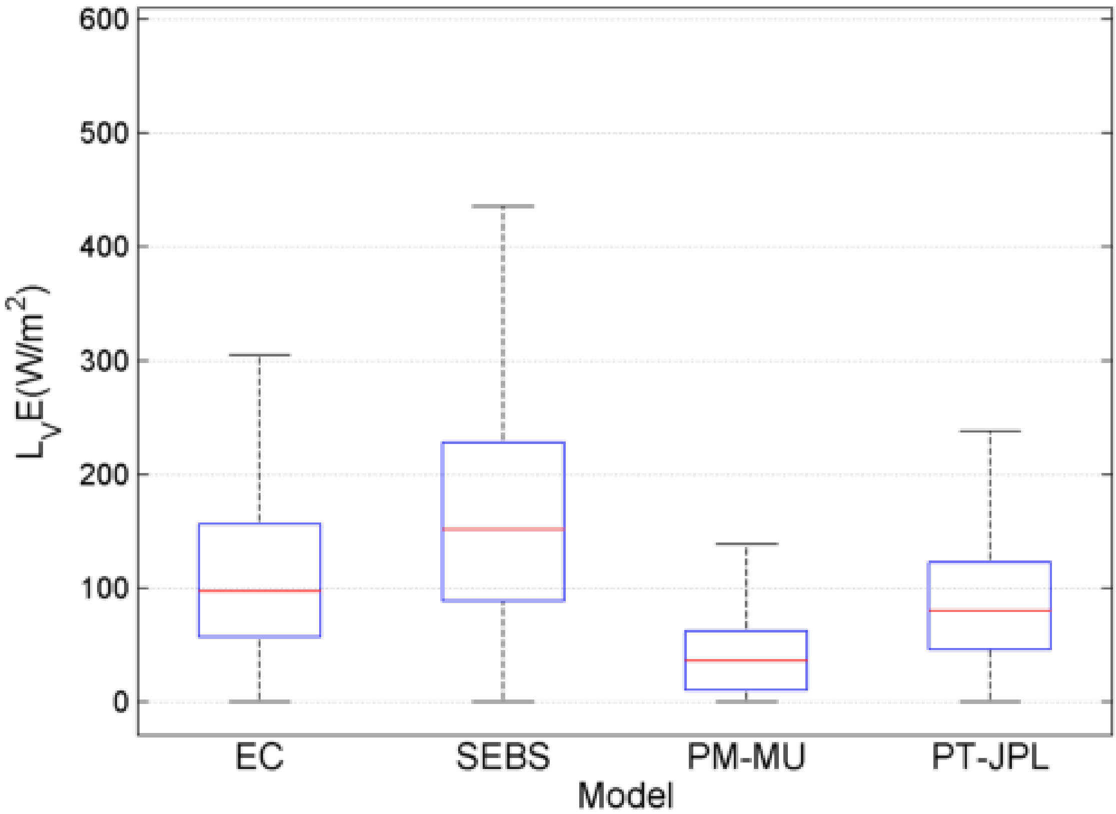

Figure 6.8: Boxplots showing the median (red line), 25th and 75th percentile (q_1, q_3) (edge of box), minima and maxima excluding outliers (whiskers) of L_vE^{Res} measured from the EC system and remote sensing models.

($\sim$ 116.71 W m^{-2}) as G (varies from 50 W m^{-2} to 170 W m^{-2}) and the energy balance non-closure ($\sim$ 80 W m^{-2}). Similarly, McCabe et al. (2015) found that a reduction in the performance of SEBS, PM-Mu and PT-JPL for arid sites, particularly for the first two.

Clearly, the low values of L_vE and non-closure of the EC system complicates the validation of remote sensing ET products, particularly for a semi-arid environment (Polhamus et al., 2013). Therefore, future studies should consider these issues in validating the performance of ET models by using a range of statistics to gauge the performance of each model. For instance, Cammalleri et al. (2014) introduced a statistical evaluation approach based on an ensemble-based inter-comparison method to better account for uncertainties in ET fluxes using EC measurements. If the interest is in the correlation of the model with the EC system, perhaps the model L_vE can be normalized with the standard deviation of L_vE_{EC} as was done for the validation of remote sensing soil moisture products in Chapter 4.

TABLE 6.5: Summary statistics comparing L_vE as a residual from the EC system and ET models. Stdev: Standard deviation r: Correlation coefficient. τ: Kendall's correlation coefficient. m and c: slope and intercept derived from linear regression.

Source	Period	Mean	Stdev	r (Pearson)	r (Spearman)	τ (Kendall)	RMSD	m	c	Bias	NSE	RE
EC	All	116.7113	82.0138	-	-	-	-	-	-	-	-	-
	Su	111.56	78.72	-	-	-	-	-	-	-	-	-
	Au	126.67	106.99	-	-	-	-	-	-	-	-	-
	Wi	99.61	58.75	-	-	-	-	-	-	-	-	-
	Sp	140.90	83.22	-	-	-	-	-	-	-	-	-
SEBS	All	168.31	107.91	0.54	0.52	0.37	107.45	0.71	86.02	-51.60	-0.72	0.92
	Su	174.10	126.26	0.27	0.28	0.19	143.97	0.43	126.60	-62.54	-2.35	1.29
	Au	163.11	103.68	0.67	0.57	0.41	93.47	0.65	81.35	-36.44	0.24	0.74
	Wi	141.53	79.45	0.59	0.56	0.40	77.29	0.80	61.54	-41.92	-0.73	0.78
	Sp	218.30	124.51	0.49	0.51	0.36	135.05	0.73	115.00	-77.40	-1.64	0.96
PM-MU	All	44.12	42.14	0.45	0.38	0.26	103.29	0.23	17.23	72.59	-0.59	0.89
	Su	10.17	17.93	0.30	0.53	0.37	126.22	0.07	2.51	101.39	-1.58	1.13
	Au	42.25	38.07	0.65	0.58	0.42	121.14	0.23	12.76	84.42	-0.28	0.96
	Wi	52.65	35.04	0.32	0.28	0.19	74.60	0.19	33.66	46.96	-0.61	0.75
	Sp	54.00	55.60	0.59	0.56	0.41	110.13	0.39	-1.24	86.90	-0.75	0.78
PT-JPL	All	92.42	65.17	0.71	0.64	0.47	63.27	0.56	26.84	24.29	0.40	0.54
	Su	63.59	42.37	0.66	0.70	0.51	76.56	0.36	23.78	47.97	0.05	0.69
	Au	105.29	81.33	0.82	0.71	0.53	65.11	0.62	26.31	21.38	0.63	0.51
	Wi	86.23	54.97	0.60	0.54	0.39	52.64	0.56	30.25	13.39	0.20	0.53
	Sp	110.12	67.74	0.69	0.67	0.49	68.63	0.56	31.34	30.78	0.32	0.49

Finally, it can be seen here that despite using the same forcing data, actual ET modelled by the three remote sensing ET models showed vast differences, with SEBS derived L_vE having the largest variation followed by PT-JPL and PM-Mu. This is because the different models employ different schemes in partitioning available energy into L_vE. In the case of SEBS, this partitioning is highly sensitive to LST (hourly input) prescribed to the model. On the other hand PM-Mu and PT-JPL partitions available energy based on the NDVI (bi-monthly input) which acts as a proxy for vegetation phenology. To further investigate the cause for different performances of the model, the hourly and seasonal performance of the models are compared below.

6.4.2.2 Diurnal and seasonal pattern

Fig. 6.9 shows the mean diurnal pattern between 7 am and 9 pm (unstable conditions) of $L_vE_{\mathrm{EC}}^{\mathrm{Res}}$ and L_vE from the models throughout the study period. As observed in the scatterplots of Fig. 6.7, SEBS overestimates L_vE whereas PM-Mu and PT-JPL underestimates. Whilst the diurnal pattern of the EC system is most closely depicted by PT-JPL, it can be seen that using similar meteorological data, L_vE from SEBS peaks approximately an hour later than PM-Mu and PT-JPL. This may be an effect of the LST input from MTSAT used by SEBS.

To derive mean diurnal patterns by seasons, due to a lack of points for certain seasons, all available measurements have been used to get a sense of L_vE from each model in

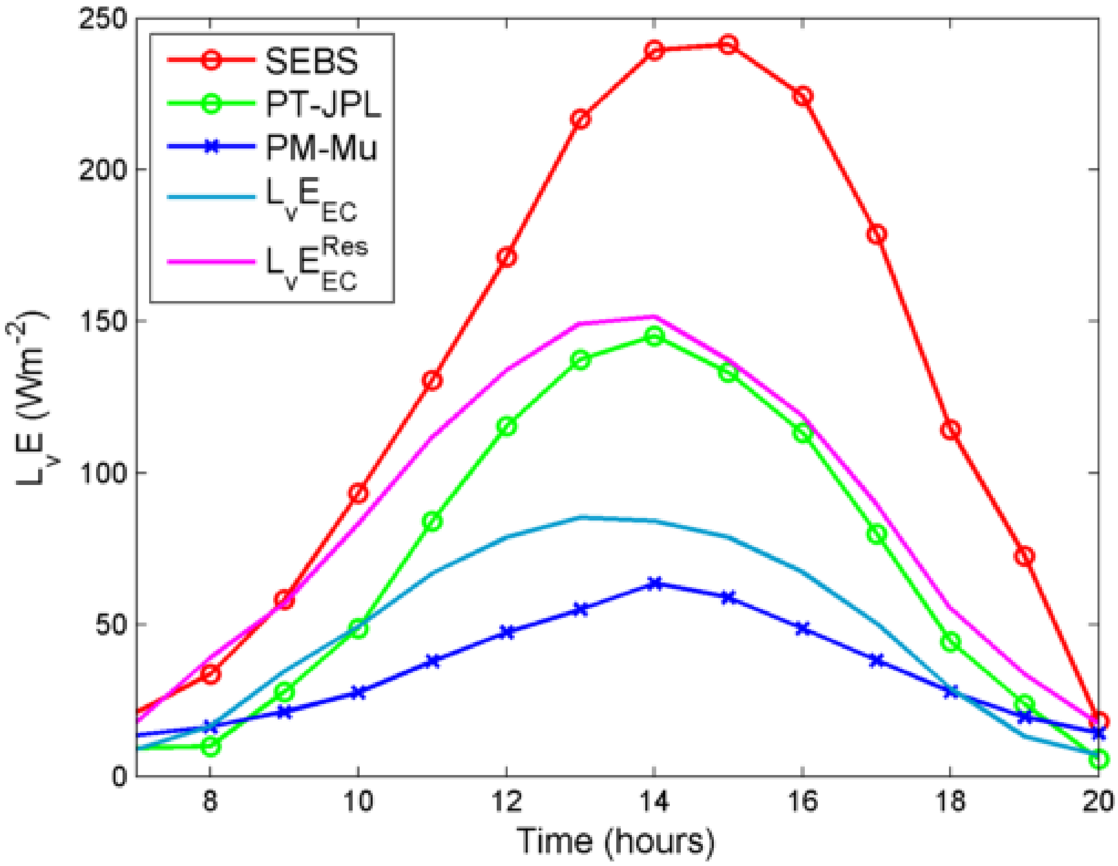

FIGURE 6.9: Daily pattern of L_vE from each ET model and $L_vE_{\mathrm{EC}}^{\mathrm{Res}}$

comparison to the EC system (Fig. 6.10). Generally, based on visual inspection, all remote sensing models are seen to perform well in summer. However, around 8 am to 10 am, $L_vE_{\mathrm{EC}}^{\mathrm{Res}}$ is seen to be higher than L_vE from the remote sensing models during autumn, winter and spring. This may be caused by uncertainties in measurements of R_n and G, or the minimum conditions defined by the remote sensing models for ET to occur may be too stringent, or soil evaporation may have been driven by G during these periods. It is to be noted, however, that the derived patterns may be biased due to the number of measurements available to derive them.

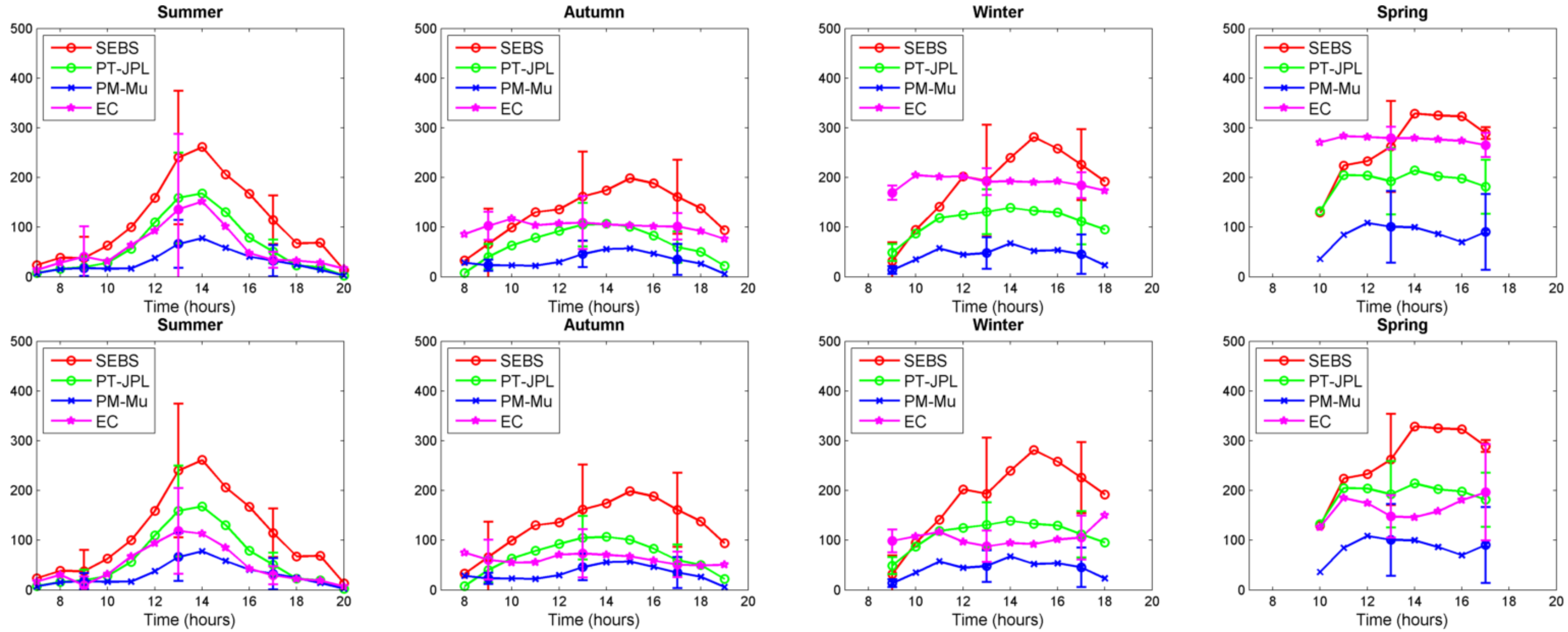

FIGURE 6.10: Diurnal pattern based on seasons for L_vE derived as a residual (top) and L_vE measured (bottom). Whiskers represent the max and min.

In terms of $L_\mathrm{v}E_\mathrm{EC}$ (Fig. 6.10, bottom), this earlier peak is also observed in autumn and winter. It is interesting to see that PM-Mu also depicts this pattern during autumn. Further investigations revealed that $L_\mathrm{v}E_\mathrm{s}$ simulated by PM-Mu was the main component of total $L_\mathrm{v}E$ the majority of the time, whereas $L_\mathrm{v}E_\mathrm{i}$ and $L_\mathrm{v}E_\mathrm{c}$ was a lot lower than that of PT-JPL, suggesting that the underestimation from PM-Mu may be due to uncertainty in the specification of vegetation type or parameters. McCabe et al. (2015) have also observed a decrease in the performance of PM-Mu for drier sites, possibly because ET consists of a small portion of total available energy (low evaporative fractions). Moreover, $L_\mathrm{v}E_\mathrm{s}$ from PM-Mu is generally higher than that of PT-JPL during summer. Finally, a closer look at the individual components of $L_\mathrm{v}E$ showed that whilst $L_\mathrm{v}E_\mathrm{i}$, $L_\mathrm{v}E_\mathrm{c}$ and $L_\mathrm{v}E_\mathrm{s}$ from PT-JPL followed the diurnal pattern of R_n, $L_\mathrm{v}E_\mathrm{s}$ from PM-Mu begins earlier than the other components, thereby leading to a small peak earlier in the morning as also observed in $L_\mathrm{v}E_\mathrm{EC}$. This suggests that whilst the magnitude of $L_\mathrm{v}E$ derived from PM-Mu is too low, the scheme used by PM-Mu to simulate $L_\mathrm{v}E_\mathrm{s}$ may be more appropriate for a semi-arid environment where ET may have been driven by G prior to sun-rise.

6.4.2.3 Hourly and seasonal performance

To investigate the hourly and seasonal performance of the models, the difference between $L_\mathrm{v}E_\mathrm{EC}$ and modelled $L_\mathrm{v}E$ was delineated based on the hour and season. Based on Fig. 6.11, the bias between the EC system and SEBS is observed to correspond to R_n and peaks at about 3 pm. As a result, RE is seen to be quite consistent throughout the day with SEBS having a lower RE than PM-Mu in the morning and inversely during the afternoon. The increase in RE and decrease in NSE across the day is likely affected by the increase in bias. If one were to establish the performance of SEBS solely on bias, RE and NSE, SEBS might have been mistaken for not performing well. However, by comparing the performance of SEBS with the other two models, it can be seen that for the majority of the time, bias, RE and NSE changed directions at similar times which indicates that the bias is likely to originate from biases in the ACCESS forcing from actual meteorological conditions, rather than errors in the ET models. However, further comparisons between the input forcing with *in situ* measurements is recommended to affirm this. Nevertheless, McCabe et al. (2015) also observed that SEBS was more sensitive to forcing data than PM-Mu and PT-JPL. Conversely, while it was also found in the aforementioned study that PM-Mu was least sensitive to the forcing, it can be

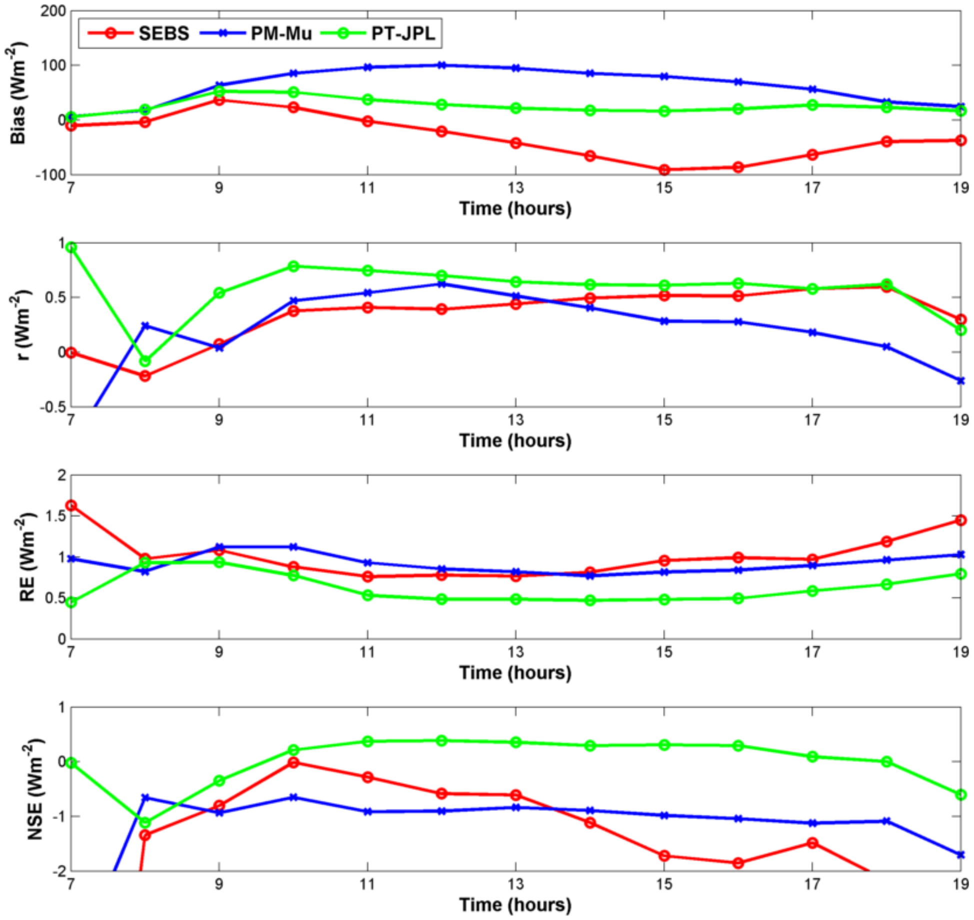

FIGURE 6.11: Hourly pattern of statistics comparing $L_{\mathrm{v}}E_{\mathrm{EC}}^{\mathrm{Res}}$ from EC systems and $L_{\mathrm{v}}E$ based on different remote sensing models.

seen in Fig 6.11 that r of PM-Mu decreases sharply after 12 pm whereas r of SEBS increases after 10 am. Unlike bias, RE and NSE, which are seen to change relative to each other, the hourly pattern of r is different. Ershadi et al. (2014) found that although SEBS overestimated evaporation, its correlation with EC measurements was high. It is possible that as the day progresses and the role of LST increases, inputs from MTSAT helped to improve the performance of SEBS.

Performance of each model for each season was investigated based on bias and plotted as boxplots (Fig. 6.12). The derived statistics are also summarized in Table 6.5. Although the amount of data available for each season will influence the results (since only times where data was available from the EC system and all models was considered), it is expected that the results will still give an indication of the spread and performance of the models relative to the EC system.

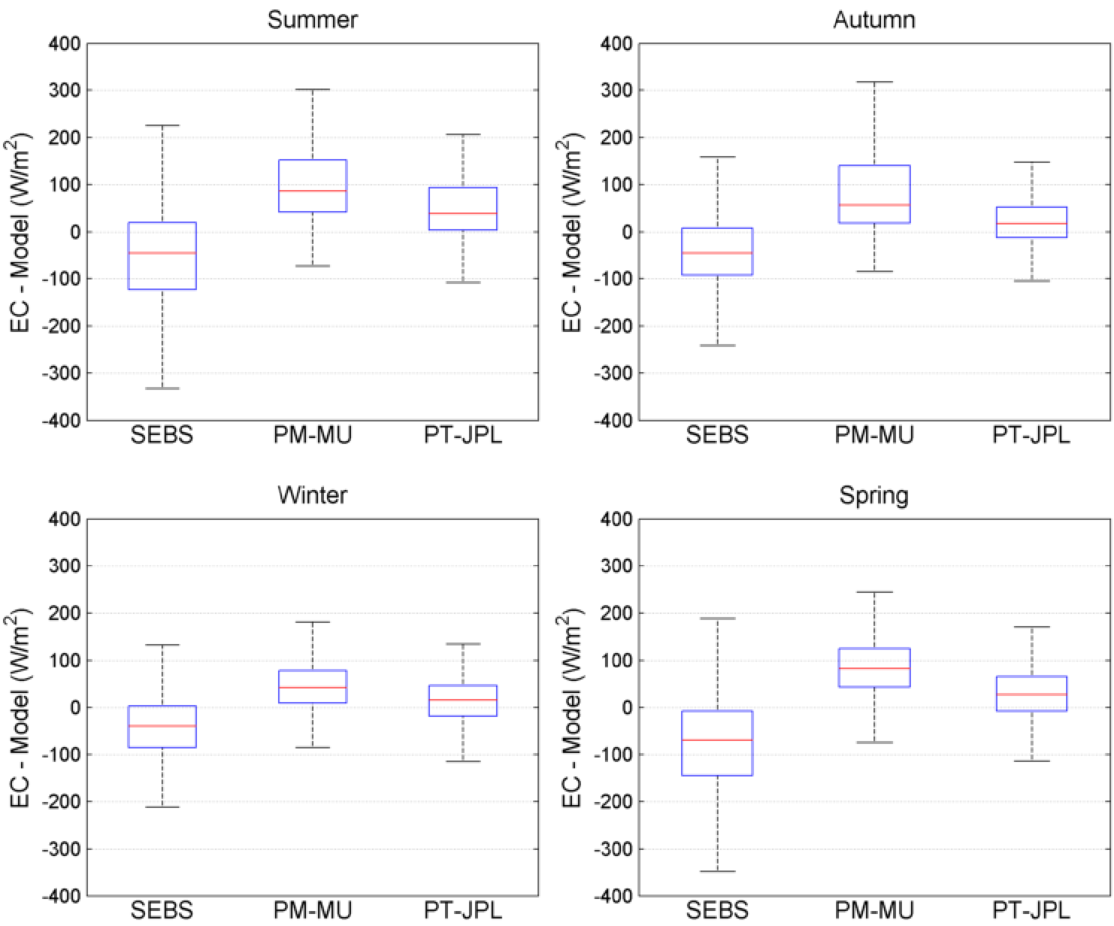

FIGURE 6.12: Boxplot of bias between $L_\mathrm{v}E$ from EC systems and $L_\mathrm{v}E$ based on different remote sensing models.

Most rainfall occurs at the site during winter. At the same time, the available energy for ET to occur during winter is low. From Table 6.5, it can be seen that $L_\mathrm{v}E^\mathrm{Res}_\mathrm{EC}$ was the lowest during winter followed by summer, autumn and spring. In terms of variation, the standard deviation of $L_\mathrm{v}E^\mathrm{Res}_\mathrm{EC}$ was the lowest in winter, followed by summer, spring and finally autumn. However, $L_\mathrm{v}E_\mathrm{EC}$, was the lowest during summer followed by winter. It is likely that during summer and winter, as the magnitude of $L_\mathrm{v}E$ is low, performance of the models will depend on the $L_\mathrm{v}E$ used to validate the ET model. During autumn and spring, as $L_\mathrm{v}E$ is larger in magnitude, the energy balance non-closure is less likely to affect the results. As before, the effect of bias on NSE and RE can be seen by comparing bias, NSE and RE of SEBS and PM-Mu.

In terms of r, based on $L_\mathrm{v}E^\mathrm{Res}_\mathrm{EC}$, it can be seen that all models had the highest correlation during autumn but their performance differed for other seasons. PT-JPL performed reasonably well regardless of season, whereas r for SEBS and PM-Mu was the lowest during summer, at 0.27 and 0.30 respectively. As vegetation phenology from all three models were similar, the schemes employed by SEBS and PM-Mu to derive roughness or aerodynamic and surface resistance from NDVI could have led to the poor performance of the models. Aerodynamic and surface resistance parameters used within PM-Mu are based on a lookup table which has been calibrated based on a number of FLUXNET sites. Consequently, it is likely that the parameters are unsuitable for the vegetation which exists in the study area, as different plant species may react differently in similar meteorological and water availability conditions (Mackay et al., 2003; Polhamus et al., 2013). In the case of SEBS, uncertainty is caused by an underestimation of H (and therefore overestimation of $L_\mathrm{v}E$). Su (2002) found that errors in the scalar roughness height for heat transfer estimated based on observations of vegetation phenology can lead to errors of the same magnitude or larger than uncertainties caused by errors in meteorological data. During summer, water availability is low whereas available energy is high. Therefore, potential $L_\mathrm{v}E$ is high and the role played by soil moisture and vegetation in the partitioning of energy increases. Conversely, although most rainfall occurs during the second half of the year, potential ET is constrained by available energy. As a result, model performance is the highest during autumn, and lowest during summer (Fig. 6.12). Previously, PM-Mu was shown to be able to simulate an early peak in $L_\mathrm{v}E$ during autumn (Fig. 6.10). However, based on statistics derived between $L_\mathrm{v}E_\mathrm{EC}$ and $L_\mathrm{v}E$ from the remote sensing ET models, r of PM-Mu during autumn (0.65) was still lower than SEBS and PT-JPL (0.67 and 0.76 respectively). Further investigations with a more complete set of measurements will be needed to investigate the influence of G.

6.4.2.4 Daily ET

To obtain daily ET, hourly $L_\mathrm{v}E$ were firstly interpolated using a cubic interpolation for gaps shorter than 18 hours. These gap-filled measurements were then converted into mm hr^{-1} for each hour and summed from 7 am to 7 pm. Therefore, the "daily flux" plotted in Fig. 6.13 is in fact only ET which occurs from 7 am to 7 pm (day-time). Only days in which measurements were available from the EC system and all ET products were used in the analysis. This reduced the number of days to just 59, in which 13 were during summer, 6 during autumn, 19 during winter, and 21 during spring (Fig. 6.13). It can be seen that both PM-Mu and PT-JPL underestimates $L_\mathrm{v}E$ in comparison to $L_\mathrm{v}E_\mathrm{EC}^\mathrm{Res}$,

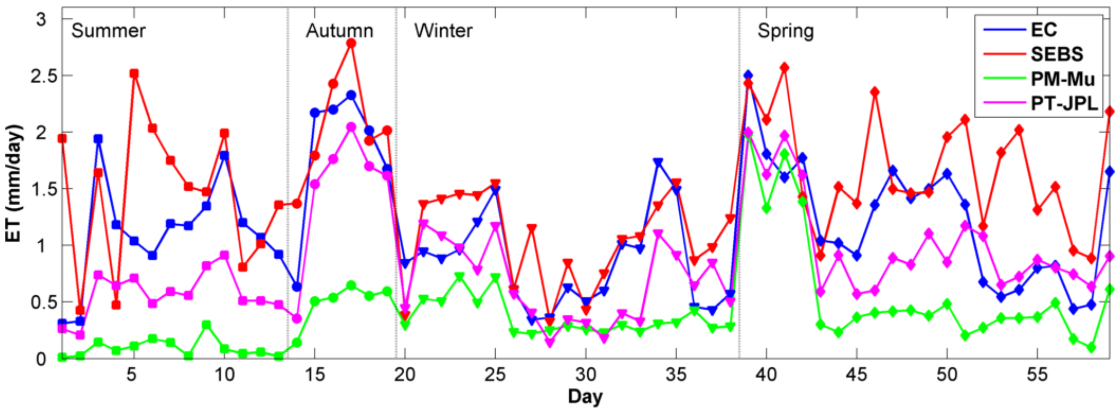

FIGURE 6.13: Comparison of daily $L_\mathrm{v}E_\mathrm{EC}^\mathrm{Res}$ and $L_\mathrm{v}E$ based on remote sensing ET models for 59 days of concurrent data. The comparisons have been lumped according to seasons whereby measurements for each seasons are not in any particular order.

but the dynamics from PT-JPL follow closely that of the EC system. Conversely, SEBS had a larger range thereby causing it to under- or overestimate.

Based on the Kruskal-Wallis test, the daily ET from these different measurement methods did not have distributions with equal medians ($p < 0.01$). It can also be clearly seen from the histograms in Fig. 6.14 that they have different distributions. Multiple comparison of the mean ranks showed that the mean rank of ET from the EC system was significantly different from PM-Mu but not SEBS and PT-JPL. Aggregating ET from hourly to daily time scales improved the agreement between all models and the EC system (Fig. 6.15) as noise in the data or any temporal mismatch and issues related to energy closure are minimized (Finnigan et al., 2003). PT-JPL had the highest r and lowest RMSD in both cases, thereby making it the most reliable model based on this validation study followed by SEBS and PM-Mu.

Ershadi et al. (2014) concluded that the accuracy of LST and air temperature, derived aerodynamic resistance and surface roughness parameters based on NDVI were the most important factors affecting the accuracy of derived ET based on SEBS. Similarly, in the case of PM-Mu, estimation of surface and aerodynamic resistance based on a combination of the predetermined lookup table and meteorological conditions are likely to contribute to uncertainties in derived ET. Moreover, as the use of a high-quality dataset in PM-Mu showed a depreciation in performance in the aforementioned study, the model's structure and physics itself may be inaccurate. The good performance of PT-JPL has been attributed to its minimal requirement of data as inputs, thereby reducing the propagation of errors from the inputs. Its simple yet robust scheme of scaling

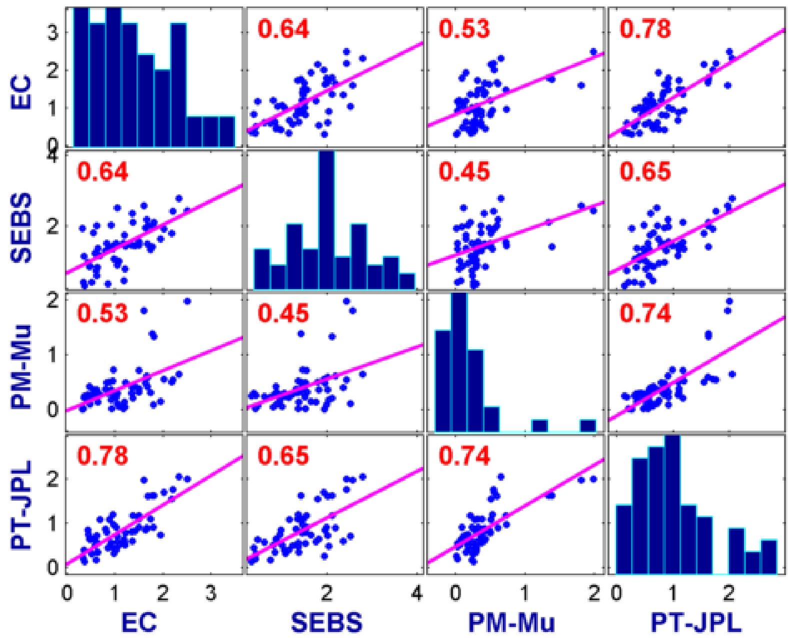

FIGURE 6.14: Correlation matrix comparison of daily $L_{\mathrm{v}}E_{\mathrm{EC}}^{\mathrm{Res}}$ and $L_{\mathrm{v}}E$ based on remote sensing ET models for 59 days of concurrent.

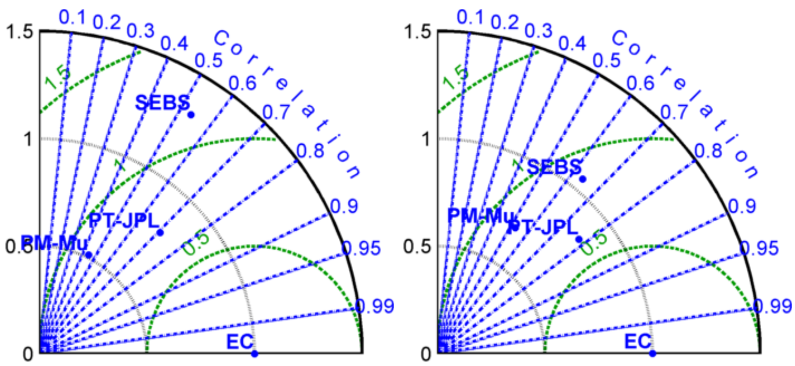

FIGURE 6.15: Taylor diagram summarizing key statistics of ET models relative to EC for hourly $L_{\mathrm{v}}E$ (left) and daily ET (right). The statistics are based on centered RMSD (green radial axis), standard deviation normalized by standard deviation of EC (black) and correlation coefficient (blue spokes).

potential ET to actual ET based on plant physiological status and soil moisture availability has been found to perform well in previous studies (e.g. Ershadi et al., 2014; McCabe et al., 2015). Nevertheless, due to the importance of soil moisture in semi-arid environments, there is still room for improving PT-JPL estimates. García et al. (2013) showed an improvement in ET estimates by incorporating observations of soil moisture (or thermal inertia as a proxy) to improve the plant and soil moisture scaling scheme of PT-JPL. The assimilation of soil moisture remote sensing products from AMSR-2, SMOS or SMAP into remote sensing ET models such as PT-JPL (and SEBS or PM-Mu)

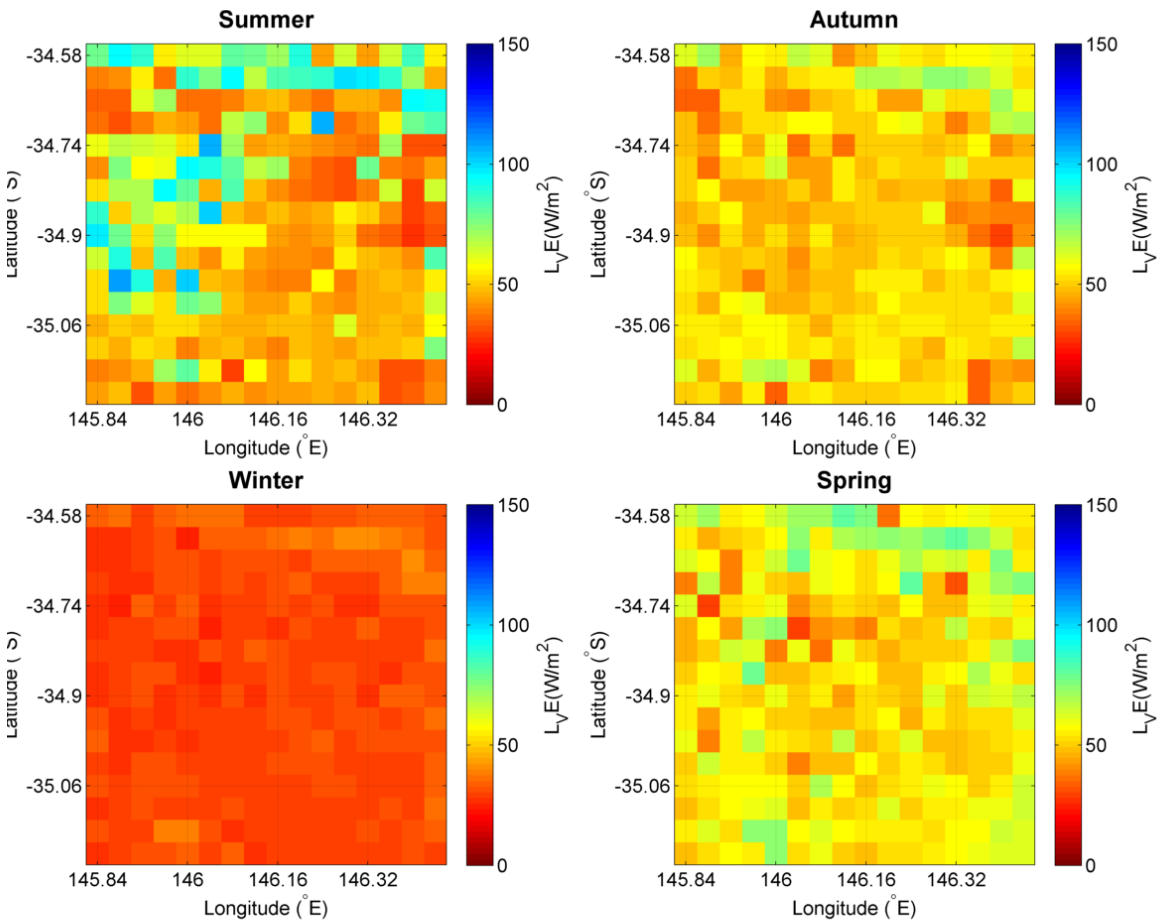

FIGURE 6.16: Average L_vE based on PT-JPL at 12 pm for each season within Yanco.

is therefore expected to improve estimates of ET.

6.4.3 PT-JPL spatial distribution of ET

As PT-JPL has been shown to be the most suitable for the semi-arid environment of the study area, the ability of the model to replicate the variability of L_vE for a bigger area was investigated. Fig. 6.16 shows the mean L_vE based on PT-JPL for each season, together with its standard deviation in Fig. 6.17 shows its standard deviation. A comparison with Fig. 6.1 shows that PT-JPL can correctly detect the higher and larger range of ET expected at the north-western corner of the site where irrigated agricultural activities can be found during summer, and where a line of trees along a river exist running from the east to north-west of the study area. The variation of L_vE was quite similar where the grasslands for grazing can be found south-east of the study area. Both the mean and standard deviation were the lowest during winter whereas the

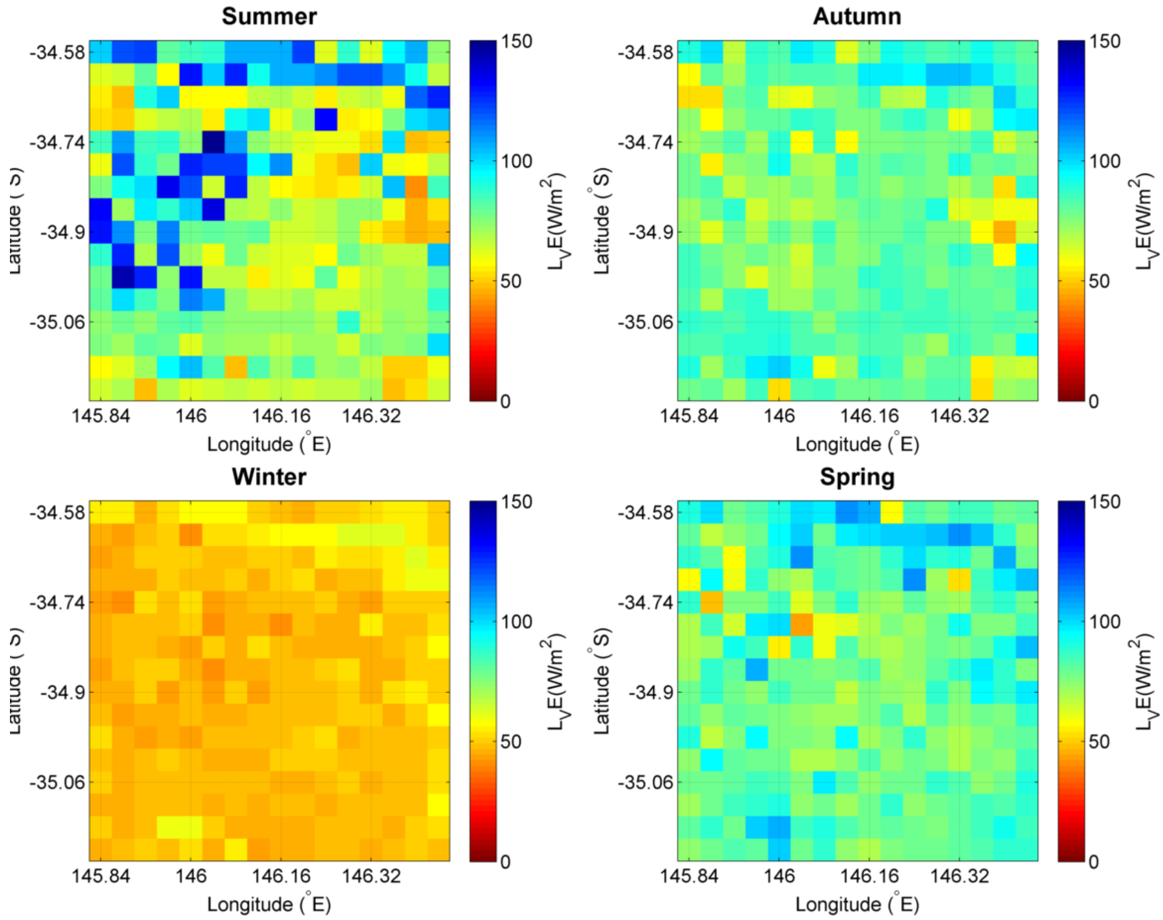

FIGURE 6.17: Standard deviation L_vE based on PT-JPL at 12 pm for each season within Yanco.

spatial variation of ET was the largest during summer due to the presence of mixed activities in the study area. Both autumn and spring showed very similar mean and standard deviation of L_vE. This shows that the PT-JPL ET product is suitable for mapping the temporal and spatial distribution of ET within the Yanco study area. As PT-JPL uses a minimum of meteorological and remote sensing inputs, it is less prone to errors in the input data itself. Moreover, as PT-JPL uses scaling function derived from the inputs themselves rather than parameters which have been tuned or calibrated (such as the lookup table of PM-Mu), it is able to perform well regardless of the biome type.

6.5 Key findings

This study investigated the representativeness of an EC tower for long-term validation of various MTSAT ET products. Scintillometers were placed across a single MTSAT ET product pixel to measure the contribution of $L_\mathrm{v}E$ from different areas within the pixel. As shown in Chapter 5, microwave scintillometers were not suitable for use in a semi-arid environment. However, based on the comparisons between two LAS, it was found that regardless of wind direction derived $L_\mathrm{v}E$ agreed with an r of 0.84 and RMSD of 48.34 W m^{-2}, whereas the two microwave scintillometers had an r of 0.79 and RMSD of 70.50 W m^{-2}. The LAS were then compared with $L_\mathrm{v}E^{\mathrm{Res}}_{\mathrm{EC}}$ and it was found that they had an r of 0.69 and 0.77 and RMSD of 58.32 W m^{-2} and 70.61 W m^{-2} respectively. Therefore, it was concluded that measurements from the EC system are representative of the entire 4 km ET product due to homogeneity within the pixel.

Following the results of the above comparison, the MTSAT ET products were validated and the PT-JPL model found to be the best performer when compared to hourly $L_\mathrm{v}E^{\mathrm{Res}}_{\mathrm{EC}}$, having an r of 0.71 and an RMSD of 63.27 W m^{-2}. However, SEBS was found to overestimate and PM-Mu to underestimate. Although PT-JPL uses a relatively simple and largely empirical formulation of the evaporative process, it was able to perform better than the other two models (Ershadi et al., 2014). As a result, ET models such as PT-JPL which i) utilizes scaling functions derived as a function of conditions of the study area itself, ii) does not require any pre-calibration or tuning of parameters, and iii) requires minimal input forcing, are observed to perform better. Conversely, as LAI, fractional vegetation cover, aerodynamic and surface resistance are calculated from NDVI data, any errors in NDVI data will affect the performance of SEBS and PM-Mu. PT-JPL was also shown to be able to represent the spatial distribution of ET within the larger Yanco area, thereby making it suitable for further application in the validation of land surface model simulations in the next chapter.

Finally, measurements and estimation of ET in semi-arid and arid environments is undeniably a very challenging matter due to its small magnitude in comparison to other energy terms of the surface energy balance equation. Yet, the ability to manage water resources for such environments are even more crucial. Accordingly, it has been shown in this study how errors in the measurement of R_n, G and the non-closure of the energy balance complicates the validation of ET models with EC systems. Therefore, it is recommended that future studies for the validation of ET models should use different statistical parameters, considering both temporal and absolute accuracy to ensure that comparisons with EC measurements are not biased by errors in measurements of input data or observational data.

6.6 Chapter summary

Scintillometers were used in this chapter to establish the representativeness of measurements from an EC system within a 4 km MTSAT ET product pixel. On the basis that the measurements were representative due to homogeneity of the pixel, measurements from the EC system were used to validate MTSAT ET products based on three different remote sensing ET models. Results showed that ET products based on the PT-JPL model performed the best, followed by SEBS and finally PM-Mu. Despite being relatively simple and largely empirical, the lower requirements of PT-JPL for forcing and input data led to the better performance compared to the other two models which requires more data. Consequently, ET products based on the PT-JPL model will be used to evaluate distributed simulations from the land surface model in the following chapter.

Chapter 7

Land surface model evaluation: A demonstration

7.1 Introduction

LSMs are commonly used to predict hydrological variables across a range of spatial and temporal scales. As LSM application evolves from point to regional to global scale, it becomes increasingly challenging to parameterize, calibrate, and evaluate LSMs based on field measurements. In order to verify LSM simulations of physical processes responsible for the exchange of energy and water between the land surface and the atmosphere, this research rationally proposed using remote sensing products in Chapter 2. To this end, Chapters 4 and 6 have rigorously established the validity of remotely sensed soil moisture and evapotranspiration (ET) products, using *in situ* measurements that were identified as representative of the area (Chapters 3 and 5). In summary, soil moisture retrievals from Soil Moisture and Ocean Salinity (SMOS) and ET from the modified Priestly Taylor model (PT-JPL) were found to perform best. Thus, it is in this chapter that we show the final goal of this research, which is to demonstrate the applicability of remote sensing products in evaluating simulations of soil moisture and ET at distributed scales. The importance of understanding the accuracy of remote sensing products prior to application is vital, and is shown clearly in this final chapter.

7.2 Study area and model set-up

The work presented in this chapter focuses on a 60 km × 60 km area within the Yanco study area. The extent of this area relative to the representative soil moisture stations (YA5 and YB7a) and the eddy covariance (EC) system, and the remote sensing product grid cells are shown in Fig. 7.1 and 7.2.

Soil moisture and ET were simulated at 1 km scale within this 60 km × 60 km area using Joint UK Land Environment Simulator (JULES) subsequent to a 10-year spin-up. JULES is an LSM which simulates the fluxes of carbon, water and energy between the land surface and the atmosphere based on four sub-models: radiation, vegetation, soil and snow (Best et al., 2011; Clark et al., 2011a, 2008). In this study, the vegetation and soil sub-models are of interest for the simulation of soil moisture and ET. For each grid cell within JULES, land cover heterogeneity can be represented by five plant functional types and four non-vegetation types. The water, energy and carbon fluxes are computed separately for each surface type, and then aggregated based on their fractional cover within each grid. As for soil processes, soil layers have been divided into four layers being 0.08 m, 0.30 m, 0.60 m and 0.90 m thick. Precipitation is partitioned by JULES into through-fall, infiltration and surface run-off. Distribution of infiltration within the soil layers is then based on a finite difference form of Richard's equation, where the extraction of soil moisture from plants for transpiration depends on the root density and soil moisture availability. In this study, soil water retention characteristics follow the model of Brooks and Corey (1964). ET in JULES is a combination of transpiration, soil evaporation and evaporation from plant canopy. Plant transpiration and soil evaporation is restricted by canopy conductance and soil moisture conditions, whereas canopy evaporation is assumed to occur at the potential rate.

The model was driven by meteorological data (incoming short-wave and long-wave radiation, temperature, specific humidity, wind speed, surface pressure and rainfall) obtained from the Australian Community Climate Earth System Simulator - Australia (ACCESS-A, Bureau of Meteorology, 2010) at hourly time-steps. ACCESS-A's 12 km grid was interpolated based on a triangulation method to derive forcing at 1 km scales. Whilst it was unclear based on previous studies as to whether ACCESS-A had a tendency to over- or under-estimate precipitation, it is generally known that the forecasts are biased (Bureau of Meteorology, 2010). Therefore, the ACCESS-A precipitation data was bias corrected based on daily 5 km Australian Water Availability Project (AWAP, Jones et al., 2007) data according to the methods described in Berg et al. (2003). The AWAP product is based on the precipitation recorded by rain-gauges. Soil parameters were derived from the Digital Atlas of Australian Soils (McKenzie et al., 2000), and land cover was based on the national dynamic land cover dataset (Lymburner and Australia, 2011) (Fig. 7.1). Simulations from this set-up were from January 2010 to July 2014, and will be referred to as JULES1.

Another scenario was carried out using the satellite based soil parameters derived by Bandara et al. (2015) and the radar based precipitation dataset from Shahrban et al. (2016) that was bias corrected using rain-gauges in the study site. The derived soil parameters include the i) Clapp and Hornberger exponent, b, ii) hydraulic conductivity at saturation, iii) soil matric suction at air entry, iv) volumetric fraction of soil moisture at saturation, v) volumetric fraction of soil moisture at the critical point, equivalent to a soil suction of 3.364 m, and vi) volumetric fraction of soil moisture at wilting point, assumed to be for a soil suction of 152.9 m, for surface (0-5 cm) soils, Horizon A (5 - 30 cm), and Horizon C (below 30 cm). The spatial extent of these products are shown in Fig. 7.1. Simulations based on these "improved" datasets were run from January 2010 up to December 2012 and will be referred to as JULES2.

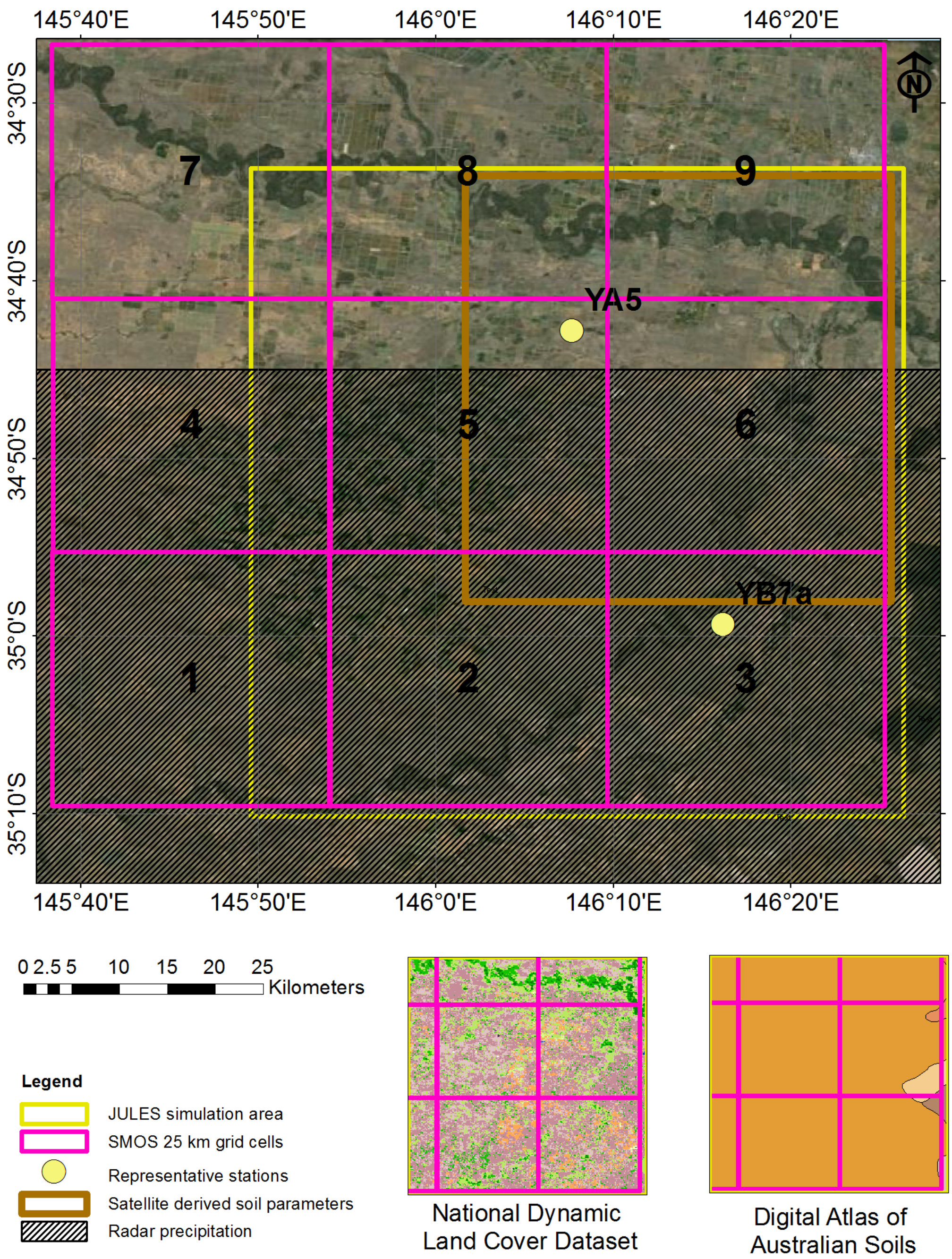

FIGURE 7.1: Map of study area showing locations of most representative soil moisture SMOS satellite centre points/grid cells, and the extent of the "improved" datasets. The insets at the bottom right show the distribution of vegetation based on the Dynamic Land Cover Map, and soil type based on the Digital Atlas of Australian Soils, within the JULES simulation area.

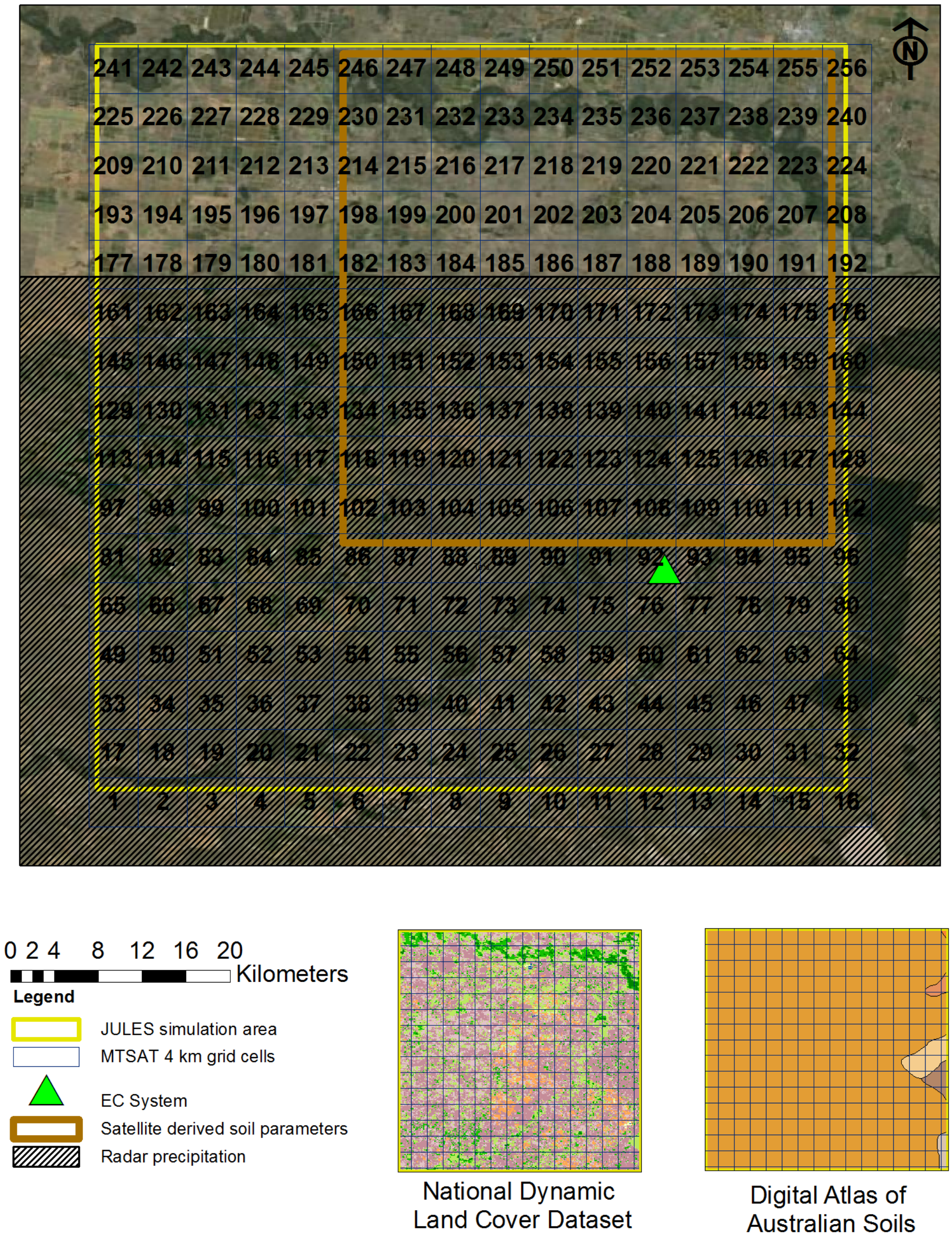

FIGURE 7.2: Map of study area showing locations of the EC station (EC3), MTSAT satellite centre points/grid cells, and the extent of the "improved" datasets. The insets at the bottom right show the distribution of vegetation based on the Dynamic Land Cover Map, and soil type based on the Digital Atlas of Australian Soils, within the JULES simulation area.

7.3 Observational data and methodology

The observational datasets used to evaluate simulations include both the *in situ* and remote sensing products extensively described in previous chapters. As mentioned earlier, the objective of this chapter is to demonstrate the evaluation of LSM simulations using remote sensing observations. However, the readily available *in situ* measurements of soil moisture and ET at the study area provides a further opportunity to verify the accuracy of these LSM simulations at the 1 km point scale. To this end, near-surface (0 - 5 cm) soil moisture from the representative stations YA5 and YB7a, and measurements of ET (expressed as $L_{\mathrm{v}}E$) from the representative EC system were used (combination of EC1, EC2 and EC3 as per Chapter 6). For this reason there are gaps in the EC time-series during periods between field campaigns. The same processing and data quality processes as per the previous chapters have been applied.

In the case of remote sensing products, the 25 km grid soil moisture derived from SMOS were used for both ascending and descending overpasses as they showed marginal differences based on the results of Chapter 7. However, as $\mathrm{LP2_X}$ and JX2 were found also found to perform well, an evaluation will also be carried out based on these two products. Furthermore, to illustrate the difference in using a well- and less-performing product, $\mathrm{LP2_{C1}}$ and $\mathrm{LP2_{C2}}$ have also been used to evaluate simulations at distributed scales. Since data from AMSR-2 was only available from July 2012, evaluation with remote sensing products were restricted from July 2012 to July 2014. However, to extend the number of simulated ET for comparison between JULES1 and JULES2, soil moisture from these two datasets were inter-compared from January 2010 to July 2014.

Finally, 4 km PT-JPL ET products validated in Chapter 6, and JULES simulated ET (expressed as $L_{\mathrm{v}}E$) were compared from January 2010 to December 2012. To understand the differences which can occur if remote sensing products are applied without a prior understanding of their accuracy, evaluations were also carried out using ET products based on the SEBS and PM-Mu model. Daily ET was computed using the same method as in Chapter 6. Due to the short overlap of data availability from all sources, all available time-steps between the remote sensing and EC measurements were used. The different periods used in the evaluation are summarized in Table 7.1. Although sub-sampling was at hourly time-scales to coincide with JULES simulations, it should be remembered that observations from SMOS are only available approximately twice a day.

Table 7.1: Data periods used for each dataset.

Variable/Data	**In-Situ**	**Remote sensing**	**JULES1**	**JULES2**
Soil moisture	Jan 2010 - Jul 2014	Jul 2012 - Jul 2014	Jan 2010 - Jul 2014	Jan 2010 - Dec 2012
Evapotranspiration	Jan 2010 - Jul 2014	Jan 2010 - Dec 2012	Jan 2010 - Dec 2014	Jan 2010 - Dec 2012

Evaluation of soil moisture and ET simulated by JULES were based on inter-comparisons between point-scale *in situ* measurements (1 km) and remote sensing products scales (25 km and 4 km for soil moisture and ET respectively). The 1 km simulations were aggregated to coincide with the grid of the coarse scale satellite products prior to evaluation. To match the near-surface soil moisture measurements at the stations with that observed by the satellite borne passive microwave sensors, JULES simulations from the top 0 - 8 cm were used for comparisons. The notation used to identify the different grid cells of each product follows the numbering of the grid cells, beginning from 1 at the bottom left hand corner, increasing from left to right, and north to south, ending at the top right hand corner as shown in Fig. 7.1 and 7.2. Soil moisture 25 km grids are preceded by 'S', and MTSAT 4 km ET grids by 'E'. For instance, soil moisture measurements from YA5 would be within the 5$^{\text{th}}$ SMOS grid cell (annotated herein as S5) and YB7a would fall within the 3$^{\text{rd}}$ SMOS grid cell (annotated herein as S3) (Fig. 7.1). Likewise, the eddy covariance (EC) system falls within the 92$^{\text{nd}}$ grid cell (annotated herein as E92) of the 4 km MTSAT ET products (Fig. 7.2).

Based on Fig. 7.1, it can be seen that due to the limited extent of the retrieved datasets, none of the aggregated JULES2 simulations to SMOS grids were fully based on the satellite derived soil parameters and radar precipitation. Similarly, E92 falls out of the area with the satellite retrieved soil parameters (Fig. 7.2). Consequently, for comparisons based on *in situ* measurements, to understand if the derived datasets have improved the simulations, aggregated JULES2 simulations of S5 were compared with YA5, whereas, YB7a were compared with S6 instead of S3 since land cover of both grids were similar. Likewise, 4 km JULES2 simulations north of E92, i.e. E108 was used as a proxy for E92 (Fig. 7.2).

7.4 Results and discussion

The model evaluation begins with comparisons within grid cells where *in situ* measurements are available. Since these sites have been explored in the earlier chapters, there is a better understanding regarding the conditions and characteristics of their surrounding area. This can assist in interpreting the general performance of JULES. No doubt local or in-depth knowledge is only limited to well-monitored sites and therefore, where this is not available, remote sensing is still required for assessing the performance of the model. Consequently, after comparisons at selected grid cells where *in situ* measurements are available, an assessment for an extended area based on remote sensing products was carried out. Both the ability of the model to correctly simulate the temporal and absolute values of soil moisture and $L_{\mathrm{v}}E$ were discussed.

7.4.1 Quantitative evaluation

Based on Fig. 7.3, JULES1 was observed to perform quite well at S5 and S3 compared to *in situ* and SMOS soil moisture measurements. Rainfall events were captured except for the time between January 2013 and March 2013. It is likely that during this period, rainfall events based on AWAP data was not well-captured and therefore was not reflected in the soil moisture evolution. Nevertheless, overall, the temporal and absolute soil moisture variability were also well captured compared to measurements from YA5, YB7a and SMOS soil moisture. Simulations of soil moisture based on JULES2 also performed well, but had a smaller range of dynamics and slower dry-down than JULES1. The movement of water between layers is defined by both soil hydraulic conductivity and soil matric suction. Whilst the soil hydraulic conductivity value defined in JULES1 and JULES2 were somewhat similar, soil matric suction based on the satellite retrieved parameters were higher.

In the case of $L_{\mathrm{v}}E$, shown as daily ET in Fig. 7.4, JULES1 and JULES2 performed similarly well between May to October (late Austral autumn to early spring). However, during late spring, JULES1 underestimated whereas JULES2 overestimated ET. Conversely, JULES1 overestimated in autumn whereas JULES2 underestimated. This led to a low correlation between JULES1 and JULES2 despite having similar vegetation parameters. Moreover, although PT-JPL and JULES1 have both been prescribed with similar meteorological information (ACCESS-A), the agreement between both datasets was not much better than JULES2 which had a different precipitation dataset. Daily ET based on PT-JPL fell in between JULES1 and JULES2.

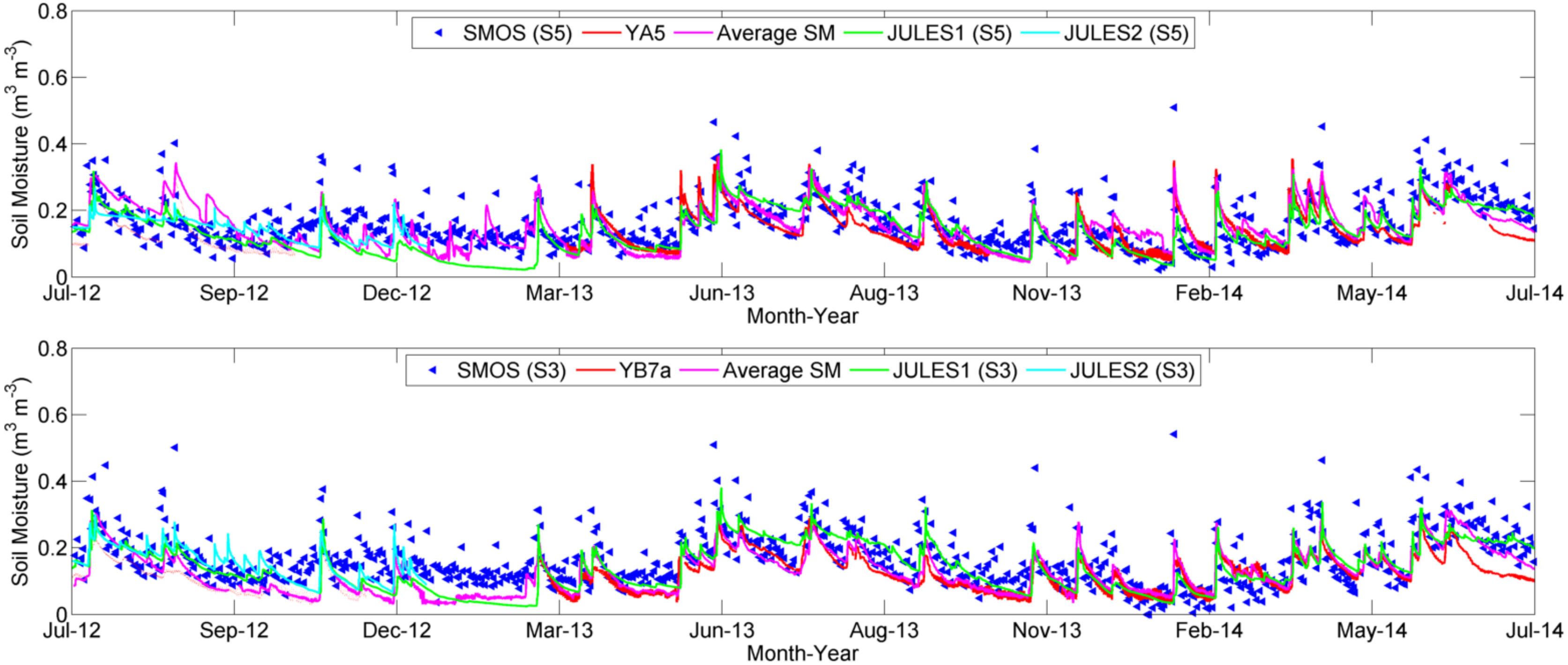

FIGURE 7.3: Timeseries comparing a) soil moisture based on YA5 station, SMOS (G5), JULES1 (G5) and JULES2 (G5) and b) soil moisture based on YB7a station, SMOS (G3) JULES1 (G3) and JULES2 (G3).

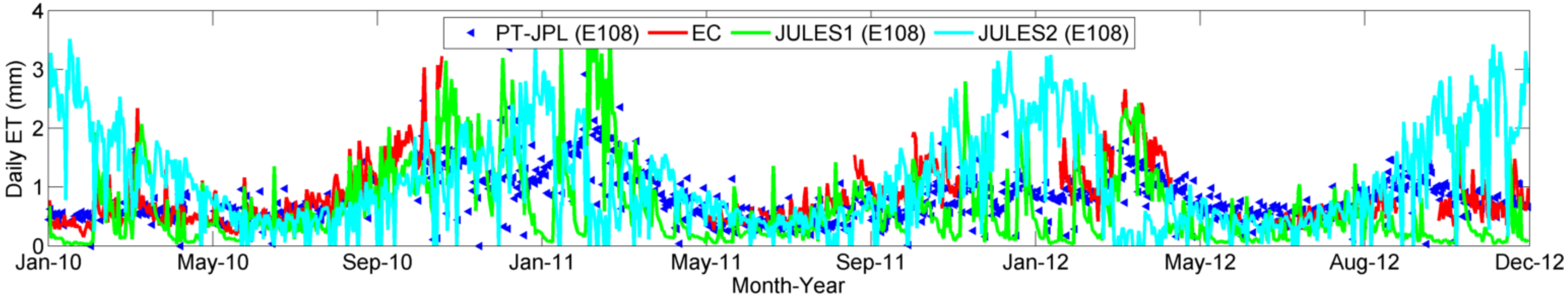

FIGURE 7.4: Timeseries comparing $L_{\mathrm{v}}E$ based on PT-JPL (E108), the EC system, JULES1 (E108) and JULES2 (E108).

Based on a qualitative comparison, after rainfall events and corresponding to peaks in soil moisture, ET simulated by JULES1 was observed to increase. As the soil moisture content decreased, ET was also diminished. Conversely, in JULES2, ET decreased immediately after rainfall events but increased during the soil moisture dry-down. Soil hydraulic conductivity controls how soil moisture is distributed within the soil layers. The distribution of soil moisture within the layers will then determine the availability of water for evaporation or transpiration by plants. Consequently, the availability of soil moisture for direct evaporation, or plant transpiration is very dependent on soil parameters prescribed in the model. Additionally, for a semi-arid area such as the study site, cracking in soils have been found to complicate the approximation of soil moisture based on LSM or remote sensing methods (Liu et al., 2010). Soil cracking increases the loss of soil moisture through direct evaporation to below the permanent wilting point. However, soil cracking is not modelled by JULES. The earlier peaks based on JULES1 compared to JULES2 suggests that soil moisture may be more readily available for direct evaporation in JULES1. An in-depth study looking at the simulations within deeper soil layers would likely provide a better insight but this is not within the scope of this study.

During spring, transpiration rate is expected to be at its peak as vegetation would be thriving. However, since the dynamics of vegetation phenology were not included in both JULES1 and JULES2 this was not reflected in the simulations. In the case of PT-JPL, information regarding vegetation conditions are provided in the form of LAI and soil moisture status is inferred based on relative humidity (Fisher et al., 2008). Consequently, a combination of differences in specification of vegetation phenology, and differences in soil parameters prescribed may have led to drastically different dynamics in ET from JULES1, JULES2 and PT-JPL. Consequently, through the concurrent evaluation of soil moisture and $L_{\mathrm{v}}E$ from JULES, the importance and interplay between both soil and vegetation parameters in controlling the rate in which ET occurs was identified.

7.4.2 Point-based quantitative evaluation

7.4.2.1 Soil moisture

The statistics derived from this inter-comparison of *in situ* measurements of soil moisture for the YA area based on YA5, and the YB area based on YB7a, with SMOS derived soil moisture and JULES simulated soil moisture are summarized in Tables 7.3 to 7.6 for root mean square difference (RMSD), Pearson correlation (r), bias, mean average error (MAE) and unbiased RMSD (ubRMSD) respectively. However, unless specified, r and RMSD are the two statistics used for evaluating the simulations. Scatterplots of these comparisons can also be found in Appendix D.

Within the YA area, the agreement between JULES1 simulations at 1 km and 25 km grids with soil moisture measurements from YA5 were comparable with an r of 0.72 and 0.71 respectively, and RMSD of 0.05 $m^3\ m^{-3}$ for both (Tables 7.2 and 7.3). The difference between these two scales (1 km and 25 km) were small with an r of 0.99 and RMSD of 0.01 $m^3\ m^{-3}$. This is due to the small variation of soil, vegetation, and rainfall. Soil moisture based on YA5 and SMOS also agreed well with an r of 0.61 and RMSD of 0.07 $m^3\ m^{-3}$ (similar to r in Chapter 4 despite a different period and length of record).

With confidence in measurements from YA5 and the SMOS soil moisture products, an evaluation of JULES1 with SMOS resulted in an r of 0.63 and RMSD of 0.07 $m^3\ m^{-3}$. Generally, while JULES1 overestimated soil moisture (bias: -0.03 $m^3\ m^{-3}$) JULES2 underestimated soil moisture compared to SMOS (bias: 0.11 $m^3\ m^{-3}$). Evaluation of JULES2 with SMOS yielded an r of 0.58 which was an improvement from an r of 0.49 when evaluated with measurements from YA5 (Figure 7.5). The different precipitation forcing and soil parameters dataset used in JULES2 degraded soil moisture simulations in comparison to *in situ* measurements but had little effect on r when compared with SMOS soil moisture products. This may be because a shorter dataset was used for comparison with JULES2 due to the short overlap period, and fewer observations were were available for comparison with SMOS compared to station measurements.

At the the YB area, comparison between simulations at S3 and S6 had a high agreement with an r of 0.97 and RMSD of 0.02 $m^3\ m^{-3}$, thereby justifying the use of simulations from S6 as a proxy for S3 to evaluate simulations from JULES2 (Tables 7.2 and 7.3). The agreement between *in situ* measurements from YB7a and JULES1 simulations were higher here (YB area) than at the YA area with an r > 0.80 and RMSD < 0.05 $m^3\ m^{-3}$ at both 1 km and 25 km scales. This is likely due to the greater homogeneity of the YB area, meaning that variability sensed within the large footprint of SMOS is lower for this area, and that measurements from YB7a are therefore more representative. When

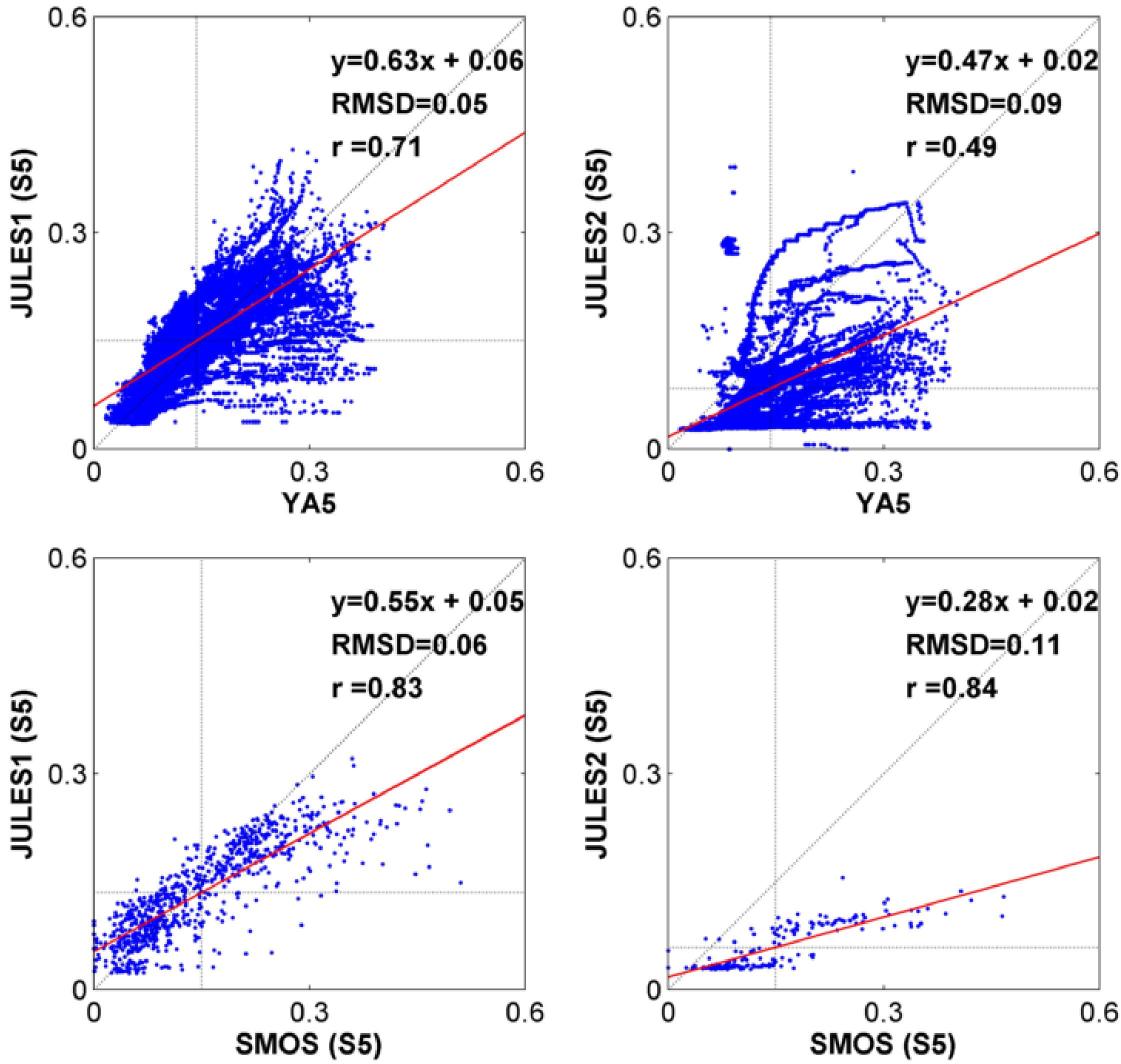

FIGURE 7.5: Scatterplot comparisons between soil moisture based on YA5, SMOS station, JULES1 and JULES2 at S5.

JULES2 simulations were compared with measurements at YB7a, r was slightly lower at 0.71 and RMSD was higher at 0.08 m^3 m^{-3}.

When evaluated with SMOS soil moisture at 25 km grids instead, r for both JULES1 and JULES2 did not change much at 0.80 and 0.70 respectively (Figure 7.6). However, as with the YA area, in terms of absolute accuracy, JULES1 also performed better than JULES2 when evaluated with SMOS. RMSD and bias of JULES1 and JULES2 were 0.06 m^3 m^{-3} and -0.01 m^3 m^{-3}, and 0.07 m^3 m^{-3} and 0.03 m^3 m^{-3} respectively (Table 7.3 and 7.5).

In both the YA and YB areas, JULES2 underperformed compared to *in situ* measurements in terms of its ability to simulate the absolute value and temporal variability of soil moisture. In spite of this, compared to SMOS, both JULES1 and JULES2 showed

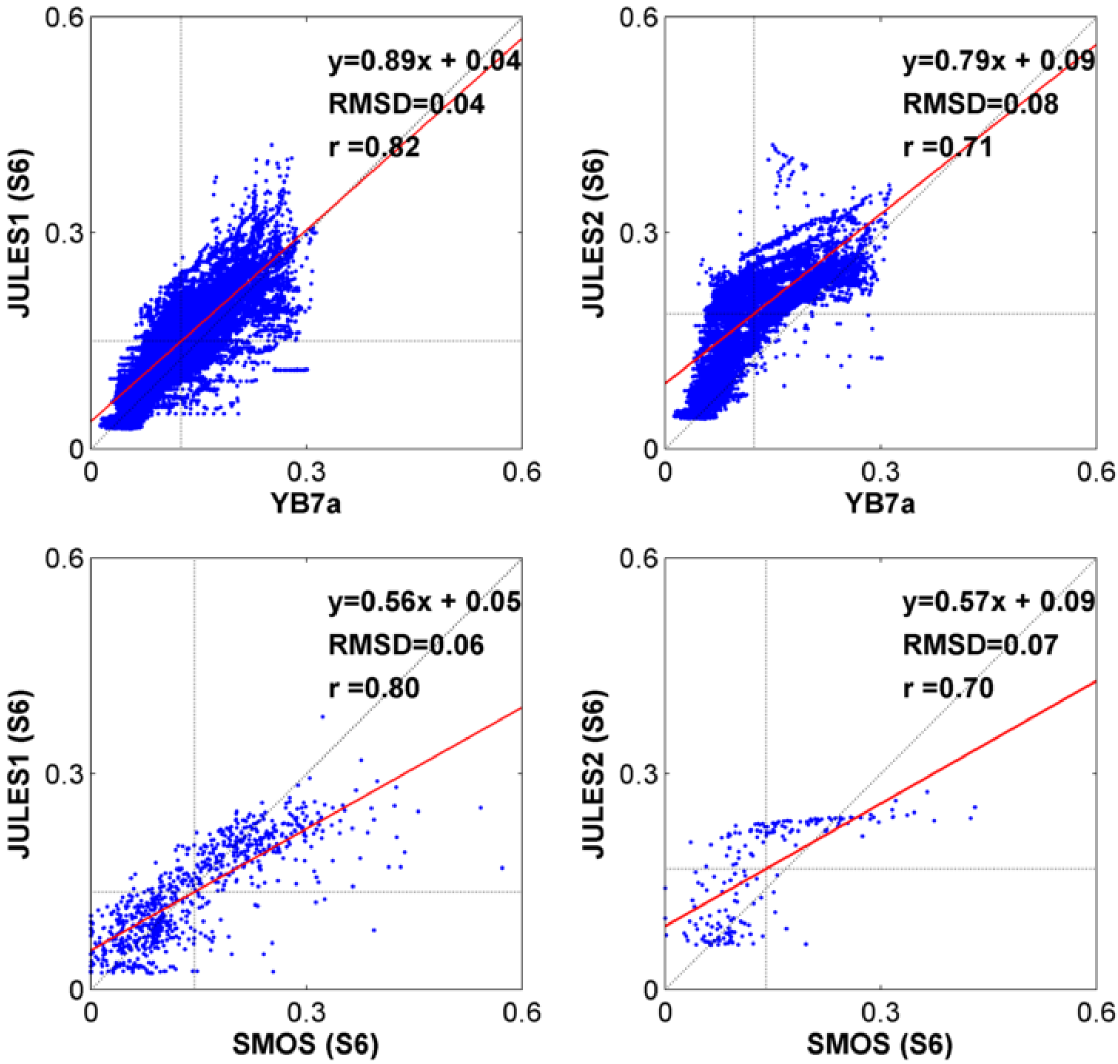

FIGURE 7.6: Scatterplot comparisons between soil moisture based on YB7a, SMOS station, JULES1 and JULES2 at S6.

relatively similar performance based on r. Yet, if absolute soil moisture was considered, i.e. performance in terms of RMSD or MAE, evaluation of soil moisture using SMOS resulted in a higher agreement with JULES1 rather than JULES2. Reasons which may have contributed to the mixed results when comparing with SMOS include: i) soil parameters from JULES2 have been derived based on a disaggregated SMOS soil moisture product (Bandara et al., 2015), ii) the evaluation period from JULES2 was shorter, and iii) comparisons with *in situ* measurements were at hourly time-steps and only twice a day with SMOS. Nevertheless, SMOS was still useful in differentiating the performance of JULES1 and JULES2 based on absolute soil moisture. This also reiterates the importance of validating remote sensing soil moisture products based on their ability to capture not only the temporal dynamics, but also absolute soil moisture values as shown

TABLE 7.2: r derived from comparing different pairs of datasets for soil moisture at the YA and YB area.

YA Dataset	JULES1 (1 km)	JULES1 (S5)	SMOS (S5)	JULES2 (S5)
In-situ (YA5)	0.72	0.71	0.72	0.49
JULES1 (1km)	-	0.99	0.62	0.50
JULES1 (S5)	-	-	0.63	0.51
SMOS (S5)	-	-	-	0.58

YB Dataset	JULES1 (1 km)	JULES1 (S3)	JULES1 (S6)	SMOS (S3)	JULES2 (S6)	SMOS (S6)
In-situ (YB7a)	0.83	0.82	0.82	0.79	0.71	0.76
JULES1 (1km)	-	1.00	0.98	0.82	0.75	0.80
JULES1 (S3)	-	-	0.97	0.82	0.75	0.79
JULES1 (S6)	-	-	-	0.82	0.78	0.80
SMOS (S3)	-	-	-	-	0.76	0.97
JULES2 (S6)	-	-	-	-	-	0.70

TABLE 7.3: RMSD derived from comparing different pairs of datasets for soil moisture at the YA and YB area.

YA Dataset	JULES1 (1 km)	JULES1 (S5)	SMOS (S5)	JULES2 (S5)
In-situ (YA5)	0.05	0.05	0.06	0.09
JULES1 (1km)	-	0.01	0.07	0.09
JULES1 (S5)	-	-	0.07	0.09
SMOS (S5)	-	-	-	0.12

YB Dataset	JULES1 (1 km)	JULES1 (S3)	JULES1 (S6)	SMOS (S3)	JULES2 (S6)	SMOS (S6)
In-situ (YB7a)	0.04	0.05	0.04	0.08	0.08	0.07
JULES1 (1km)	-	0.01	0.01	0.06	0.05	0.06
JULES1 (S3)	-	-	0.02	0.06	0.05	0.06
JULES1 (S6)	-	-	-	0.06	0.06	0.06
SMOS (S3)	-	-	-	-	0.06	0.03
JULES2 (S6)	-	-	-	-	-	0.07

TABLE 7.4: Bias derived from comparing different pairs of datasets for soil moisture at the YA and YB area.

YA Dataset	JULES1 (1 km)	JULES1 (S5)	SMOS (S5)	JULES2 (S5)
In-situ (YA5)	-0.01	-0.01	-0.03	0.06
JULES1 (1km)	-	0.00	-0.03	0.07
JULES1 (S5)	-	-	-0.03	0.07
SMOS (S5)	-	-	-	0.11

YB Dataset	JULES1 (1 km)	JULES1 (S3)	JULES1 (S6)	SMOS (S3)	JULES2 (S6)	SMOS (S6)
In-situ (YB7a)	-0.03	-0.03	-0.02	-0.04	-0.06	-0.03
JULES1 (1km)	-	0.00	0.00	-0.01	-0.04	0.00
JULES1 (S3)	-	-	0.01	-0.01	-0.03	0.00
JULES1 (S6)	-	-	-	-0.01	-0.04	-0.01
SMOS (S3)	-	-	-	-	-0.02	0.01
JULES2 (S6)	-	-	-	-	-	0.03

in Chapter 4.

7.4.2.2 Evapotranspiration

Tables 7.7 to 7.11 compares EC measured L_vE with satellite retrieved L_vE based on PT-JPL, and L_vE simulated based on JULES1 and JULES2 at different spatial scales at hourly time-steps. Scatterplots of comparisons between EC measurements and modelled ET can be found in Appendix D. A good agreement was found between EC measurements

Table 7.5: MAE derived from comparing different pairs of datasets for soil moisture at the YA and YB area.

YA Dataset	JULES1 (1 km)	JULES1 (S5)	SMOS (S5)	JULES2 (S5)
In-situ (YA5)	0.03	0.04	0.05	0.07
JULES1 (1 km)	-	0.00	0.05	0.08
JULES1 (S5)	-	-	0.05	0.08
SMOS (S5)	-	-	-	0.11

YB Dataset	JULES1 (1 km)	JULES1 (S3)	JULES1 (S6)	SMOS (S3)	JULES2 (S6)	SMOS (S6)
In-situ (YB7a)	0.04	0.04	0.03	0.06	0.07	0.05
JULES1 (1 km)	-	0.00	0.01	0.04	0.04	0.04
JULES1 (S3)	-	-	0.01	0.04	0.04	0.04
JULES1 (S6)	-	-	-	0.04	0.04	0.04
SMOS (S3)	-	-	-	-	0.05	0.02
JULES2 (S6)	-	-	-	-	-	0.05

Table 7.6: ubRMSD derived from comparing different pairs of datasets for soil moisture at the YA and YB area.

YA Dataset	JULES1 (1 km)	JULES1 (S5)	SMOS (S5)	JULES2 (S5)
In-situ (YA5)	0.05	0.05	0.06	0.07
JULES1 (1 km)	-	0.01	0.06	0.06
JULES1 (S5)	-	-	0.06	0.06
SMOS (S5)	-	-	-	0.05

YB Dataset	JULES1 (1 km)	JULES1 (S3)	JULES1 (S6)	SMOS (S3)	JULES2 (S6)	SMOS (S6)
In-situ (YB7a)	0.03	0.03	0.04	0.07	0.05	0.07
JULES1 (1 km)	-	0.01	0.01	0.06	0.04	0.06
JULES1 (S3)	-	-	0.01	0.06	0.04	0.06
JULES1 (S6)	-	-	-	0.06	0.04	0.06
SMOS (S3)	-	-	-	-	0.06	0.02
JULES2 (S6)	-	-	-	-	-	0.06

Table 7.7: RMSD derived from comparing different pairs of datasets for L_vE.

ET Dataset	JULES1 (1 km)	JULES1 (E92)	JULES1 (E108)	PTJPL (E92)	JULES2 (E108)	PTJPL (E108)
In-situ (EC)	78.88	78.41	79.36	61.88	147.00	61.87
JULES1 (1 km)	-	2.64	6.60	54.06	126.75	60.01
JULES1 (E92)	-	-	7.51	53.64	126.49	59.65
JULES1 (E108)	-	-	-	53.81	127.00	60.08
PTJPL (E92)	-	-	-	-	103.43	18.53
JULES2 (E108)	-	-	-	-	-	92.37

and JULES1 simulations at the 1 km grid in which the EC system was located, and 4 km PT-JPL scales for both E92 and E108 with an r and RMSD of approximately 0.68 and 79 W m^{-2}. PT-JPL derived L_vE was found to compare well with EC measurements as seen in the previous chapter, with an r of 0.73 and 0.67, and RMSD of 61.88 W m^{-2} and 61.87 W m^{-2} at E92 and E108 respectively. However, a poor agreement was found between EC measurements and JULES2 simulations with an r of 0.24 and an RMSD of 147 W m^{-2}.

The agreement between L_vE based on JULES1 (1 km) and PT-JPL at E92 and E108 were similar with comparisons made between L_vE from JULES1 (1 km) and the EC system. This indicates that simulations at this point were well described by JULES1.

TABLE 7.8: r derived from comparing different pairs of datasets for L_vE (top rows).

ET Dataset	JULES1 (1 km)	JULES1 (E92)	JULES1 (E108)	PTJPL (E92)	JULES2 (E108)	PTJPL (E108)
In-situ (EC)	0.68	0.68	0.67	0.73	0.24	0.67
JULES1 (1 km)	-	1.00	1.00	0.71	0.35	0.68
JULES1 (E92)	-	-	1.00	0.71	0.35	0.68
JULES1 (E108)	-	-	-	0.70	0.34	0.67
PTJPL (E92)	-	-	-	-	0.63	0.97
JULES2 (E108)	-	-	-	-	-	0.74

TABLE 7.9: Bias derived from comparing different pairs of datasets for L_vE.

ET Dataset	JULES1 (1 km)	JULES1 (E92)	JULES1 (E108)	PTJPL (E92)	JULES2 (E108)	PTJPL (E108)
In-situ (EC)	36.12	35.91	36.81	27.80	-24.93	13.85
JULES1 (1 km)	-	-0.01	0.53	-1.57	-4.20	-8.99
JULES1 (E92)	-	-	0.54	-1.46	-4.19	-8.88
JULES1 (E108)	-	-	-	-2.30	-4.73	-9.71
PTJPL (E92)	-	-	-	-	-10.41	-7.22
JULES2 (E108)	-	-	-	-	-	3.37

TABLE 7.10: MAE derived from comparing different pairs of datasets for L_vE.

ET Dataset	JULES1 (1 km)	JULES1 (E92)	JULES1 (E108)	PTJPL (E92)	JULES2 (E108)	PTJPL (E108)
In-situ (EC)	58.47	58.07	58.79	46.13	103.70	46.41
JULES1 (1 km)	-	1.41	2.80	28.19	79.71	32.85
JULES1 (E92)	-	-	3.50	28.13	79.56	32.78
JULES1 (E108)	-	-	-	28.08	80.07	32.85
PTJPL (E92)	-	-	-	-	63.88	8.63
JULES2 (E108)	-	-	-	-	-	58.73

TABLE 7.11: ubRMSD derived from comparing different pairs of datasets for L_vE.

ET Dataset	JULES1 (1 km)	JULES1 (E92)	JULES1 (E108)	PTJPL (E92)	JULES2 (E108)	PTJPL (E108)
In-situ (EC)	70.12	69.70	70.30	55.29	144.87	60.30
JULES1 (1 km)	-	2.64	6.58	54.04	126.68	59.34
JULES1 (E92)	-	-	7.49	53.62	126.42	58.98
JULES1 (E108)	-	-	-	53.76	126.92	59.29
PTJPL (E92)	-	-	-	-	102.90	17.06
JULES2 (E108)	-	-	-	-	-	92.31

Furthermore, both 4 km aggregated simulations agree highly with an r of 1 and RMSD of 7.51 W m^{-2} (Table 7.7), confirming the earlier assumption that JULES2 E92 and E108 are similar, and therefore simulations at E108 can be used as a proxy of simulations at E92 for comparisons with JULES2 simulations. Yet, when EC measured L_vE and JULES2 simulations at E108 were compared, r was 0.24 and RMSD was 147 W m^{-2}. JULES2 overestimated L_vE by 24.93 W m^{-2} (Table 7.9). This indicates that despite using the satellite retrieved soil parameters and bias corrected radar precipitation, performance of the simulations did not improve.

Comparisons of PT-JPL derived L_vE at E108 showed a better agreement with JULES2 simulations than JULES1 in terms of r (0.74 and 0.67 respectively), but ubRMSD was higher (59.29 W m^{-2} and 92.31 W m^{-2} respectively) (Figure 7.7). As with measurements from the EC system, JULES2 was observed to overestimate L_vE compared to PT-JPL. Availability of net radiation, R_n drives the pattern in which surface heat fluxes like L_vE

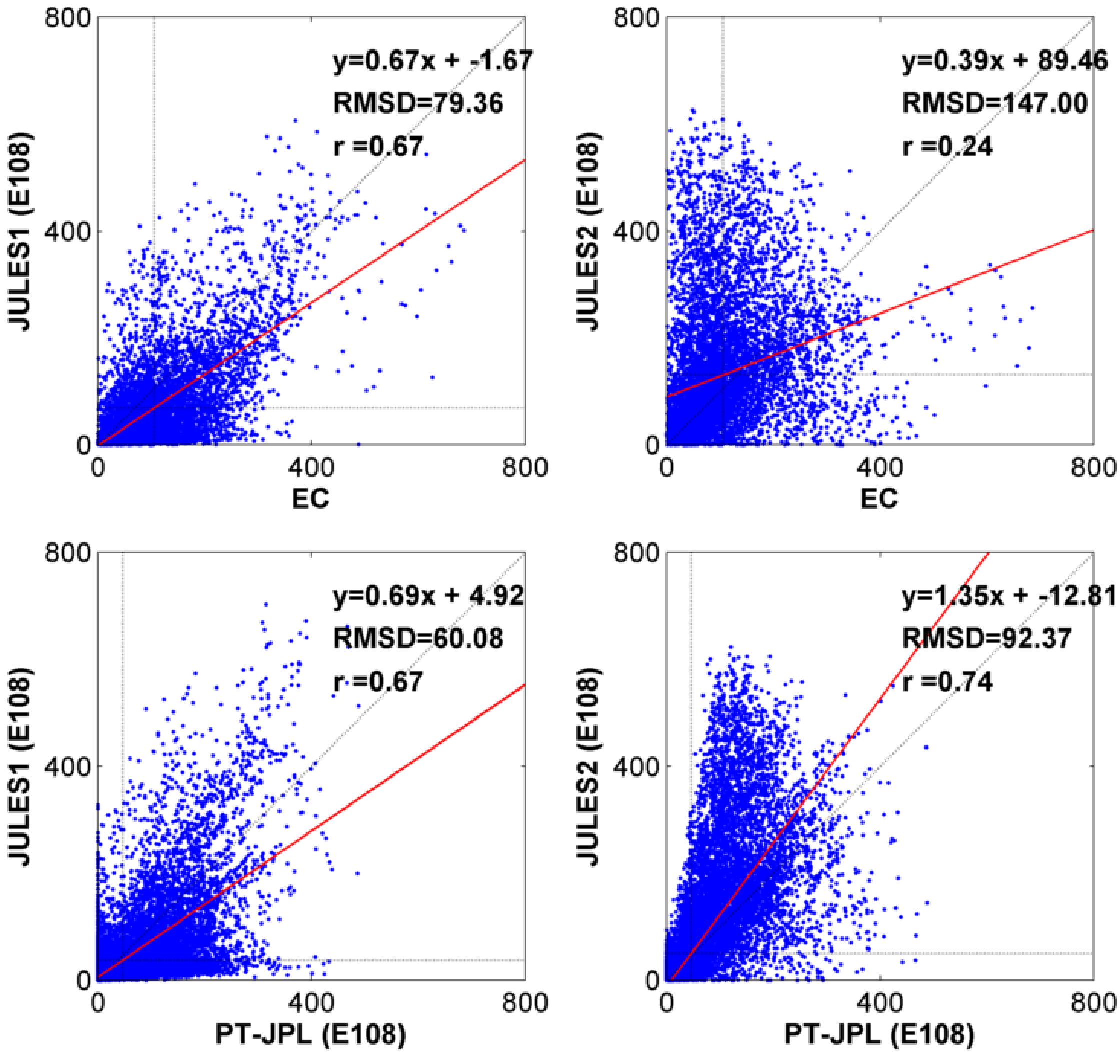

FIGURE 7.7: Scatterplot comparisons between soil moisture based on YB7a, SMOS station, JULES1 and JULES2 at S6.

varies across the day. Therefore, since R_n prescribed in the JULES1, JULES2 and PT-JPL are from ACCESS-A, and therefore similar, it is not surprising that r was similar. However, RMSD would be more dependent on the total amount of water available for ET to occur, i.e. precipitation. The different precipitation products used in JULES1 and JULES2 are likely to have led to large differences in RMSD. As a result, since RMSD and outliers can degrade r, the large RMSD between EC measurements and JULES2 simulations led to very low r between them despite having a more similar r when compared with L_vE based on PT-JPL.

Drawing from results here, the effect which soil parameters can have on simulations of L_vE is undeniable despite having the same radiation, atmospheric forcing, and vegetation parameters. Similar to soil moisture, L_vE based on PT-JPL was found to have a

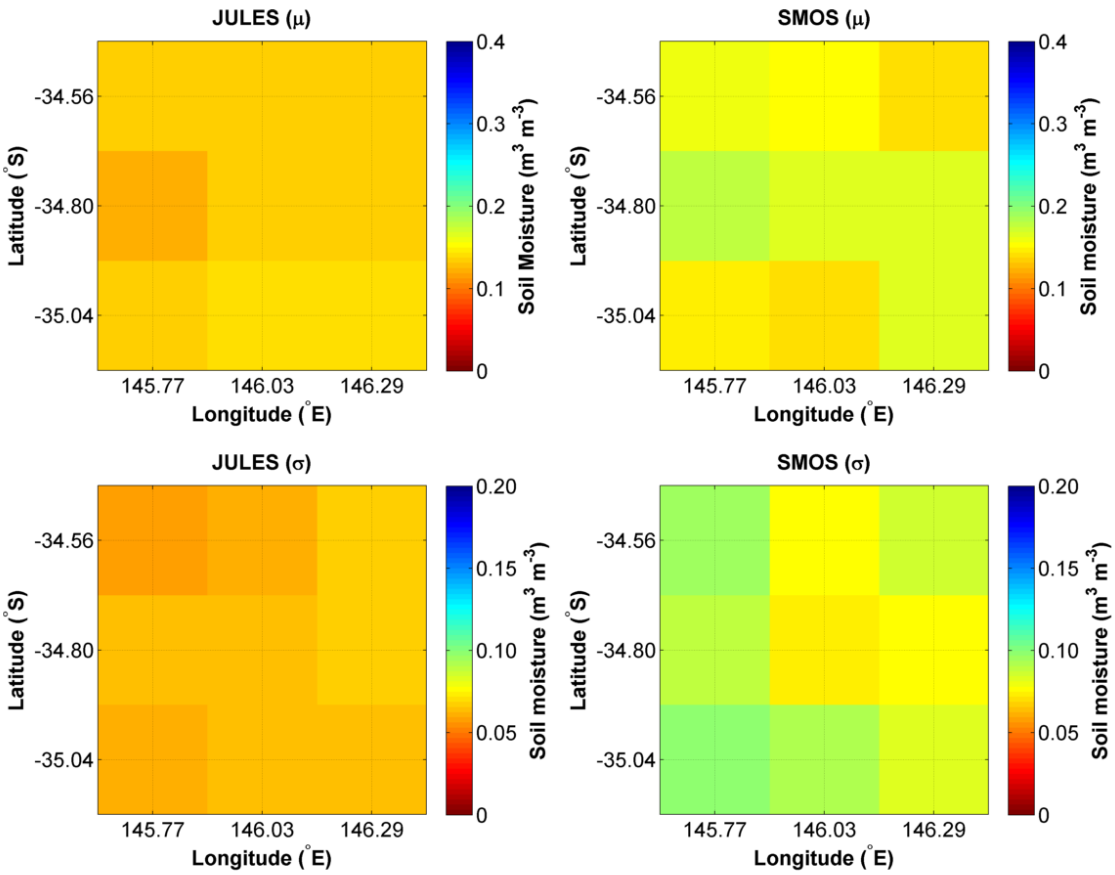

FIGURE 7.8: Spatial plot of mean and standard deviation of soil moisture based on JULES1 simulations and SMOS 25 km product.

similar r as both JULES1 and JULES2 simulations; but, based on RMSD, JULES1 performed better. Therefore, it appears that the performance of a model or remote sensing product should not be restricted to r as it does not give a complete picture. Instead, the ability to accurately simulate absolute quantities should be considered.

7.4.3 Spatial quantitative evaluation

Having compared *in situ* measurements with remote sensing products and JULES simulations, spatially distributed simulations from JULES1 were evaluated using the intensively validated SMOS soil moisture and PT-JPL L_vE products. Due to differences in gridding, the area covered by the SMOS soil moisture product is larger than the aggregated product of JULES1 for grid cells S1, S4, S7, S8 and S9 (Fig. 7.1). This should be kept in mind as evaluations may be affected.

The spatial mean (μ) and standard deviation (σ) of soil moisture based on aggregated 25 km JULES1 simulations and SMOS soil moisture products (Fig. 7.8), and L_vE based

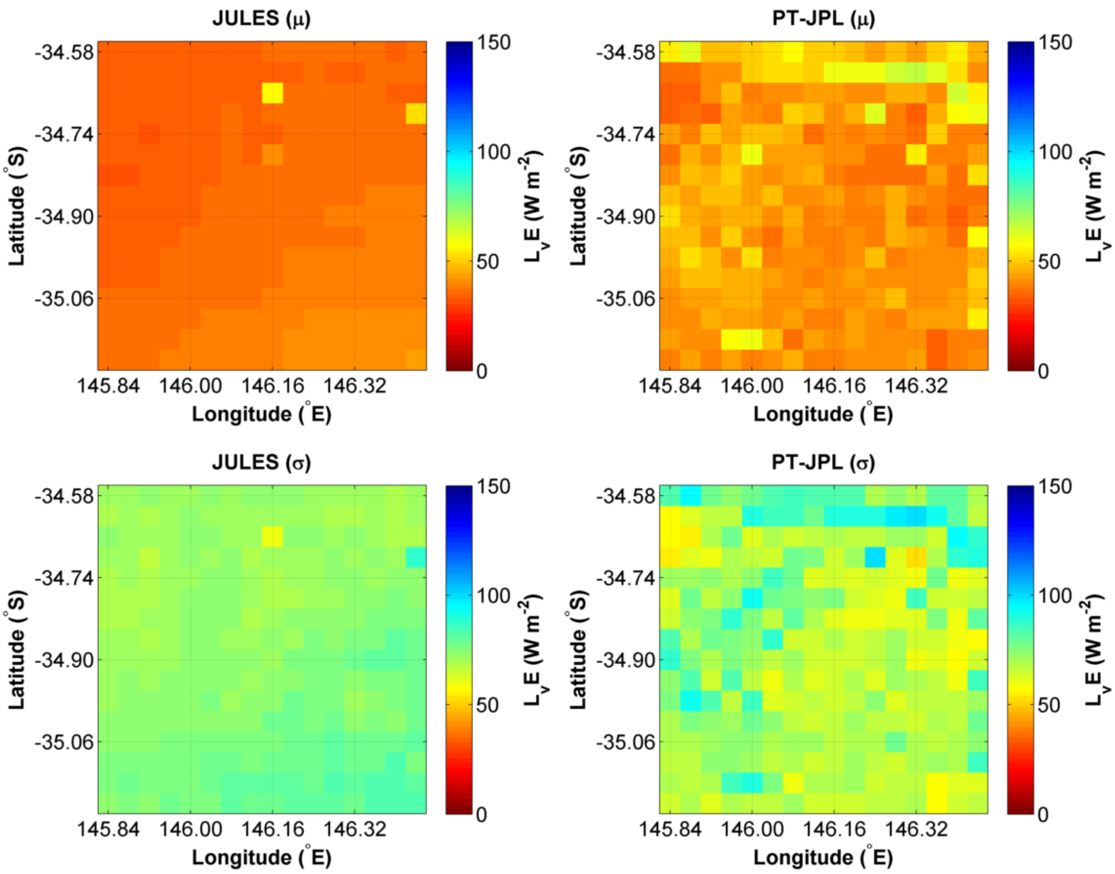

FIGURE 7.9: Spatial plot of mean and standard deviation of $L_{\mathrm{v}}E$ based on JULES1 simulations and PT-JPL 4 km product.

on aggregated 4 km JULES1 simulations and PT-JPL ET products (Fig. 7.9) were computed using only time-steps where data was available from both remote sensing products and JULES1 simulations. Generally, mean and standard deviation of soil moisture and $L_{\mathrm{v}}E$ based on remote sensing products was higher than simulations from JULES1. As expected, based on remote sensing products, a higher variation of soil moisture was detected in the YA area which was irrigated, compared to YB area which consists mainly of grasslands. However, this was not observed in the JULES1 simulations. Soil characteristics provided by the Digital Atlas of Australian Soils have a very coarse resolution where the majority of the area was of loam type (shown as a brown in the bottom right inset of Fig. 7.1), a small pocket of sand at the top-right corner of S6, and the remaining areas consist of soil which falls between these two types. Consequently, variation of soil moisture within JULES1 was very low for all grid cells. Moreover, whilst it is difficult to model the timing of irrigation activities within JULES, this is sensed by the space-borne sensors.

In the case of mean $L_{\mathrm{v}}E$, the diagonal pattern in JULES1 coincides with ACCESS-A's 12 km grids, thereby indicating that mean $L_{\mathrm{v}}E$ was determined by atmospheric forcing. The spatial variation of standard deviation is dictated to a slight degree by the distribution of vegetation based on the National Dynamic Land Cover dataset (bottom left inset of Fig. 7.2). However, the lower variation (σ) within each grid is expected since the vegetation dynamics of JULES was not switched on as this chapter serves as a demonstration rather than an in-depth study. This means that vegetation parameters which control changes in the canopy and root density were kept constant throughout the year. Conversely, the PT-JPL model was provided with temporal information regarding vegetation states based on MODIS. Therefore, variations in mean and standard deviation were more pronounced. If the vegetation dynamic module of JULES, i.e. TRIFFID was turned on, the simulations based on JULES would be expected to improve.

Soil parameters are very difficult to retrieve whilst some vegetation parameters can still be directly observed as the canopy is visible from space. Field measurements are also difficult due to high spatial variability of soil parameters. Nevertheless, soil hydraulic parameters of an area should not change significantly over time even though the 'effective' parameters can change. Therefore, conceptually, soil parameters can be derived based on inverse modelling using remote sensing information with a high spatial resolution as done to retrieve soil parameters for JULES2 (Bandara et al., 2015). However, as seen earlier, simulations of both soil moisture and $L_{\mathrm{v}}E$ based on JULES2 did not improve. In retrieving these soil parameters with 12 months of data, the surface was assumed to consist of bare soil (Bandara et al., 2015). This would imply the soil is exposed for direct evaporation when in reality vegetation would have a role to play in interception of rainfall and uptake of soil moisture for transpiration. Furthermore, the accuracy of the retrieved parameters are prone to errors in the model and observations of soil moisture and vegetation used to derive the parameters. Soil structure can be affected by soil cracking, roots from vegetation, agricultural practices and micro-organisms, all of which are not well described in models. This may have resulted in the poorer performance of JULES2.

Generally, an underestimation of soil moisture by JULES1 was found, with a bias ranging from -0.01 $\mathrm{m}^3\ \mathrm{m}^{-3}$ to -0.06 $\mathrm{m}^3\ \mathrm{m}^{-3}$ (Fig. 7.10). This magnitude was largest within the western edges. This may be due to a combined effect of standing water from irrigation activities and the presence of vegetation along the river which affects retrievals based

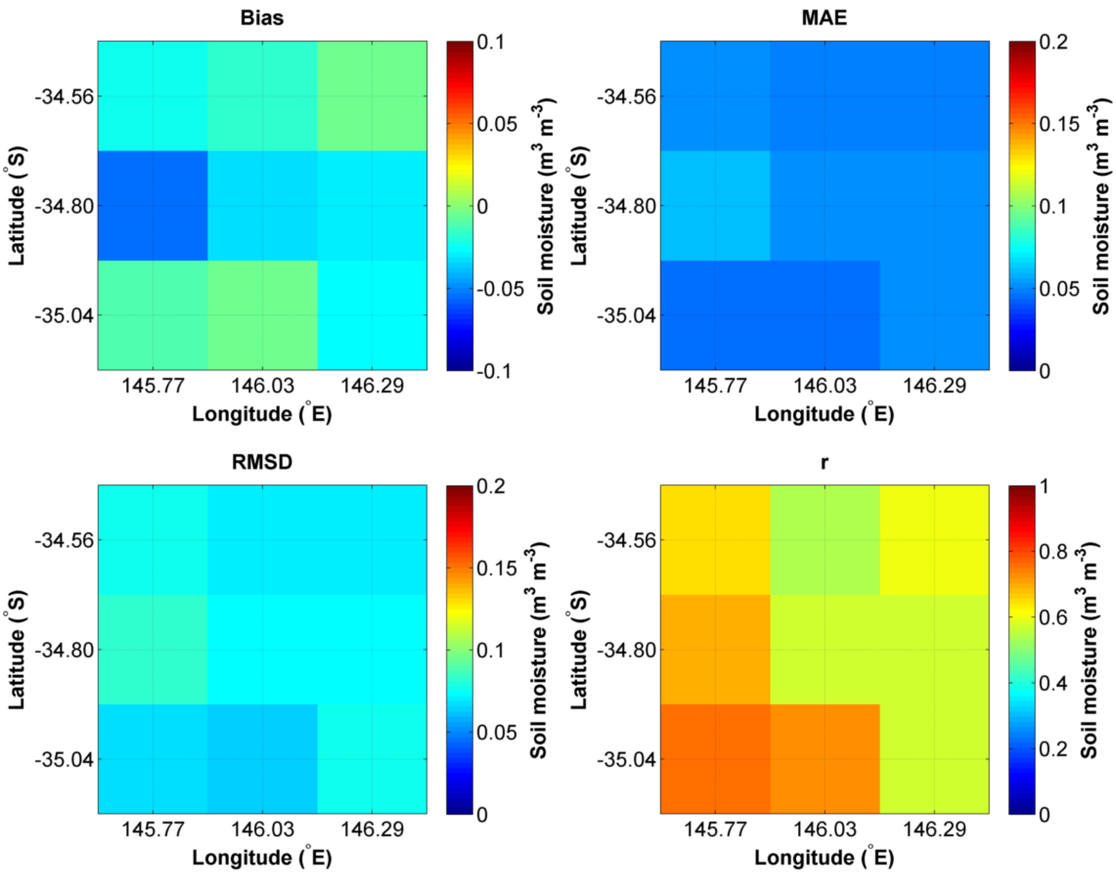

FIGURE 7.10: Spatial plot of bias, MAE, RMSD and r comparing soil moisture based on JULES1 and SMOS 25 km product.

on SMOS and was also not simulated by JULES1. Agreement of absolute soil moisture based on MAE and RMSD, ranged from 0.05 m^3 m^{-3} to 0.06 m^3 m^{-3}, and 0.07 m^3 m^{-3} to 0.08 m^3 m^{-3} respectively. Surprisingly, differences were larger for the YB area rather than YA area. Likewise, r was higher to the west of the study area rather than the east. Two reasons may have contributed to this. Firstly, based on the Digital Atlas of Australian Soils, the soil type at the S6 was sand as opposed to loam at remaining areas. Secondly, there was a smaller overlap of JULES simulations within the western SMOS grids (Fig. 7.1). Nevertheless, performance in the YB area was very consistent, Also, provided that the timing of the precipitation forcing is accurate, JULES was able to capture temporal variability well (Fig. 7.3).

JULES similarly underestimated L_vE where irrigation plots were present (by 20 W m^{-2}) and where riverine vegetation exists (about 30 W m^{-2}) (Fig. 7.11). Performance within the homogeneous areas was better with an MAE of $\approx$ 30 W m^{-2}. For the entire study area, r ranged from 0.47 to 0.76. Temporal patterns following the diurnal pattern of meteorological forcing are easier to capture whereas absolute L_vE is harder to determine.

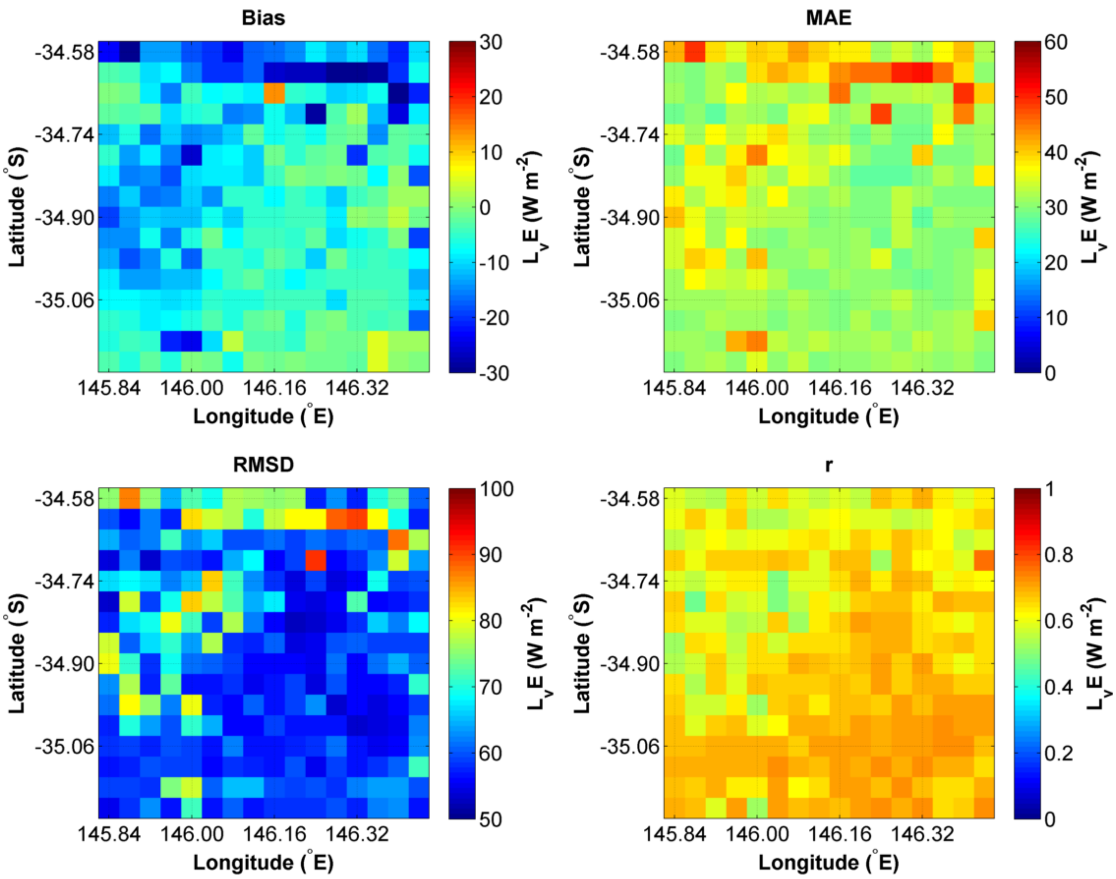

FIGURE 7.11: Spatial plot of bias, MAE, RMSD and r comparing L_vE based on JULES1 and PT-JPL 4 km.

Yet, absolute L_vE is important in applications for water resource management. For models to perform well, the ability of spatially characterizing soil and vegetation characteristics and their interactions is key. Soil parameters such as volumetric soil moisture content at wilting point and critical point will affect the rate in which ET occurs. At the same time, plant roots extract soil moisture from different layers of the soils. Without improvement in this, improvements in global LSM simulations will continue to be constrained.

How the use of remote sensing products to evaluate LSM simulations, without prior validation with selected representative stations as carried out in this study, can affect results is also illustrated using $LP2_{C2}$ as an example. Results using JX1, JX2 and $LP2_{C2}$ are also shown in Appendix D. Fig. 7.12 summarizes the statistics derived from evaluating simulations of soil moisture 25 km soil moisture products derived using the LPRM algorithm (C1 band / 6.9 GHz; combination of morning and evening overpasses).

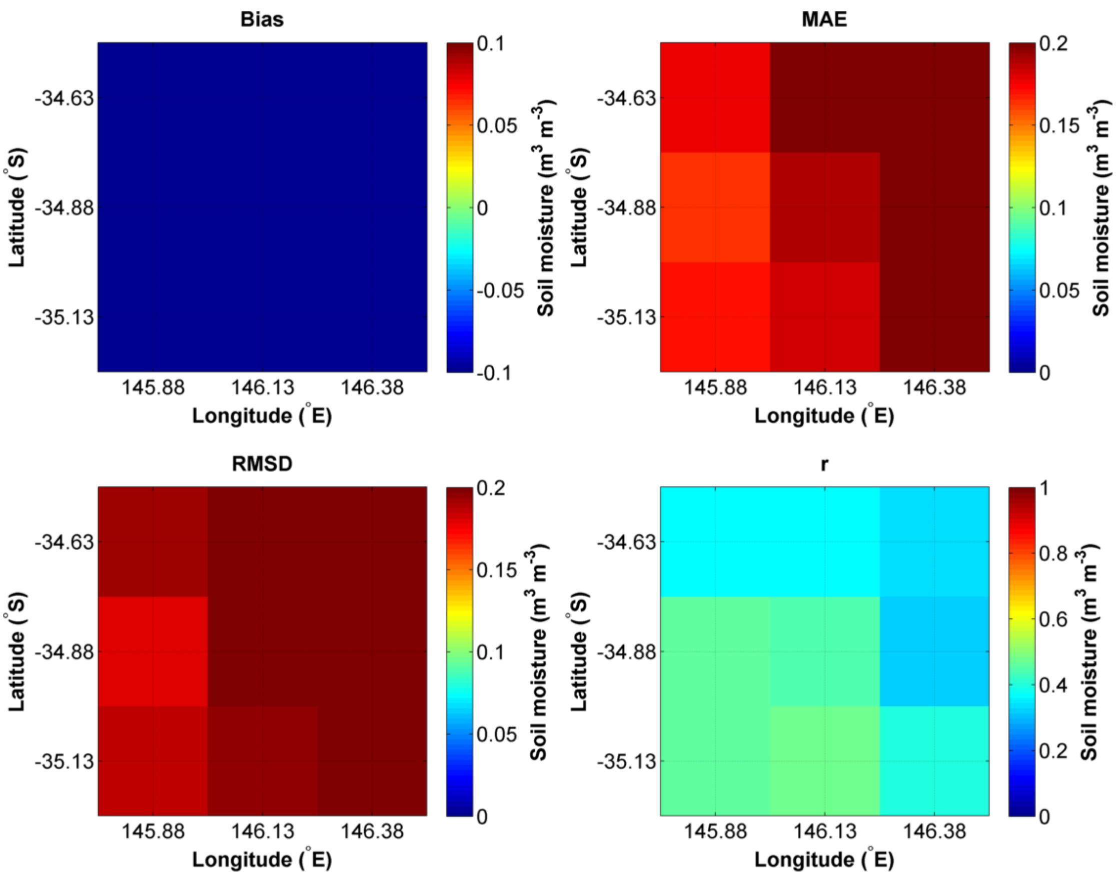

FIGURE 7.12: Spatial plot of bias, MAE, RMSD and r derived from evaluating JULES1 soil moisture based on $LP1_{C1}$.

Since AMSR-2 and SMOS have different grids, the grid used for evaluating JULES1 with AMSR-2 products was based on the AMSR-2 grid. It is clear from the Fig. 7.12 that the agreement between products based on LP1 (C-band) with JULES soil moisture simulations were extremely low. This is expected as the LP1 C-band products were found to have a negative correlation with *in situ* measurements in Chapter 4. Theoretically, C-band observations should coincide better with the 0 - 8 cm soil moisture simulated by JULES than X-band observations. Based on this assumption, without careful validation such as carried out in this research, it is likely that remote sensing product users would choose the C-band products over the X-band products. Evidently, if $LP1_{C1}$ were used to evaluate of LSM simulations, conclusions drawn regarding the performance of the LSM would be inaccurate.

In the case of ET, products based on the SEBS and PM-Mu ET model were also used to evaluate LSM simulations of ET. Earlier in Chapter 6, SEBS ET products was found to overestimate and from PM-Mu to underestimate. Moreover, the PM-Mu model was

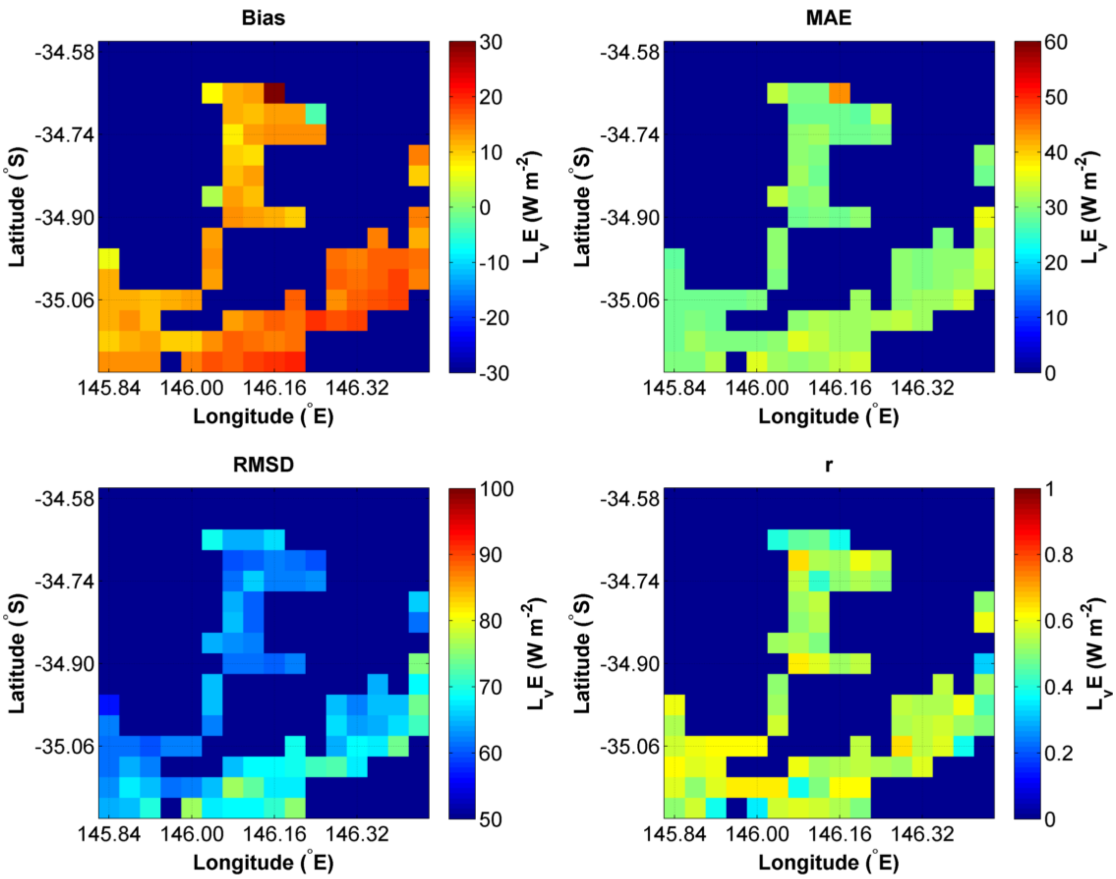

FIGURE 7.13: Spatial plot of bias, MAE, RMSD and r derived from evaluating JULES1 $L_{\mathrm{v}}E$ based on PM-Mu.

shown in Chapter 6 to perform badly. Here, we concentrate on evaluation of the JULES based on ET products based on PM-Mu (Fig. 7.13) whereas results based on SEBS can be found in Appendix D. It can be seen that if PM-Mu was used, the effect on the evaluation study would be large as PM-Mu does not provide realistic simulations of ET (expressed as $L_{\mathrm{v}}E$) at certain grids (Fig. 7.13). Therefore, it is crucial to verify the accuracy of remotely sensed products, such as performed in this thesis, prior to application in the evaluation of LSMs run at distributed scales. However, in the case of evaluating results from two different simulations such as JULES1 and JULES2, a less accurate remote sensing product can still be valuable in diagnosing relative changes in temporal metrics.

7.5 Key findings

This study demonstrated the utility of remote sensing soil moisture and ET products in evaluating LSMs run at distributed scales. These remote sensing products have been carefully validated in earlier chapters using selected representative stations. Based on a visual inspection, and concurrent evaluation of soil moisture and ET simulations, it was found that the impact of soil parameters prescribed to the model towards the timing of ET was larger than the effect it had on near-surface soil moisture. This demonstrates the merit of assessing LSMs based on multiple observations as proposed in this thesis.

When *in situ* measurements, remote sensing products and JULES simulations of soil moisture and ET were compared, it was found that *in situ* measurements agreed with simulations from JULES1 but not JULES2. However, when JULES1 and JULES2 were inter-compared with satellite products, their performances based on r were comparable. Nevertheless, when statistical measures involving absolute quantities such as RMSD was included, it was clear that JULES2 underperformed. The temporal variability of soil moisture and ET are to a certain extent easier to capture since they are more dependent on meteorological conditions such as precipitation, R_n and cloud conditions, which can be better observed or measured. However, the absolute quantities of soil moisture and ET are controlled by complex interactions between the soil and vegetation which are harder to simulate. Consequently, the evaluation of LSM or remote sensing products should include r and other statistical measures of absolute quantities (e.g. RMSD, MAE, ubRMSD).

Evaluation of distributed simulations from the LSM based on validated remote sensing products showed that a lack in spatial information regarding soil parameters and vegetation phenology led to an inability of JULES to correctly simulate the spatial variation of soil moisture and seasonal variation of ET. Generally, it appears that the model is more sensitive to meteorological forcing than prescribed parameters. This is expected as vegetation phenology have not been allowed to vary in this model, and the soil parameters prescribed were relatively homogeneous. The satellite retrieved soil parameters might not have improved simulations because the role of vegetation was not considered in the derivation of the parameters. Consequently, vegetation information should be incorporated in future efforts to derive soil parameters based on satellite observations. This may include turning on the TRIFFID module, or assimilating vegetation information into the model. Nevertheless, the preliminary evaluation of distributed simulations from JULES based on two carefully selected remote sensing products to identify errors in parameterization of soil and vegetation characteristics, forcing data and model physics have been successfully demonstrated.

Finally, the study also illustrated the importance of understanding the accuracy of remote sensing products prior to application by contrasting the results when evaluation was made with other remote sensing products previously validated in earlier chapters. Results revealed a large effect on results if LP1 C-band soil moisture products and PM-Mu derived ET was applied instead of products derived from SMOS and PT-JPL respectively. Consequently, it is crucial to understand the accuracy of remote sensing products prior to application.

7.6 Chapter summary

To date, the preferred method for evaluating LSMs are still based on dense networks of *in situ* measurements. However, as the availability of a dense monitoring networks outside of experimental test beds such as the Yanco study area is limited, evaluation of soil moisture and ET simulations by LSMs at distributed scales are even more complicated. Remote sensing yields an opportunity to provide not only consistent soil moisture and ET retrievals in time and space, but also other hydrological variables. Based on an improved understanding regarding the performance of each soil moisture and ET remote sensing product from results in the previous chapters, distributed simulations from the land surface JULES were evaluated. Results showed the important role played by soil parameters prescribed to JULES with respect to the rate of ET. Moreover, it was clearly demonstrated that the utilization of a less accurate product such as the LPRM C-band soil moisture and PM-Mu ET product can lead to detrimental effects. In conclusion, a rigorous and systematic validation of remote sensing products such as the one demonstrated in this thesis is crucial prior to their application.

Chapter 8

Conclusions and Future Work

Through a series of experimental studies, this research undertook a rigorous and systematic validation of soil moisture and ET satellite products at selected grids prior to demonstrating an assessment approach for LSM simulation. This demonstration was undertaken for a larger area using the validated remote sensing products. Here, the key findings are presented and broad conclusions discussed. Finally, some recommendations for future plans are proposed.

8.1 Conclusions

This research was divided into three main parts: i) validating soil moisture remote sensing products, ii) validating ET remote sensing products, and iii) demonstrating the proposed approach for evaluating model derived soil moisture and evapotranspiration (ET) using the Joint UK Land Environment Simulator (JULES) in conjunction with validated remote sensing products. The work of these three parts were broken down into the five tasks covered in **Chapters 3** to **7**.

Through these five tasks, the representativeness of a soil moisture stations and a eddy covariance (EC) system was established for remote sensing product pixels. A unique suite of soil moisture and surface flux observations were used (**Chapters 3** and **5**). Measurements from these representative systems were then used to validate satellite soil moisture (Advanced Microwave Scanning Radiometer - 2; AMSR-2 and Soil Moisture and Ocean Salinity; SMOS) and ET (Surface Energy Balance System; SEBS, Modified Penman

Monteith; PM-Mu, and Modified Priestley Taylor; PT-JPL) products (**Chapter 4** and **6**). The SMOS soil moisture product and PT-JPL ET product were found to perform the best. Finally, by using these verified products a demonstration of JULES run at distributed scales was performed in **Chapter 7**.

8.1.1 Representativeness of soil moisture stations within the Yanco area

The validation of remotely sensed soil moisture products using *in situ* monitoring stations is difficult due to the high spatial and temporal variability of soil moisture. Consequently, the work in **Chapter 3** overcame this issue by identifying the most representative station. While this work was done in the context of NASA's Soil Moisture Active Passive (SMAP) satellite launched in January 2015, having products at 3 km for radar, 9 km for radar-radiometer and 36 km for radiometer pixels, this analysis applies equally to the AMSR-2 and SMOS grid soil moisture postings at similar spatial resolutions. This investigation was carried out based on temporal stability and geostatistical studies using long-term soil moisture records, intensive ground measurements and airborne soil moisture products. In addition, the centered-variogram analysis was applied for the first time to understand the representativeness of soil moisture stations within the study area.

Results revealed that stations which were found to be representative based on mean relative difference (MRD) in temporal stability analysis were not necessarily representative of the areal average soil moisture. Those identified from standard deviation of the relative difference (SDRD) were found to be dry-biased. Therefore, it is recommended that where intensive measurements are available, stations which are most representative of the areal mean should be used. Additionally, temporal stability analysis is not recommended in the presence of cropping activities. Instead, a good distribution of stations, or a weighting method to account for variability within the pixel is important. Nevertheless, in the absence of intensive measurements, temporal stability analysis is adequate provided that stations are well distributed within the area of interest and the appropriate performance indicator selected, i.e. Root Mean Square Error of the station; RMSE_s.

Finally, since stations within the OzNet were well distributed within different land use types, YA5 and YB7e were identified as representative stations for the local YA (irrigated) and YB (grazing) areas respectively, whereas YA5 was identified as representative of the Yanco region as a whole. Airborne soil moisture products were also shown to provide useful *a priori* information for identifying representative locations based on point-to-pixel comparisons. Consequently, other high resolution measurements such as the 1 km soil moisture product based on the Environmental Satellite (ENVISAT) Advanced Synthetic Aperture Radar (ASAR) Global Mode (Doubkova et al., 2009) and Sentinel-1 (Wagner et al., 2009) might also be used to estimate spatial representative soil moisture monitoring locations.

8.1.2 Satellite soil moisture error assessment based on representative stations

After identifying stations which were representative of the local and regional Yanco area, AMSR-2 soil moisture products from two different versions of two different algorithms (Japanese Aerospace exploration Agency; JAXA and Land Parameter Retrieval Model; LPRM), and the SMOS soil moisture product were validated in **Chapter 4**. Firstly, it was shown that the use of unrepresentative stations can have a large impact on validation results (r of -0.16 as opposed to 0.60), particularly for non-homogeneous areas. Therefore, prior to any validation or calibration, the representativeness of stations needs to be well understood as shown in **Chapter 3**.

Validation based on representative stations showed that the later versions of the JAXA (JX2) and LPRM (LP2) products were improved over the former ones (JX1, LP2). Generally, JAXA products were found to underestimate soil moisture by ≈ 0.05 m^3 m^{-3} whereas LPRM products overestimated by between 0.05 and 0.20 m^3 m^{-3}. Comparing the accuracy of products derived from X- and C-band observations based on the LP2 algorithm showed that X-band observations were superior over C-band. However, C-band observations should correlate better with the 0 - 5 cm soil moisture measurements since the depth sensed at C-band is closer to this depth than X-band. It is therefore postulated that as most AMSR-based studies have concentrated on the development of the higher frequencies (X-band) due to widespread occurrence of RFI at C-band in North America, Europe and East Asia, the algorithms have been calibrated to match

X-band. Moreover, in terms of overpasses, AMSR-2 day (1:30 PM) retrievals were found to perform better than night (1:30 AM). Nevertheless, the difference between morning (6:00 AM) and evening (6:00 PM) retrievals was marginal for SMOS.

Based on the results of this study, in the application of soil moisture products, where accuracy in absolute and temporal soil moisture is needed, SMOS soil moisture retrievals for both morning and evening observations can be combined with confidence that they will be consistent. Overall, considering absolute and temporal accuracy, SMOS soil moisture products were the most accurate, followed closely by X-band observations based on LP2.

8.1.3 Inter-comparison of ET measurement methods

In **Chapter 5**, measurements from an EC system were compared with sensible (H) and latent ($L_{\mathrm{v}}E$) heat derived from two optical scintillometers (LAS) and two microwave scintillometers (MWS) of two frequencies and two polarizations in stand-alone and two-wavelength configurations placed within the footprint of the EC system. This study was conducted to obtain a better understanding of the individual performances of these methods and the relationship to the EC prior to their application in understanding the spatial variability and long-term record of ET (also expressed as $L_{\mathrm{v}}E$) in **Chapter 6**.

Results showed a good agreement between H and $L_{\mathrm{v}}E$ derived as a residual of the energy balance from the EC system and optical scintillometers. Conversely, MWSs were found to be less accurate due to the semi-arid environment of the site. It was observed that assumptions made regarding the correlation coefficient between temperature and humidity fluctuations, r_{TQ}, contributed to differences between the EC system with the MWS systems and the two-wavelength method. This uncertainty was exacerbated with increasing Bowen ratios, β, due to the existence of a non-unique solution for a stand-alone MWS. Whilst the two stand-alone LAS compared well with the EC system, the two MWS only agreed well with each other.

In conclusion, the LAS is recommended for applications in a semi-arid environments. Nevertheless, both LAS and MWS would still be used to evaluate the representativeness of measurements from the EC system for the single Multi-functional Transport SATellites (MTSAT) 4 km ET product grid over the long-term.

8.1.4 Error assessment of remote sensing based ET products with a representative EC system

Following the inter-comparison of different ET measurement methods in **Chapter 5**, the representativeness of measurements from the EC tower were assessed for use as long-term validation of the MTSAT ET product in **Chapter 6**. Firstly, the same suit of scintillometers from **Chapter 5** were placed across a single 4 km MTSAT ET product pixel to measure the contribution of L_vE from different areas within the pixel.

Comparisons between the two LAS, and the two MWS, showed that regardless of wind direction, L_vE derived from these scintillometers were similar. This means that the difference between fluxes measured within different areas of the 4 km pixels was small. Moreover, comparisons between the LAS and the EC system had an r of 0.69 to 0.77 and RMSD of 58.32 Wm^{-2} to 70.61 Wm^{-2} respectively. Therefore, it was concluded that measurements from the EC system are representative of the entire 4 km ET product due to homogeneity within the pixel.

Since measurements from the EC system were found to be representative, MTSAT ET products based on three models, i.e. SEBS, PT-JPL and PM-Mu were validated for the selected pixel using the long-term EC record. Derived L_vE based on SEBS was found to overestimate, while PM-Mu was found to underestimate. The L_vE based on the PT-JPL model was found to be most similar with measurements from the EC system.

Conclusively, although PT-JPL uses a relatively simple and largely empirical formulation of the evaporative process, possibly due to lower uncertainties in the required forcing data, it was able to perform better than the other two models. The spatial distribution of ET within the larger Yanco area was also found to be well represented by PT-JPL, making it suitable for application in evaluating the JULES land surface model simulations in **Chapter 7**.

8.1.5 Evaluation of LSM simulations of soil moisture and ET using validated remote sensing products

Drawing from the results of foregoing chapters, **Chapter 7** demonstrated the utility of rigorously validated remote sensing soil moisture and ET products in the evaluation of

LSM simulations run at 1 km resolution for a 60 km × 60 km area near Yanco. Simulations were carried out for two scenarios: the first (JULES1) used Australian Community Climate and Earth-System Simulator - Australia (ACCESS-A) precipitation data that was bias corrected based on the daily Australian Water Availability Project (AWAP) data and soil parameters derived from the Digital Atlas of Australian Soils (McKenzie et al., 2000); the second (JULES2) utilized rain-gauge calibrated radar precipitation Shahrban et al. (2016) data and remote sensing derived soil parameters (Bandara et al., 2015).

Evaluation of soil moisture and ET simulations based on SMOS soil moisture products and PT-JPL ET products revealed that the impact of soil parameters prescribed to the model towards the timing of $L_{\mathrm{v}}E$ was large. Although JULES1 and JULES2 both performed similarly based on correlation, when statistical measures involving absolute quantities such as RMSD were considered, JULES2 under-performed relative to the satellite products. Since the absolute quantities of soil moisture and $L_{\mathrm{v}}E$ are controlled by complex interactions between the soil, vegetation and atmosphere, the evaluation of LSM with remote sensing product should include r and other statistical measures of absolute quantities (e.g. bias, mean average error; MAE and unbiased RMSD; ubRMSD).

Finally, by utilizing products known to be less accurate, through analysis in earlier chapters - i.e. the LP2 C-band soil moisture products and PM-MU ET products, very different conclusions were drawn when evaluating the same simulations. Consequently, it is paramount for the accuracy of these remote sensing products to be carefully verified prior to application in the evaluation of LSMs run at distributed scales, as demonstrated in this research.

8.2 Future Work

This research has made a preliminary assessment of simulations from a LSM run at distributed scales, based on two carefully selected remote sensing products. The purpose of this assessment being to identify errors in parameterization of soil and vegetation characteristics, forcing data and model physics. In addition to the conclusions already presented, several overarching items of future work were identified.

8.2.1 Investigating representativeness of soil moisture and ET measurements

Results from Chapters 3 and 4 showed that the use of unrepresentative stations can have a large impact on validation results, particularly for non-homogeneous areas. Moreover, as the methodology employed in this research for identifying the most representative soil moisture stations focused on two carefully selected pixels, the results may be site dependent. Therefore, the procedure employed in **Chapters 3 and 4** should be repeated at other sites. Similarly, the representativeness of measurements from other EC systems around the world should be investigated as in **Chapter 5** prior to application in validating remote sensing products or model simulations.

8.2.2 Up-scaling soil moisture and ET measurements

One of the methods suggested to up-scale point measurements to regional or global scales includes using simulations from an LSM to derive a transfer function for up-scaling (Crow et al., 2012). However, the LSM simulations in **Chapter 7** were found to inadequately represent the spatio-temporal variability of soil moisture and ET due to limitations in the resolution of soil parameter maps. These simulations are also highly prone to errors in the forcing data used to drive the models, and structural errors within the models themselves. Hence, unless high resolution maps of soil parameters exists, the up-scaling of point measurements based on LSM simulations will continue to be constrained. High resolution remote sensing observations provide an alternative option for up-scaling point measurements of soil moisture and ET in space (e.g. Qin et al., 2013). Therefore, instead of LSM simulations, it is recommended to use high resolution observations to derive a transfer function for up-scaling point measurements to regional or global scales.

8.2.3 Progressing the scintillometer technique

In **Chapter 5**, assumptions made regarding r_{TQ} were found to be the main cause for differences with the EC system. Moreover, for a stand-alone MWS, this uncertainty increased with increasing β due to the non-unique solution in β. Considering the ability of scintillometers to measure areal averaged surface heat fluxes, it is desirable to further investigate these issues. Hence, it is recommended for a sensitivity analysis or an inverse calculation based on measurements derived from the EC system to be carried out to obtain further insights regarding r_{TQ}.

8.2.4 Benchmarking remote sensing products

Users within the remote sensing and modelling community tend to prioritize the accuracy of the remote sensing product in terms of capturing the temporal patterns or its performance in terms of absolute value, depending on the application. In **Chapter 5**, it was shown that although AMSR-2 products based on the JX2 algorithm achieved the mission objective which, was based on MAE (absolute), it had a lower correlation compared to products based on LP2, which did not achieve the mission objective. Similarly, errors in the measurements of net radiation, ground heat flux and the non-closure of the energy balance complicates the validation of ET models with EC systems. The approach used to address this non-closures can lead to different interpretations regarding the performance of the ET models. Moreover, the higher performance of ET products based on PT-JPL was likely because of its minimal need for input data. Hence, for future comparisons of soil moisture and ET observations, it is advisable that a combination of statistical parameters which account for both correlation and absolute values be considered. This calls for continued collaborations between both the remote sensing and the modelling community in defining mission objectives, benchmarks and statistical methods used to validate remote sensing products (e.g. Abramowitz, 2005; Blyth et al., 2011; Jackson et al., 2010; Prentice et al., 2015).

8.2.5 Advancing remote sensing

Validation of soil moisture products derived based on observations from different overpass times showed differences according to seasons (**Chapter 5**). Therefore, further investigations should be carried out to understand how the soil temperature profile at different crossing times may have contributed to this, such that corrections can be made.

In the case of remote sensing ET products, the use of hourly observations to improve the temporal variability of ET cannot be fully exploited in PT-JPL and PM-Mu unless these models are modified to allow for inputs of land surface temperature and cloud cover from a geo-stationary satellite. Moreover, due to the importance of soil moisture in semi-arid environments, ET estimates can be improved by incorporating soil moisture information or observations into the remote sensing ET models.

8.2.6 Improving LSM modelling

As it was found that the temporal variability of vegetation parameters and spatial variability of soil parameters prescribed within the LSM heavily influences the timing of simulated ET, the need for improvements in global soil parameter datasets is central for enhancing LSM simulations of soil moisture and ET in semi-arid environments such as the study area. Although satellite retrieved soil parameters did not improve simulations based on JULES2 in this study, it is the most conceivable and practical approach for deriving soil parameters for applications in distributed land surface modelling. Nevertheless, the assimilation of varying vegetation information (e.g. from MODIS) together with improvements in model physics to include changes in soil structure due to soil cracking, roots from vegetation, agricultural practices, and micro-organisms, is expected to improve the accuracy of remote sensing derived soil parameters. Simulations derived from assimilation of remote sensing observations can then be used to retrieve soil parameters based on inverse modelling as carried out in Bandara et al. (2015).

For this reason, it is desirable to have a satellite dedicated to obtaining fine-resolution products of soil moisture and vegetation at global scales such that finer scale soil parameters can be retrieved. Combining these finer resolution soil moisture products with the centered-variogram analysis proposed in **Chapter 4**, the representativeness of soil moisture stations can also be repeated with a larger set of observations covering a more extensive period and area. Until then, the role of field campaigns, and ground and aircraft measurements, continue to play an important role in ensuring the feasibility of these methods. This type of analysis is not restricted to soil moisture and can be applied using vegetation indices from MODIS or aircraft measurements of surface heat fluxes to understand the distribution of surface heat fluxes within a study area (e.g. Panciera et al., 2014; Prueger et al., 2005).

8.3 Summary of Conclusions and Future work

This research at the Australian core validation site has:

1. identified YA5 and YB7e to be the most representative soil moisture stations within the YA and YB areas respectively, and YA5 as representative of the Yanco region as a whole based on geostatistical and temporal stability methods;
2. identified that SMOS soil moisture products followed by AMSR-2 soil moisture products based on the LPRM algorithm from X-band observations to be the most accurate;
3. identified the LAS system to be more suitable than MWS for use in a semi-arid environment;
4. established the representativeness of the EC system at Yanco region of a 4 km MTSAT ET product pixel;
5. identified 4 km MTSAT derived remote sensing ET products based on PT-JPL to be most accurate; and
6. demonstrated the importance of using carefully validated remote sensing products to evaluate distributed simulations from LSMs.

The main recommendations for future work include:

1. extending the investigation of soil moisture and ET measurements to other study areas;
2. spatial up-scaling of point measurements using high resolution remote sensing observations rather than LSM simulations;
3. studying the effects of r_{TQ} on the accuracy of derived surface heat fluxes;
4. the need for a comprehensive approach for bench-marking remote sensing products;
5. further investigations on the effects of soil temperature profile at different overpass times towards the accuracy of satellite soil moisture products;
6. the inclusion soil moisture information into remote sensing models to improve estimates of ET for semi-arid environments; and
7. the assimilation of soil moisture and vegetation observations to derive soil parameters in an inverse modelling framework.

In conclusion, the major contribution of this work was the demonstration of a comprehensive and systematic methodology towards the evaluation of LSMs using validated remote sensing products.

Appendix A

Remote sensing soil moisture validation diagrams

Product	Summer	Autumn	Winter	Spring
$\mathrm{JX1}^{\mathrm{YA}}_{\mathrm{X(M)},25}$	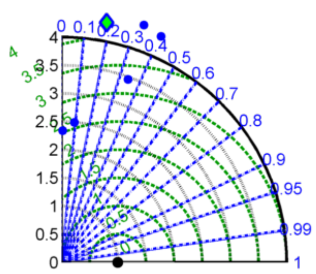	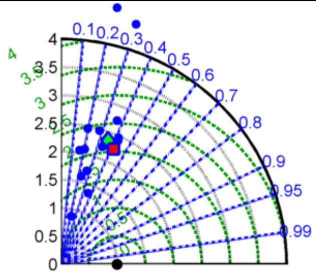	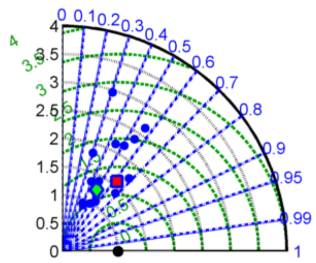	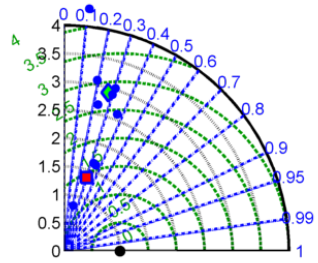
$\mathrm{JX2}^{\mathrm{YA}}_{\mathrm{X(M)},25}$	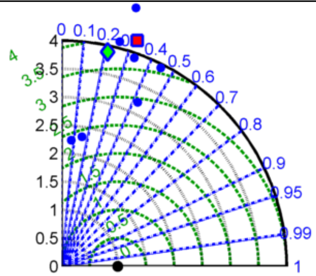	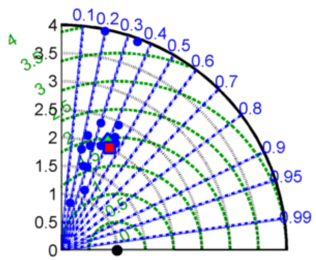	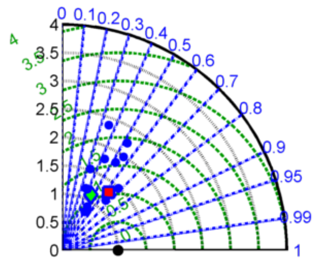	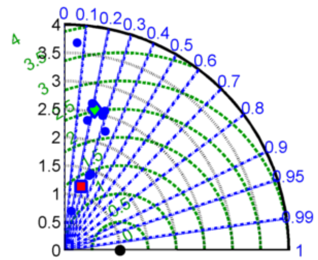

FIGURE A.1: Taylor diagrams for JAXA 25 km morning products in the YA area. Satellite products are treated as the baseline soil moisture (black dot). □: Representative station. ◇: Average. ○: Individual stations.

Product	Summer	Autumn	Winter	Spring
$\mathrm{LP1}^{\mathrm{YA}}_{\mathrm{X(M)},25}$	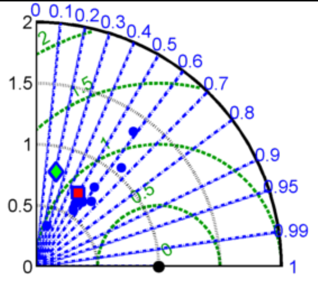	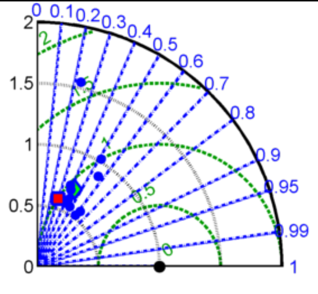	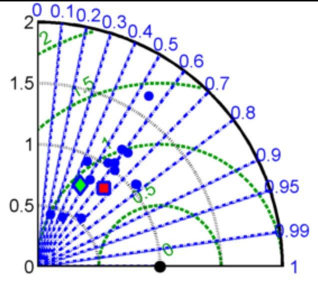	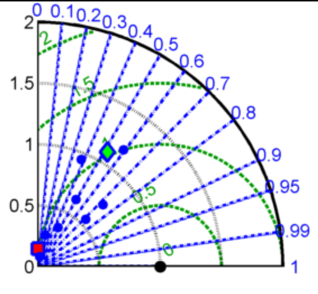
$\mathrm{LP1}^{\mathrm{YA}}_{\mathrm{C1(M)},25}$	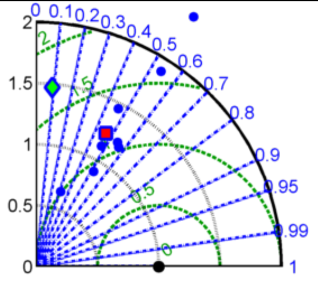	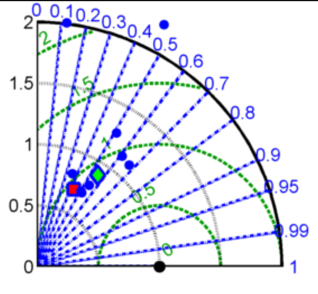	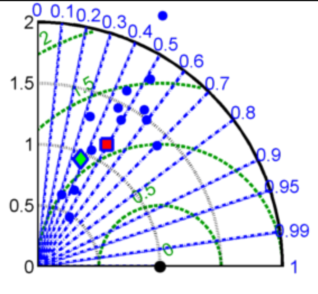	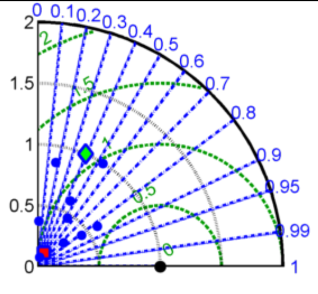
$\mathrm{LP1}^{\mathrm{YA}}_{\mathrm{C2(M)},25}$	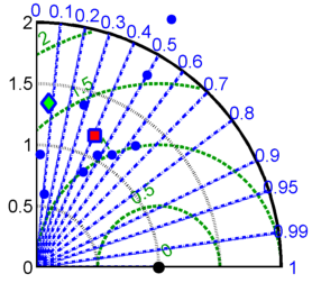	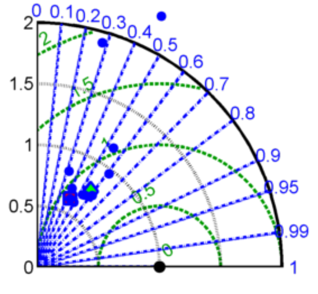	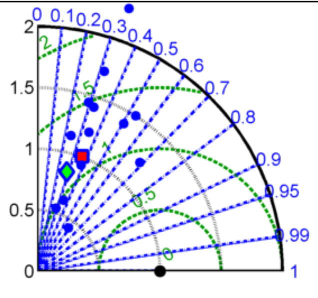	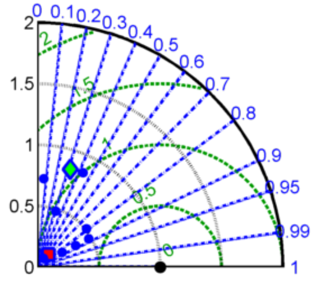

FIGURE A.2: Taylor diagrams for LP1 25 km morning products in the YA area. Satellite products are treated as the baseline soil moisture (black dot). □: Representative station. ◇: Average. ◯: Individual stations.

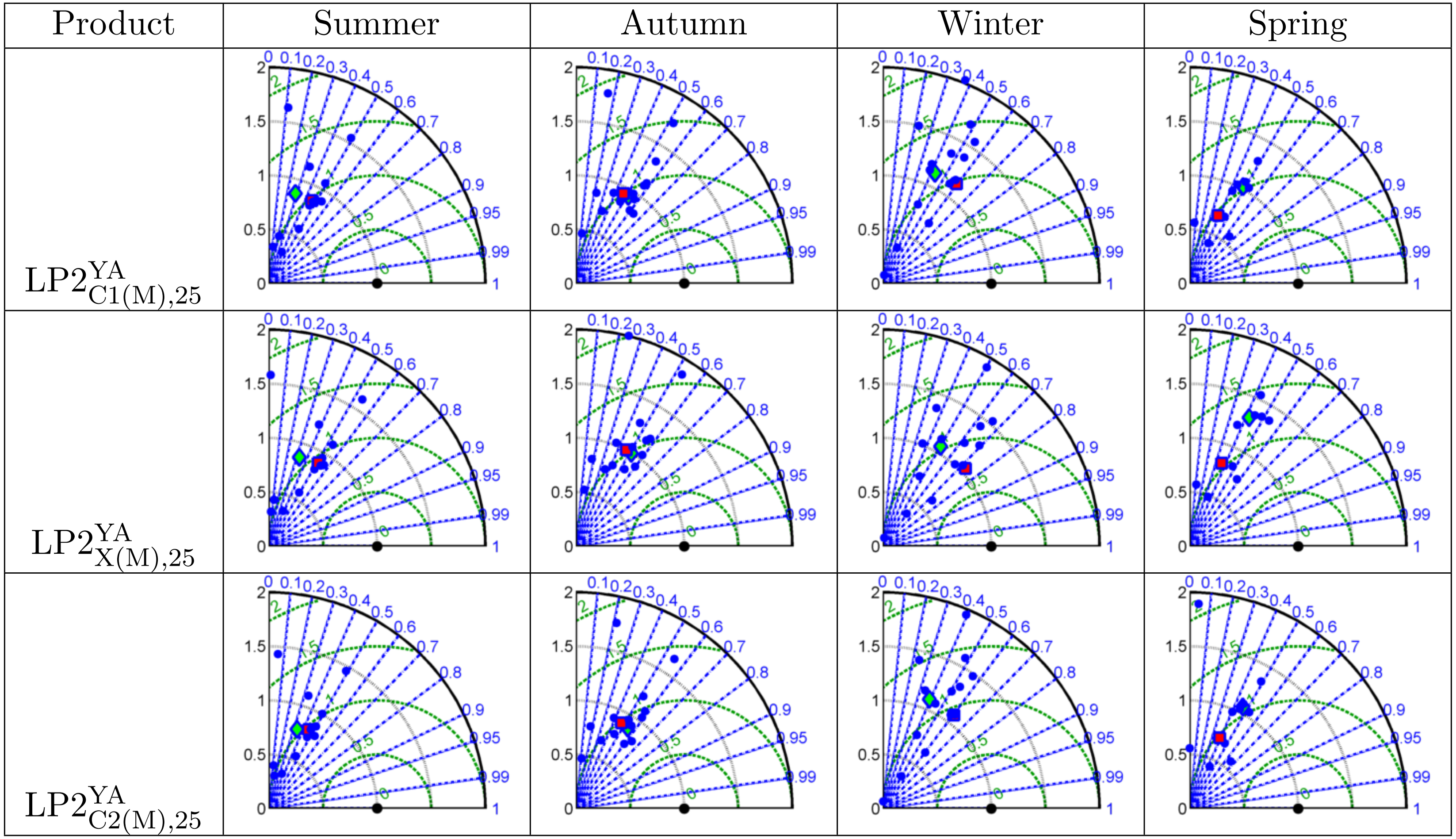

FIGURE A.3: Taylor diagrams for LP2 25 km morning products in the YA area. Satellite products are treated as the baseline soil moisture (black dot). □: Representative station. ◇: Average. ◯: Individual stations.

Product	Summer	Autumn	Winter	Spring
$JX1^{YB}_{X(M),25}$	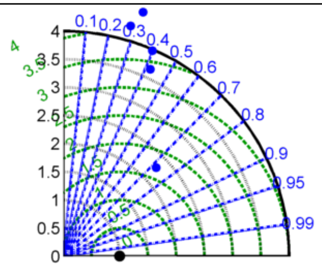	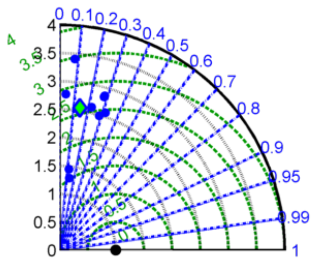	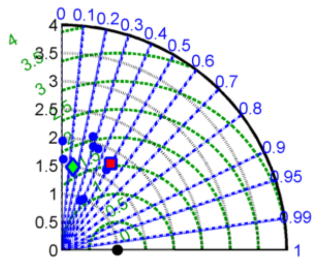	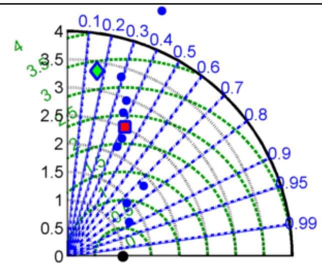
$JX2^{YB}_{X(M),25}$	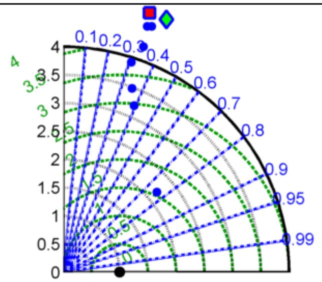	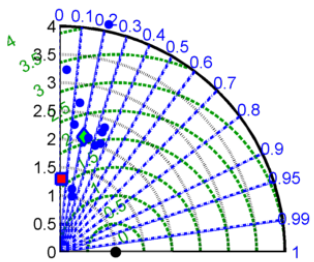	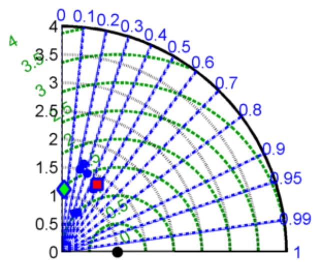	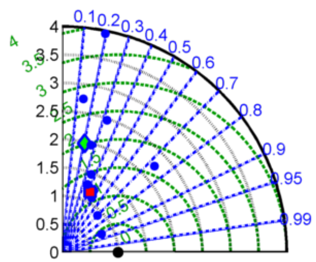

FIGURE A.4: Taylor diagrams for JAXA 25 km morning products in the YB area. Satellite products are treated as the baseline soil moisture (black dot). □: Representative station. ◇: Average. ◯: Individual stations.

Product	Summer	Autumn	Winter	Spring
$\mathrm{LP1}^{\mathrm{YB}}_{\mathrm{X(M)},25}$	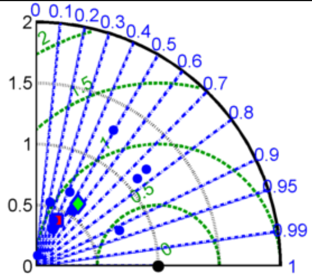	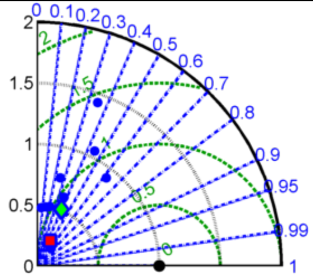	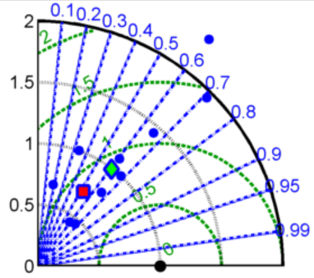	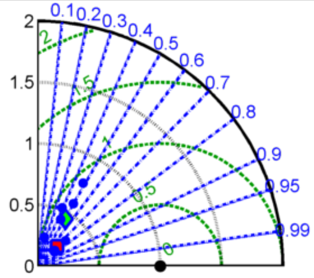
$\mathrm{LP1}^{\mathrm{YB}}_{\mathrm{C1(M)},25}$	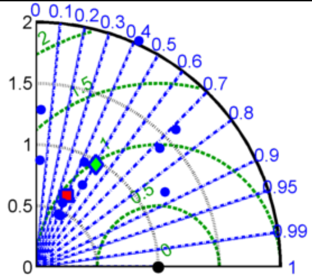	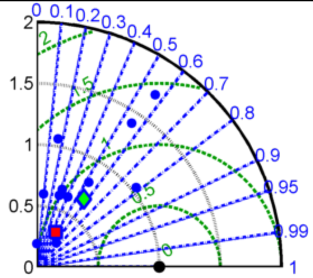	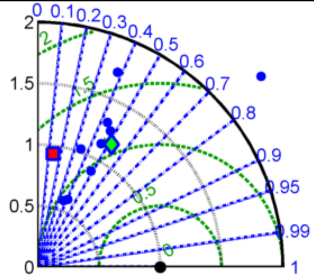	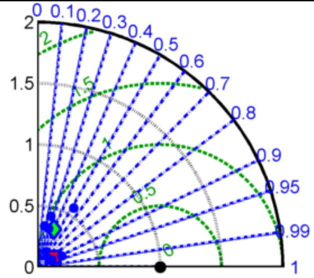
$\mathrm{LP1}^{\mathrm{YB}}_{\mathrm{C2(M)},25}$	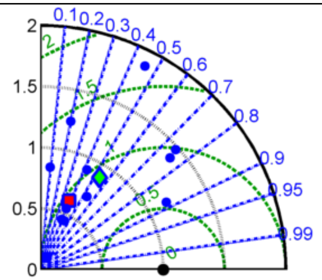	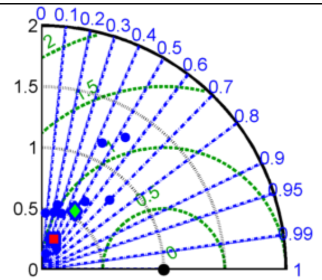	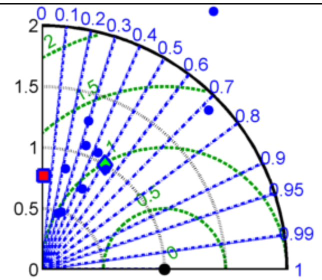	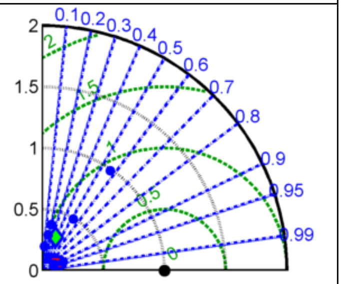

FIGURE A.5: Taylor diagrams for LP1 25 km morning products in the YB area. Satellite products are treated as the baseline soil moisture (black dot). □: Representative station. ◊: Average. ◯: Individual stations.

Product	Summer	Autumn	Winter	Spring
$LP2^{YB}_{X(M),25}$	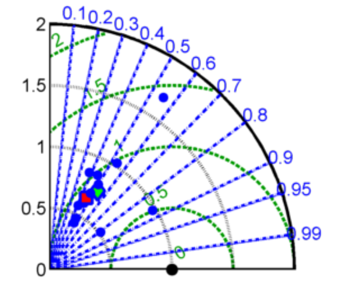	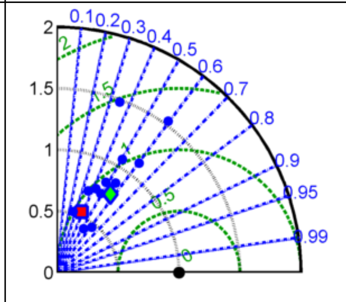	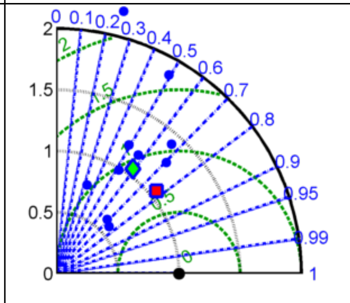	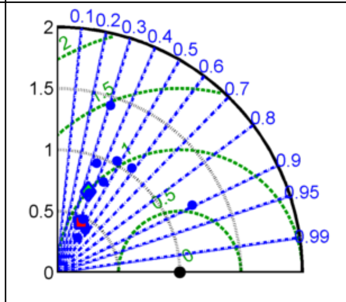
$LP2^{YB}_{C1(M),25}$	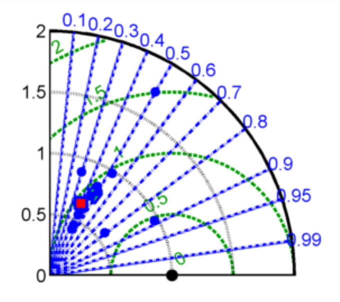	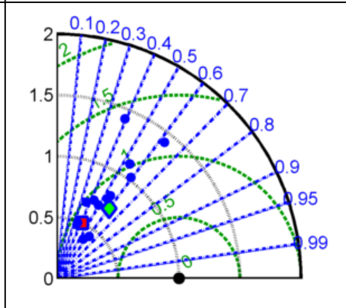	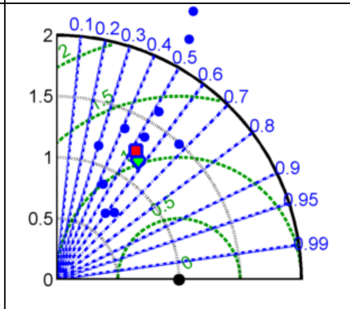	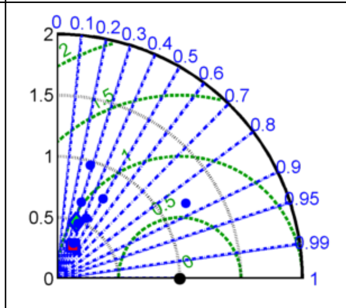
$LP2^{YB}_{C2(M),25}$	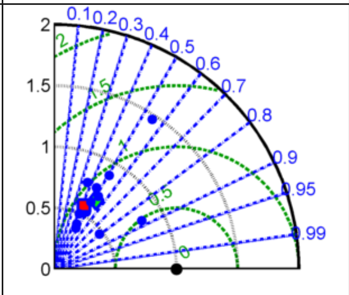	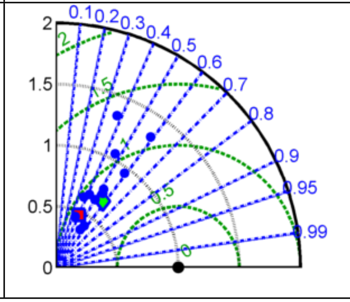	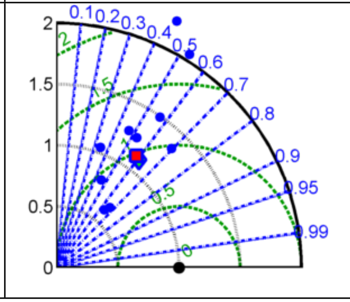	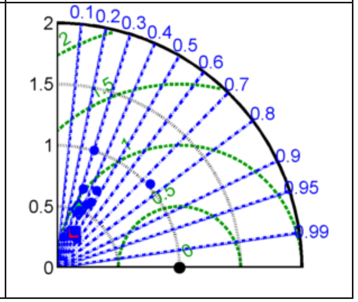

FIGURE A.6: Taylor diagrams for LP2 25 km morning products in the YB area. Satellite products are treated as the baseline soil moisture (black dot). □: Representative station. ◇: Average. ◯: Individual stations. Note the difference in scale for JAXA products.

Appendix B

Scintillometry theory

B.1 Theory

A scintillometer consists of a transmitter which emits electromagnetic wave signals to a receiver which records the intensity of this signal from a distance, L (m). As the signal propagates through the atmosphere towards the receiver, it is scattered by turbulent eddies in the atmosphere. These turbulent eddies are driven by surface forces such as wind shears from the frictional drag of winds flowing over the ground, heat fluxes from the ground caused by heating of the sun and turbulent wakes from obstacles like trees deflecting the flow of air (Stull, 1988).

Behind the derivation of surface heat fluxes based on scintillometry is a complex combination of different theories which eventually falls together nicely such that its application becomes more straight forward. In the following sections, the theoretical physics of atmospheric turbulence (section B.2) and of electromagnetic wave propagation (section B.3), together with how they are combined to enable sensible heat and latent heat to be derived (section B.4) is discussed. The chart below (Fig. B.1) gives a summary of the key equations and concepts that are needed to understand how these different theories are combined to derive surface heat fluxes.

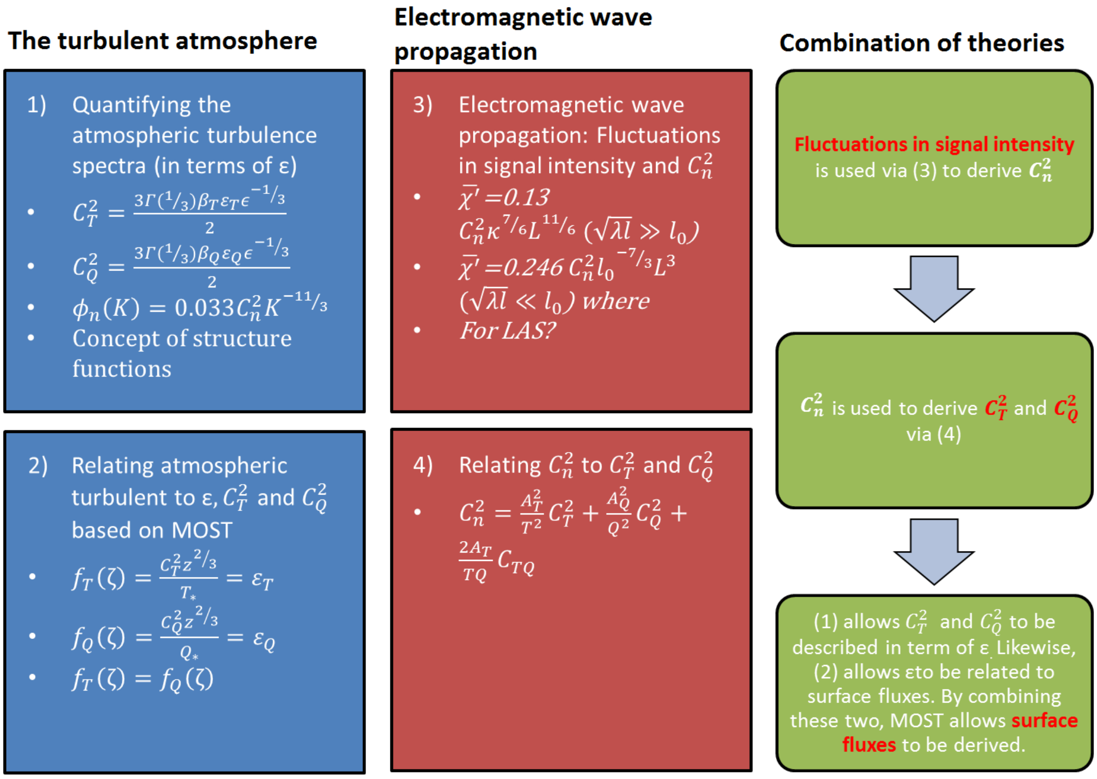

FIGURE B.1: Summary of scintillometer theory. A) The turbulent atmosphere. B) Electromagnetic wave propagation. C) Combination of theories.

B.2 The turbulent atmosphere

In the atmospheric boundary layer, wind shear and temperature gradient (convection) causes the formations of large scale eddies which breaks down into smaller and smaller eddies until these eddies dissipate into heat. This process is known as the energy cascade. Figure B.2 shows the schematic representation of the energy spectrum of turbulence which depends on the wave-number, $K = \frac{2\pi}{\text{eddy size}}$, as derived by Kolmogorov (Kolmogorov, 1941). This 1-dimensional spectrum derived by Kolmogorov is applicable for all turbulent systems. From this figure, it can be seen that the energy spectrum of turbulence can be classified into the production range, inertial sub-range and dissipation range, defined by $K = \frac{2\pi}{L_0}$ and $K = \frac{2\pi}{\ell_0}$, where L_0 is the outer scale and ℓ_0, the inner scale. According to Kolmogorov, eddies larger than the L_0 lie in the production range and is where energy is introduced into the turbulent spectrum by wind shear and convection. As eddies break up, and $L_0 \to \ell_0$, kinetic energy is transferred from the larger eddies to the smaller eddies until they become small enough for viscosity to effectively dissipate the kinetic energy into heat. In between L_0 and ℓ_0 is the inertial sub-range

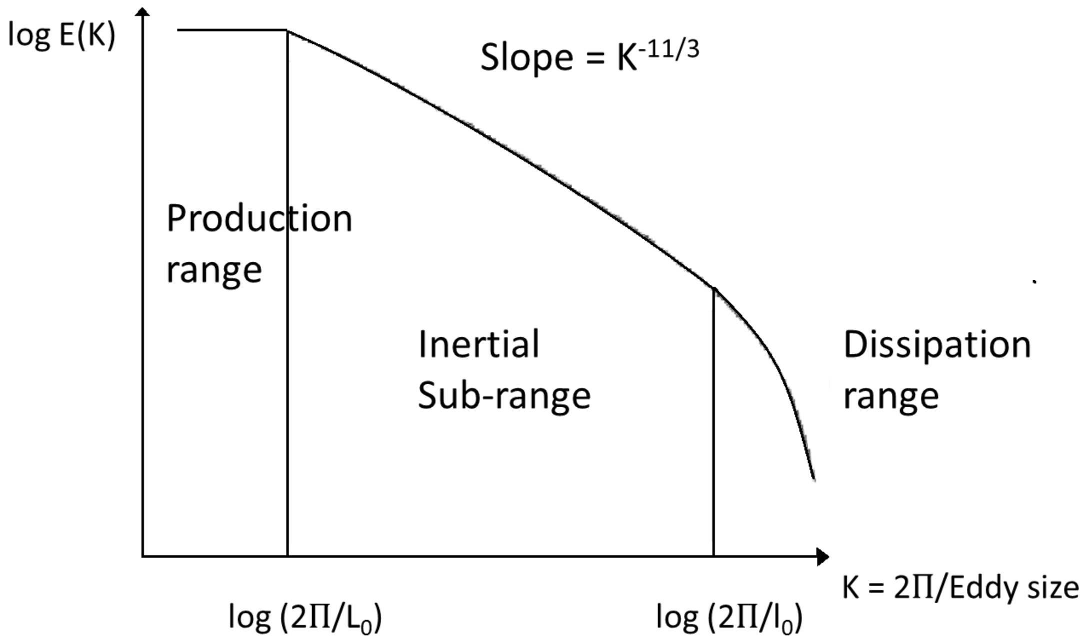

Figure B.2: Schematic representation of the energy spectrum of turbulence

where eddies do not store, release or produce energy. Within this range, turbulence is isotropic and the spectrum is proportional to $K^{-5/3}$. The spectral exponent, $(-\frac{5}{3})$, has been observed in many experiments. To better illustrate this, we refer to Ishimaru (1978). The kinetic energy of turbulence per unit mass of fluid per unit time is on the order of:

$$\frac{V^2}{\tau} = \frac{V^3}{L} \tag{B.1}$$

where V is the velocity of the flow, L is the size of the eddy and τ is the characteristic time associated with the eddy, L/V. The dissipation energy per unit mass per unit time or energy dissipation rate, ε, on the other hand is in the order of $\frac{\nu V^2}{L^2}$ where ν is kinematic viscosity.

When an eddy of the size L_0 cascades into smaller eddies, all the energy is transferred to these smaller eddies as dissipation is negligible. Therefore, for eddies of sizes $L_0 > L_1 > L_2 ... > L_n$ and the corresponding velocities $V_0, V_1, V_2 ... V_n$, their kinetic energies per unit mass per unit time will be approximately the same, i.e.:

$$\frac{V_0^3}{L_0} \simeq \frac{V_1^3}{L_1} \simeq \frac{V_2^3}{L_2} \simeq ... \simeq \frac{V_n^3}{L_n}. \tag{B.2}$$

However, as they become smaller, viscosity comes into play until the size of the eddies reaches ℓ_0 such that dissipation energy and kinetic energy reaches the same order,

$$\frac{V_0^3}{L_0} \simeq \frac{V_1^3}{L_1} \simeq ... \simeq \frac{V_\ell^3}{\ell_0} \simeq \frac{\nu V_\ell^2}{\ell_0^2} \simeq \varepsilon. \tag{B.3}$$

From here, it can be seen that for eddies between the sizes of the outer scale, L_0 and the inner scale, ℓ_0, the fluctuation velocity, V depends on the size of the eddy, L, and ε:

$$V = (\varepsilon L)^{1/3}. \tag{B.4}$$

Random fluctuations of wind speed, air temperature and humidity, refractive index and so on in a turbulent atmosphere are difficult to determine or quantify. Therefore, Kolmogorov (1941) quantified the energy cascade process using structure functions (Refer to section B.2.1).

In the inertial sub-range, the structure function is determined by the energy dissipation, ε since the separation r is large compared to the inner-scale, ℓ_0 ($\ell_0 \ll r \ll L_0$). Using the Buckingham-Π theorem, and then inserting the inertial sub-range, Kolmogorov (1941) derived the following relationship between the structure function of the random variable u, D_{uu}, and the structure function parameter for a turbulent velocity field u, C_u^2 such that:

$$D_{uu}(r) = C\varepsilon^{2/3} r^{2/3} = C_u^2 r^{2/3}, \tag{B.5}$$

where, $C_u^2 = C\varepsilon^{2/3} = \frac{3\Gamma(\frac{1}{3})}{2}\alpha\varepsilon^{2/3}$, α is the Kolmogorov constant, 0.52, and $\Gamma(\frac{1}{3})$ is the gamma function with argument $\frac{1}{3}$ (Monin and Yaglom, 1971)

Similarly, this can be applied in describing the structure functions of a conservative scalar such as temperature (T), humidity (Q), and refractive index of fluctuations (n) which can be measured by a scintillometer (Corrsin, 1951; Obukhov, 1949). In this case, if the magnitude of the fluctuations of a scalar, x, with an average of $\overline{x}$, is x' where:

$$x = \overline{x} + x' \tag{B.6}$$

then, analogous to Eq. B.1, for the amount of fluctuation or x', associated with the size L_0 and velocity, V_0:

$$\tau_0 = \frac{L_0}{V_0} \tag{B.7a}$$

$$\frac{x'^2}{\tau_0} = \frac{V_0 x'^2}{L_0}. \tag{B.7b}$$

Likewise, the rate in which x' dissipates is of the order of $\frac{Dx'^2}{L_0^2}$ where D is the coefficient of molecular diffusion. When the eddy is between the sizes L_0 and ℓ_0, dissipation is again negligible and as the fluctuations cascades to a smaller size until it reaches the inner scale ℓ_0, as described in Eq. B.3,

$$\frac{V_0 x_0'^2}{L_0} \simeq \frac{V_1 x_1'^2}{L_1} \simeq ... \simeq \frac{V_\ell x_\ell'^2}{\ell_0} \simeq \frac{D x_\ell'^2}{\ell_0^2} \simeq N_x. \tag{B.8}$$

where N_x is the fluctuation rate of scalar x. Now $Vx'^2/L \simeq N_x$ and by inserting Eq. B.4,

$$x'^2 \sim \frac{N_x L^{2/3}}{\varepsilon^{1/3}} \tag{B.9}$$

The structure function for the fluctuations of the scalar x can now be written as:

$$D_{xx}(r) = C_x^2 r^{2/3}, \tag{B.10}$$

for $\ell_0 \ll r \ll L_0$, where, $C_x^2 = \frac{aN_x}{\varepsilon^{1/3}}$, a is a universal constant which ranges from 1.5 to 3.5 (Ishimaru, 1978). C_x is the structure constant for the scalar x. For the purpose of this research, structure function parameters which are relevant is that of the refractive index, C_n^2, temperature, C_T^2 ($\mathrm{K^2 m^{-2/3}}$) and humidity , C_Q^2 ($\mathrm{g^2 m^{-6} m^{-2/3}}$):

$$C_T^2 = a\varepsilon_\theta \varepsilon^{-1/3} = \frac{3\Gamma(\frac{1}{3})}{2}\beta_\theta \varepsilon\theta \varepsilon^{-1/3} \tag{B.11a}$$

$$C_Q^2 = a\varepsilon_Q \varepsilon^{-1/3} = \frac{3\Gamma(\frac{1}{3})}{2}\beta_Q \varepsilon_Q \varepsilon^{-1/3} \tag{B.11b}$$

where β_θ is the Obukhov-Corrsin constant and β_θ=β_Q=0.86. To obtain the three-dimensional Kolmogorov spectrum, $\Phi_{xx}(K)$, for the scalar quantity x in the inertial sub-range, Eq. B.10 is substituted into Eq. B.35 to obtain:

$$\Phi_{xx}(K) = 0.033 C_x^2 K^{-11/3}. \tag{B.12}$$

This equation is valid for any passive scalar. Now that the spectrum has been quantified, scintillometry can be used to estimate C_x^2 and ℓ_0 (which is related to ε).

If it is assumed that all the energy loss from dissipation, i.e. ε is used to produce the atmospheric surface heat fluxes, by applying the atmospheric flow and budget equations, the following relationships between ε (dissipation of turbulent kinetic energy), ε_θ (dissipation of heat) and ε_Q (dissipation of humidity) with atmospheric fluxes are derived:

$$\varepsilon = \frac{g(\overline{w'\theta_v'})}{\overline{\theta_v}} - \overline{u'w'}\frac{\delta\overline{u}}{\delta z} \qquad \text{(conservation of momentum)} \qquad \text{(B.13a)}$$

$$\varepsilon_\theta = \overline{-\theta'w'}\frac{\delta\overline{\theta}}{\delta z} \qquad \text{(conservation of enthalpy)} \qquad \text{(B.13b)}$$

$$\varepsilon_Q = \overline{-Q'w'}\frac{\delta\overline{Q}}{\delta z} \qquad \text{(conservation of scalar quantities, i.e. humidity)} \qquad \text{(B.13c)}$$

where θ_v, u, θ and Q are virtual potential temperature, wind velocity, potential temperature and specific humidity respectively. Following this, by applying the Buckingham-Π theorem, Monin and Obukhov (1954) related the surface layer dimensionless parameter, $\zeta = \frac{z}{L_{\text{Ob}}}$ with dimensionless groups of surface layer variables to provide a link between surface heat fluxes and C_x^2. L_{Ob} is the Obukhov length, z is height of the surface. The following equations show the relationship between L_{Ob} with friction velocity (u_*), temperature scale (T_*) and humidity scale (Q_*):

$$L_{\text{Ob}} = -\frac{{u_*}^2\overline{\theta_v}}{g\kappa_{\text{v}}\theta_{v*}} = -\frac{\rho {u_*}^3}{g\kappa_v(\frac{H}{c_pT} + 0.61E)} \qquad \text{(B.14)}$$

$$\theta_{v*} = -\overline{w'\theta_v'}/u_* \qquad \text{(B.15)}$$

$$u_* = (\overline{u'w'})^{1/2}, \qquad \text{(B.16)}$$

$$T_* = \frac{\overline{w'T'}}{u_*} = \frac{-H}{\rho c_p u_*}, \qquad \text{(B.17)}$$

$$Q_* = \frac{\overline{w'Q'}}{u_*} = \frac{-L_{\text{v}}E}{L_{\text{v}}u_*}, \qquad \text{(B.18)}$$

where κ_{v} is the von Kármán constant (0.4), H is the sensible heat flux, E is the evaporation rate, ρ is the mean air density, T' and Q' are temperature and specific humidity fluctuations, c_p (1005 J kg^{-1} K^{-1}) is the specific heat capacity of dry air at constant pressure, and L_{v} is the latent heat of vaporization (J kg^{-1}). $\overline{w'\theta_v'}$, $\overline{w'T'}$ and $\overline{w'Q'}$ are kinematic buoyancy, temperature and humidity flux at the surface. Kinematic flux is related to its dynamic form (transfer of variable per unit area per unit time) by:

$$H = \rho c_p \overline{w'T'} \tag{B.19}$$

$$L_\text{v}E = \rho L_\text{v} \overline{w'Q'} \tag{B.20}$$

Assuming that H represents the buoyancy flux, and since $\overline{w'\theta_v'} = \overline{w'\theta'} + 0.61\overline{Tw'Q'}$, another expression for L_Ob in terms of H and $L_\text{v}E$ can be derived as the second part of Eq. B.15 (Kohsiek, 1982). According to Monin-Obukhov similarity theory (MOST), every dimensionless group that can be formed must be a function of ζ through the following relationships (e.g. Stull, 1988).

$$\frac{\kappa_v z}{u_*}\frac{\delta u}{\delta z} = \phi_m(\zeta) \tag{B.21a}$$

$$\frac{\kappa_v z}{\theta_*}\frac{\delta \theta}{\delta z} = \phi_T(\zeta) \tag{B.21b}$$

$$\frac{\kappa_v z}{Q_*}\frac{\delta Q}{\delta z} = \phi_Q(\zeta) \tag{B.21c}$$

where $\phi_m(\zeta)$, $\phi_T(\zeta)$ and $\phi_Q(\zeta)$ are dimensionless functions of ζ. Substituting equations B.21a, B.21b and B.21c into equations B.13a, B.13b, B.13c,

$$\varepsilon = \frac{u_*^3}{\kappa_v z}(-\zeta + \phi_m) \tag{B.22a}$$

$$\varepsilon_T = \frac{u_*\theta_*^2}{\kappa_v z}\phi_T \tag{B.22b}$$

$$\varepsilon_Q = \frac{u_* Q_*^2}{\kappa_v z}\phi_Q. \tag{B.22c}$$

Next, rearrange B.5, B.11a, B.11b to obtain ε, ε_θ and ε_Q, and the C_u^2, C_T^2 and C_Q^2 and ε measured from a scintillometer can be related to the dimensionless functions of ζ:

$$\varepsilon = \frac{C_u^2 z^{2/3}}{u_*^2} = \frac{3\Gamma(\frac{1}{3})\alpha(-\zeta + \phi_m)^{2/3}}{2\kappa_v^{2/3}} = f_v(\zeta) \tag{B.23}$$

$$\varepsilon_\theta = \frac{C_T^2 z^{2/3}}{\theta_*^2} = \frac{3\Gamma(\frac{1}{3})\beta_\theta\phi_T(-\zeta + \phi_m)^{-1/3})}{2\kappa_v^{2/3}} = f_T(\zeta) \tag{B.24}$$

$$\varepsilon_Q = \frac{C_Q^2 z^{2/3}}{Q_*^2} = \frac{3\Gamma(\frac{1}{3})\beta_Q\phi_Q(-\zeta + \phi_m)^{-1/3}}{2\kappa_v^{2/3}} = f_Q(\zeta) \tag{B.25}$$

For this study, we are interested in the surface heat fluxes H and $L_\text{v}E$ and therefore the remaining sections will focus on C_T^2 and C_Q^2.

It is common practice to assume that β_θ and β_Q, and ϕ_Q and ϕ_T are the same such that $f_T(\zeta) = f_Q(\zeta)$. According to similarity theory, the dimensionless functions are universal. It is noted however that many different expressions for $f_T(\zeta)$ and $f_Q(\zeta)$ have been derived (Hill, 1997; Moene, 2003; Savage, 2009). In addition, Katul et al. (1995) and Katul and Hsieh (1999) demonstrated that assumptions made of similarity between $f_T(\zeta)$ and $f_Q(\zeta)$ may be inaccurate due to the differences in transport inefficiencies of heat and water vapour, dissimilarity in heat and water vapour sources and sinks and non-uniformity in the sources and sink of water vapour itself. Nevertheless, in the application of scintillometry to determine surface heat fluxes, once a similarity function (f_{Ob}) has been identified or selected, C_T^2 and C_Q^2 estimated from a scintillometer can be used to derive H and $L_{\mathrm{v}}E$. We summarize the relationship between the dimensionless function and measured structure parameters as:

$$\frac{C_{\mathrm{T}}^2(z_{\mathrm{s}} - d_0)^{2/3}}{T_*^2} = \frac{C_{\mathrm{Q}}^2(z_{\mathrm{s}} - d_0)^{2/3}}{Q_*^2} = f_{Ob}\left(\frac{z_{\mathrm{s}} - d_0}{L_{\mathrm{Ob}}}\right) \tag{B.26}$$

where z_{s} is scintillometer beam height and d_0 is the zero-plane displacement height. Generally the functions can be described in the following form:

$$f_{Ob}(x) = c_1(1 - c_2 x)^{-2/3} \quad \text{(unstable conditions/daytime where} L_{\mathrm{Ob}} < 0) \tag{B.27a}$$

$$f_{Ob}(x) = c_1(1 + c_3 x^{2/3}) \quad \text{(stable conditions/night time where} L_{\mathrm{Ob}} < 0) \tag{B.27b}$$

In this study, $c_1 = 4.9$, $c_2 = 6.1$ (see Andreas, 1989) and $c_3 = 2.2$ (see Wyngaard, JC and Izumi, Y and Collins, Stuart A, 1971) were used. u_* can be estimated from:

$$u_* = \frac{\kappa_v u}{\ln\left(\frac{z_u - d_0}{z_0}\right) - \Psi\left(\frac{z_u - d_0}{L_{\mathrm{Ob}}}\right) + \Psi\left(\frac{z_0}{L_{\mathrm{Ob}}}\right)}, \tag{B.28}$$

where Ψ is the Businger-Dryer expression

$$\Psi\left(\frac{z}{L_{\mathrm{Ob}}}\right) = 2\ln\left(\frac{1+x}{2}\right) + \ln\left(\frac{1+x^2}{2}\right) - 2\arctan(x) + \left(\frac{\pi}{2}\right), \tag{B.29}$$

with

$$x = \left(1 - 16\frac{z}{L_{\mathrm{Ob}}}\right)^{1/4}, \tag{B.30}$$

for unstable or daytime ($L_{\mathrm{Ob}} < 0$) and

$$\Psi\left(\frac{z}{L_{\mathrm{Ob}}}\right) = -5\left(\frac{z}{L_{\mathrm{Ob}}}\right), \tag{B.31}$$

for stable, night time ($L_{\mathrm{Ob}} > 0$) conditions (De Bruin et al., 1995).

B.2.1 Structure functions

Statistical methods such as Reynolds decomposition and the concept of moments can be used to determine or quantify random fluctuations (Monin and Yaglom, 1971). According to Reynolds decomposition, the random variable, u, can be decomposed into a mean part, $\overline{u}$ (considered as ensemble average here) and its deviation from that mean, u' such that:

$$u = \overline{u} + u' \tag{B.32}$$

The mean of u', i.e. $\overline{u'}$ is zero by definition. The over-bar denotes the ensemble average (Monin and Yaglom, 1971). Additionally, the concept of moments can be used to describe the statistical moments of the turbulent flow in space and time. Since we are only interested in the lower order moments of the turbulent flow. The first order central moment is zero and the second order central moment (variance) of two points can be defined as:

$$B_{uu}(M_1, M_2) = \overline{u'(M_1)u'(M_2)}, \tag{B.33}$$

where M is the three dimensional position of the point at time t such that $M = (x, y, z, t)$. The spatial and temporal moments can be considered separately such that $M = r_n = (x_n, y_n, z_n)$ or t. B_{uu}, can be used to define three simple cases of turbulence, i.e. stationary, homogeneous and isotropic case (as shown in Table B.1).

Table B.1: Second order moments for stationary, homogeneous and isotropic random variables or processes

Conditions	Description	Second order moment (B_{uu})	Second order structure function (D_{uu})
Stationary	$\overline{u(t)}$, is constant. B_{uu} dependent only on $\tau = t_1 - t_2$	$B_{uu}(t_1, t_2)$ $= B_{uu}(t_1 - t_2) = B_{uu}(t_2 - t_1)$	$D_{uu}(t_1, t_2) = D_{uu}(t_1 - t_2) = D_{uu}(t_2 - t_1) = D_{uu}(\tau)$ $= \overline{(u(t+\tau) - u(t))^2}$
Homogeneous	$\overline{u(r_n)}$ is constant. B_{uu} dependent only on $r_1 - r_2$	$B_{uu}(r_1, r_2)$. $= B_{uu}(r_1 - r_2) = B_{uu}(r_2 - r_1)$	$D_{uu}(r_1, r_2) = D_{uu}(r_1 - r_2) = D_{uu}(r_2 - r_1)$ $= (u(r_1) - u(r_2))^2$.
Isotropic	$\overline{u(r_n)}$ is constant. B_{uu} dependent only on $r = \mid r_1 - r_2 \mid$	$B_{uu}(r_1, r_2)$. $= B_{uu} \mid r_1 - r_2 \mid = B_{uu}(r)$	$D_{uu}(r_1, r_2) = D_{uu} \mid r_1 - r_2 \mid = D_{uu}(r)$ $= \overline{(u(r + r_1) - u(r_1))^2}$

However, in a turbulent atmosphere, $\overline{u(t)}$ is not constant and therefore is difficult to describe in terms of statistics. Therefore, Kolmogorov (1941) proposed that instead of $\overline{u(t)}$ being stationary, the increments in $\overline{u(t)}$ (u'), are stationary, i.e. $U_\tau = u(t+\tau) - u(t)$ is constant. The basic assumption behind this theory according to Tatarskii (1971), is that the difference between $u(r_1)$ and $u(r_2)$ is dependent only by inhomogeneities of the field $u(r)$ in which scale sizes are smaller than the distance $\mid r \mid$ ($\mid r_1 - r_2 \mid$). Scale sizes larger than this distance have no effect on $u(r_1) - u(r_2)$. Therefore, in the manner of Eq. B.33, the second order moment of U_τ, can be written as:

$$B_{U_\tau U_\tau}(t) = \overline{U_\tau(t_1)U_\tau(t_2)} = \overline{(u(t_1+\tau) - u_1(t))(u(t_2+\tau) - u(t_2))} \tag{B.34}$$

Just like B_{uu}, the second order moment or structure function of a random field with stationary increments, D_{uu} can therefore be described for stationary, homogeneous and isotropic conditions (Table B.1). D_{uu} has the same unit as the variance of the field. Based on Fourier analysis, D_{uu} can also be described in terms of the 3-dimensional spectral density, $\Phi_{uu}(K)$ which leads to (Tatarskii, 1971):

$$D_{uu}(r) = 8\pi \int_0^\infty 1 - \frac{\sin(Kr)}{Kr} \Phi_{uu}(K) K^2 dK \tag{B.35}$$

where K is the magnitude of the wave number. With the equations derived in Table B.1, we are able to describe random fluctuations as structure functions and Eq. B.35 gives us the relationship between the structure functions to its 3-dimensional spectral form.

B.3 Electromagnetic wave propagation

A scintillometer consist of a transmitter that emits electromagnetic wave signal, and a distance L (m) from it, a receiver that detects this signal. As the electromagnetic wave travels through the atmosphere to the receiver, it is scattered by turbulent eddies in the atmosphere. The scattering of the signal causes fluctuations in the intensity of the signal detected by the receiver. As a result, the strength of these fluctuations, which can be described as variances of measurements by the receiver can be used to infer information regarding the atmospheric conditions causing the turbulence. In the earlier section, the relationship between atmospheric turbulence and the structure parameters of scalars such as T (C_T^2) and Q (C_Q^2) have been described. In this section, the wave propagation theory will be described to understand how electromagnetic waves are affected by turbulence in the atmosphere.

The characteristics of the signal measured by the receiver of the scintillometer can be quantified mathematically based on the application of small angel scattering theory assuming that atmospheric absorption does not occur. Note however that in reality, the wavelength of the electromagnetic wave, λ, always coincides with some atmospheric absorption lines.

Scattering of electromagnetic waves in the atmosphere is caused by differences in densities of the atmosphere as a result of differences in T and Q of each parcel of air (or turbulent eddy). As a result, these eddies have a different refractive index, n and act like small lenses which causes electromagnetic waves to be bend at different angles depending on n. n is an index which indicates how much the speed of an electromagnetic wave is reduced as compared to its speed in a vacuum (due to turbulence in the atmosphere in this case). n depends not only on the eddy but also the wavelength of the electromagnetic wave, λ. Thus, in scintillometery, the signal emitted by the transmitter needs to be as monochromatic as possible.

An important concept to understand is that of the first Fresnel zone because eddies of the size of the first Fresnel zone, F, is scattered most efficiently.. The first Fresnel zone is the diameter of the first destructive interference ring. Eddies of the size of the first Fresnel zone, F, is scattered most efficiently. F is given by:

$$F = 2\sqrt{\lambda 0.5L(L - 0.5L)/L} = \sqrt{\lambda L} \tag{B.36}$$

since its maximum diameter is at the midpoint of L, i.e. $0.5L$ (Jenkins and White, 1957).

Scattering of electromagnetic waves in scintillometry applications consist of refraction and diffraction. Refraction is a change in direction and/or speed of the wave and this happens dominantly when the smallest eddies are still larger than the beam, i.e. $\sqrt{\lambda L} \ll \ell_0$. Diffraction on the other hand is the bending or spreading of the wave and this occurs dominantly when the beam is larger than the smallest eddies, i,e, $\sqrt{\lambda L} \gg \ell_0$. When diffraction occurs, the wave starts to move further and in wider directions, thereby causing the receiver to receive parts of the signal in phase and parts out of phase due to differences in distance travelled.

The relative size of F in comparison to the aperture size of the scintillometer, D also gives rise to the Small Aperture Scintillometer (SAS) and the Large Aperture Scintillometer (LAS) where $F \gg D$ in the first case and $F \ll D$ in the second. At millimeter wavelengths, F is much larger than D and therefore a millimetre or microwave scintillometer (MWS) is classified as an SAS.

The propagation of a monochromatic wave through turbulent atmosphere, assuming that polarization effects are negligible can be described by the wave equation, also known as the Helmholtz equation:

$$\nabla^2 E(r) + \kappa^2 n^2(r) E(r) = 0, \text{ where} \tag{B.37a}$$

$$\nabla^2 = \frac{\delta^2}{\delta x^2} + \frac{\delta^2}{\delta y^2} + \frac{\delta^2}{\delta z^2}. \tag{B.37b}$$

$\kappa = 2\pi/\lambda$ is the wave number of the electromagnetic wave (take note that this is different from K which is the wave number of the eddy), E is the amplitude of the electric field and n is the refractive index of the medium (Tatarskii, 1971). This equation is highly non-linear so by assuming a homogeneous and locally isotopic medium and that only small-angle scattering occurs (this solution is therefore only applicable SASs), Tatarskii (1971) solved it using the Rytov approximation.

In brief, the Rytov method assumes that the signal received at the receiver consist of a perturbed part (A and S) and an unperturbed part (A_0 and S_0) where:

$$\text{Amplitude fluctuations, } \chi = \log(\frac{A}{A_0}), \text{ and} \tag{B.38a}$$

$$\text{Phase fluctuations, } S' = S - S_0. \tag{B.38b}$$

The unperturbed part is the signal which would be received in a perfect vacuum whereas the perturbed part is caused by scattering in the turbulent atmosphere. In applications, the unperturbed part is the mean signal which varies slowly with atmospheric conditions. The full solution for this will not be covered here but eventually, a link between the amplitude fluctuations of the perturbed wave, i.e. variance of χ, σ_χ^2, with the Kolmogorov spectrum of refractive index fluctuations C_n^2, $\Phi(K)$ can be made:

$$\sigma_\chi^2 = 4\pi^2\kappa^2 \int_0^L \int_0^\infty K\Phi_{nn}(K)\sin^2\frac{K^2x(L-x)}{2\kappa L}dxdK. \tag{B.39}$$

where x is the normalized position along the propagating path from the source. Further inserting Eq. B.12 into Eq. B.39 and integrating gives the relationship between σ_χ^2 and the path averaged C_n^2:

$$\sigma_\chi^2 = 0.124 C_n^2 \kappa^{7/6} L^{11/6} \tag{B.40}$$

for $\sqrt{\lambda L} \gg \ell_0$ and $\sigma_\chi^2 < 0.3$ as in the case of a MWS, since small scale effects can be ignored. However, in the case where $\sqrt{\lambda L} \ll \ell_0$, which occurs when the wavelength lies between the optical and near-infrared wavelength, small scale effects cannot be ignored and an accurate 3-dimensional spectrum must be prescribed accurately (i.e. the Hill spectrum Hill and Clifford, 1978) which leads to

$$\sigma_\chi^2 = 0.246 C_n^2 \ell_0^{-7/3} L^3 \tag{B.41}$$

for $\sqrt{\lambda L} \ll \ell_0$, i.e. optical SASs. Eq. B.39 is only valid for weak scattering medium and when the turbulence becomes intense, there is a possibility that saturation of the signal may occur. This occurs when $\sigma_\chi^2 > 0.3$. When this happens Eq. B.39 is no longer valid and this often occurs over long distances. To avoid this, Wang et al. (1978) developed the large aperture scintillometer (LAS) which as the name suggests, has an aperture size larger than the SAS. This modification led to the change of the relationship between $C_{n_{\mathrm{LAS}}}^2$ and σ_χ^2 for a LAS such that:

$$\sigma_\chi^2 = 0.223 C_n^2 D^{-7/3} L^3 \tag{B.42}$$

As scintillometers often measure intensity, I, σ_χ^2 can be related to I as shown:

$$4\sigma_\chi^2 = 4\sigma_{\mathrm{lnA}}^2 = \sigma_{\mathrm{lnI}}^2 \tag{B.43}$$

B.4 Combining atmospheric turbulence and scintillometry

In sections B.2 and B.3, we derived Eq. B.26 and B.40 and B.42. In this section, we will show how these can be combined such that H and $L_{\mathrm{v}}E$ can be inferred from measurements of fluctuations in I measured by the receiver of the scintillometer. The missing link between these two equations is the relationship between C_n^2 with C_T^2 and C_Q^2. C_n^2 can be derived from scintillometer measurements whereas atmospheric turbulence theory tells us how C_T^2 and C_Q^2 are related to H and $L_{\mathrm{v}}E$.

In the turbulent atmosphere, C_n^2 has been shown to depend only on temperature and humidity fluctuations (Moene, 2003). Their relative contributions depend on the wavelength of the electromagnetic wave used for measurements. C_T^2 and C_Q^2 are related to one another through the temperature-humidity cross structure parameter, C_{TQ}. Therefore, the relationship between C_n^2 with C_T^2 and C_Q^2 can be written as:

$$C_n^2 = A_{\mathrm{T}}^2 \frac{C_{\mathrm{T}}^2}{T^2} + A_{\mathrm{Q}}^2 \frac{C_{\mathrm{Q}}^2}{Q^2} + 2A_T A_Q \frac{C_{TQ}}{TQ}, \tag{B.44}$$

where A_{T} and A_{Q} are related to λ and the mean of air temperature, T (K), atmospheric pressure, P (Pa) and humidity (Q, kg m^{-3}). $A_{T_{\mathrm{LAS}}}$ and $A_{Q_{\mathrm{LAS}}}$ for visible and near infrared wavelengths (LAS) were defined by Andreas (1989) as:

$$A_{T_{\mathrm{LAS}}} = m_1(\lambda)(\frac{P}{T}) - R_v m_2(\lambda) Q \tag{B.45a}$$

$$A_{Q_{\mathrm{LAS}}} = R_v m_2(\lambda) Q, \tag{B.45b}$$

where R_v is the specific gas constant for water vapour (461.5 J K^{-1} kg^{-1}). For LASs, $m_1(\lambda) = -0.27 \times 10^{-3}$ and $m_2(\lambda) = -0.70 \times 10^{-6}$ for typical atmospheric conditions (P = 10^5 Pa, T = 288 K, Q = 0.012 kg m^{-3}). For MWSs, $A_{T_{\mathrm{MWS}}}$ and $A_{Q_{\mathrm{MWS}}}$ are slightly different and are given by as:

$$A_{T_{\mathrm{MWS}}} = -b\frac{p}{T} - c\frac{Q}{T} \tag{B.46a}$$

$$A_{Q_{\mathrm{MWS}}} = c\frac{Q}{T} \tag{B.46b}$$

where $b = 0.776 \times 10^{-6}$ K Pa^{-1} and $c = 1.723$ K m^3 kg^{-1}. With that, we are now able to relate C_n^2 with C_T^2 and C_Q^2 which in turns allows us to derive H and $L_{\mathrm{v}}E$ based on MOST.

Appendix C

Calculation of fluxes from scintillometers

C.1 Calculations

In the prior section, we have shown very briefly how two complicated theories of turbulence atmosphere and scintillometry come together beautifully such that scintillometry can be applied easily for measuring surface heat fluxes. However, in practice, due to differences in wavelength, λ, aperture size and design, different classes of scintillometers have be made and tested in different environments.

It can be seen from Eq. B.45a, B.45b B.46a and B.46b that A_Q is much smaller than A_T in the near infrared wavelengths but of similar magnitude in the millimetre wavelength. This means that T fluctuations (C_T^2) is the major contributor to C_n^2 for LASs whereas both T and Q fluctuations are important for MWSs. As a result, LASs can be used on its own. Whilst MWSs are often used in combination with LASs in the two-wavelength method, Leijnse et al. (2007) have shown a possibility of using a stand-alone MWS in relatively wet conditions by introducing the energy budget constraint and found that the stand-alone MWS was suitable for use on its own in wet to moderately dry conditions where $\beta \leq 2$.

Here, the LAS and MWS are of interest. These two classes of scintillometers can be used on their own and also combined in the two-wavelength method (LAS-MWS). The

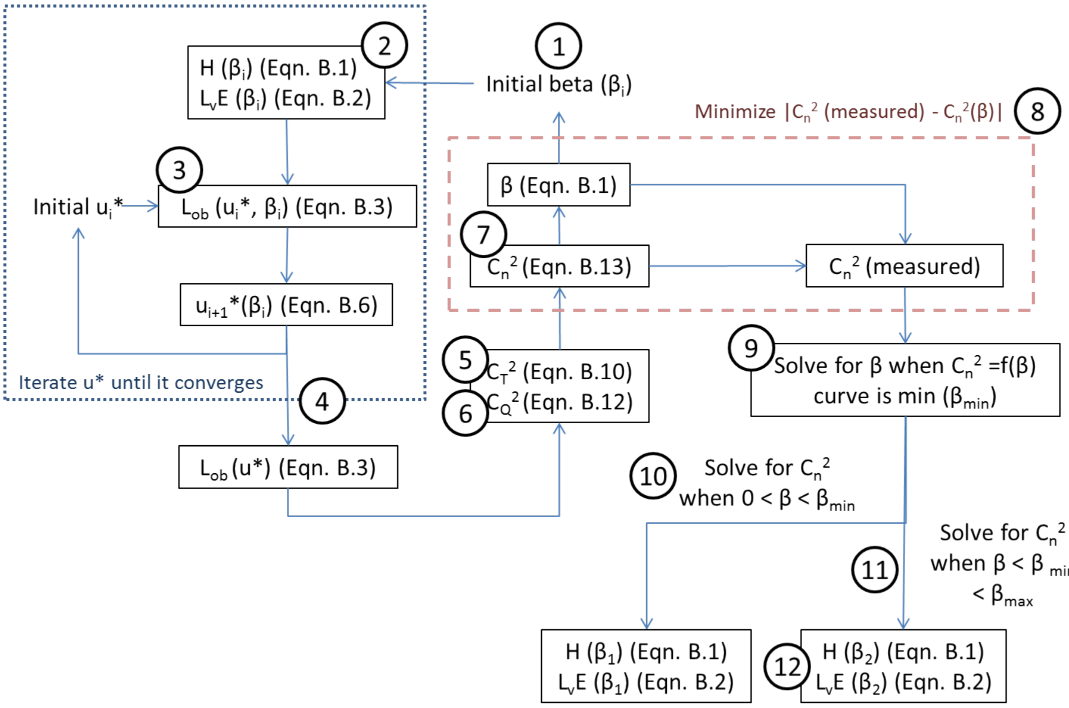

FIGURE C.1: Surface heat flux derivation flow chart. Step no. indicated in circles.

following sections will therefore discuss how surface heat fluxes can be derived from 1) a stand-alone near LAS 2) a stand-alone MWS and 3) the two-wavelength method (LAS-MWS), and the equations and procedures to do so. A brief description of the calculation of H and $L_\mathrm{v}E$ from C_n^2 measured by the scintillometers is presented here. We refer to Leijnse et al. (2007) for a comprehensive description of the derivations required for the calculation of these fluxes.

An iterative procedure (Fig. C.1) using two loops was employed to calculate H and $L_\mathrm{v}E$ from the available measurements at 30-min intervals.

From an initial guess of Bowen ratio (Step 1), $\beta = H/L_\mathrm{v}E$, H and $L_\mathrm{v}E$ were calculated as

$$H = \frac{\beta}{1+\beta}\left(R_\mathrm{n} - G\right), \tag{C.1}$$

and

$$L_\mathrm{v}E = \frac{1}{1+\beta}(R_n - G), \tag{C.2}$$

where R_n and G were measured or estimated from measured data (Step 2).

An initial guess of u_* was then used to calculate L_{Ob} expressed as

$$L_{\mathrm{Ob}} = -\frac{\rho u_*^3}{\kappa g \left[H/(c_p T) + 0.61(L_{\mathrm{v}} E)/L_{\mathrm{v}}\right]}, \tag{C.3}$$

where $c_p = 1005$ J kg^{-1} K^{-1} is the specific heat of air at constant pressure, T is the air temperature, and κ is the von Kármán constant, assumed to equal 0.4 (Step 3). The density of moist air, ρ, is

$$\rho = \frac{p}{R_d T} - 0.61\ Q, \tag{C.4}$$

with R_d being the gas constant of dry air equal to 287.04 J kg^{-1}K^{-1}. L_{v} is calculated as

$$L_{\mathrm{v}} = 1000 \cdot (2501 - 2.361\ (T - 273.15)). \tag{C.5}$$

A new value of u_* is then calculated from

$$u_* = \frac{\kappa u}{\ln\left(\frac{z_u - d_0}{z_0}\right) - \Psi\left(\frac{z_u - d_0}{L_{\mathrm{Ob}}}\right) + \Psi\left(\frac{z_0}{L_{\mathrm{Ob}}}\right)}, \tag{C.6}$$

where u is wind speed at the height z_u and $\Psi(\cdot)$ is the Businger-Dyer function, expressed as

$$\Psi(y) = 2\ln\left(\frac{1+x}{2}\right) + \ln\left(\frac{1+x^2}{2}\right) - 2\arctan(x) + \frac{\pi}{2}, \tag{C.7}$$

with

$$x = (1 - 16y)^{1/4}. \tag{C.8}$$

Roughness length, z_0, and d_0 were calculated as

$$\begin{cases} z_0 & = & \dfrac{h_0}{8} \\ d_0 & = & \dfrac{2h_0}{3}. \end{cases} \tag{C.9}$$

The value of u_* calculated from Eq. (C.6) was compared to the guessed value; if the two were different, the new u_* was used in Eq. (C.3) and the procedure repeated until the difference between the initial u_* and that calculated with Eq. (C.6) became lower than 10^{-6} (Step 4). This value of u_* was used to calculate the structure parameter of temperature, C_T^2 (Step 5), with the formula

$$C_T^2 = \frac{H^2}{\rho^2 c_p^2} \frac{1}{u_*^2 (z_\mathrm{s} - d_0)^{2/3}} f_{Ob} \left(\frac{z_\mathrm{s} - d_0}{L_\mathrm{Ob}} \right), \tag{C.10}$$

where z_s [m] is the effective beam height. For unstable conditions, the stability function, $f_\mathrm{Ob}(.)$, can be written as

$$f_\mathrm{Ob}(x) = c_1 (1 - c_2 x)^{-2/3}, \tag{C.11}$$

with $c_1 = 4.9$ and $c_2 = 6.1$ (Andreas, 1989). The structure parameter of moisture, C_Q^2, was calculated (Step 6) as

$$C_Q^2 = \frac{L_\mathrm{v} E^2}{L_\mathrm{v}^2} \frac{1}{u_*^2 (z_\mathrm{s} - d_0)^{2/3}} f_\mathrm{Ob} \left(\frac{z_\mathrm{s} - d_0}{L_\mathrm{Ob}} \right). \tag{C.12}$$

These were used to calculate C_n^2 (Step 7) with the expression

$$C_n^2 = A_T^2 \frac{C_T^2}{T^2} + A_Q^2 \frac{C_Q^2}{Q^2} + 2A_T A_Q \frac{C_{TQ}}{TQ}, \tag{C.13}$$

where the cross-structure parameter of temperature and humidity, C_{TQ}, is

$$C_{TQ} = r_{TQ} C_T C_Q, \tag{C.14}$$

with r_{TQ} assumed to equal 1.

The dimensionless sensitivity coefficients of the refractive index, A_T and A_Q, differ for LAS and MWS.

For LAS systems, they read

$$\begin{cases} A_{T_{\mathrm{LAS}}} &= m_1(\lambda)(\frac{P}{T}) - R_v m_2(\lambda) Q \\ A_{Q_{\mathrm{LAS}}} &= R_v m_2(\lambda) Q, \end{cases} \tag{C.15}$$

where R_v is the specific gas constant for water vapour (461.5 J K^{-1} kg^{-1}), $m_1(\lambda) = -0.27 \times 10^{-3}$ and $m_2(\lambda) = -0.70 \times 10^{-6}$ for typical atmospheric conditions ($P = 10^5$ Pa, $T = 288$ K, $Q = 0.012$ kg m^{-3}) (Andreas, 1989).

For the MWS systems, $A_{T_{\mathrm{MWS}}}$ and $A_{Q_{\mathrm{MWS}}}$ are

$$\begin{cases} A_{T_{\mathrm{MWS}}} &= -b\frac{p}{T} - c\frac{Q}{T} \\ A_{Q_{\mathrm{MWS}}} &= c\frac{Q}{T}, \end{cases} \tag{C.16}$$

where the constant b is equal to $0.776 \cdot 10^{-6}$ K Pa^{-1}, and the constant c is equal to 1.723 K m^3 kg^{-1}.

If the initial guess of β were correct, C_n^2 calculated from Eq. (C.13) would equal the measured C_n^2. In the case when the calculated and measured values of C_n^2 were different, a different guess of β should be used and the procedure should be repeated from Eq. (C.1). This gives a relationship between C_n^2 and β for given atmospheric conditions (measured P, T, Q, R_n, G, u). Using a minimization function, the β value which minimizes the difference between the scintillometer derived C_n^2 and $C_n^2(\beta)$ is found (i.e. $\mid C^2_{n_{\text{measured}}}$ - $C_n^2(\beta) \mid$) (Step 8). The accuracy of β was set to 10^{-12}.

While the solution of this minimization is unique for LAS, each measured value of C_n^2 with MWS corresponded to two possible solutions of β (Leijnse et al., 2007). To find these two solutions, the minimum or turning point of $C_n^2(\beta)$, which is the lowest C_n^2 value possible based on the given atmospheric conditions, was first determined (Step 9). Its corresponding β, herein referred to as β_{min}, acts as a bound to the two possible β solutions; β_{min} was then used to limit the solver to solve for β for the given C_n^2 in the case where β was lower than β_{min} ($0 < \beta < \beta_{\text{min}}$) to derive β_1. Similarly, β_2 was derived in the case where β was between β_{min} and a large value, β_{max}, which was assumed to be 30 ($\beta_{\text{min}} < \beta < \beta_{\text{max}}$) (Step 11). These solutions were then used to compute H and $L_{\text{v}}E$ (Step 12).

In the two-wavelength method, the same procedure was followed, with C_T^2 and C_Q^2 determined as (Hill et al., 1988)

$$\begin{cases} C_Q^2 & = & \dfrac{A^2_{T_{\text{MWS}}} C^2_{n_{\text{LAS}}} + A^2_{T_{\text{LAS}}} C^2_{n_{\text{MWS}}} + 2 r_{TQ} \sqrt{C^2_{n_{\text{MWS}}} C^2_{n_{\text{LAS}}}}}{(T\Pi)^2} \\ C_T^2 & = & \dfrac{A^2_{Q_{\text{MWS}}} C^2_{n_{\text{LAS}}} + A^2_{Q_{\text{LAS}}} C^2_{n_{\text{MWS}}} + 2 r_{TQ} \sqrt{C^2_{n_{\text{MWS}}} C^2_{n_{\text{LAS}}}}}{(Q\Pi)^2} \\ \Pi & = & \dfrac{A_{T_{\text{MWS}}} A_{Q_{\text{LAS}}} - A_{Q_{\text{MWS}}} A_{T_{\text{LAS}}}}{TQ}, \end{cases} \tag{C.17}$$

where, r_{TQ} was assumed to be 1.

Appendix D

Land surface model evaluation diagrams

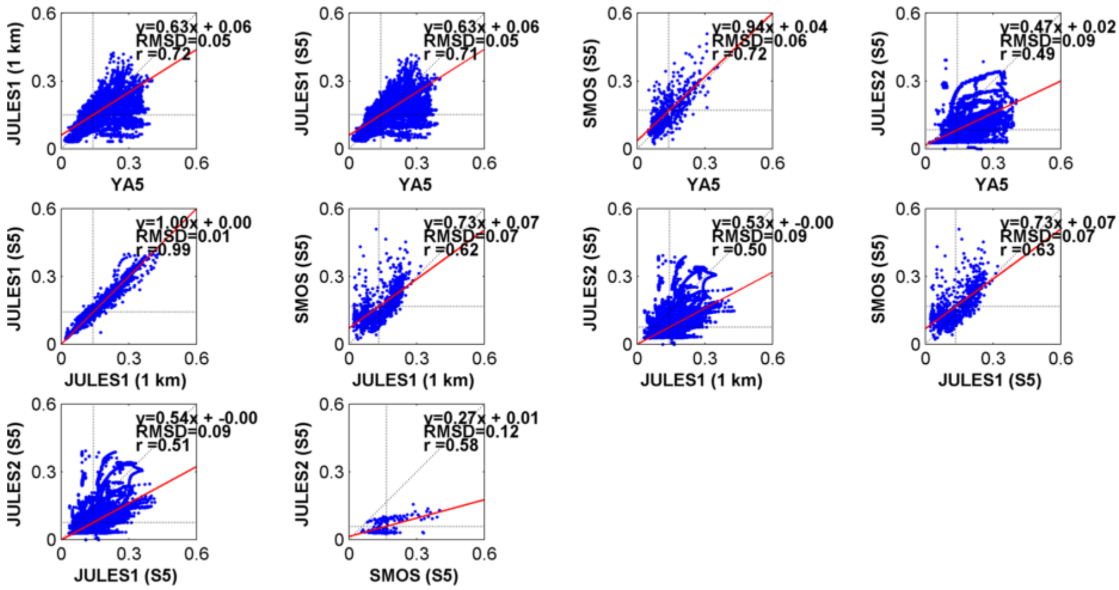

FIGURE D.1: Scatterplot comparisons between soil moisture based on SMOS, YA5 station, JULES1 and JULES2 at S5.

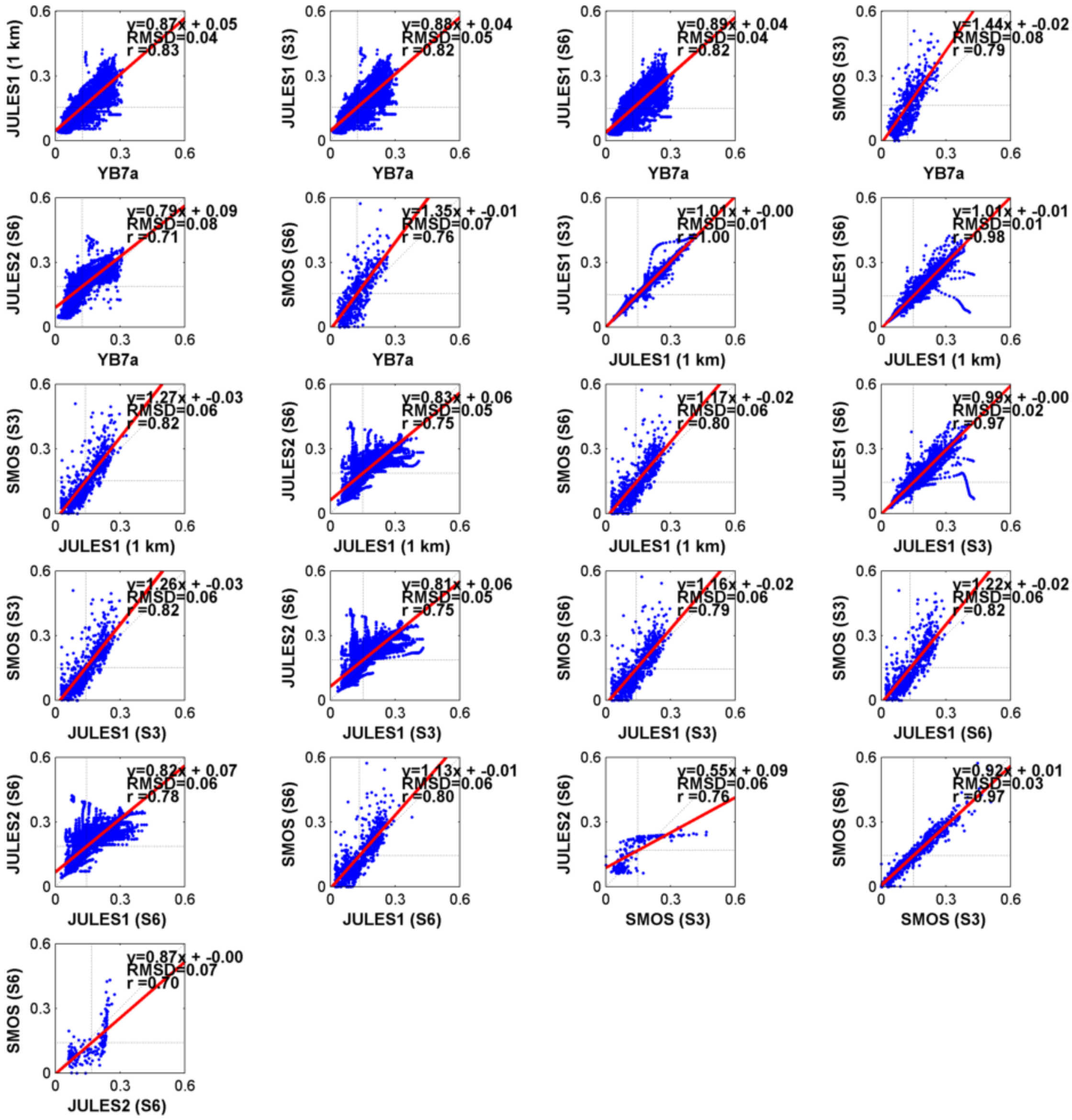

Figure D.2: Scatterplot comparisons between soil moisture based on SMOS, YB7a station, JULES1 and JULES2 at S3 and S6.

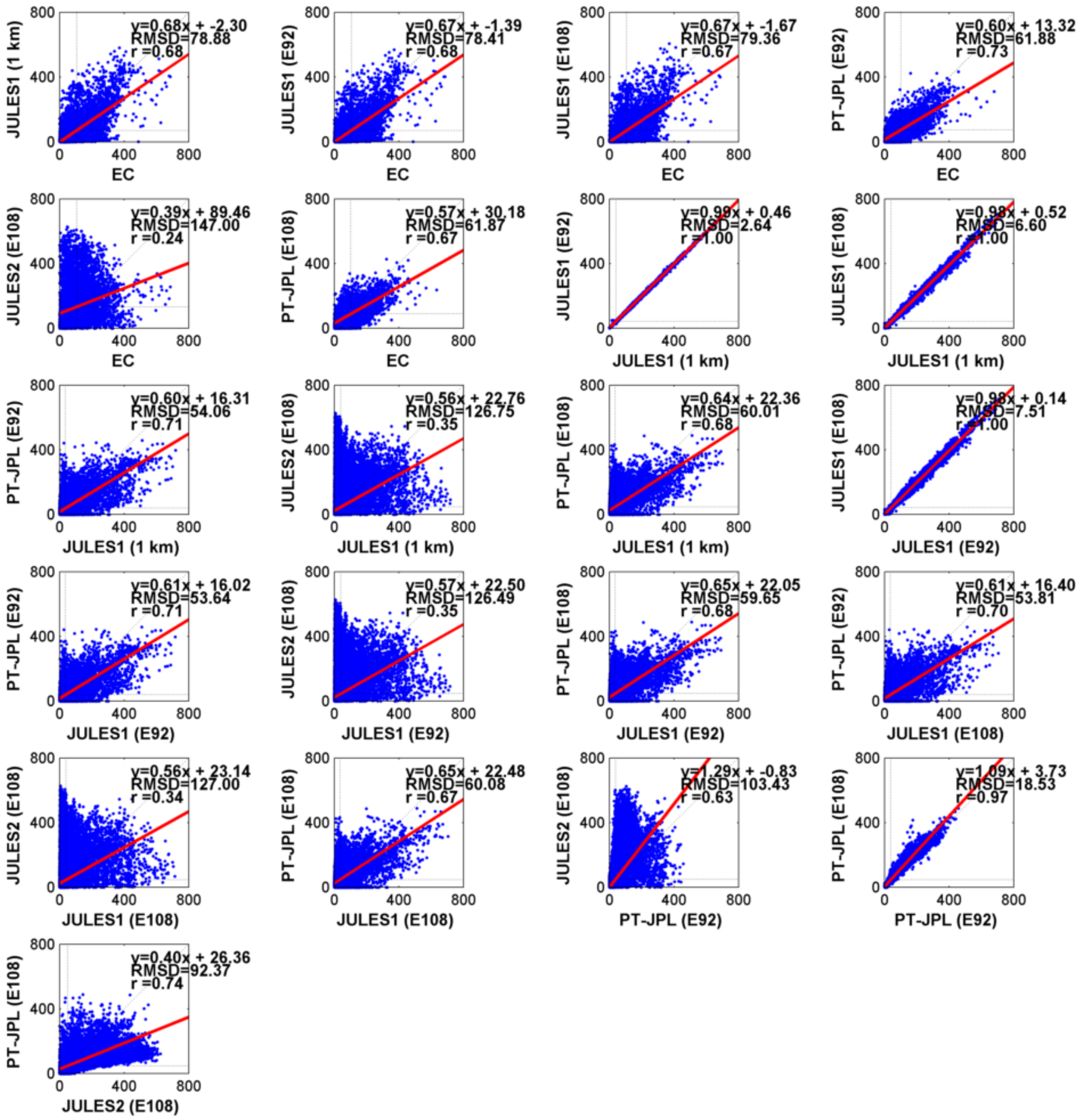

FIGURE D.3: Scatterplot comparisons between$L_{\mathrm{v}}E$ based on PT-JPL, the EC system, JULES1 and JULES2 at E92 and E108.

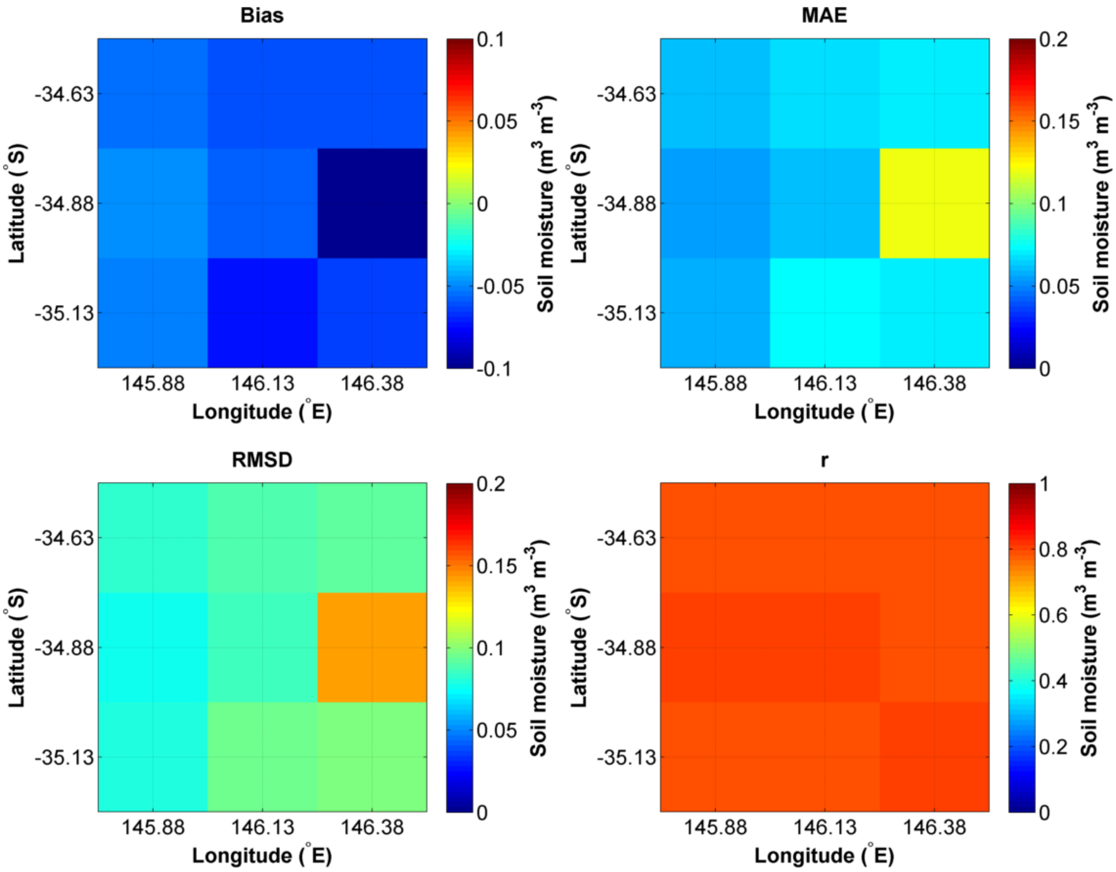

FIGURE D.4: Spatial plot of bias, MAE, RMSD and r derived from evaluating JULES1 soil moisture based on $LP1_X$.

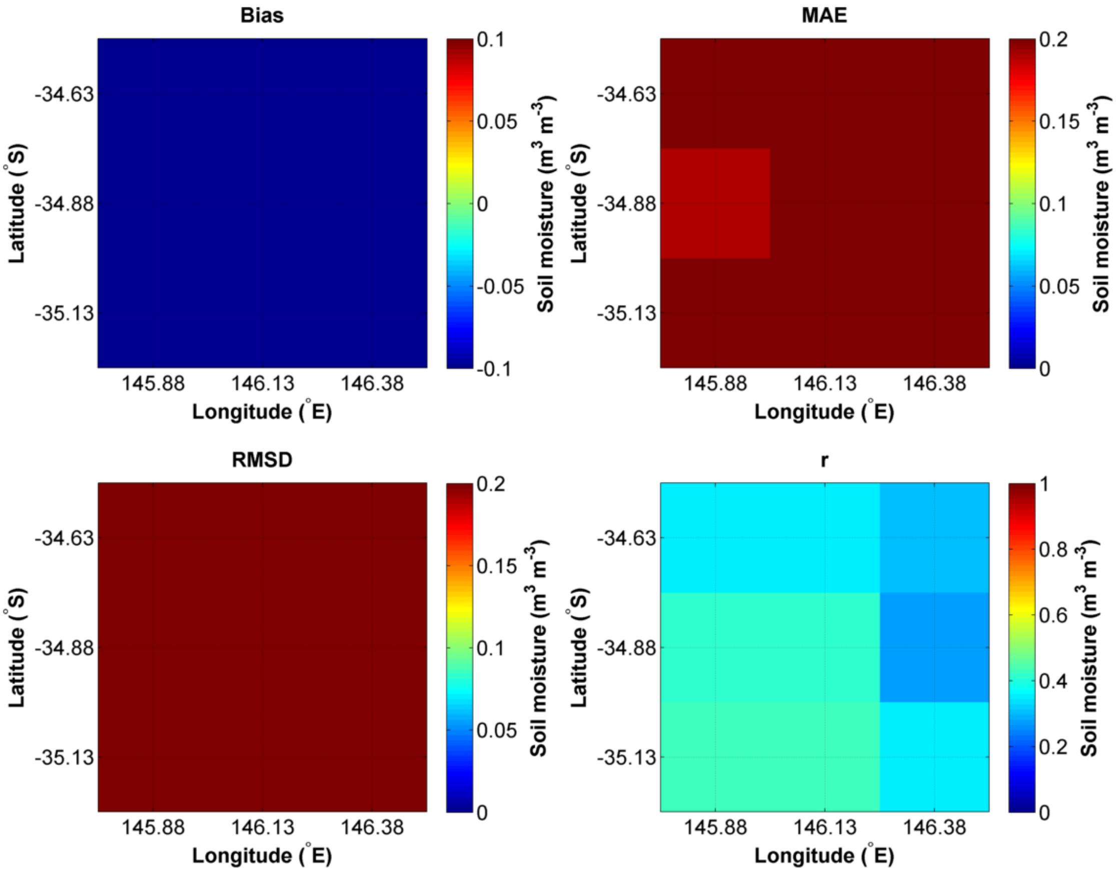

FIGURE D.5: Spatial plot of bias, MAE, RMSD and r derived from evaluating JULES1 soil moisture based on LP1$_{C2}$.

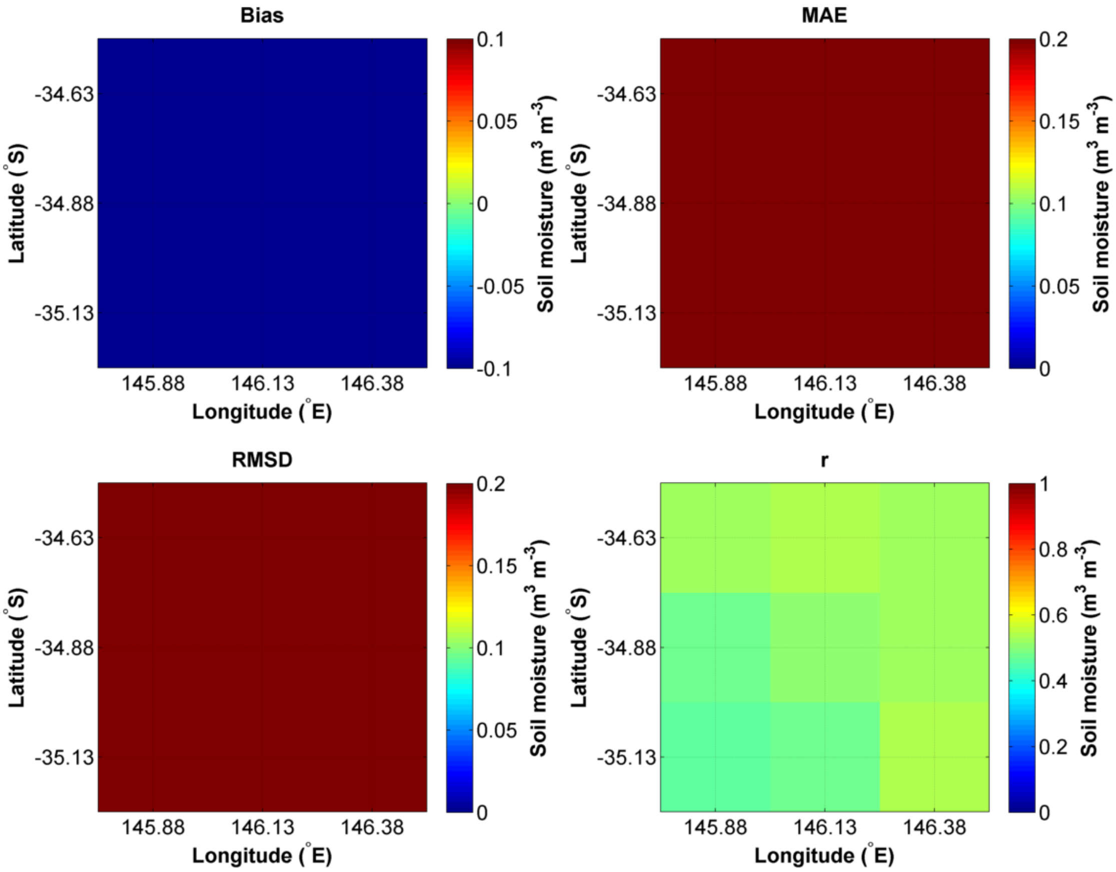

FIGURE D.6: Spatial plot of bias, MAE, RMSD and r derived from evaluating JULES1 soil moisture based on JX1.

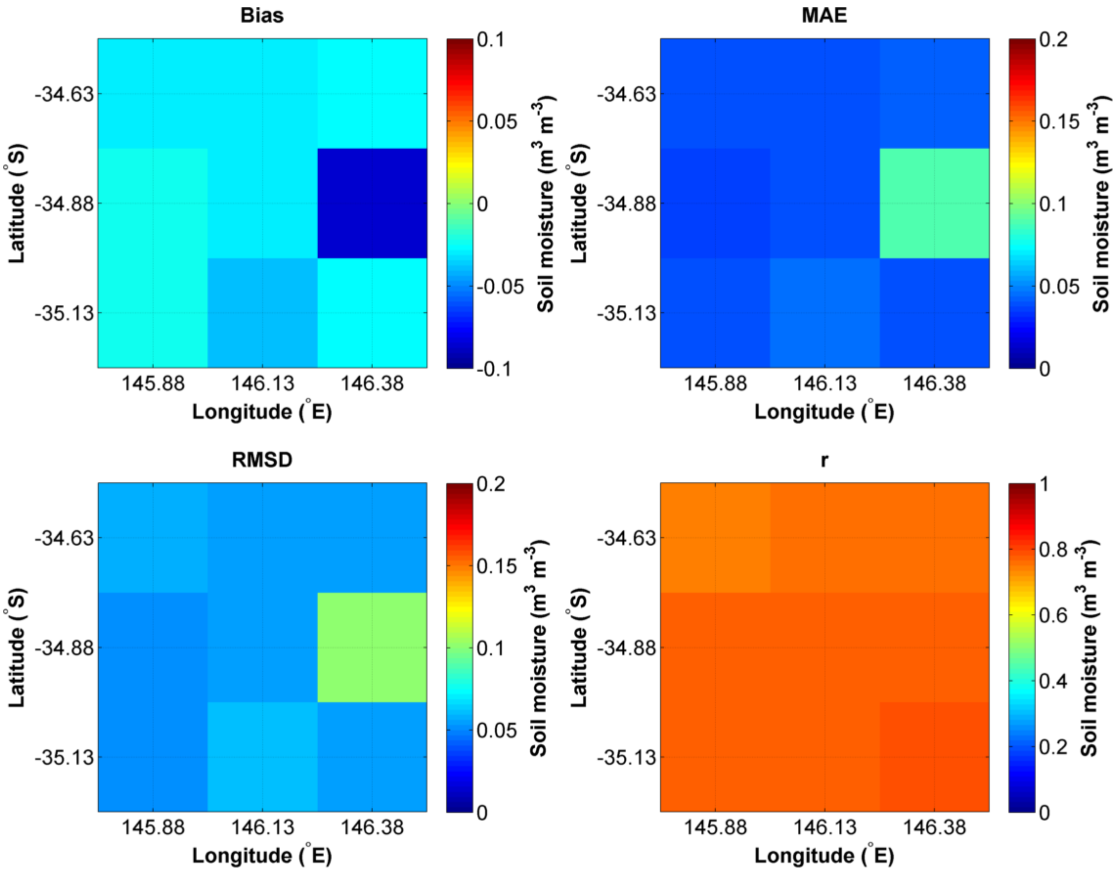

FIGURE D.7: Spatial plot of bias, MAE, RMSD and r derived from evaluating JULES1 soil moisture based on $LP2_X$.

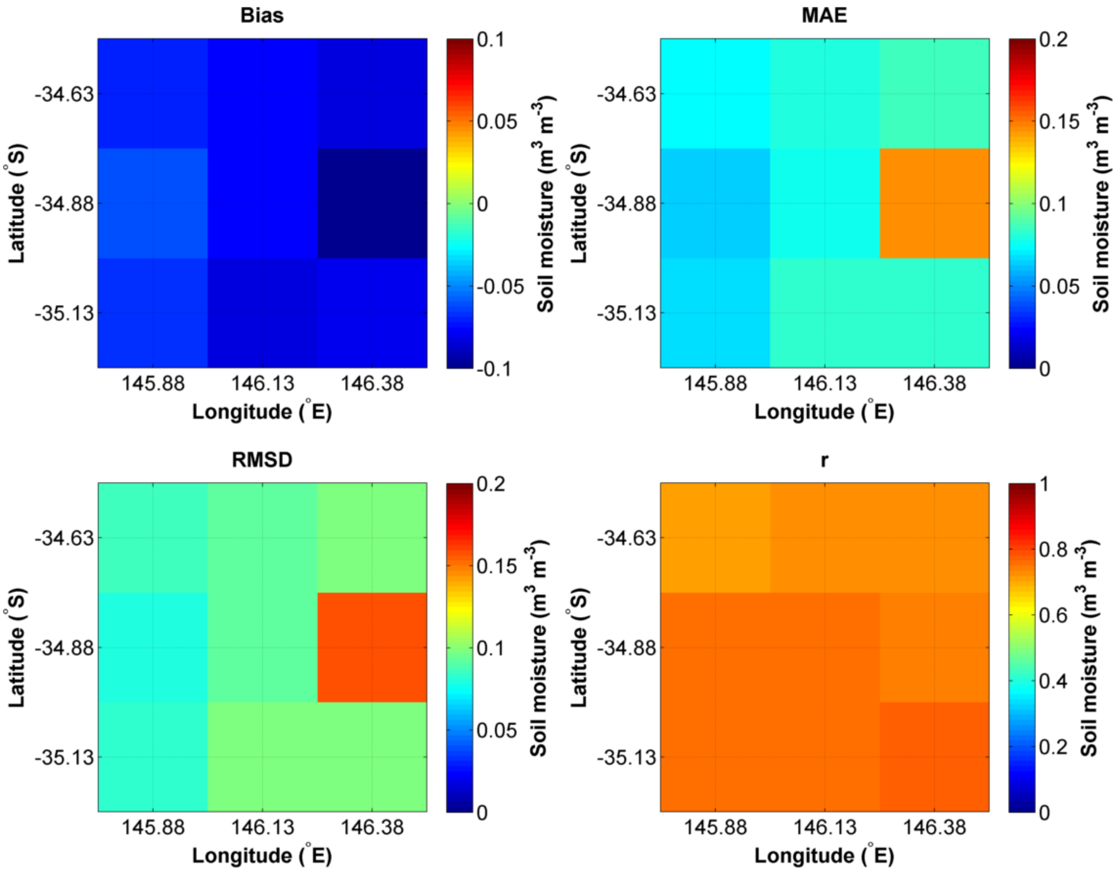

FIGURE D.8: Spatial plot of bias, MAE, RMSD and r derived from evaluating JULES1 soil moisture based on $LP2_{C1}$.

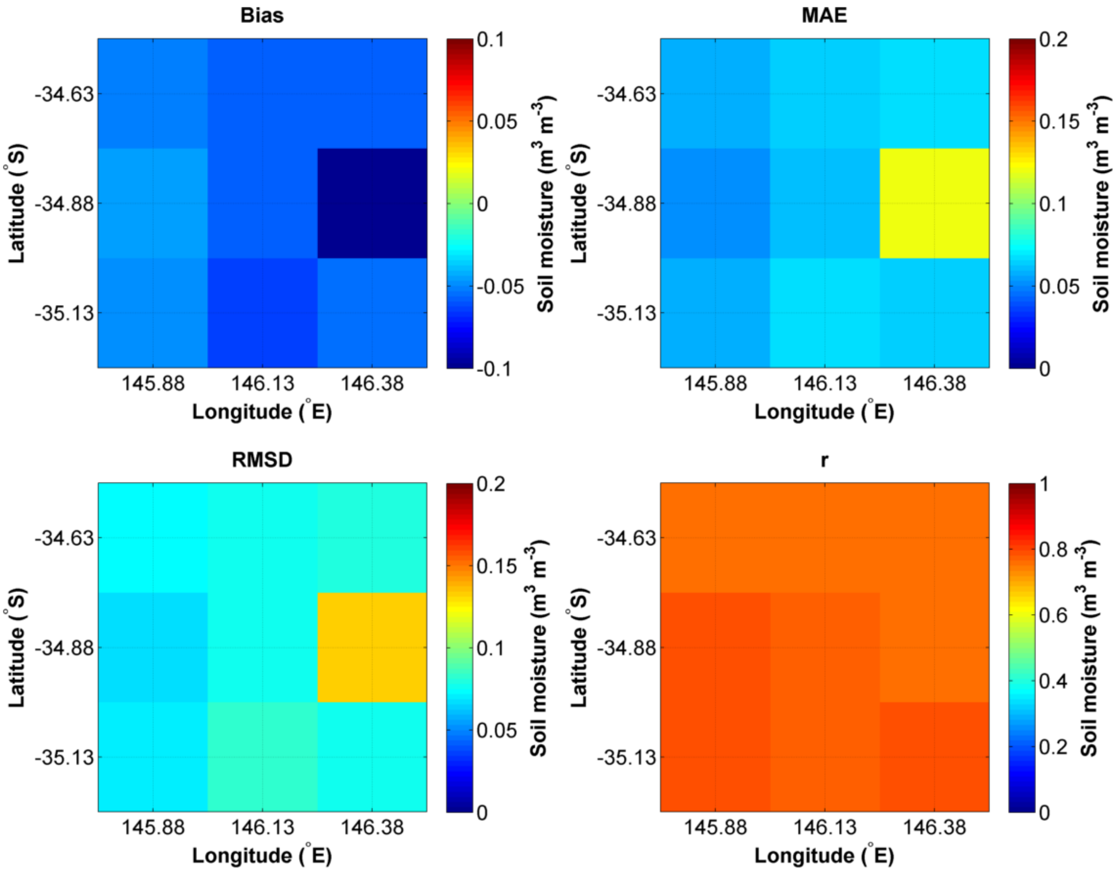

FIGURE D.9: Spatial plot of bias, MAE, RMSD and r derived from evaluating JULES1 soil moisture based on LP2$_{C2}$.

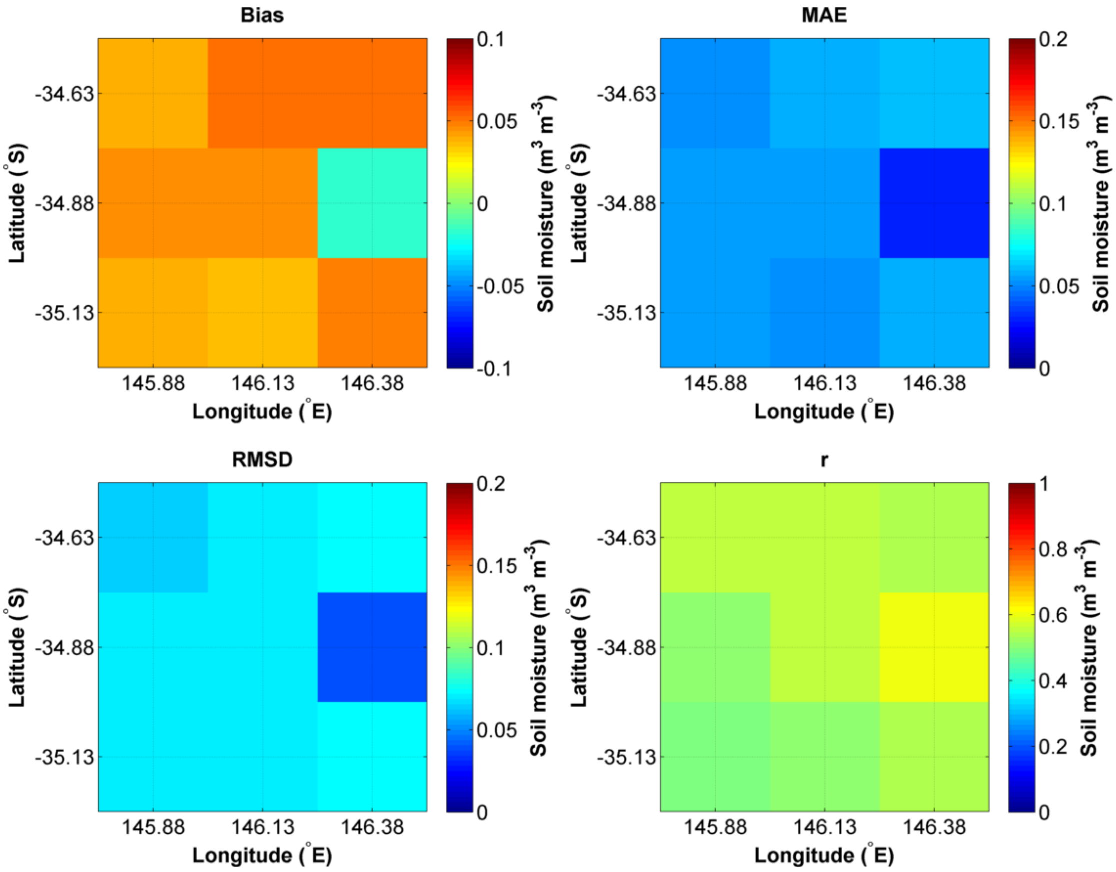

FIGURE D.10: Spatial plot of bias, MAE, RMSD and r derived from evaluating JULES1 soil moisture based on JX2.

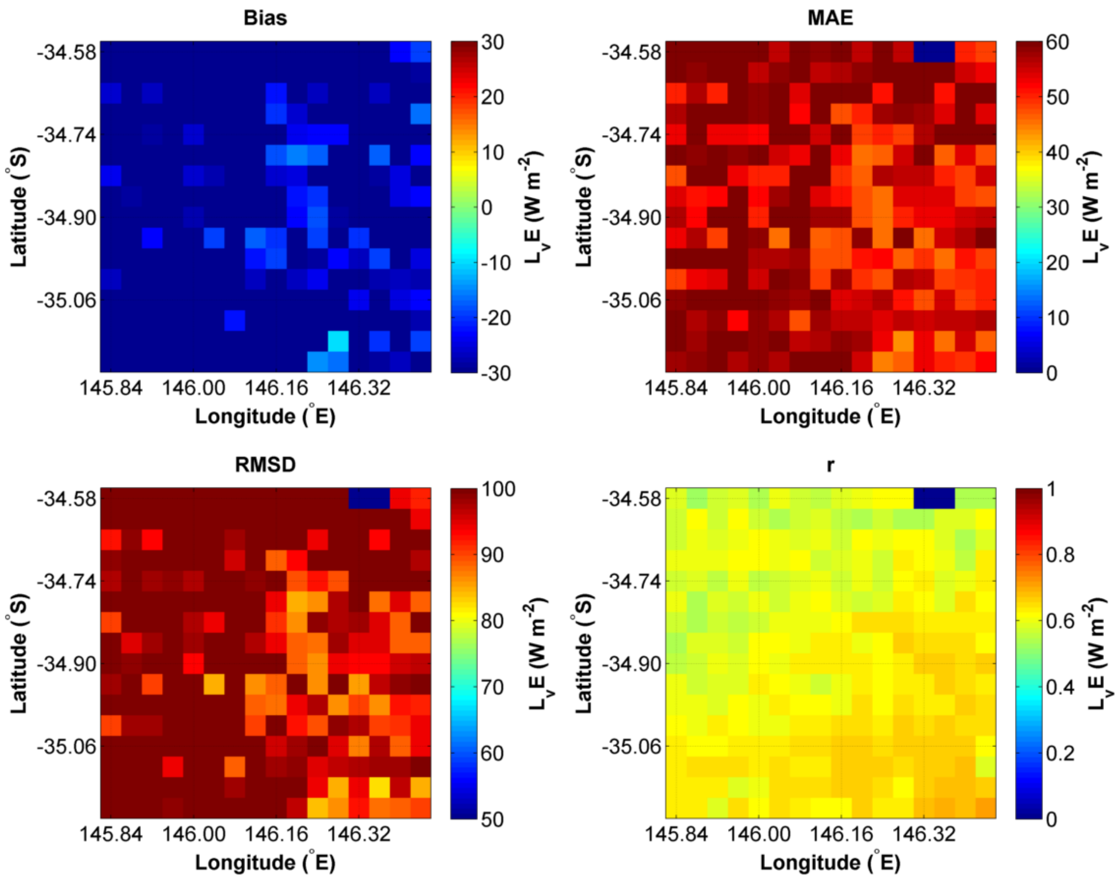

FIGURE D.11: Spatial plot of bias, MAE, RMSD and r derived from evaluating JULES1 $L_{\mathrm{v}}E$ based on SEBS.

Bibliography

Abramowitz, G. (2005). Towards a benchmark for land surface models. *Geophysical Research Letters*, 32(22):L22702.

Adams, J. R., McNairn, H., Berg, A. A., and Champagne, C. (2015). Evaluation of near-surface soil moisture data from an AAFC monitoring network in Manitoba, Canada: Implications for L-band satellite validation. *Journal of Hydrology*, 521:582 – 592.

Al Bitar, A., Leroux, D., Kerr, Y. H., Merlin, O., Richaume, P., Sahoo, A., and Wood, E. F. (2012). Evaluation of SMOS soil moisture products over continental US using the SCAN/SNOTEL network. *Geoscience and Remote Sensing, IEEE Transactions on*, 50(5):1572–1586.

Al-Yaari, A., Wigneron, J.-P., Ducharne, A., Kerr, Y., Wagner, W., De Lannoy, G., Reichle, R., Al Bitar, A., Dorigo, W., Richaume, P., and Mialon, A. (2014). Global-scale comparison of passive (SMOS) and active (ASCAT) satellite based microwave soil moisture retrievals with soil moisture simulations (MERRA-Land). *Remote Sensing of Environment*, 152:614–626.

Albergel, C., de Rosnay, P., Gruhier, C., Muñoz-Sabater, J., Hasenauer, S., Isaksen, L., Kerr, Y., and Wagner, W. (2012). Evaluation of remotely sensed and modelled soil moisture products using global ground-based in situ observations. *Remote Sensing of Environment*, 118:215–226.

Alfieri, J. G., Blanken, P. D., Smith, D., and Morgan, J. (2009). Concerning the Measurement and Magnitude of Heat, Water Vapor, and Carbon Dioxide Exchange from a Semiarid Grassland. *J. Appl. Meteor. Climatol.*, 48(5):982–996.

Allen, R. G., Pereira, L. S., Howell, T. A., and Jensen, M. E. (2011). Evapotranspiration information reporting: I. factors governing measurement accuracy. *Agricultural Water Management*, 98(6):899–920.

Anderson, M. C., Kustas, W. P., and Norman, J. M. (2007). Upscaling flux observations from local to continental scales using thermal remote sensing. *Agronomy Journal*, 99(1):240–254.

Anderson, M. C., Kustas, W. P., Norman, J. M., Hain, C. R., Mecikalski, J. R., Schultz, L., González-Dugo, M. P., Cammalleri, C., D'Urso, G., Pimstein, A., and Gao, F. (2011). Mapping daily evapotranspiration at field to continental scales using geostationary and polar orbiting satellite imagery. *Hydrology and Earth System Sciences*, 15(1):223–239.

Andreas, E. L. (1989). Two-wavelength method of measuring path-averaged turbulent surface heat fluxes. *Journal of Atmospheric and Oceanic Technology*, 6(2):280–292.

Andrews, L. C., Phillips, R. L., and Hopen, C. Y. (2001). *Laser beam scintillation with applications*, volume 99. SPIE press.

Aubinet, M., Grelle, A., Ibrom, A., Rannik, U., Moncrieff, J. B., Foken, T., Kowalski, A. S., Martin, P. H., Berbigier, P., Bernhofer, C., Clement, R., Elbers, J., Granier, A., Grunwald, T., Morgenstern, K., Pilegaard, K., Rebmann, C., Snijders, W., Valentini, R., and Vesala, T. (2000). Estimates of the annual net carbon and water exchange of European forests: the EUROFLUX methodology. *Advances in Ecological Research*, 30:113–173.

Azcurra, C. and Walker, J. P. (2009). Towards SMOS validation in south-eastern Australia. In *18th World IMACS Congress and MODSIM09 International Congress on Modelling and Simulation. Modelling and Simulation Society of Australia and New Zealand and International Association for Mathematics and Computers in Simulation*, pages 3675–3681.

Baghdadi, N., Cerdan, O., Zribi, M., Auzet, V., Darboux, F., El Hajj, M., and Kheir, R. B. (2007). Operational performance of current synthetic aperture radar sensors in mapping soil surface characteristics in agricultural environments: application to hydrological and erosion modelling. *Hydrological Processes*, 22(1):9–20.

Bai, J., Jia, L., Liu, S., Xu, Z., Hu, G., Zhu, M., and Song, L. (2015). Characterizing the Footprint of Eddy Covariance System and Large Aperture Scintillometer Measurements to Validate Satellite-Based Surface Fluxes. *Geoscience and Remote Sensing Letters, IEEE*, 12(5):943–947.

Baldocchi, D., Falge, E., Gu, L., Olson, R., Hollinger, D., Running, S., Anthoni, P., Bernhofer, C., Davis, K., Evans, R., Fuentes, J., Goldstein, A., Katul, G., Law, B., Lee, X., Malhi, Y., Meyers, T., Munger, W., Oechel, W., Paw, K. T., Pilegaard, K., Schmid, H. P., Valentini, R., Verma, S., Vesala, T., Wilson, K., and Wofsy, S. (2001). Fluxnet: A new tool to study the temporal and spatial variability of ecosystem-scale carbon dioxide, water vapor, and energy flux densities. *Bull. Amer. Meteor. Soc.*, 82(11):2415–2434.

Bandara, H. R. S. (2013). *Development of a soil hydraulic parameter estimator*. PhD thesis, Monash University.

Bandara, H. R. S., Walker, J. P., Rüdiger, C., Pipunic, R., Dharssi, I., and Gurney, R. (2011). Towards soil hydraulic parameter retrieval from Land Surface Models using near-surface soil moisture data. In *International Congress on Modelling and Simulation. Modelling and Simulation Society of Australia and New Zealand, Perth, Australia.*

Bandara, R., Walker, J. P., Rüdiger, C., and Merlin, O. (2015). Towards soil property retrieval from space: An application with disaggregated satellite observations. *Journal of Hydrology*, 522:582 – 593.

Barcza, Z., Kern, A., Haszpra, L., and Kljun, N. (2009). Spatial representativeness of tall tower eddy covariance measurements using remote sensing and footprint analysis. *Agricultural and Forest Meteorology*, 149(5):795–807.

Barrett, B. W. and Petropoulos, G. P. (2013). Satellite remote sensing of surface soil moisture. *Remote Sensing of Energy Fluxes and Soil Moisture Content*, page 85.

Berg, A. A., Famiglietti, J. S., Walker, J. P., and Houser, P. R. (2003). Impact of bias correction to reanalysis products on simulations of North American soil moisture and hydrological fluxes. *J. Geophys. Res.*, 108(D16):4490.

Beringer, J., Hutley, L. B., Tapper, N. J., and Cernusak, L. A. (2007). Savanna fires and their impact on net ecosystem productivity in North Australia. *Global Change Biology*, 13(5):990–1004.

Best, M. J., Abramowitz, G., Johnson, H. R., Pitman, A. J., Balsamo, G., Boone, A., Cuntz, M., Decharme, B., Dirmeyer, P. A., Dong, J., Ek, M., Guo, Z., Haverd, V., van den Hurk, B. J. J., Nearing, G. S., Pak, B., Peters-Lidard, C., Santanello, J. A., Stevens, L., and Vuichard, N. (2015). The Plumbing of Land Surface Models: Benchmarking Model Performance. *Journal of Hydrometeorology*, 16(3):1425–1442.

Best, M. J., Pryor, M., Clark, D. B., Rooney, G. G., Essery, R. L. H., Ménard, C. B., Edwards, J. M., Hendry, M. A., Porson, A., Gedney, N., Mercado, L. M., Sitch, S., Blyth, E., Boucher, O., Cox, P. M., Grimmond, C. S. B., and Harding, R. J. (2011). The Joint UK Land Environment Simulator (JULES), Model description - Part 1: Energy and water fluxes. *Geoscientific Model Development*, 4(3):677–699.

Betts, A. K., Ball, J. H., Beljaars, A. C. M., Miller, M. J., and Viterbo, P. A. (1996). The land surface-atmosphere interaction: A review based on observational and global modeling perspectives. *Journal of Geophysical Research*, 101(D3):7209.

Beven, K. (1993). Prophecy, reality and uncertainty in distributed hydrological modelling. *Advances in Water Resources*, 16(1):41–51.

Beven, K. and Freer, J. (2001). Equifinality, data assimilation, and uncertainty estimation in mechanistic modelling of complex environmental systems using the GLUE methodology. *Journal of Hydrology*, 249(1-4):11–29.

Beyrich, F., De Bruin, H. A. R., Meijninger, W. M. L., Schipper, J. W., and Lohse, H. (2002). Results from one-year continuous operation of a large aperture scintillometer over a heterogeneous land surface. *Boundary-Layer Meteorology*, 105(1):85–97.

Beyrich, F., Kouznetsov, R. D., Leps, J.-P., Lüdi, A., Meijninger, W. M. L., and Weisensee, U. (2005). Structure parameters for temperature and humidity from simultaneous eddy-covariance and scintillometer measurements. *Meteorologische Zeitschrift*, 14(5):641–649.

Bindlish, R., Jackson, T. J., Gasiewski, A. J., Klein, M., and Njoku, E. G. (2006). Soil moisture mapping and AMSR-E validation using the PSR in SMEX02. *Remote Sensing of Environment*, 103(2):127–139.

Biswas, A. K. (2004). Integrated Water Resources Management: A Reassessment. *Water International*, 29(2):248–256.

Bittelli, M. (2011). Measuring soil water content: A review. *HortTechnology*, 21(3):293–300.

Blöschl, G. (2001). Scaling in hydrology. *Hydrological Processes*, 15(4):709–711.

Blyth, E., Clark, D. B., Ellis, R., and George, C. (2012). Using earth observation data to evaluate a land surface model in three Siberian catchments. *Boreal Environment Research*, 17(6):484–494.

Blyth, E., Clark, D. B., Ellis, R., Huntingford, C., Los, S., Pryor, M., Best, M., and Sitch, S. (2011). A comprehensive set of benchmark tests for a land surface model of simultaneous fluxes of water and carbon at both the global and seasonal scale. *Geoscientific Model Development*, 4(2):255–269.

Blyth, E., Gash, J., Lloyd, A., Pryor, M., Weedon, G. P., and Shuttleworth, J. (2010). Evaluating the JULES Land Surface Model Energy Fluxes Using FLUXNET Data. *Journal of Hydrometeorology*, 11(2):509–519.

Brocca, L., Hasenauer, S., Lacava, T., Melone, F., Moramarco, T., Wagner, W., Dorigo, W., Matgen, P., Martínez-Fernández, J., Llorens, P., Latron, J., Martin, C., and Bittelli, M. (2011). Soil moisture estimation through ASCAT and AMSR-E sensors: An intercomparison and validation study across Europe. *Remote Sensing of Environment*, 115(12):3390–3408.

Brocca, L., Moramarco, T., Melone, F., Wagner, W., Hasenauer, S., and Hahn, S. (2012a). Assimilation of surface-and root-zone ASCAT soil moisture products into rainfall - runoff modeling. *IEEE Transactions on Geoscience and Remote Sensing*, 50(7):2542–2555.

Brocca, L., Tullo, T., Melone, F., Moramarco, T., and Morbidelli, R. (2012b). Catchment scale soil moisture spatial-temporal variability. *Journal of Hydrology*, 422-423(0):63–75.

Brooks, R. and Corey, A. (1964). Hydraulic properties of porous media. *Hydrology Papers. Colorado State University*, (3).

Brunsell, N. A. and Gillies, R. R. (2003a). Length Scale Analysis of Surface Energy Fluxes Derived from Remote Sensing. *Journal of Hydrometeorology*, 4(6):1212–1219.

Brunsell, N. A. and Gillies, R. R. (2003b). Scale issues in land - atmosphere interactions: implications for remote sensing of the surface energy balance. *Agricultural and Forest Meteorology*, 117(3-4):203–221.

Brunsell, N. A., Ham, J. M., and Arnold, K. A. (2011). Validating remotely sensed land surface fluxes in heterogeneous terrain with large aperture scintillometry. *International Journal of Remote Sensing*, 32(21):6295–6314.

Brutsaert, W. (2005). *Hydrology: An Introduction*, volume 61. Wiley Online Library.

Bureau of Meteorology (2010). Operational implementation of the ACCESS Numerical Weather Prediction systems. *Operations Bulletin*, (83):1–35.

Calvet, J.-C., Noilhan, J., Roujean, J.-L., Bessemoulin, P., Cabelguenne, M., Olioso, A., and Wigneron, J.-P. (1998). An interactive vegetation SVAT model tested against data from six contrasting sites. *Agricultural and Forest Meteorology*, 92(2):73–95.

Cammalleri, C., Anderson, M. C., and Kustas, W. P. (2014). Upscaling of evapotranspiration fluxes from instantaneous to daytime scales for thermal remote sensing applications. *Hydrology and Earth System Sciences*, 18(5):1885–1894.

Campbell, J. et al. (2002). *Introduction to remote sensing.* Number 3. Taylor & Francis.

Champagne, C., Rowlandson, T., Berg, A., Burns, T., L'Heureux, J., Tetlock, E., Adams, J. R., McNairn, H., Toth, B., and Itenfisu, D. (2015). Satellite surface soil moisture from SMOS and Aquarius: Assessment for applications in agricultural landscapes. *International Journal of Applied Earth Observation and Geoinformation.*

Chehbouni, A., Watts, C., Lagouarde, J.-P., Kerr, Y. H., Rodriguez, J.-C., Bonnefond, J.-M., Santiago, F., Dedieu, G., Goodrich, D. C., and Unkrich, C. (2000). Estimation of heat and momentum fluxes over complex terrain using a large aperture scintillometer. *Agricultural and forest meteorology*, 105(1):215–226.

Chen, B., Black, T. A., Coops, N. C., Hilker, T., (Tony) Trofymow, J. A., and Morgenstern, K. (2009). Assessing Tower Flux Footprint Climatology and Scaling Between Remotely Sensed and Eddy Covariance Measurements. *Boundary-Layer Meteorology*, 130(2):137–167.

Chen, B., Coops, N. C., Fu, D., Margolis, H. A., Amiro, B. D., Black, T. A., Arain, M. A., Barr, A. G., Bourque, C. P.-A., Flanagan, L. B., Lafleur, P. M., McCaughey, J. H., and Wofsy, S. C. (2012). Characterizing spatial representativeness of flux tower eddy-covariance measurements across the Canadian Carbon Program Network using remote sensing and footprint analysis. *Remote Sensing of Environment*, 124:742–755.

Chen, M., Willgoose, G. R., and Saco, P. M. (2014). Spatial prediction of temporal soil moisture dynamics using HYDRUS-1D. *Hydrol. Process.*, 28(2):171–185.

Chen, T. H., Henderson-Sellers, A., Milly, P. C. D., Pitman, A. J., Beljaars, A. C. M., Polcher, J., Abramopoulos, F., Boone, A., Chang, S., Chen, F., Dai, Y., Desborough, C. E., Dickinson, R. E., Dümenil, L., Ek, M., Garratt, J. R., Gedney, N., Gusev, Y. M., Kim, J., Koster, R., Kowalczyk, E. A., Laval, K., Lean, J., Lettenmaier, D., Liang, X., Mahfouf, J.-F., Mengelkamp, H.-T., Mitchell, K., Nasonova, O. N., Noilhan, J., Robock, A., Rosenzweig, C., Schaake, J., Schlosser, C. A., Schulz, J.-P., Shao, Y., Shmakin, A. B., Verseghy, D. L., Wetzel, P., Wood, E. F., Xue, Y., Yang, Z.-L., and Zeng, Q. (1997). Cabauw Experimental Results from the Project for Intercomparison of Land-Surface Parameterization Schemes. *Journal of Climate*, 10(6):1194–1215.

Cho, E., Moon, H., and Choi, M. (2015). First Assessment of the Advanced Microwave Scanning Radiometer 2 (AMSR2) Soil Moisture Contents in Northeast Asia. *Journal of the Meteorological Society of Japan. Ser. I*, 93(1):117–129.

Choi, M. (2012). Evaluation of multiple surface soil moisture for Korean regional flux monitoring network sites: Advanced Microwave Scanning Radiometer E, land surface model, and ground measurements. *Hydrological Processes*, 26(4):597–603.

Choi, M. and Jacobs, J. M. (2008). Temporal Variability Corrections for Advanced Microwave Scanning Radiometer E (AMSR-E) Surface Soil Moisture: Case Study in Little River Region, Georgia, U.S. *Sensors*, 8(4):2617–2627.

Choi, M., Jacobs, J. M., and Bosch, D. D. (2008). Remote sensing observatory validation of surface soil moisture using Advanced Microwave Scanning Radiometer E, Common Land Model, and ground based data: Case study in SMEX03 Little River Region, Georgia, U.S. *Water Resources Research*, 44(8):W08421.

Clapp, R. B. and Hornberger, G. M. (1978). Empirical equations for some soil hydraulic properties. *Water Resources Research*, 14(4):601–604.

Clark, D., Harris, P., Pryor, M., and Hendry, M. (2011a). *Joint UK Land Environment Simulator (JULES) Version 3.0 User Manual.*

Clark, D. B., Mercado, L. M., Sitch, S., Jones, C. D., Gedney, N., Best, M. J., Pryor, M., Rooney, G. G., Essery, R. L. H., and Blyth, E. (2011b). The Joint UK Land Environment Simulator (JULES), Model description - Part 2: Carbon fluxes and vegetation. *Geoscientific Model Development Discussions*, 4:641–688.

Clark, M. P., Rupp, D. E., Woods, R. A., Zheng, X., Ibbitt, R. P., Slater, A. G., Schmidt, J., and Uddstrom, M. J. (2008). Hydrological data assimilation with the ensemble Kalman filter: Use of streamflow observations to update states in a distributed hydrological model. *Advances in Water Resources*, 31(10):1309–1324.

Collow, T. W., Robock, A., Basara, J. B., and Illston, B. G. (2012). Evaluation of SMOS retrievals of soil moisture over the central United States with currently available in situ observations. *Journal of Geophysical Research: Atmospheres*, 117(D9):D9. D09113.

Corrsin, S. (1951). On the spectrum of isotropic temperature fluctuations in an isotropic turbulence. *Journal of Applied Physics*, 22(4):469–473.

Cosh, M. H. (2004). Watershed scale temporal and spatial stability of soil moisture and its role in validating satellite estimates. *Remote Sensing of Environment*, 92(4):427–435.

Cosh, M. H., Jackson, T. J., Starks, P., and Heathman, G. (2006). Temporal stability of surface soil moisture in the Little Washita River watershed and its applications in satellite soil moisture product validation. *Journal of Hydrology*, 323(1-4):168–177.

Cox, P. M., Huntingford, C., and Harding, R. J. (1998). A canopy conductance and photosynthesis model for use in a GCM land surface scheme. *Journal of Hydrology*, 212-213(0):79–94.

Crossley, J. F., Polcher, J., Cox, P. M., Gedney, N., and Planton, S. (2000). Uncertainties linked to land-surface processes in climate change simulations. *Climate Dynamics*, 16(12):949–961.

Crow, W. T., Berg, A. A., Cosh, M. H., Loew, A., Mohanty, B. P., Panciera, R., de Rosnay, P., Ryu, D., and Walker, J. P. (2012). Upscaling sparse ground-based soil moisture observations for the validation of coarse-resolution satellite soil moisture products. *Reviews of Geophysics*, 50(2):RG2002.

Crow, W. T., Ryu, D., and Famiglietti, J. S. (2005). Upscaling of field-scale soil moisture measurements using distributed land surface modeling. *Advances in Water Resources*, 28(1):1–14.

Dai, Y., Zeng, X., Dickinson, R. E., Baker, I., Bonan, G. B., Bosilovich, M. G., Denning, A. S., Dirmeyer, P. A., Houser, P. R., Niu, G., Oleson, K. W., Schlosser, C. A., and Yang, Z.-L. (2003). The Common Land Model. *Bulletin of the American Meteorological Society*, 84(8):1013–1023.

Dall'Amico, J. T., Schlenz, F., Loew, A., and Mauser, W. (2012). First results of smos soil moisture validation in the upper danube catchment. *Geoscience and Remote Sensing, IEEE Transactions on*, 50(5):1507–1516.

De Bruin, H. A. R., den Hurk, B., and Kohsiek, W. (1995). The scintillation method tested over a dry vineyard area. *Boundary-Layer Meteorology*, 76(1-2):25–40.

De Lannoy, G. J. M., Verhoest, N. E. C., Houser, P. R., Gish, T. J., and Van Meirvenne, M. (2006). Spatial and temporal characteristics of soil moisture in an intensively monitored agricultural field (OPE 3). *Journal of Hydrology*, 331(3-4):719–730.

de Nijs, A., Parinussa, R., de Jeu, R., Schellekens, J., and Holmes, T. (2015). A methodology to determine radio-frequency interference in amsr2 observations. *Geoscience and Remote Sensing, IEEE Transactions on*, 53(9):5148–5159.

de Wit, A. and van Diepen, C. (2007). Crop model data assimilation with the Ensemble Kalman filter for improving regional crop yield forecasts. *Agricultural and Forest Meteorology*, 146(1-2):38–56.

Delworth, T. L. and Manabe, S. (1988). The Influence of Potential Evaporation on the Variabilities of Simulated Soil Wetness and Climate. *J. Climate*, 1(5):523–547.

Dente, L., Su, Z., and Wen, J. (2012a). Validation of SMOS Soil Moisture Products over the Maqu and Twente Regions. *Sensors*, 12(12):9965–9986.

Dente, L., Vekerdy, Z., Wen, J., and Su, Z. (2012b). Maqu network for validation of satellite-derived soil moisture products. *International Journal of Applied Earth Observation and Geoinformation*, 17:55–65.

Dirmeyer, P. A. (2011). A History and Review of the Global Soil Wetness Project (GSWP). *Journal of Hydrometeorology*, 12(5):729–749.

Dirmeyer, P. A., Dolman, A. J., and Sato, N. (1999). The Pilot Phase of the Global Soil Wetness Project. *Bulletin of the American Meteorological Society*, 80(5):851–878.

Disseldorp, D., Yee, M., Monerris, A., and Walker, J. (2013). A temporal stability analysis of the Australian SMAP mission validation site. In Boland, J. and Piantadosi, J., editors, *20th International Congress on Modelling and Simulation*, pages 2869–2875. Modelling and Simulation Society of Australia and New Zealand, Adelaide.

Djamai, N., Magagi, R., Goïta, K., Hosseini, M., Cosh, M. H., Berg, A., and Toth, B. (2015). Evaluation of SMOS soil moisture products over the CanEx-SM10 area. *Journal of Hydrology*, 520:254 – 267.

Dorigo, W., de Jeu, R., Chung, D., Parinussa, R., Liu, Y., Wagner, W., and Fernández-Prieto, D. (2012). Evaluating global trends (1988-2010) in harmonized multi-satellite surface soil moisture. *Geophysical Research Letters*, 39(18):L18405. L18405.

Dorigo, W. A., Wagner, W., Hohensinn, R., Hahn, S., Paulik, C., Xaver, A., Gruber, A., Drusch, M., Mecklenburg, S., van Oevelen, P., Robock, A., and Jackson, T. (2011). The International Soil Moisture Network: a data hosting facility for global in situ soil moisture measurements. *Hydrology and Earth System Sciences*, 15(5):1675–1698.

Doubkova, M., Bartsch, A., Pathe, C., Sabel, D., and Wagner, W. (2009). The medium resolution soil moisture dataset: Overview of the SHARE ESA DUE TIGER project. In *2009 IEEE International Geoscience and Remote Sensing Symposium*, volume 1, pages I–116–I–119. IEEE.

Draper, C. S., Walker, J. P., Steinle, P. J., de Jeu, R. A. M., and Holmes, T. R. H. (2009). An evaluation of AMSR-E derived soil moisture over Australia. *Remote Sensing of Environment*, 113(4):703–710.

Drusch, M., Wood, E. F., and Gao, H. (2005). Observation operators for the direct assimilation of TRMM microwave imager retrieved soil moisture. *Geophysical Research Letters*, 32:15.

Drusch, M., Wood, E. F., Gao, H., and Thiele, A. (2004). Soil moisture retrieval during the Southern Great Plains Hydrology Experiment 1999: A comparison between experimental remote sensing data and operational products. *Water resources research*, 40(2):W02504.

Du, J., Jackson, T. J., Bindlish, R., Cosh, M. H., Li, L., Hornbuckle, B. K., and Kabela, E. D. (2012). Effect of dew on aircraft-based passive microwave observations over an agricultural domain. *Journal of Applied Remote Sensing*, 6(1):063571–1–063571–10.

Dumedah, G. and Walker, J. P. (2014). Intercomparison of the JULES and CABLE land surface models through assimilation of remotely sensed soil moisture in southeast Australia. *Advances in Water Resources*, 74:231–244.

El Maayar, M., Chen, J. M., and Price, D. T. (2008). On the use of field measurements of energy fluxes to evaluate land surface models. *Ecological Modelling*, 214(2-4):293–304.

El Maayar, M., Price, D. T., Black, T. A., Humphreys, E. R., and Jork, E.-M. (2002). Sensitivity tests of the integrated biosphere simulator to soil and vegetation characteristics in a pacific coastal coniferous forest. *Atmosphere-Ocean*, 40(3):313–332.

Ellis, R. J., Taylor, C. M., Weedon, G. P., Gedney, N., Clark, D. B., and Los, S. (2009). Evaluating the Simulated Seasonality of Soil Moisture with Earth Observation Data. *Journal of Hydrometeorology*, 10(6):1548–1560.

Engman, E. T. (1990). Progress in Microwave Remote Sensing of Soil Moisture. *Canadian Journal of Remote Sensing*, 16(3):6–14.

Engman, E. T. (1991). Applications of microwave remote sensing of soil moisture for water resources and agriculture. *Remote Sensing of Environment*, 35(2-3):213–226.

Entekhabi, D., Njoku, E. G., O'Neill, P. E., Kellogg, K. H., Crow, W. T., Edelstein, W. N., Entin, J. K., Goodman, S. D., Jackson, T. J., Johnson, J., Kimball, J., Piepmeier, J. R., Koster, R. D., Martin, N., McDonald, K. C., Moghaddam, M., Moran, S., Reichle, R., Shi, J. C., Spencer, M. W., Thurman, S. W., Tsang, L., and Van Zyl, J. (2010a). The soil moisture active passive (SMAP) mission. *Proceedings of the IEEE*, 98(5):704–716.

Entekhabi, D., Reichle, R. H., Koster, R. D., and Crow, W. T. (2010b). Performance Metrics for Soil Moisture Retrievals and Application Requirements. *Journal of Hydrometeorology*, 11(3):832–840.

Entekhabi, D., Rodriguez-Iturbe, I., and Castelli, F. (1996). Mutual interaction of soil moisture state and atmospheric processes. *Journal of Hydrology*, 184(1-2):3–17.

Entin, J. K., Robock, A., Vinnikov, K. Y., Hollinger, S. E., Liu, S., and Namkhai, A. (2000). Temporal and spatial scales of observed soil moisture variations in the extratropics. *Journal of Geophysical Research: Atmospheres*, 105(D9):11865–11877.

Ershadi, A., McCabe, M., Evans, J., Chaney, N., and Wood, E. (2014). Multi-site evaluation of terrestrial evaporation models using FLUXNET data. *Agricultural and Forest Meteorology*, 187(0):46–61.

Ershadi, A., McCabe, M., Evans, J., and Wood, E. (2015). Impact of model structure and parameterization on penman-monteith type evaporation models. *Journal of Hydrology*, 525:521–535.

Escorihuela, M.-J., Chanzy, A., Wigneron, J.-P., and Kerr, Y. (2010). Effective soil moisture sampling depth of L-band radiometry: A case study. *Remote Sensing of Environment*, 114(5):995–1001.

Evans, J. and De Bruin, H. (2011). The effective height of a two-wavelength scintillometer system. *Boundary-Layer Meteorology*, 141(1):165–177.

Evans, J., McNeil, D., Finch, J., Murray, T., Harding, R., and Verhoef, A. (2010). Evaporation measurements at kilometre scales determined using two-wavelength scintillometry. In *BHS Third International Symposium: Role of Hydrology in Managing Consequences of a Changing Global Environment, Newcastle University, 19-23 July 2010*. British Hydrological Society.

Evans, J. G. (2009). *Long-Path Scintillometry over Complex Terrain to Determine Areal-Averaged Sensible and Latent Heat Fluxes*. PhD thesis, The University of Reading.

Ezzahar, J., Chehbouni, A., Hoedjes, J., and Chehbouni, A. (2007). On the application of scintillometry over heterogeneous grids. *Journal of Hydrology*, 334(3 - 4):493 – 501.

Ezzahar, J., Chehbouni, A., Hoedjes, J., Ramier, D., Boulain, N., Boubkraoui, S., Cappelaere, B., Descroix, L., Mougenot, B., and Timouk, F. (2009). Combining scintillometer measurements and an aggregation scheme to estimate area-averaged latent heat flux during the AMMA experiment. *Journal of Hydrology*, 375(1):217–226.

Famiglietti, J. S., Ryu, D., Berg, A. A., Rodell, M., and Jackson, T. J. (2008). Field observations of soil moisture variability across scales. *Water Resources Research*, 44(1):W01423.

Fang, Y., Sun, G., Caldwell, P., McNulty, S. G., Noormets, A., Domec, J.-C., King, J., Zhang, Z., Zhang, X., Lin, G., Zhou, G., Xiao, J., and Chen, J. (2015). Monthly land cover-specific evapotranspiration models derived from global eddy flux measurements and remote sensing data. *Ecohydrology*.

Fensholt, R., Anyamba, A., Stisen, S., Sandholt, I., Pak, E., and Small, J. (2007). Comparisons of Compositing Period Length for Vegetation Index Data from Polar-orbiting and Geostationary Satellites for the Cloud-prone Region of West Africa. *Photogrammetric Engineering & Remote Sensing*, 73(3):297–309.

Ferguson, C. R., Sheffield, J., Wood, E. F., and Gao, H. (2010). Quantifying uncertainty in a remote sensing-based estimate of evapotranspiration over continental USA. *International Journal of Remote Sensing*, 31(14):3821–3865.

Finnigan, J. J., Clement, R., Malhi, Y., Leuning, R., and Cleugh, H. A. (2003). A re-evaluation of long-term flux measurement techniques part I: averaging and coordinate rotation. *Boundary-Layer Meteorology*, 107(1):1–48.

Fisher, J. B., Tu, K. P., and Baldocchi, D. D. (2008). Global estimates of the land-atmosphere water flux based on monthly AVHRR and ISLSCP-II data, validated at 16 FLUXNET sites. *Remote Sensing of Environment*, 112(3):901–919.

Foken, T. (2008). The energy balance closure problem: An overview. *Ecological Applications*, 18(6):1351–1367.

Foken, T., Aubinet, M., Finnigan, J. J., Leclerc, M. Y., Mauder, M., and Paw U, K. T. (2011). Results of a panel discussion about the energy balance closure correction for trace gases. *Bulletin of the American Meteorological Society*, 92(4):ES13—-ES18.

Fritschen, L. J., Qian, P., Kanemasu, E. T., Nie, D., Smith, E. A., Stewart, J. B., Verma, S. B., and Wesely, M. L. (1992). Comparisons of surface flux measurement systems used in FIFE 1989. *Journal of Geophysical Research: Atmospheres*, 97(D17):18697–18713.

Fujii, H., Koike, T., and Imaoka, K. (2009). Improvement of the AMSR-E Algorithm for Soil Moisture Estimation by Introducing a Fractional Vegetation Coverage Dataset Derived from MODIS Data. *Journal of The Remote Sensing Society of Japan*, 29(1):282–292.

Gao, X., Wu, P., Zhao, X., Wang, J., Shi, Y., Zhang, B., Tian, L., and Li, H. (2013). Estimation of spatial soil moisture averages in a large gully of the Loess Plateau of China through statistical and modeling solutions. *Journal of Hydrology*, 486:466–478.

Gao, Y., Walker, J. P., Ye, N., Monerris, A., Panciera, R., Ryu, D., and Rudiger, C. (2016). Calibration and validation of the tau-omega model with SMAPEx data sets for passive microwave soil moisture retrieval. Unpublished results.

García, M., Sandholt, I., Ceccato, P., Ridler, M., Mougin, E., Kergoat, L., Morillas, L., Timouk, F., Fensholt, R., and Domingo, F. (2013). Actual evapotranspiration in drylands derived from in-situ and satellite data: Assessing biophysical constraints. *Remote Sensing of Environment*, 131:103–118.

Gash, J. H. C. and Shuttleworth, W. J. (2007). *Evaporation*. Benchmark papers in hydrology. IAHS Press.

Glenn, E. P., Huete, A. R., Nagler, P. L., Hirschboeck, K. K., and Brown, P. (2007). Integrating Remote Sensing and Ground Methods to Estimate Evapotranspiration. *Critical Reviews in Plant Sciences*, 26(3):139–168.

Gómez-Plaza, A., Alvarez-Rogel, J., Albaladejo, J., and Castillo, V. M. (2000). Spatial patterns and temporal stability of soil moisture across a range of scales in a semi-arid environment. *Hydrological Processes*, 14(7):1261–1277.

Grayson, R. B. and Western, A. W. (1998). Towards areal estimation of soil water content from point measurements: Time and space stability of mean response. *Journal of Hydrology*, 207(1-2):68–82.

Green, A. E., Astill, M. S., McAneney, K. J., and Nieveen, J. P. (2001). Path-averaged surface fluxes determined from infrared and microwave scintillometers. *Agricultural and Forest Meteorology*, 109(3):233–247.

Griesfeller, A., Lahoz, W. A., Jeu, R., Dorigo, W., Haugen, L. E., Svendby, T. M., and Wagner, W. (2015). Evaluation of satellite soil moisture products over Norway using ground-based observations. *International Journal of Applied Earth Observation and Geoinformation*, 4.

Gruber, A., Dorigo, W., Zwieback, S., Xaver, A., and Wagner, W. (2013). Characterizing Coarse-Scale Representativeness of in situ Soil Moisture Measurements from the International Soil Moisture Network. *Vadose Zone Journal*, 12(2):0.

Guo, Z. and Dirmeyer, P. A. (2006). Evaluation of the second global soil wetness project soil moisture simulations: 1. intermodel comparison. *Journal of Geophysical Research: Atmospheres*, 111(D22):D22S02.

Gupta, H. V., Bastidas, L. A., Sorooshian, S., Shuttleworth, W. J., and Yang, Z. L. (1999). Parameter estimation of a land surface scheme using multicriteria methods. *Journal of Geophysical Research*, 104(D16):491–503.

Guzinski, R., Nieto, H., Stisen, S., and Fensholt, R. (2015). Inter-comparison of energy balance and hydrological models for land surface energy flux estimation over a whole river catchment. *Hydrology and Earth System Sciences*, 19(4):2017–2036.

Hartogensis, O., Watts, C., Rodriguez, J., and De Bruin, H. (2003). Derivation of an effective height for scintillometers: La poza experiment in northwest mexico. *Journal of hydrometeorology*, 4(5):915–928.

Heathman, G. C., Cosh, M. H., Han, E., Jackson, T. J., McKee, L., and McAfee, S. (2012). Field scale spatiotemporal analysis of surface soil moisture for evaluating point-scale in situ networks. *Geoderma*, 170(0):195–205.

Hemakumara, H., Chandrapala, L., and Moene, A. F. (2003). Evapotranspiration fluxes over mixed vegetation areas measured from large aperture scintillometer. *Agricultural Water Management*, 58(2):109–122.

Henderson-Sellers, A., Pitman, A. J., Love, P. K., Irannejad, P., and Chen, T. H. (1995). The Project for Intercomparison of Land Surface Parameterization Schemes (PILPS): Phases 2 and 3. *Bulletin of the American Meteorological Society*, 76(4):489–503.

Henderson-Sellers, A., Yang, Z. L., and Dickinson, R. E. (1993). The Project for Intercomparison of Land-surface Parameterization Schemes. *Bulletin of the American Meteorological Society*, 74(7):1335–1349.

Hendrickx, Jan MH and Kleissl, Jan and Vélez, Jesús D Gómez and Hong, Sung-ho and Duque, José R Fábrega and Vega, David and Ramírez, Hernán A Moreno and Ogden, Fred L (2007). Scintillometer networks for calibration and validation of energy balance and soil moisture remote sensing algorithms. *Proc. SPIE*, 6565:65650W–65650W–16.

Hill, R. and Clifford, S. (1978). Modified spectrum of atmospheric temperature fluctuations and its application to optical propagation. *JOSA*, 68(7):892–899.

Hill, R. J. (1997). Algorithms for obtaining atmospheric surface-layer fluxes from scintillation measurements. *J. Atmos. Oceanic Technol.*, 14(3):456–467.

Hill, R. J., Bohlander, R. A., Clifford, S. F., McMillan, R. W., Priestly, J. T., and Schoenfeld, W. P. (1988). Turbulence-induced millimeter-wave scintillation compared with micrometeorological measurements. *Geoscience and Remote Sensing, IEEE Transactions on*, 26(3):330–342.

Hill, R. J., Clifford, S. F., and Lawrence, R. S. (1980). Refractive-index and absorption fluctuations in the infrared caused by temperature, humidity, and pressure fluctuations. *JOSA*, 70(10):1192–1205.

Hoedjes, J. C. B., Chehbouni, A. ., Ezzahar, J., Escadafal, R., and De Bruin, H. A. R. (2007). Comparison of Large Aperture Scintillometer and Eddy Covariance Measurements: Can Thermal Infrared Data Be Used to Capture Footprint-Induced Differences? *J. Hydrometeor*, 8(2):144–159.

Hoedjes, J. C. B., Zuurbier, R. M., and Watts, C. J. (2002). Large aperture scintillometer used over a homogeneous irrigated area, partly affected by regional advection. *Boundary-Layer Meteorology*, 105(1):99–117.

Hornbuckle, B. and England, A. (2005). Diurnal variation of vertical temperature gradients within a field of maize: implications for satellite microwave radiometry. *Geoscience and Remote Sensing Letters, IEEE*, 2(1):74–77.

Hornbuckle, J., Christen, E. W., Land, C., and Water. (1999). *Physical properties of soils in the Murrumbidgee and Coleambally irrigation areas / J. Hornbuckle and E. Christen*. CSIRO Land and Water Canberra, A.C.T.

Hou, Z., Huang, M., Leung, L. R., Lin, G., and Ricciuto, D. M. (2012). Sensitivity of surface flux simulations to hydrologic parameters based on an uncertainty quantification framework applied to the community land model. *Journal of Geophysical Research: Atmospheres*, 117(D15):n/a–n/a. D15108.

Hu, W., Tallon, L. K., and Si, B. C. (2012). Evaluation of time stability indices for soil water storage upscaling. *Journal of Hydrology*, 475:229–241.

Hutley, L. B., Leuning, R., Beringer, J., and Cleugh, H. A. (2005). The utility of the eddy covariance techniques as a tool in carbon accounting: tropical savanna as a case study. *Australian Journal of Botany*, 53(7):663.

Imaoka, K., Kachi, M., Fujii, H., Murakami, H., Hori, M., Ono, A., Igarashi, T., Nakagawa, K., Oki, T., Honda, Y., and Shimoda, H. (2010). Global Change Observation Mission (GCOM) for Monitoring Carbon, Water Cycles, and Climate Change. *Proceedings of the IEEE*, 98(5):717–734.

Ishimaru, A. (1978). *Wave propagation and scattering in random media*, volume 2. Academic Press New York.

Jackson, T., Moran, M., and O'Neill, P. (2008). Introduction to soil moisture experiments 2004 (SMEX04). *Remote Sens. Environ*, 112(2):301–303.

Jackson, T., Schmugge, T., Nicks, A., Coleman, G., and Engman, E. (1981). Soil moisture updating and microwave remote sensing for hydrological simulation/la remise à jour de l'état d'humidité des sols en vue de la simulation hydrologique. *Hydrological Sciences Journal*, 26(3):305–319.

Jackson, T. J. (1993a). Description of Soil Moisture Retrieval Algorithm for ADEOS II AMSR. (V).

Jackson, T. J. (1993b). Iii. measuring surface soil moisture using passive microwave remote sensing. *Hydrological processes*, 7(2):139–152.

Jackson, T. J., Bindlish, R., Cosh, M. H., Zhao, T., Starks, P. J., Bosch, D. D., Seyfried, M., Moran, M. S., Goodrich, D. C., Kerr, Y. H., and Leroux, D. (2012). Validation of Soil Moisture and Ocean Salinity (SMOS) Soil Moisture Over Watershed Networks in the U.S. *IEEE Transactions on Geoscience and Remote Sensing*, 50(5):1530–1543.

Jackson, T. J., Cosh, M. H., Bindlish, R., Starks, P. J., Bosch, D. D., Seyfried, M., Goodrich, D. C., Moran, M. S., and Du, J. (2010). Validation of Advanced Microwave Scanning Radiometer Soil Moisture Products. *IEEE Transactions on Geoscience and Remote Sensing*, 48(12):4256–4272.

Jackson, T. J., Gasiewski, A. J., Oldak, A., Klein, M., Njoku, E. G., Yevgrafov, A., Christiani, S., and Bindlish, R. (2002). Soil moisture retrieval using the C-band polarimetric scanning radiometer during the Southern Great Plains 1999 Experiment. *Geoscience and Remote Sensing, IEEE Transactions on*, 40(10):2151–2161.

Jacobs, J. M., Mohanty, B. P., Hsu, E.-C., and Miller, D. (2004). SMEX02: Field scale variability, time stability and similarity of soil moisture. *Remote Sensing of Environment*, 92(4):436–446.

Jacquette, E., Al Bitar, A., Mialon, A., Kerr, Y., Quesney, A., Cabot, F., and Richaume, P. (2010). SMOS CATDS level 3 global products over land. In *Remote Sensing*, volume 7824, pages 78240K–78240K–6.

Janis, M. J. and Robeson, S. M. (2004). Determining the Spatial Representativeness of Air-Temperature Records Using Variogram-Nugget Time Series. *Physical Geography*, 25(6):513–530.

JAXA (2015). Release of update AMSR2 products (Version 2.1). Online. Accessed: 2016-04-01.

JAXA (n.d.). Data products. `http://suzaku.eorc.jaxa.jp/GCOM_W/data/data_w_index.html`. Accessed: 2015-09-03.

Jenkins, F. A. and White, H. E. (1957). *Fundamentals of optics*. Tata McGraw-Hill Education.

Jiménez, C., Prigent, C., and Aires, F. (2009). Toward an estimation of global land surface heat fluxes from multisatellite observations. *Journal of Geophysical Research*, 114(D6):D06305.

Jones, D. A., Wang, W., and Fawcett, R. (2007). *Climate Data for the Australian Water Availability Project: Final Milestone Report*. Australian Bureau of Meteorology.

Joshi, C. and Mohanty, B. P. (2010). Physical controls of near-surface soil moisture across varying spatial scales in an agricultural landscape during SMEX02. *Water Resources Research*, 46(12):W12503.

Jung, M., Reichstein, M., and Bondeau, A. (2009). Towards global empirical upscaling of FLUXNET eddy covariance observations: validation of a model tree ensemble approach using a biosphere model. *Biogeosciences*, 6(10):2001–2013.

Kaimal, J. C. and Finnigan, J. J. (1994). *Atmospheric boundary layer flows: their structure and measurement*. Oxford University Press, New York.

Kalma, J. D., McVicar, T. R., and McCabe, M. F. (2008). Estimating land surface evaporation: a review of methods using remotely sensed surface temperature data. *Surveys in Geophysics*, 29(4):421–469.

Katul, G., Goltz, S. M., Hsieh, C.-I., Cheng, Y., Mowry, F., and Sigmon, J. (1995). Estimation of surface heat and momentum fluxes using the flux-variance method above uniform and non-uniform terrain. *Boundary-Layer Meteorology*, 74(3):237–260.

Katul, G. and Hsieh, C.-I. (1999). A Note on the Flux-Variance Similarity Relationships for Heat and Water Vapour in the Unstable Atmospheric Surface Layer. *Boundary-Layer Meteorology*, 90(2):327–338.

Kerr, Y., Waldteufel, P., Richaume, P., Wigneron, J.-P., Ferrazzoli, P., Mahmoodi, A., Al Bitar, A., Cabot, F., Gruhier, C., Juglea, S., Leroux, D., Mialon, A., and Delwart, S. (2012). The SMOS Soil Moisture Retrieval Algorithm. *Geoscience and Remote Sensing, IEEE Transactions on*, 50(5):1384–1403.

Kerr, Y., Waldteufel, P., Wigneron, J.-P., Delwart, S., Cabot, F., Boutin, J., Escorihuela, M.-J., Font, J., Reul, N., Gruhier, C., Juglea, S., Drinkwater, M., Hahne, A., Martin-Neira, M., and Mecklenburg, S. (2010). The SMOS Mission: New Tool for Monitoring Key Elements of the Global Water Cycle. *Proceedings of the IEEE*, 98(5):666–687.

Kerr, Y. H., Waldteufel, P., Wigneron, J. P., Martinuzzi, J. M., Font, J., and Berger, M. (2001). Soil moisture retrieval from space: The Soil Moisture and Ocean Salinity (SMOS) mission. *IEEE Transactions on Geoscience and Remote Sensing*, 39(8):1729–1735.

Kim, J., Guo, Q., Baldocchi, D., Leclerc, M., Xu, L., and Schmid, H. (2006). Upscaling fluxes from tower to landscape: Overlaying flux footprints on high-resolution (IKONOS) images of vegetation cover. *Agricultural and Forest Meteorology*, 136(3-4):132–146.

Kim, S., Liu, Y., Johnson, F. M., Parinussa, R. M., and Sharma, A. (2015). A global comparison of alternate AMSR2 soil moisture products: Why do they differ? *Remote Sensing of Environment*, 161:43–62.

Kite, G. W. and Droogers, P. (2000). Comparing evapotranspiration estimates from satellites, hydrological models and field data. *Journal of Hydrology*, 229(1-2):3–18.

Kleissl, J., Hong, S. H., and Hendrickx, J. (2009a). New mexico scintillometer network in support of remote sensing, and hydrologic and meteorological models. *Bull Amer Meteorol Soc*, 90(2).

Kleissl, J., Watts, C. J., Rodriguez, J. C., Naif, S., and Vivoni, E. R. (2009b). Scintillometer intercomparison study—continued. *Boundary-layer meteorology*, 130(3):437–443.

Klemeš, V. (1986). Dilettantism in hydrology: Transition or destiny? *Water Resources Research*, 22(9S):177S–188S.

Kohsiek, W. (1982). Measuring C_T^2, C_Q^2, and C_{TQ} in the unstable surface layer, and relations to the vertical fluxes of heat and moisture. *Boundary-Layer Meteorology*, 24(1):89–107.

Kohsiek, W. and Herben, M. (1983). Evaporation derived from optical and radio-wave scintillation. *Applied optics*, 22(17):2566–2570.

Kolmogorov, A. N. (1941). The local Structure of turbulence in incompressible viscous fluid for very large Reynolds numbers [In Russian]. In *Dokl. Akad. Nauk SSSR*, volume 30, pages 299–303.

Koster, R. D. (2004). Regions of strong coupling between soil moisture and precipitation. *Science*, 305:1138–1140.

Koster, R. D., Guo, Z., Yang, R., Dirmeyer, P. a., Mitchell, K., and Puma, M. J. (2009). On the Nature of Soil Moisture in Land Surface Models. *Journal of Climate*, 22(16):4322–4335.

Krinner, G., Viovy, N., de Noblet-Ducoudré, N., Ogée, J., Polcher, J., Friedlingstein, P., Ciais, P., Sitch, S., and Prentice, I. C. (2005). A dynamic global vegetation model for studies of the coupled atmosphere-biosphere system. *Global Biogeochemical Cycles*, 19(1).

Kurc, S. A. and Small, E. E. (2007). Soil moisture variations and ecosystem-scale fluxes of water and carbon in semiarid grassland and shrubland. *Water Resources Research*, 43(6):n/a—-n/a.

Lacava, T., Faruolo, M., Pergola, N., Coviello, I., and Tramutoli, V. (2012). A comprehensive analysis of amsre c- and x-bands radio frequency interferences. In *Microwave Radiometry and Remote Sensing of the Environment (MicroRad), 2012 12th Specialist Meeting on*, pages 1–4.

Lagouarde, J.-P., Bonnefond, J.-M., Kerr, Y. H., McAneney, K. J., and Irvine, M. (2002). Integrated sensible heat flux measurements of a two-surface composite landscape using scintillometry. *Boundary-layer meteorology*, 105(1):5–35.

Lagouarde, J.-P., Irvine, M., Bonnefond, J.-M., Grimmond, C. S. B., Long, N., Oke, T. R., Salmond, J. A., and Offerle, B. (2006). Monitoring the Sensible Heat Flux over Urban Areas using Large Aperture Scintillometry: Case Study of Marseille City During the Escompte Experiment. *Boundary-Layer Meteorology*, 118(3):449–476.

Lei, F., Crow, W., Shen, H., Parinussa, R., and Holmes, T. (2015). The Impact of Local Acquisition Time on the Accuracy of Microwave Surface Soil Moisture Retrievals over the Contiguous United States. *Remote Sensing*, 7(10):13448–13465.

Leijnse, H., Uijlenhoet, R., and Stricker, J. N. M. (2007). Hydrometeorological application of a microwave link: 2. Precipitation. *Water resources research*, 43(4).

Leuning, R., van Gorsel, E., Massman, W. J., and Isaac, P. R. (2012). Reflections on the surface energy imbalance problem. *Agricultural and Forest Meteorology*, 156(0):65 – 74.

Li, D. and Shao, M. (2015). Temporal stability of soil water storage in three landscapes in the middle reaches of the Heihe River, northwestern China. *Environmental Earth Sciences*, 73(7):3095–3107.

Li, F., Kustas, W. P., Anderson, M. C., Prueger, J. H., and Scott, R. L. (2008). Effect of remote sensing spatial resolution on interpreting tower-based flux observations. *Remote Sensing of Environment*, 112(2):337–349.

Li, Z.-L., Tang, R., Wan, Z., Bi, Y., Zhou, C., Tang, B., Yan, G., and Zhang, X. (2009). A Review of Current Methodologies for Regional Evapotranspiration Estimation from Remotely Sensed Data. *Sensors*, 9(5):3801–3853.

Lillesand, T. M., Kiefer, R. W., and Chipman, J. W. (2004). *Remote sensing and image interpretation*. John Wiley & Sons Ltd.

Liu, S. M., Xu, Z. W., Zhu, Z. L., Jia, Z. Z., and Zhu, M. J. (2013). Measurements of evapotranspiration from eddy-covariance systems and large aperture scintillometers in the Hai River Basin, China. *Journal of Hydrology*, 487(0):24–38.

Liu, Y. Y., Evans, J. P., McCabe, M. F., de Jeu, R. A. M., van Dijk, A. I. J. M., and Su, H. (2010). Influence of cracking clays on satellite estimated and model simulated soil moisture. *Hydrology and Earth System Sciences*, 14(6):979–990.

Liu, Y. Y., Parinussa, R. M., Dorigo, W. A., De Jeu, R. A. M., Wagner, W., van Dijk, A. I. J. M., McCabe, M. F., and Evans, J. P. (2011). Developing an improved soil moisture dataset by blending passive and active microwave satellite-based retrievals. *Hydrology and Earth System Sciences*, 15(2):425–436.

Lüdi, A., Beyrich, F., and Mätzler, C. (2005). Determination of the turbulent temperature–humidity correlation from scintillometric measurements. *Boundary-layer meteorology*, 117(3):525–550.

Lymburner, L. and Australia, G. (2011). *The National Dynamic Land Cover Dataset*. Geoscience Australia.

Mackay, D. S., Samanta, S., Ahl, D. E., Ewers, B. E., Gower, S. T., and Burrows, S. N. (2003). Automated Parameterization of Land Surface Process Models Using Fuzzy Logic. *Transactions in GIS*, 7(1):139–153.

Maeda, T., Imaoka, K., Kachi, M., Fujii, H., Shibata, A., Naoki, K., Kasahara, M., Ito, N., Nakagawa, K., and Oki, T. (2011). Status of GCOM-W1/AMSR2 development, algorithms, and products. *Proc. SPIE*, 8176:81760N–81760N–7.

Maeda, T. and Taniguchi, Y. (2013). Descriptions of GCOM-W1 AMSR2 Level 1R and Level 2 Algorithms. Online. NDX-120015A.

Manabe, S. (1969). Climate and the ocean circulation1. *Monthly weather review*, 97(11):739–774.

Martínez, G., Pachepsky, Y. A., and Vereecken, H. (2014). Temporal stability of soil water content as affected by climate and soil hydraulic properties: a simulation study. *Hydrological Processes*, 28(4):1899–1915.

Martínez-Fernández, J. and Ceballos, A. (2003). Temporal stability of soil moisture in a large-field experiment in Spain. *Soil Science Society of America Journal*, 67(6):1647–1656.

Martínez-Fernández, J. and Ceballos, A. (2005). Mean soil moisture estimation using temporal stability analysis. *Journal of Hydrology*, 312(1-4):28–38.

McCabe, M., Miralles, D., Jimenez, C., Ershadi, A., Fisher, J., Mu, Q., Liang, M., Mueller, B., Sheffield, J., Seneviratne, S., and Others (2013). Global-Scale Estimation of Land Surface Heat Fluxes from Space: Product Assessment and Intercomparison. *Remote Sensing of Energy Fluxes and Soil Moisture Content*, page 249.

McCabe, M. F., Ershadi, A., Jimenez, C., Miralles, D. G., Michel, D., and Wood, E. F. (2015). The GEWEX LandFlux project: evaluation of model evaporation using tower-based and globally-gridded forcing data. *Geoscientific Model Development Discussions*, 8(8):6809–6866.

McCabe, M. F., Gao, H., and Wood, E. F. (2005). Evaluation of AMSR-E-Derived Soil Moisture Retrievals Using Ground-Based and PSR Airborne Data during SMEX02. *Journal of Hydrometeorology*, 6(6):864–877.

McCabe, M. F. and Wood, E. F. (2006). Scale influences on the remote estimation of evapotranspiration using multiple satellite sensors. *Remote Sensing of Environment*, 105(4):271–285.

McJannet, D., Cook, F., McGloin, R., McGowan, H., Burn, S., and Sherman, B. (2013). Long-term energy flux measurements over an irrigation water storage using scintillometry. *Agricultural and Forest Meteorology*, 168(0):93–107.

McJannet, D. L., Cook, F. J., McGloin, R. P., McGowan, H. A., and Burn, S. (2011). Estimation of evaporation and sensible heat flux from open water using a large-aperture scintillometer. *Water Resources Research*, 47(5):W05545.

McKenzie, N. J., Jacquier, D., Ashton, L., and Cresswell, H. (2000). *Estimation of soil properties using the Atlas of Australian Soils*. CSIRO Land and Water Canberra.

Meijninger, W., Hartogensis, O., Kohsiek, W., Hoedjes, J., Zuurbier, R., and De Bruin, H. (2002a). Determination of area-averaged sensible heat fluxes with a large aperture scintillometer over a heterogeneous surface–Flevoland field experiment. *Boundary-Layer Meteorology*, 105(1):37–62.

Meijninger, W. M. L. and De Bruin, H. A. R. (2000). The sensible heat fluxes over irrigated areas in western Turkey determined with a large aperture scintillometer. *Journal of Hydrology*, 229(1):42–49.

Meijninger, W. M. L., Green, a. E., Hartogensis, O. K., Hoedjes, J. C. B., Zuurbier, R. M., and de Bruin, H. a. R. (2002b). Determination of area averaged water vapour fluxes with a large aperture and radio wave scinillometer over a heterogeneous surface - Flevoland experiment. *Boundary-Layer Meteorol.*, 105:63–83.

Merlin, O., Walker, J. P., Kalma, J. D., Kim, E. J., Hacker, J., Panciera, R., Young, R., Summerell, G., Hornbuckle, J., Hafeez, M., and Jackson, T. (2008). The NAFE06 data set: Towards soil moisture retrieval at intermediate resolution. *Advances in Water Resources*, 31(11):1444–1455.

Merlin, O., Walker, J. P., Panciera, R., Young, R., Kalma, J. D., and Kim, E. J. (2007). Soil Moisture Measurement in Heterogeneous Terrain. *Modsim 2007: International Congress on Modelling and Simulation*, pages 2604–2610.

Moene, A. F. (2003). Effects of water vapour on the structure parameter of the refractive index for near-infrared radiation. *Boundary-Layer Meteorology*, 107(3):635–653.

Mohanty, B. P. and Skaggs, T. H. (2001). Spatio-temporal evolution and time-stable characteristics of soil moisture within remote sensing footprints with varying soil, slope, and vegetation. *Advances in Water Resources*, 24(9-10):1051–1067.

Moncrieff, J., Clement, R., Finnigan, J., and Meyers, T. (2005). Averaging, Detrending, and Filtering of Eddy Covariance Time Series. In Lee, X., Massman, W., and Law, B., editors, *Handbook of Micrometeorology*, volume 29 of *Atmospheric and Oceanographic Sciences Library*, pages 7–31. Springer Netherlands.

Monin, A. and Obukhov, A. (1954). Basic laws of turbulent mixing in the surface layer of the atmosphere. *Contrib. Geophys. Inst. Acad. Sci. USSR*, 24(151):163–187.

Monin, A. and Yaglom, A. (1971). Statistical fluid dynamics. *Vol. I and II MIT Press, Cambridge.*

Monteith, J. L. (1965). Evaporation and environment. In *Symp. Soc. Exp. Biol*, volume 19, page 4.

Mu, Q., Heinsch, F. A., Zhao, M., and Running, S. W. (2007). Development of a global evapotranspiration algorithm based on MODIS and global meteorology data. *Remote Sensing of Environment*, 111(4):519–536.

Mu, Q., Zhao, M., and Running, S. W. (2011). Improvements to a MODIS global terrestrial evapotranspiration algorithm. *Remote Sensing of Environment*, 115(8):1781–1800.

Mu, Q., Zhao, M., and Running, S. W. (2013). MODIS Global Terrestrial Evapotranspiration (ET) Product (NASA MOD16A2/A3). *Algorithm Theoretical Basis Document, Collection*, 5.

Naeimi, V., Bartalis, Z., and Wagner, W. (2009). ASCAT soil moisture: An assessment of the data quality and consistency with the ERS scatterometer heritage. *Journal of Hydrometeorology*, 10(2):555–563.

Natural Resources Advisory Council, N. (2010). Understanding our native grasslands: Agricultural, environmental and indigenous values and management for the future. Technical report, State of New South Wales.

Nieveen, J. and Green, A. (1999). Measuring sensible heat flux density over pasture using the ct2-profile method. *Boundary-Layer Meteorology*, 91(1):23–35.

Njoku, E. and Li, L. (1999). Retrieval of land surface parameters using passive microwave measurements at 6-18 ghz. *Geoscience and Remote Sensing, IEEE Transactions on*, 37(1):79–93.

Njoku, E. G., Ashcroft, P., Chan, T. K., and Li, L. (2005). Global survey and statistics of radio-frequency interference in AMSR-E land observations. *Geoscience and Remote Sensing, IEEE Transactions on*, 43(5):938–947.

Njoku, E. G., Jackson, T. J., Lakshmi, V., Chan, T. K., and Nghiem, S. V. (2003). Soil moisture retrieval from AMSR-E. *IEEE Transactions on Geoscience and Remote Sensing*, 41(2 PART 1):215–228.

Nobel, P. S. (1999). *Physicochemical and environmental plant physiology.* Academic press.

Noilhan, J. and Mahfouf, J.-F. (1996). The ISBA land surface parameterisation scheme. *Global and Planetary Change*, 13(1 - 4):145 – 159. Soil Moisture Simulation.

Noilhan, J. and Planton, S. (1989). A simple parameterization of land surface processes for meteorological models. *Monthly Weather Review*, 117(3):536–549.

North, M. R., Petropoulos, G. P., Ireland, G., and McCalmont, J. P. (2015). Appraising the capability of a land biosphere model as a tool in modelling land surface interactions: results from its validation at selected European ecosystems. *Earth System Dynamics Discussion*, 6:217–265.

Obukhov, A. (1949). Temperature field structure in a turbulent flow. *Izv. Acad. Nauk SSSR Ser. Geog. Geofiz*, 13:58–69.

Ogunjemiyo, S. O., Kaharabata, S. K., Schuepp, P. H., MacPherson, I. J., Desjardins, R., and Roberts, D. A. (2003). Methods of estimating CO_2, latent heat and sensible heat fluxes from estimates of land cover fractions in the flux footprint. *Agricultural and Forest Meteorology*, 117(3–4):125–144.

Oke, T. R. (2002). *Boundary layer climates.* Routledge.

Oki, T. and Kanae, S. (2006). Global Hydrological Cycles and World Water Resources. *Science*, 313(5790):1068–1072.

Overgaard, Jesper and Rosbjerg, Dan and Butts, MB (2006). Land-surface modelling in hydrological perspective - a review. *Biogeosciences*, 3(2).

Owe, M., de Jeu, R., and Holmes, T. (2008). Multisensor historical climatology of satellite-derived global land surface moisture. *Journal of Geophysical Research F: Earth Surface*, 113(F1):F1.

Owe, M., De Jeu, R., and Walker, J. (2001). A methodology for surface soil moisture and vegetation optical depth retrieval using the microwave polarization difference index. *Geoscience and Remote Sensing, IEEE Transactions on*, 39(8):1643–1654.

Pal, J. S. and Eltahir, E. A. B. (2003). A feedback mechanism between soil-moisture distribution and storm tracks. *Quarterly Journal of the Royal Meteorological Society*, 129(592):2279–2297.

Panciera, R., Walker, J. P., Jackson, T. J., Gray, D. A., Tanase, M. A., Ryu, D., Monerris, A., Yardley, H., Rüdiger, C., Wu, X., Gao, Y., and Hacker, J. M. (2014). The Soil Moisture Active Passive Experiments (SMAPEx): Toward Soil Moisture Retrieval From the SMAP Mission. *Geoscience and Remote Sensing, IEEE Transactions on*, 52(1):490–507.

Panciera, R., Walker, J. P., Kalma, J. D., Kim, E. J., Hacker, J. M., Merlin, O., Berger, M., and Skou, N. (2008). The NAFE'05/CoSMOS data set: Toward SMOS soil moisture retrieval, downscaling, and assimilation. *Geoscience and Remote Sensing, IEEE Transactions on*, 46(3):736–745.

Papale, D., Reichstein, M., Aubinet, M., Canfora, E., Bernhofer, C., Kutsch, W., Longdoz, B., Rambal, S., Valentini, R., Vesala, T., and Yakir, D. (2006). Towards a standardized processing of Net Ecosystem Exchange measured with eddy covariance technique: algorithms and uncertainty estimation. *Biogeosciences*, 3(4):571–583.

Parinussa, R., Yilmaz, M., Anderson, M., Hain, C., and Jeu, R. (2014). An intercomparison of remotely sensed soil moisture products at various spatial scales over the Iberian Peninsula. *Hydrological Processes*, 28(18):4865–4876.

Parinussa, R. M., Holmes, T. R. H., Wanders, N., Dorigo, W. A., and de Jeu, R. A. M. (2015). A preliminary study toward consistent soil moisture from AMSR2. *Journal of Hydrometeorology*, 16(2):932–947.

Pauwels, V., Timmermans, W., and Loew, A. (2008). Comparison of the estimated water and energy budgets of a large winter wheat field during AgriSAR 2006 by multiple sensors and models. *Journal of Hydrology*, 349(3):425–440.

Pauwels, V. R. and Lannoy, G. J. D. (2015). Error covariance calculation for forecast bias estimation in hydrologic data assimilation. *Advances in Water Resources*, 86, Part B:284 – 296.

Peischl, S., Walker, J. P., Rüdiger, C., Ye, N., Kerr, Y. H., Kim, E., Bandara, R., and Allahmoradi, M. (2012). The AACES field experiments: SMOS calibration and validation across the Murrumbidgee River catchment. *Hydrology and Earth System Sciences*, 16:1697–1708.

Peng, J., Niesel, J., Loew, A., Zhang, S., and Wang, J. (2015). Evaluation of Satellite and Reanalysis Soil Moisture Products over Southwest China Using Ground-Based Measurements. *Remote Sensing*, 7(11):15729.

Penna, D., Brocca, L., Borga, M., and Dalla Fontana, G. (2013). Soil moisture temporal stability at different depths on two alpine hillslopes during wet and dry periods. *Journal of Hydrology*, 477:55–71.

Pitman, A. J. (2003). The evolution of, and revolution in, land surface schemes designed for climate models. *International Journal of Climatology*, 23(5):479–510.

Pitman, A. J. and Henderson-Sellers, A. (1998). Recent progress and results from the project for the intercomparison of landsurface parameterization schemes. *Journal of Hydrology*, 212 - 213(0):128–135.

Polhamus, A., Fisher, J. B., and Tu, K. P. (2013). What controls the error structure in evapotranspiration models? *Agricultural and Forest Meteorology*, 169:12–24.

Prentice, I. C., Liang, X., Medlyn, B. E., and Wang, Y.-P. (2015). Reliable, robust and realistic: the three r's of next-generation land-surface modelling. *Atmospheric Chemistry and Physics*, 15(10):5987–6005.

Prigent, C., Aires, F., Rossow, W. B., and Robock, A. (2005). Sensitivity of satellite microwave and infrared observations to soil moisture at a global scale: Relationship of satellite observations to in situ soil moisture measurements. *Journal of Geophysical Research: Atmospheres*, 110(D7):D07110.

Prueger, J. H., Hatfield, J. L., Parkin, T. B., Kustas, W. P., Hipps, L. E., Neale, C. M. U., MacPherson, J. I., Eichinger, W. E., and Cooper, D. I. (2005). Tower and Aircraft Eddy Covariance Measurements of Water Vapor, Energy, and Carbon Dioxide Fluxes during SMACEX. *Journal of Hydrometeorology*, 6(6):954–960.

Qin, J., Yang, K., Lu, N., Chen, Y., Zhao, L., and Han, M. (2013). Spatial upscaling of in-situ soil moisture measurements based on MODIS-derived apparent thermal inertia. *Remote Sensing of Environment*, 138(0):1–9.

Raju, S., Chanzy, A., Wigneron, J.-P., Calvet, J.-C., Kerr, Y., and Laguerre, L. (1995). Soil moisture and temperature profile effects on microwave emission at low frequencies. *Remote Sensing of Environment*, 54(2):85 – 97.

Rana, G. and Katerji, N. (2000). Measurement and estimation of actual evapotranspiration in the field under Mediterranean climate: a review. *European Journal of Agronomy*, 13(2-3):125–153.

Refsgaard, J. C. (1997). Parameterisation, calibration and validation of distributed hydrological models. *Journal of Hydrology*, 198(1-4):69–97.

Reichle, R. H. and Koster, R. D. (2004). Bias reduction in short records of satellite soil moisture. *Geophysical Research Letters*, 31(19):2–5.

Rhoads, J., Dubayah, R., Lettenmaier, D., O'Donnell, G., and Lakshmi, V. (2001). Validation of land surface models using satellite-derived surface temperature. *Journal of Geophysical Research: Atmospheres*, 106(D17):20085–20099.

Richards, L. A. (1931). Capillary conduction of liquids through porous mediums. *Journal of Applied Physics*, 1(5):318–333.

Robock, A., Vinnikov, K. Y., Srinivasan, G., Entin, J. K., Hollinger, S. E., Speranskaya, N. A., Liu, S., and Namkhai, A. (2000). The Global Soil Moisture Data Bank. *Bulletin of the American Meteorological Society*, 81(6):1281–1299.

Román, M. O., Schaaf, C. B., Woodcock, C. E., Strahler, A. H., Yang, X., Braswell, R. H., Curtis, P. S., Davis, K. J., Dragoni, D., and Goulden, M. L. (2009). The MODIS (Collection V005) BRDF/albedo product: Assessment of spatial representativeness over forested landscapes. *Remote Sensing of Environment*, 113(11):2476–2498.

Rosero, E., Yang, Z.-L., Wagener, T., Gulden, L. E., Yatheendradas, S., and Niu, G.-Y. (2010). Quantifying parameter sensitivity, interaction, and transferability in hydrologically enhanced versions of the noah land surface model over transition zones during the warm season. *Journal of Geophysical Research: Atmospheres*, 115(D3):D03106.

Rötzer, K., Montzka, C., Bogena, H., Wagner, W., Kerr, Y. H., Kidd, R., and Vereecken, H. (2014). Catchment scale validation of SMOS and ASCAT soil moisture products using hydrological modeling and temporal stability analysis. *Journal of Hydrology*, 519:934–946.

Rowlandson, T. L., Hornbuckle, B. K., Bramer, L. M., Patton, J. C., and Logsdon, S. D. (2012). Comparisons of Evening and Morning SMOS Passes Over the Midwest United States. *Geoscience and Remote Sensing, IEEE Transactions on*, 50(5):1544–1555.

Rüdiger, C., Calvet, J.-C., Gruhier, C., Holmes, T. R. H., de Jeu, R. a. M., and Wagner, W. (2009). An Intercomparison of ERS-Scat and AMSR-E Soil Moisture Observations with Model Simulations over France. *Journal of Hydrometeorology*, 10(2):431–447.

Rüdiger, C., Western, A. W., Walker, J. P., Smith, A. B., Kalma, J. D., and Willgoose, G. R. (2010). Towards a general equation for frequency domain reflectometers. *Journal of Hydrology*, 383(3-4):319–329.

Ryu, D. and Famiglietti, J. S. (2006). Multi-scale spatial correlation and scaling behavior of surface soil moisture. *Geophysical Research Letters*, 33(8):L08404.

Samain, B., Defloor, W., and Pauwels, V. R. N. (2012a). Continuous Time Series of Catchment-Averaged Sensible Heat Flux from a Large Aperture Scintillometer: Efficient Estimation of Stability Conditions and Importance of Fluxes under Stable Conditions. *Journal of Hydrometeorology*, 13(2):423–442.

Samain, B., Ferket, B. V. A., Defloor, W., and Pauwels, V. R. N. (2011). Estimation of catchment averaged sensible heat fluxes using a large aperture scintillometer. *Water Resources Research*, 47(5).

Samain, B., Simons, G. W. H., Voogt, M. P., Defloor, W., Bink, N.-J., Pauwels, V. R. N., and Loew, A. (2012b). Consistency between hydrological model, large aperture scintillometer and remote sensing based evapotranspiration estimates for a heterogeneous catchment. *Hydrology & Earth System Sciences*, 16(7).

Savage, M. J. (2009). Estimation of evaporation using a dual-beam surface layer scintillometer and component energy balance measurements. *Agricultural and Forest Meteorology*, 149(3):501–517.

Schlosser, C. A., Slater, A. G., Robock, A., Pitman, A. J., Vinnikov, K. Y., Henderson-Sellers, A., Speranskaya, N. A., Mitchell, K., and The, P. C. (2000). Simulations of a Boreal Grassland Hydrology at Valdai, Russia: PILPS Phase 2(d). *Monthly weather review*, 128(2):301–321.

Schmid, H. P. (1994). Source areas for scalars and scalar fluxes. *Boundary-Layer Meteorology*, 67(3):293–318.

Schmugge, T. J., Kustas, W. P., Ritchie, J. C., Jackson, T. J., and Rango, A. (2002). Remote sensing in hydrology. *Advances in Water Resources*, 25(8-12):1367–1385.

Schneider, K., Huisman, J. A., Breuer, L., Zhao, Y., and Frede, H.-G. (2008). Temporal stability of soil moisture in various semi-arid steppe ecosystems and its application in remote sensing. *Journal of Hydrology*, 359(1-2):16–29.

Schüttemeyer, D., Schillings, C., Moene, A. F., and De Bruin, H. A. R. (2007). Satellite-based actual evapotranspiration over drying semiarid terrain in West Africa. *Journal of Applied Meteorology and Climatology*, 46(1):97–111.

Sellers, P. J., Dickinson, R. E., Randall, D. A., Betts, A. K., Hall, F. G., Berry, J. A., Collatz, G. J., Denning, A. S., Mooney, H. A., Nobre, C. A., Sato, N., Field, C. B., and Henderson-Sellers, A. (1997a). Modeling the Exchanges of Energy, Water, and Carbon Between Continents and the Atmosphere. *Science*, 275(5299):502–509.

Sellers, P. J., Heiser, M. D., Hall, F. G., Verma, S. B., Desjardins, R. L., Schuepp, P. M., and MacPherson, J. I. (1997b). The impact of using area-averaged land surface properties topography, vegetation condition, soil wetnessin calculations of intermediate scale (approximately 10 km^2) surface-atmosphere heat and moisture fluxes. *Journal of Hydrology*, 190(3-4):269–301.

Sellers, P. J., Mintz, Y., Sud, Y. C., and Dalcher, A. (1986). A Simple Biosphere Model (SIB) for Use within General Circulation Models. *Journal of the Atmospheric Sciences*, 43(6):505–531.

Senay, G. B., Friedrichs, M., Singh, R. K., and Velpuri, N. M. (2016). Evaluating Landsat 8 evapotranspiration for water use mapping in the Colorado River Basin . *Remote Sensing of Environment*. In Press.

Seneviratne, S. I. (2010). Investigating soil moisture-climate interactions in a changing climate: a review. *Earth Sci. Rev.*, 99:99–174.

Shahrban, M., Walker, J. P., Wang, Q. J., Seed, A., and Steinle, P. (2016). An evaluation of numerical weather prediction based rainfall forecasts. *Hydrological Sciences Journal*. In Press.

Sivapalan, M., Blöschl, G., Zhang, L., and Vertessy, R. (2003). Downward approach to hydrological prediction. *Hydrological processes*, 17(11):2101–2111.

Slevin, D., Tett, S. F. B., and Williams, M. (2015). Multi-site evaluation of the JULES land surface model using global and local data. *Geoscientific Model Development*, 8(2):295–316.

Smith, A. B., Walker, J. P., Western, A. W., Young, R. I., Ellett, K. M., Pipunic, R. C., Grayson, R. B., Siriwardena, L., Chiew, F. H. S., and Richter, H. (2012). The Murrumbidgee soil moisture monitoring network data set. *Water Resources Research*, 48(7):W07701.

Solignac, P., Brut, A., Selves, J., Béteille, J., and Gastellu-Etchegorry, J. (2012). Attenuating the Absorption Contribution on C_{n^2} Estimates with a Large-Aperture Scintillometer. *Boundary-Layer Meteorology*, 143(2):261–283.

Stöckli, R., Lawrence, D. M., Niu, G.-Y., Oleson, K. W., Thornton, P. E., Yang, Z.-L., Bonan, G. B., Denning, A. S., and Running, S. W. (2008). Use of FLUXNET in the Community Land Model development. *Journal of Geophysical Research*, 113(G1):G01025.

Stöckli, R. and Vidale, P. L. (2005). Modeling diurnal to seasonal water and heat exchanges at European Fluxnet sites. *Theoretical and Applied Climatology*, 80(2-4):229–243.

Stull, R. B. (1988). *An introduction to boundary layer meteorology*, volume 13. Springer.

Su, C. H., Ryu, D., Young, R. I., Western, A. W., and Wagner, W. (2013). Inter-comparison of microwave satellite soil moisture retrievals over the Murrumbidgee Basin, southeast Australia. *Remote Sensing of Environment*, 134(2013):1–11.

Su, H., McCabe, M. F., Wood, E. F., Su, Z., and Prueger, J. H. (2005). Modeling Evapotranspiration during SMACEX: Comparing Two Approaches for Local- and Regional-Scale Prediction. *Journal of Hydrometeorology*, 6(6):910–922.

Su, Z. (2002). The Surface Energy Balance System (SEBS) for estimation of turbulent heat fluxes. *Hydrology and Earth System Sciences Discussions*, 6(1):85–100. ¡hal-00304651¿.

Sulkava, Mika and Luyssaert, Sebastiaan and Zaehle, Sönke and Papale, Dario (2011). Assessing and improving the representativeness of monitoring networks: The European flux tower network example. *Journal of Geophysical Research: Biogeosciences*, 116(G3).

Tatarskii, V. I. (1971). *The effects of the turbulent atmosphere on wave propagation.* Nauka, Moscow, 1967, Israel Program for Scientific Translations, U.S. Dept. of Commerce.

Taylor, C. M., Birch, C. E., Parker, D. J., Dixon, N., Guichard, F., Nikulin, G., and Lister, G. M. S. (2013). Modeling soil moisture-precipitation feedback in the Sahel: Importance of spatial scale versus convective parameterization. *Geophysical Research Letters*, 40(23):6213–6218. 2013GL058511.

Taylor, K. E. (2001). Summarizing multiple aspects of model performance in a single diagram. *Journal of Geophysical Research: Atmospheres*, 106(D7):7183–7192.

Twine, T. E., Kustas, W. P., Norman, J. M., Cook, D. R., Houser, P. R., Meyers, T. P., Prueger, J. H., Starks, P. J., and Wesely, M. L. (2000). Correcting eddy-covariance flux underestimates over a grassland. *Agricultural and Forest Meteorology*, 103(3):279–300.

Vachaud, G., de Silans, A., Balabanis, P., and Vauclin, M. (1985). Temporal stability of spatially measured soil water probability density function. *Soil Science Society of America Journal*, 49(4):822–828.

van der Schalie, R., Parinussa, R. M., Renzullo, L. J., van Dijk, A., Su, C.-H., and de Jeu, R. A. M. (2015). SMOS soil moisture retrievals using the land parameter retrieval model: Evaluation over the Murrumbidgee Catchment, southeast Australia. *Remote Sensing of Environment*, 163:70–79.

van Emmerik, T., Steele-Dunne, S., Judge, J., and van de Giesen, N. (2015). Impact of diurnal variation in vegetation water content on radar backscatter from maize during water stress. *Geoscience and Remote Sensing, IEEE Transactions on*, 53(7):3855–3869.

Van Genuchten, M. T. (1980). A closed-form equation for predicting the hydraulic conductivity of unsaturated soils. *Soil science society of America journal*, 44(5):892–898.

Van Kesteren, B. (2012). *Measuring water-vapour and carbon-dioxide fluxes at field scales with scintillometry.* [Sl: sn].

Van Kesteren, B., Beyrich, F., Hartogensis, O. K., and Braam, M. (2015). Long-Term Evaluation of the Scintec Boundary-Layer Scintillometer and the Wageningen Large-Aperture Scintillometer: Implications for Scintillometer Users. *Boundary-Layer Meteorology*, 156(2):303–323.

Van Niel, T. G., McVicar, T. R., Roderick, M. L., van Dijk, A. I., Beringer, J., Hutley, L. B., and van Gorsel, E. (2012). Upscaling latent heat flux for thermal remote sensing studies: Comparison of alternative approaches and correction of bias. *Journal of Hydrology*, 468-469:35–46.

Vanderlinden, K., Vereecken, H., Hardelauf, H., Herbst, M., Martínez, G., Cosh, M. H., and Pachepsky, Y. A. (2012). Temporal stability of soil water contents: a review of data and analyses. *Vadose Zone Journal*, 11(4).

Vereecken, H., Huisman, J., Pachepsky, Y., Montzka, C., van der Kruk, J., Bogena, H., Weihermüller, L., Herbst, M., Martinez, G., and Vanderborght, J. (2014). On the spatio-temporal dynamics of soil moisture at the field scale. *Journal of Hydrology*, 516:76–96.

Verseghy, D. L. (1991). Class - A Canadian land surface scheme for GCMS. I. Soil model. *International Journal of Climatology*, 11(2):111–133.

Vinnikov, K. Y., Robock, A., Qiu, S., and Entin, J. K. (1999a). Optimal design of surface networks for observation of soil moisture. *Journal of Geophysical Research: Atmospheres*, 104(D16):19743–19749.

Vinnikov, K. Y., Robock, A., Qiu, S., Entin, J. K., Owe, M., Choudhury, B. J., Hollinger, S. E., and Njoku, E. G. (1999b). Satellite remote sensing of soil moisture in Illinois, United States. *Journal of Geophysical Research*, 104(D4):4145–4168.

Vinukollu, R. K., Wood, E. F., Ferguson, C. R., and Fisher, J. B. (2011). Global estimates of evapotranspiration for climate studies using multi-sensor remote sensing data: Evaluation of three process-based approaches. *Remote Sensing of Environment*, 115(3):801–823.

Wagner, W., Hahn, S., Kidd, R., Melzer, T., Bartalis, Z., Hasenauer, S., Figa-Saldaña, J., de Rosnay, P., Jann, A., Schneider, S., Komma, J., Kubu, G., Brugger, K., Aubrecht, C., Züger, J., Gangkofner, U., Kienberger, S., Brocca, L., Wang, Y., Blöschl, G., Eitzinger, J., Steinnocher, K., Zeil, P., and Rubel, F. (2013). The ASCAT soil moisture product: A review of its specifications, validation results, and emerging applications. *Meteorologische Zeitschrift*, 22:5–33.

Wagner, W., Naeimi, V., Scipal, K., de Jeu, R., and Martínez-Fernández, J. (2007). Soil moisture from operational meteorological satellites. *Hydrogeology Journal*, 15(1):121–131.

Wagner, W., Sabel, D., Doubkova, M., Bartsch, A., and Pathe, C. (2009). The potential of Sentinel-1 for monitoring soil moisture with a high spatial resolution at global scale. In *Symposium of Earth Observation and Water Cycle Science*.

Wagner, W., Scipal, K., Pathe, C., Gerten, D., Lucht, W., and Rudolf, B. (2003). Evaluation of the agreement between the first global remotely sensed soil moisture data with model and precipitation data. *Journal of Geophysical Research: Atmospheres*, 108(D19).

Walker, J. P. and Houser, P. R. (2001). A methodology for initializing soil moisture in a global climate model: Assimilation of near-surface soil moisture observations. *Journal of Geophysical Research*, 106(D11):11761.

Walker, J. P. and Houser, P. R. (2004). Requirements of a global near-surface soil moisture satellite mission: accuracy, repeat time, and spatial resolution. *Advances in Water Resources*, 27(8):785–801.

Wang, K. and Dickinson, R. E. (2012). A review of global terrestrial evapotranspiration: Observation, modeling, climatology, and climatic variability. *Reviews of Geophysics*, 50(2):RG2005.

Wang, T.-i., Ochs, G., and Clifford, S. (1978). A saturation-resistant optical scintillometer to measure C_n^2. *JOSA*, 68(3):334–338.

Wang, Y. P., Kowalczyk, E., Leuning, R., Abramowitz, G., Raupach, M. R., Pak, B., van Gorsel, E., and Luhar, A. (2011). Diagnosing errors in a land surface model (CABLE) in the time and frequency domains. *Journal of Geophysical Research: Biogeosciences*, 116(G1):G01034.

Ward, H. C., Evans, J. G., and Grimmond, C. S. B. (2013). Multi-season eddy covariance observations of energy, water and carbon fluxes over a suburban area in Swindon, UK. *Atmospheric Chemistry and Physics*, 13(9):4645–4666.

Ward, H. C., Evans, J. G., and Grimmond, C. S. B. (2014). Multi-scale sensible heat fluxes in the suburban environment from large-aperture scintillometry and eddy covariance. *Boundary-Layer Meteorology*, 152(1):65–89.

Ward, H. C., Evans, J. G., and Grimmond, C. S. B. (2015a). Infrared and millimetre-wave scintillometry in the suburban environment – Part 2: Large-area sensible and latent heat fluxes. *Atmospheric Measurement Techniques*, 8(3):1407–1424.

Ward, H. C., Evans, J. G., Grimmond, C. S. B., and Bradford, J. (2015b). Infrared and millimetre-wave scintillometry in the suburban environment – Part 1: Structure parameters. *Atmospheric Measurement Techniques*, 8(3):1385–1405.

Webb, E. K., Pearman, G. I., and Leuning, R. (1980). Correction of flux measurements for density effects due to heat and water vapour transfer. *Quarterly Journal of the Royal Meteorological Society*, 106(447):85–100.

Wehrli, C. (1985). Extraterrestrial solar spectrum. *WRC Pub*, 615.

Wen, J. and Su, Z. (2003). A time series based method for estimating relative soil moisture with ers wind scatterometer data. *Geophysical Research Letters*, 30(7):1397. 1397.

Wesely, M. L. (1976). The combined effect of temperature and humidity fluctuations on refractive index. *J. Appl. Meteor.*, 15(1):43–49.

Western, A. W., Blöschl, G., and Grayson, R. B. (1998). Geostatistical characterisation of soil moisture patterns in the Tarrawarra catchment. *Journal of Hydrology*, 205(1-2):20–37.

Whittle, P. (1954). On Stationary Processes in the plane. *Biometrika*, 41(3-4):434–449.

Wigneron, J.-P., Kerr, Y., Waldteufel, P., Saleh, K., Escorihuela, M.-J., Richaume, P., Ferrazzoli, P., de Rosnay, P., Gurney, R., Calvet, J.-C., Grant, J., Guglielmetti, M., Hornbuckle, B., Mätzler, C., Pellarin, T., and Schwank, M. (2007). L-band Microwave Emission of the Biosphere (L-MEB) Model: Description and calibration against experimental data sets over crop fields . *Remote Sensing of Environment*, 107(4):639 – 655.

Williams, M., Richardson, A. D., Reichstein, M., Stoy, P. C., Peylin, P., Verbeeck, H., Carvalhais, N., Jung, M., Hollinger, D. Y., Kattge, J., Leuning, R., Luo, Y., Tomelleri, E., Trudinger, C. M., and Wang, Y. P. (2009). Improving land surface models with FLUXNET data. *Biogeosciences*, 6(7):1341–1359.

Wilson, K., Goldstein, A., Falge, E., Aubinet, M., Baldocchi, D., Berbigier, P., Bernhofer, C., Ceulemans, R., Dolman, H., and Field, C. (2002). Energy balance closure at FLUXNET sites. *Agricultural and Forest Meteorology*, 113(1):223–243.

Wu, Q., Liu, H., Wang, L., and Deng, C. (2015). Evaluation of AMSR2 soil moisture products over the contiguous United States using in situ data from the International Soil Moisture Network. *International Journal of Applied Earth Observation and Geoinformation*, 45:187–199.

Wyngaard, JC and Izumi, Y and Collins, Stuart A (1971). Behavior of the Refractive-Index-Structure Parameter near the Ground*. *JOSA*, 61(12):1646–1650.

Xiao, J., Chen, J., Davis, K. J., and Reichstein, M. (2012). Advances in upscaling of eddy covariance measurements of carbon and water fluxes. *Journal of Geophysical Research: Biogeosciences*, 117(G1).

Xiao, J., Zhuang, Q., Law, B. E., Baldocchi, D. D., Chen, J., Richardson, A. D., Melillo, J. M., Davis, K. J., Hollinger, D. Y., Wharton, S., Oren, R., Noormets, A., Fischer, M. L., Verma, S. B., Cook, D. R., Sun, G., McNulty, S., Wofsy, S. C., Bolstad, P. V., Burns, S. P., Curtis, P. S., Drake, B. G., Falk, M., Foster, D. R., Gu, L., Hadley, J. L., Katul, G. G., Litvak, M., Ma, S., Martin, T. A., Matamala, R., Meyers, T. P., Monson, R. K., Munger, J. W., Oechel, W. C., Paw, U. K. T., Schmid, H. P., Scott, R. L., Starr, G., Suyker, A. E., and Torn, M. S. (2011). Assessing net ecosystem carbon exchange of U.S. terrestrial ecosystems by integrating eddy covariance flux measurements and satellite observations. *Agricultural and Forest Meteorology*, 151(1):60–69.

Yang, Y., Uddstrom, M., Revell, M., and Moore, S. (2014). Soil moisture simulation by JULES in New Zealand: verification and sensitivity tests. *Meteorological Applications*, 21(4):888–897.

Yee, M. S., Pauwels, V. R., Daly, E., Beringer, J., Rüdiger, C., McCabe, M. F., and Walker, J. P. (2015). A comparison of optical and microwave scintillometers with eddy covariance derived surface heat fluxes. *Agricultural and Forest Meteorology*, 213:226–239.

You-Jun, C. (2006). Letter to the Editor on “rank stability or temporal stability”. *Soil Science Society of America Journal*, 70(1):306.

Zeng, J., Li, Z., Chen, Q., Bi, H., Qiu, J., and Zou, P. (2015). Evaluation of remotely sensed and reanalysis soil moisture products over the tibetan plateau using in-situ observations. *Remote Sensing of Environment*, 163:91 – 110.

Zeweldi, D. A., Gebremichael, M., Wang, J., Sammis, T., Kleissl, J., and Miller, D. (2010). Intercomparison of sensible heat flux from large aperture scintillometer and eddy covariance methods: Field experiment over a homogeneous semi-arid region. *Boundary-layer meteorology*, 135(1):151–159.

Zhang, H., Pak, B., Wang, Y. P., Zhou, X., Zhang, Y., and Zhang, L. (2013). Evaluating surface water cycle simulated by the Australian community land surface model (CABLE) across different spatial and temporal domains. *Journal of Hydrometeorology*, 14(4):1119–1138.

Zhao, Y., Peth, S., Wang, X. Y., Lin, H., and Horn, R. (2010). Controls of surface soil moisture spatial patterns and their temporal stability in a semi-arid steppe. *Hydrological Processes*, 24(18):2507–2519.

Zhou, J., Fu, B., Gao, G., Lü, N., Lü, Y., and Wang, S. (2015). Temporal stability of surface soil moisture of different vegetation types in the Loess Plateau of China. *CATENA*, 128(0):1–15.

Zulkafli, Z., Buytaert, W., Onof, C., Lavado, W., and Guyot, J. L. (2013). A critical assessment of the JULES land surface model hydrology for humid tropical environments. *Hydrology and Earth System Sciences*, 17(3):1113–1132.